TECHNISCHE UNIVERSITÄT
CHEMNITZ

Inkjet printing of photonic structures and thin-film transistors based on evaporation-driven material transportation and self-assembly

by Enrico Sowade, born on 09.11.1984 in 09405 Zschopau, Germany

Dissertation

Approved by the Faculty of Mechanical Engineering at

Technische Universität Chemnitz to obtain the academic degree of

Doktor-Ingenieur (Dr.-Ing.)

Reviewers:

Prof. Dr. Reinhard R. Baumann

Technische Universität Chemnitz, Germany

Prof. Dr. Senentxu Lanceros-Méndez

University of Minho, Portugal

Date of Submission: 23.11.2016 Date of Defense: 09.06.2017

Bibliography

Author:

Enrico Sowade

Dissertation title:

Inkjet printing of photonic structures and thin-film transistors based on evaporation-driven material transportation and self-assembly

Dissertation at Technische Universität Chemnitz, Faculty of Mechanical Engineering, Department of Digital Printing and Imaging Technology, Chemnitz, 2017.

Number of pages: 191

Number of figures: 72

Number of tables: 6

Number of references: 307

Keywords: inkjet printing, printed photonics, printed electronics, spherical colloidal assemblies, printed thin-film transistors, manufacturing yield

Abstract

Inkjet printing has emerged from a digital graphic arts printing technology to become a versatile tool for the patterned deposition of functional materials. This thesis contributes to the research in the area of functional inkjet printing by focusing on two different topics: (i) inkjet printing of colloidal suspensions to study the principles of deposit formation and to develop deposits with photonic properties based on self-assembly, and (ii) the development of a reliable manufacturing process for all-inkjet-printed thin-film transistors, highlighting the importance of selection of materials and inks, print pattern generation, and the interplay between ink, substrate and printing conditions.

(i) Colloidal suspensions containing nanospheres were applied as ink formulation in order to study the fundamental processes of layer formation and to develop structures with periodically arranged nanospheres allowing the modulation of electromagnetic waves. Evaporation-driven self-assembly was found to be the main driver for the formation of the final deposit morphology. Fine-tuning of inkjet process parameters allows the deposition of highly ordered structures of nanospheres to be arranged as monolayer, multilayer or even three-dimensional assemblies with a microscopic spherical shape.

(ii) This thesis demonstrates the development of a manufacturing process for thin-film transistors based on inkjet printing. The knowledge obtained from the study with the colloidal nanospheres is used to generate homogeneous and continuous thin films that are stacked well-aligned to each other to form transistors. Industrial printheads were applied in the manufacturing process, allowing for the up-scaling of the manufacturing by printing of several thousands of devices, and thus the possibility to study the process yield as a function of printing parameters. The discrete droplet-by-droplet nature of the inkjet printing process imposes challenges on the control of printed patterns. Inkjet printing of electronic devices requires a detailed understanding about the process and all of the parameters that influence morphological or functional characteristics of the deposits, such as the selection of appropriate inks and materials, the orientation of the print pattern layout to the deposition process and the reliability of the inkjet process.

Preface and acknowledgements

This dissertation presents research work that was mainly carried out at the Department of Digital Printing and Imaging Technology of Technische Universität Chemnitz. The research work was financially supported by the following publicly-funded projects:

- Federal Ministry of Education and Research, *Mikrohips II* (no. 03FO2142)
- Federal Ministry for Economic Affairs and Energy, *Lasabs* (no. 16IN0648)
- European Commission, FP7 project *Technology and Design Kit for Printed Electronics* (*TDK4PE*, no. 287682)

Most of the results presented were published in scientific, peer-reviewed journals and at conferences. Some figures and sections of text of the journal publications were included in this dissertation. This is indicated at the corresponding positions within the running text, as well as at the end of corresponding chapters for a better overview. The comprehensive and partially published research carried out in many different project activities has been consolidated in this dissertation, aiming to form a consistent storyline about layer formation processes in functional inkjet printing and their relevance for printed electronic applications.

The study at TU Chemnitz as an undergraduate student as well as a PhD student under the supervision of Prof. Dr. Reinhard R. Baumann provided me with professional and highly skilled collaborators, productive research environment, excellent research facilities and great freedom concerning research directions, which allowed me to pursue own research interests.

From the beginning of my studies, my academic training was shaped by an exceptionally high degree of interdisciplinarity, inspiring me to see things differently and to cross boundaries of subject areas. At the beginning, this interdisciplinary approach was very demanding since it required me to study and to work across the multiple and in some cases completely different disciplines at the same time. In addition, it takes much effort to acquire knowledge in very different disciplines. However, finally I feel very comfortable with this interdisciplinary approach, since nothing exists in isolation from the rest of the world. To become acquainted with different subjects, mindsets, methods, styles, and of course different people is quite interesting, and can also be highly enlightening.

I would like to express my sincere gratitude to Prof. Dr. Reinhard R. Baumann for giving me the chance to gain experience and learn from his research group, and to contribute to its development.

He was always focusing on an open collaboration with other researchers all over the world, allowing me to experience different scientific mindsets and to establish networks that resulted in joint projects, publications and even friendships. Without the encouraging, energetic and persistent support of Prof. R. Reinhard Baumann, it would have not been possible to submit this thesis. I always felt his trust in me and my research work, and his enthusiasm for both fundamental science and applied, industrial research. I also thank Prof. Dr. Senentxu Lanceros-Méndez for his support and his time, for the valuable and motivating discussions, helpful comments and thoughts, interesting and innovative ideas, the open-mindedness, and the trust he placed in our research group. It was a pleasure to work with you on different topics in the field of printed electronics.

I would like to thank my project partners all around Europe for fruitful scientific discussions, especially within the project TDK4PE: Dr. Ana Alcalde, Prof. Dr. Jordi Carrabina, Maurice Clair, Prof. Dr. Henrique L. Gomes, Rocco Kundt, David Marin, Carme Martinez-Domingo, Prof. Dr. Iain McCulloch, Dr. Eloi Ramon, and Dr. Fulvia Villani. I am very thankful for experiencing international joint research activities with our guest scientists Dr. Helder Castro, Dr. Jinju Chen, Dr. Vitor Correia, Dr. Jorge Hernando Garcia, Dr. Hyunkyoo Kang, Ana Moya Lara, Dr. Panida Lorwongtragool, Mijal Mass, Dr. Leandro Monsalve, Dr. Juha Niittynen, and Juliana Oliveira. It was my pleasure to work with you and to learn from you.

I would like to thank all my current and former co-workers at Technische Universität Chemnitz and at Fraunhofer ENAS. I would like to express special gratitude to Dr. Thomas Blaudeck, who entrusted me with a very interesting research topic during my Magister study course, who supported me since the beginning of my employment with his expertise in natural sciences and with countless inspiring and fruitful scientific discussions (and of course, scientific lessons). I also express special gratitude to Kalyan Yoti Mitra for his encouraging and highly ambitious support in TDK4PE. The time you spent in the lab with me or on your own, printing thousands of devices, was really amazing. I also would like to thank Dr. Andreas Willert and Dr. Ralf Zichner for critically reviewing the first draft of this thesis and for all the scientific discussions and lessons.

I would also like to thank all former students who contributed to this thesis through both large and small support efforts in the laboratory: Andrea Arreba, Christian Belgardt, Zhongchen Feng, Frank Göthel, Sunil Kapadia, Mario Krohn, Maik Müller, Jessica Mammitzsch, Michael Pabsdorf, Maxim Polomoshnov, Parvin Rastegar, Sascha Riedel, Sabine Riemenschneider, Tobias Seifert, Christoph Sternkiker, Anastasia Vlasova, Stefan Wobst, and Zhenxing Xu.

Finally, I thank my friends, my parents and my family. I would like to say a big thank you to Annett, Lina and Nevio. You have been consistently supportive through the ups and downs during my PhD studies. I thank you for your patience and understanding for all the years when I once again spent too many hours in the laboratory or office, and taking work at home.

On the major results and novelty of the thesis

The following collection of bullet points conveys the core findings of the thesis and provides an overview of the highlights (chronological order according to the thesis structure):

Basic understanding of layer and structure formation of printed deposits

- Development of an understanding of functional inkjet printing as bottom-up manufacturing approach based on evaporation-driven self-assembly
- Study of the influence of surface energy on the evaporation-driven self-assembly of nanospheres in inkjet-printed droplets
- Inkjet printing of organic and inorganic nanospheres for the development of highly ordered structures with photonic properties

Inkjet printing of spherical colloidal assemblies

- Study on the influence of the waveform applied to piezoelectric inkjet printheads on the morphology of the printed deposits
- Exploitation of usually unintended droplet formation in inkjet printing for the development of spherical colloidal assemblies
- Relocation of the layer formation process from the substrate to the ejected droplet in-flight

Process optimization in printed electronics

- Demonstration of the importance of prepress issues (print pattern generation) and importance of the orientation of the print pattern layout related to the deposition process
- Exploitation of the coffee-ring effect for thin and smooth dielectric layers applied in thin-film transistor
- Selection of ink formulations and benchmark of silver nanoparticle inks used as electrodes for the inkjet-printed thin-film transistors

Manufacturing of thin-film transistors

- Development of a process chain for the manufacturing of all-inkjet-printed thin-film transistors and up-scaling of the manufacturing towards transistor arrays based on industrial inkjet printheads
- Manufacturing of thousands of thin-film transistors on flexible polymer films, in ambient conditions and without a requirement for cleanroom conditions, without any masks, and at low temperatures compatible with polymer substrates with manufacturing yields of > 90 % for small transistor sizes and an optimized transistor design

Table of contents

Bibliography ..... **II**
Abstract ..... **III**
Preface and acknowledgements ..... **IV**
On the major results and novelty of the thesis ..... **VII**
Table of contents ..... **VIII**
List of abbreviations and symbols ..... **X**
List of figures ..... **XII**
List of tables ..... **XX**
1 Introduction **1**
2 Fundamentals **6**
2.1 Inkjet printing – an overview 6
2.2 Piezoelectric inkjet technology and a historical overview of inkjet printing 10
2.3 Pattern and film formation in inkjet printing under the scheme of self-assembly 20
2.4 Inkjet printing of colloidal nanospheres 27
2.5 Spherical colloidal assemblies 29
2.6 All-inkjet-printed thin film transistors 31
3 Experimental section **35**
3.1 Inkjet printing systems and accessories 35
3.2 Inks and substrates 38
3.3 Print patterns 43
3.4 Post-processing 46
3.5 Optical, morphological and functional characterization 47
4 Inkjet printing of colloidal nanospheres: Evaporation-driven self-assembly based on ink-substrate interaction **49**
4.1 Single droplet deposit morphology: Interaction of substrate and ink 49
4.2 Optical properties of inkjet-printed single droplet monolayers and multilayers 54
5 Inkjet printing of colloidal nanospheres: Evaporation-driven self-assembly of SCAs independent on substrate properties **58**
5.1 Inkjet printing of spherical colloidal assemblies and their identification 58
5.2 Fine-tuning of the waveform applied to the printhead 60
5.3 Interaction of substrate and ink 66
5.4 Structures, morphologies and materials of SCAs 68

5.5 Optical properties of SCAs 76
6 Inkjet printing of TFTs: Process development and process reliability 80
6.1 Influence of print layout design 80
6.2 Selection of materials and inks 91
6.3 Manufacturing workflow and electrical TFT parameters 108
6.4 Manufacturing yields and failure origins 113
7 Summary and conclusion 124
References 127
Documentation of authorship and contribution of third persons 149
List of publications 151
APPENDIX A Formation of colloidal hemispheres on hydrophobic PTFE substrates 161
APPENDIX B Inkjet-printed higher-order cluster with N < 100 using BL280 162
APPENDIX C Inkjet-printed SCAs based on BS305 with similar sizes and inkjet-printed SCA based on PSC221 163
APPENDIX D Microreflectance spectra of SCAs and the processing of the spectra using the Savitzky-Golay filter with a second-order polynomial and a moving window of 100 data points 164
APPENDIX E Waveform, drop ejection and photographs of the printed patterns of Sun Chemical EMD5603 and UTDots UTDAgIJ1 165
APPENDIX F Smoothening of profiles obtained by profilometry of EMD5603 and UTDAgIJ1 and dependency of print resolution of layer height 166
APPENDIX G Percentage of area increase based on a 4 mm x 4 mm digital print pattern using the ink Harima NPS-JL and influence of print resolution and post-treatment temperature on sheets resistance 168
APPENDIX H Cross-sectional view of a TFT stack printed with the dielectric Sun Chemical EMD6415 that shows high layer thickness due to ink contraction after the deposition as presented in Figure 46 169
APPENDIX I Influence of printing parameters on the dielectric layer applied in the TFT 170
APPENDIX J Reduction of channel length by decreasing the S-D electrode channel length in the print pattern layout 171

List of abbreviations and symbols

Abbreviations

1D	One-dimensional
2D	Two-dimensional
3D	Three-dimensional
AFM	Atomic force microscopy
BL280	Nanospheres from Bangs Laboratories with 280 nm diameter
BS305	Nanospheres from BS-Partikel GmbH with 305 nm diameter
BSE	Back-scattered electron
cPVP	Cross-linked poly-4-vinylphenol
CNT	Carbon nanotube
dpi	Dots per inch
DMC	Dimatix Materials Cartridge
DMP 2831	Dimatix Materials Printer 2831
DMP 3000	Dimatix Materials Printer 3000
DTP	Desktop publishing
EDX	Energy-dispersive X-ray
fcc	Face-centered cubic
FIB	Focused ion beam
FWHM	Full-width at half-maximum wavelength
HMDS	Hexamethyldisilazane
OTS	Octadecyltrichlorosilane
PC	Polycarbonate
PEDOT:PSS	poly(3,4-ethylenedioxythiophene) polystyrene sulfonate
PES	Polyether sulfone
PET	Polyethylene terephthalate
PEN	Polyethylene naphthalate
PGMEA	Propylene glycol monomethyl ether acetate
PI	Polyimide
PMFM	Poly(melamine-co-formaldehyde) methylated
PP	Polypropylene
PS	Polystyrene
PSC221	Nanospheres from Polysciences with 221 nm diameter
PVC	Polyvinylchlodride
PVP	Poly-4-vinylphenol
RCA	Radio Corporation of America
S-D	Source-Drain
SCA	Spherical colloidal assembly
SEM	Scanning electron microscopy
TFT	Thin-film transistor
UV	Ultra violet

Symbols

d_{drop}	m	Droplet diameter
d_P	m	Diameter of nanosphere
d_S	m	Diameter of SCA
D111	m	Lattice constant/interplanar spacing
L	m	Channel length between source and drain electrode
n_A		Refractive index of air voids
n_P		Refractive index of nanospheres
N		Number of constituent nanospheres in a SCA
s_{drop}	m	Center-to-center distance between droplets, drop space
s_e	m	Center-to-center distance between droplets at the edge of a print element ($\neq s_{drop}$)
t_{dwell}	s	Dwell time of waveform amplitude
t_{fall}	s	Fall time of waveform
t_{rise}	s	Rise time of waveform
T_g	°C	Glass transition temperature
W	m	Channel width along source and drain electrode
β	°	Print pattern orientation angle
λ	nm	Wavelength
μ	$cm^2/(V \cdot s)$	Charge carrier mobility
μ_e	(μm/sec)/(V/cm)	Electrophoretic mobility
σ_{LV}	N/m	Surface tension liquid-vapor interface
σ_{SL}	N/m	Surface tension solid-liquid interface
σ_{SV}	N/m	Surface tension solid-vapor interface
θ	°	Equilibrium contact angle of a liquid on a surface
ζ	V	Zeta potential
¤		Print start position

List of figures

Figure 1: Application landscape of inkjet printing (adapted and revised from Gilboa[1]) 2
Figure 2: Overview of the main storyline and structure of the thesis 3
Figure 3: Working principle of the inkjet printing process system 7
Figure 4: Simple and complex polar driving waveforms and unipolar driving waveform (adapted from Wu[39]).....11
Figure 5: Drop formation cycle with 10 µs intervals after application of the waveform to the piezoelectric transducer (inkjet printhead: Fujifilm Dimatix QS256, ink: ANP DGP 40LT-15C) 12
Figure 6: Overview and classification of print pattern elements; (A) deposition of single droplets without droplet coalescence, (B) lines upon droplet coalescence with one droplet in width termed 1D films and (C) 2D films consisting of deposited droplet with coalescence in x- and y-direction; (D) is a top view schematic of (A) indicating print origin, drop space s_{drop} and droplet diameter d_{drop}, (E) shows the formation of lines differentiating between lines deposited along the printing path and perpendicular to the printing path (unidirectional printing, for reasons of simplification a printhead with only one nozzle activated is assumed for (E)) 21
Figure 7: (A) liquid sessile droplet on a flat solid surface reaching its equilibrium contact angle θ at the three phase contact line, (B) different wetting behavior of droplets on solid flat surfaces according to the contact angle, (C) two basic evaporation modes – constant contact area and constant contact angle – for sessile droplets on solid surfaces (adapted and revised from Daly, Jung and Talbot[15]) 23
Figure 8: Utilization of inkjet printing and the principle of self-assembly to form from a disordered state with microscopic randomness of functional constituents deposits with higher order of the functional constituents 26
Figure 9: Examples of SCA by inkjet printing on solid substrates: (A) top view and (B) side view; (C) is a model of the SCA showing the arrangement of the nanospheres within the SCA; (D) and (E) depict schematically two basic concepts applied for the manufacturing of the SCA: (D) WSA method and (E) DSA method 30
Figure 10: Image representing exemplarily the state-of-the-art of all-inkjet-printed TFTs: (A) photograph showing four printed TFTs on flexible polymer substrate and (B) is a magnified section depicting a TFT with a simple one-channel design (adapted from [176]).....34

Figure 11: (A) image of the inside of the inkjet system DMP 2831 with installed DMC printhead and (B) the DMC consisting of fluid module and printhead (adapted from [222]); the insets are microscopic images of a section of the nozzle plate with the square-shaped nozzles 35
Figure 12: (A) image of the inside of the inkjet system DMP 3000; (B)-(E) show images of the printhead assembly required for the use with industrial inkjet printheads; (B) is the main assembly plate with the mounted printhead, (C) the printhead carrier with installed printhead as bottom view, (D) the printhead assembly with ink development reservoir on the back and (E) the installed printhead assembly in the cartridge carriage of the DMP 3000 37
Figure 13: (A) print pattern layout (print areas are shown in black) consisting of lines with a line width of 500 µm at different orientation angles β (angles shown in °, blue color) to the printing process and with measurement pads; the coordinate axes at the top left indicate the print origin (¤), printing direction (x), and transfer direction (y); (B) – (D) are detailed images of the red-marked section in (A) depicting the digital pixel grid at the end of the designed line (adapted from [95]) 44
Figure 14: (A) scheme of the print pattern layout for the conductive ink formulations consisting of 13 lines (1D films) with different print resolutions (not true to scale, number of droplets not representative); (B) microscopic image of the ink UTDAgIJ1 from UTDots on silicon substrate printed with the line test layout shown in (A).....45
Figure 15: Architecture of the printed TFTs as (A) top view and (B) cross-sectional view; the electrodes are based on silver nanoparticles, the dielectric and the OSC are organic materials (adapted from [176]) 46
Figure 16: (A) measured water contact angle and measured droplet diameter of the inkjet-printed deposits of the suspensions BS305 and DS300 as a function of surface treatment method; (B) schematic cross-sectional view of the principle morphology of the inkjet-printed deposits; (C)-(G) are SEM images of typical deposits using the suspension BS305 of the highlighted (color code) data points of (A) (all adapted from [98]).....50
Figure 17: Deposits of inkjet-printed colloidal suspensions on cleaned glass slides; the deposit (A) was obtained with one droplet of the BS305 and (B) with printing two droplets of BS305 on top of each other; (C) was obtained with one droplet of BL280 diluted to 2 wt% and formulated with 60 wt% formamide and (D) with printing two droplets of this suspension on top of each other; (E) is a side-view of (D) at about 85° substrate inclination[98] 52
Figure 18: (A) single-droplet deposit using 2 wt% BS305 on cleaned glass, and (B) a detailed section of (A) showing the high ordering of the particles in hexagonal arrays with a few point and line defects; (C) shows an inkjet-printed deposit with randomly arranged nanospheres obtained by addition of 6.25 wt% diethylene glycol to the 1.5 wt% BS305 suspension; (D)

close-packed two-dimensional colloidal array with hexagonal structure by addition of 2.5 wt% formamide (adapted from [98]) 53
Figure 19: (A)-(D) are microreflectance spectra of the inkjet-printed deposits using (A) BL280, (B) BS305 (2 wt%), (C) BS305 & BL280 and (D) PSC221; (E) shows a single droplet deposit (BS305) with reflected light microscopy (the measurement position for the spectroscopy is indicated) and (F) a similar deposit by SEM; (G) shows a printed deposit comprising multilayers as well as a monolayers (BS305); the white bright part of the multilayer is shown in higher magnification in (H) and as SEM image in (J); (I) is a light microscopy image of a multilayer deposit using PSC221 55
Figure 20: SEM images in BSE mode of deposits using the binary suspension BS305 & BL280, (A) monolayer with hexagonally close-packed structure, (B) enhanced contrast of the image obtained by the BSE mode and (C) EDX mapping of the same image position displayed in (B) (adapted from [154]) 57
Figure 21: Inkjet-printed SCAs based on BS305 on cleaned glass substrates, (A) is a top-view incident light microscopy image in bright-field mode with a 50x magnification objective, (B) the corresponding top-view SEM image, (C) SEM image with tilted view (about 60 °) and (D) magnification of the centered SCA of (C) with 60 ° tilt.....59
Figure 22: Light microscopy images of deposits obtained using BL280, (A) top-view with incident light mode, (B) the same sample position as (A) but in dark field mode; (C) shows the different appearance of SCAs and normal monolayer and multilayer deposits (adapted from [154]) 60
Figure 23: Three differently designed waveforms applied to the inkjet printheads for the deposition of the colloidal suspensions[154].....61
Figure 24: Influence of the waveform applied to the inkjet printhead on the droplet ejection and the resulting deposit on the substrate; (A) and (E) depict two classes of waveforms (both driven with a frequency of 3 kHz), (B) and (F) are schematics of the basic principle of the droplet ejection based on waveform A and B (waveform C shows similar drop ejection as Waveform B); (C) and (G) show the droplet ejection captured with the DMP 2831 built-in drop watcher camera corresponding to the two different waveforms; (D) and (H) are SEM images showing the different final deposit morphologies obtained on the substrate as a result of waveform A and B (adapted from [154]).....62
Figure 25: Reliability of the manufacturing method of SCAs using the DMP 2831 represented by (A) the manufacturing yield, and (B) the number of manufactured SCAs per area as a function of applied waveform and solids content of the suspension; the print pattern was defined as rectangle with an area of 0.35 mm² at 5080 dpi (adapted from [154]) 64

Figure 26: (A) large field with small dark dots, each of the dots represents an SCA; (B) is a magnified section of (A), some of the SCAs are marked and presented in the inset at higher magnification – in general most of the dots shown here are SCAs.....66
Figure 27: Development of SCAs based on BS305 independent on substrate surface properties; (A) is a scheme indicating the expected wetting states formed by sessile droplets of the colloidal suspensions with the differently treated substrates; (B)-(F) are top-view SEM images of SCAs obtained on the differently treated substrates proofing that the formation of SCAs is independent on the substrate properties (adapted from [166]) 67
Figure 28: Tilted view by SEM of SCAs based on BS305 with changing number of constituent nanospheres: (A) N ≈ 140, (B) N ≈ 1900, (C) N ≈ 31800; (D) and (E) show variable sizes of the assemblies obtained in a line arrangement as well as randomly distributed as a result of one individual droplet spray signal, (F) presents the line-up of particles with similar size[154] 69
Figure 29: SCAs based on silver nanoparticles using the ink NPS-JL from Harima; (A) is a SCA which was inkjet-printed and subsequently simply dried at 60 °C for several hours; (B) is a SCA which was dried at 60 °C and subsequently sintered on hot plate at 200 °C 71
Figure 30: Internal structure of SCAs based on BS305 revealed by the micro-force apparatus; (A) top-view of a broken SCA, and (B) side-view at 60 ° substrate tilt of the SCA of (A); (C) is a deformed SCA, the opened area is shown with higher magnification in (D) (adapted from [154,166]) 72
Figure 31: Structure of an inkjet-printed SCA based on BS305; (A) is a top-view and (B) a side-view of a SCA that was cut by FIB; (C) is a magnified section of (A) highlighting the hexagonal packing order of the nanospheres on the surface of the SCA; (D) is a cross-section view on the hemispherical area resulting from the FIB cut, the marked rectangles are depicted with higher magnification in (E) and (F) (adapted from [154]).....73
Figure 32: Top-view images of inkjet-printed SCAs based on the binary suspension BS305 & BL280 imaged by SEM in BSE mode; (B) is the same SCA as shown in (A) but with intensified contrast to indicate the distribution of PS and SiO_2 nanospheres (adapted from [154]).....75
Figure 33: (A) scheme of the selective removal of PS nanospheres from the initially binary SCAs by heating in a furnace; (B) to (D) are spherical skeletons of SiO_2 nanospheres obtained by the removal of PS from the inkjet-printed SCAs with different numbers of constituent nanospheres representing initially (B) higher-order clusters, (C) supraparticles and (D) supraballs[154].....76
Figure 34: Normalized microreflectance spectra of representative SCAs based on BL280, BS305 and PSC221 (adapted from [154]) 77

Figure 35: Reflectance spectra of SCAs based on BS305; SCAs with different number of constituent nanospheres were measured representing the three categories higher-order cluster, supraprticle, and supraball 79
Figure 36: (A) and (B) are schematics showing exemplarily the influence of the orientation of a line pattern on the number of pixels; as indicated in the scheme, the angle of the pixel grid is constant, as well as the desired print pattern area which corresponds to the line area; (A) represents a print pattern element with a fixed print resolution and an orientation angle β = 0 ° consisting of 85 px; (B) shows the same line element having exactly the same area size and the same pixel grid but with β = 22.5 °, here the number of pixels reduced to 77; (C) is a graph with the calculated number of pixels for the print pattern layouts at different print resolutions of Figure 13A (only the line elements are considered, not the measurement pads), green horizontal lines in the graph indicate the reference which is the defined number of pixels for β = 0 ° for each print resolution (adapted from [95]) 82
Figure 37: (A) average line widths and line peak heights of inkjet-printed 1D film deposits as a function of print resolution and orientation angle β (please note: the axis for the line peak height is inverted to avoid overlaying of the data plots); (B) exemplarily depicts microscopic images of the printed lines with a print resolution of 2540 dpi, 847 dpi and 564 dpi at β = 0 ° (first row) and β = 90 ° (second row) (adapted from [96]) 83
Figure 38: Schematic illustration of the influence of the pattern orientation angle β for exemplarily (A) β = 0 ° and (B) β = 90 ° on the deposited number of droplets per printing pass; the number of droplets per printing pass is much higher for the line pattern element with β = 0 ° than β = 90 °; therefore, the deposition of the print pattern element in (B) requires much more printing passes and thus longer time duration than in (A) (adapted from [95]) 84
Figure 39: (A) and (C) are schematics showing exemplarily the influence of the orientation angle β on the shape of the edges (marked red) of the printed elements; (B) and (D) are the corresponding microscopic images of the lines printed using EMD5603 from Sun Chemical at a print resolution of 847 dpi (adapted from [95]) 86
Figure 40: Average line widths of inkjet-printed lines (2D films) of (A) EMD5603, and (B) UTDAgIJ1 as a function of orientation angle β and print resolution; layer profiles obtained with profilometry of (C) EMD5603 and (D) UTDAgIJ1 at a print resolution of 1016 dpi (adapted from [95]); (E) and (F) present the maximum heights for EMD5603 and UTDAgIJ1 of the profiles of (C) and (D) as a function of orientation angle β 89
Figure 41: Average line resistance of lines inkjet-printed with (A) EMD5603, and (B) UTDAgIJ1 as a function of print resolution and line orientation β; (C) is an idealized comparison of the main parameters investigated as a function of line orientation, the color code indicates qualitatively

a range from low to high with respect to the parameters under comparison (adapted from [95]) 91
Figure 42: (A) measured line widths of commercially available silver ink formulations as a function of print resolution and drop space; (B) is a sectional view of (A) up to a line width of about 140 µm; all of the inks were printed with the Fujifilm Dimatix DMC printheads (10 pL nominal droplet volume) on PEN substrates which were heated to about 50 °C 95
Figure 43: Average standard deviation of the line width measurements of the inkjet-printed silver inks as indicator for the edge sharpness of the lines; all of the inks were printed with the Fujifilm Dimatix DMC printheads (10 pL nominal droplet volume) on PEN substrates heated to about 50 °C 97
Figure 44: (A) inkjet-printed silver gate electrode pattern using PVnanocell I30EG-1, (B) and (D) are detailed microscopic images of different rectangles having an area of 750 x 750 µm² and 1000 µm x 1200 µm, (C) and (E) are 3D profiles done by laser microscopy 98
Figure 45: Comparison of sheet resistance of the inkjet-printed silver ink formulations; printing was done at 1270 dpi (corresponds to 20 µm drop space) on PEN substrate and drying and sintering at 160 °C for 30 min (sheet resistance not normalized to layer thickness) 99
Figure 46: (A) percentage area coverage of Sun Chemical EMD6415 printed as 2 mm x 2 mm square on Sun Chemical EMD5603 silver layer indicating decrease/lateral shrinkage due to ink contraction; (B) microscopic images showing the inkjet-printed layer and the contraction at different time periods after the deposition 101
Figure 47: (A) average layer thickness of the dielectric ink Tritron V Photon Clear NonWet as a function of print resolution/drop space; inkjet printing of squared print patterns with 15 mm x 15 mm area size was performed with the SX3 printhead and the DMP 3000; (B) Cross-sectional view of the dielectric layer embedded between silver gate and silver drain electrode (adapted from [201]) 102
Figure 48: (A) layer stack of silver gate electrode, dielectric cPVP layer and silver S-D electrodes; the dielectric is designed such that the coffee ring is outside the active TFT area; (B) is a profile of the dielectric layer morphology nearby the measurement position indicated in (A) (adapted from [301]) 104
Figure 49: Inkjet-printed TFT using cPVP as dielectric; (A) cross-sectional view on the TFT layer stack; (B) is a magnified image section of (A) and (C) is the surface profile of the S-D electrodes printed on top of the cPVP dielectric, the schematic inset shows the measurement direction 106
Figure 50: Inkjet-printed OSC layers with a print resolution of 1270 dpi on PEN substrate at (A) 20 °C substrate temperature, (B) 30 °C substrate temperature, (C) 60 °C substrate

temperature and (D) at 60 °C substrate temperature deposited directly on the Gate/dielectric/S-D electrode layer stack to complete the TFT (white dotted lines indicate the designed layer size for the OSC layer)[176] 107
Figure 51: Scheme of the developed manufacturing workflow for all-inkjet-printed TFTs 108
Figure 52: (A) 924 all-inkjet-printed TFTs arranged in six pattern arrays on a PEN DIN A4 sheet, (B)-(E) layer-by-layer manufacturing approach for the all-inkjet-printed TFTs: (B) silver gate electrode, (C) cPVP dielectric layer deposited on gate electrode, (D) silver S-D electrodes printed on the cPVP dielectric with overlap to the gate electrode and (E) OSC printed as last layer to complete the TFT (adapted from [176]) 110
Figure 53: Typical (A) transfer characteristics and (B) output characteristics, exemplarily for a TFT with a designed channel length of about 100 µm (W/L = 140) using 508 dpi print resolution for the S-D electrodes and 564 dpi print resolution for the cPVP dielectric layer; (C)-(F) Electrical characteristics of about 400 functional TFTs: (C) charge carrier mobility, (D) I_{ON}/I_{OFF}, (E) threshold voltage and (F) maximum drain-source current as a function of W/L (adapted from [176]) 112
Figure 54: (A) percentage of S-D electrodes short-circuited and measured channel length as a function of print resolution; (B)-(E) are microscopic images of the TFT S-D electrodes for each print resolution considered in the graph (A) (adapted from [176]) 114
Figure 55: (A) percentage of functional S-D electrodes as a function of W/L (about 132 TFTs were considered per W/L); (B)-(H) are microscopic images showing the inkjet-printed layer stack of gate electrode, cPVP dielectric and S-D electrodes with varying W/L: (B) 20, (C) 40, (D) 80, (E) 100, (F) 140, (G) 180, (H) 240 (adapted from [176]).....115
Figure 56: Yield of 924 all-inkjet-printed TFTs indicated by the percentage of functional TFTs as a function of W/L[176] 116
Figure 57: Overview of failures detected in inkjet-printed layers of the all-inkjet-printed TFTs; (A)-(C) are failures due to wetting properties of the deposited ink on the printed surface, (A) depicts a printed gate electrode with intense spreading on PEN, (B) shows intense ink spreading of the S-D electrodes on cPVP resulting in a short-circuit and (C) depicts inhomogeneous layer formation of the OSC due to the surface energy contrast between cPVP layer and S-D silver electrodes; (D) shows satellite droplets of silver ink and (E) is a magnification of the marked area in (D); (F) and (G) represent short-circuited S-D electrodes due to odd droplet jetting; (H) is an example of a short circuit between S-D and (F) between drain and gate electrode due to dirt and dust particles; (J) and (L) present TFTs with an open circuit due to missing droplets in the gate and the S-D layer, and (K) shows the dielectric layer with missing lines due to inkjet nozzle clogging (adapted from [301]) 117

Figure 58: Example of jetting oddness of Sun Chemical EMD5603 using a D128/10 DPN printhead in the DMP 3000, the image was obtained with the build-in drop-watcher camera, the colored lines were added to make the different droplet trajectories and distances more clear 119
Figure 59: (A) position map of inkjet-printed TFTs; each color pixel represents the position of a defective TFT: the red pixels indicate TFTs with S-D short circuits, the blue pixels TFTs with gate-source and/or drain short circuits, grey pixels open circuits and cyan pixels high leakage currents through the dielectric; (B) is a schematic of the different defects under consideration, and (C) is a histogram based on the position map showing the number of defective TFTs as a function of W/L (adapted from [301]).....121

List of tables

Table 1: Overview of technology benefits of the inkjet printing process based on different categories (information gathered from [16,20–24]) 9

Table 2: Specification overview for the used printheads based on Fujifilm Dimatix data sheets[222–226,228] and accessories price list from 2011[229] 38

Table 3: Characteristics of the colloidal nanosphere suspensions used for the experiments[98,154] 39

Table 4: Measured contact angles of sessile deionized water droplets on the differently treated glass surfaces[166] 40

Table 5: Overview of the printed commercially available silver inks and their characteristics according to the corresponding product data sheets provided by the manufacturers; costs are calculated based on quotes provided to the Technische Universität Chemnitz for 100 mL or 100 g of the silver ink formulations 41

Table 6: Qualitative summary of main trends of single droplet morphology based on correlations between printing results and varying printing parameters[98] 51

1 Introduction

According to the latest news and forecasts[a], the market development of inkjet printing technology during the last few years has been dramatically expanding. While other print sectors, especially the conventional printing market, are facing economic challenges, the interest in digital inkjet printing is increasing continuously and forecasts indicate further market growth. Among others, there might be two main drivers for this development:

1) During the last several years, many efforts in the inkjet technology development were dedicated towards an improvement in speed, reliability, fluid compatibility, and print quality to meet the demands of industrial and home users.
2) There is an increasing demand for product individualization and increasing product diversity, which in turn has caused shorter print runs down to print run one.

Figure 1 shows the application landscape of inkjet printing technology. Inkjet printing is a well-established process for printing texts and images on paper substrates. During approximately the last 20 years, the technology has been increasingly applied in the small office and home office environments. Of course, the electrophotography process is also a mature digital printing technology. However, there are limitations concerning the format, substrate flexibility, and the costs of both the price per page and the machine itself, especially considering full color printing. For several years, inkjet printing has also become more and more relevant for industrial manufacturing. The technology is nowadays extensively used for product coding, labelling and marking, addressing, in-plant printing, wide and super-wide format printing, printing on non-flat, irregular substrate shapes, and for home office applications. Because new inkjet printheads are able to jet a high range of fluids, the printing process can be applied to nearly any solid substrate. In addition, inkjet printing turned out as a promising technology for new fields of industrial manufacturing such as the industrial decoration of ceramics, textiles and garments, flooring and

[a] a) Smithers Pira market reports, e.g., “The Future of Inkjet Printing to 2019”;
b) IT Strategies market reports, e.g., “The Continuous Feed Inkjet Production Market in 2014”;
c) BBC market research, e.g., “Emerging Inkjet Printing Technologies, Applications and Global Markets”
d) InfoTrends market research, e.g., “Western European Digital Production Printing Application Forecast: 2012-2017”
e) www.inplantgraphics.com/article/inkjet-the-future-of-in-plant-printing-services/; by Dennis Amorosano, 04.12.2015
f) www.myprintresource.com/article/12014244/2015-production-inkjet-market-trends; by Denise M. Gustavson, 30.11.2014
g) www.myprintresource.com/article/12134320/production-inkjet-papers-are-the-engine-for-inkjet-growth; by John Crumbough, 01.12.2015
h) www.piworld.com/article/inkjets-rapid-acceleration/; by Marco Boer, 01.04.2015
i) www.inkworldmagazine.com/contents/view_online-exclusives/2014-05-28/advances-in-inkjet-printing-technology-drives-growth-in-market; by David Savastano, 28.05.2014

laminates, furnishings, wallpapers, and many others. The different fields of application proof the versatility of inkjet printing.

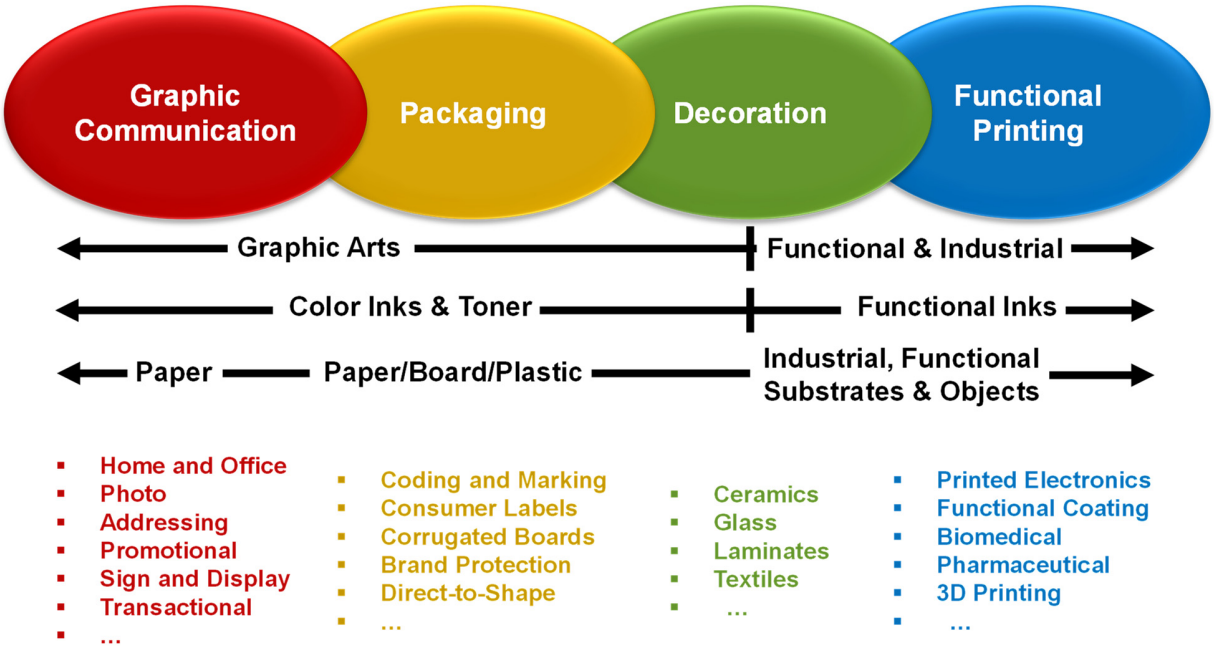

Figure 1: Application landscape of inkjet printing (adapted and revised from Gilboa[1])

In recent years, inkjet printing technology has been increasingly applied as a versatile and advanced deposition tool for various materials in the field of functional printing (see Figure 1). Functional printing is a hypernym referring to the application of both traditional and digital printing technologies for the deposition of functional material patterns. In this scheme, “functional” means that these patterns are equipped with functionalities beyond the generation of a color impression for the visual sense of the human eye. Printed patterns can have specialized electrical, optical, mechanical, biological, chemical or many other functionalities. The most prominent subsets of functional printing are currently printed electronics and three-dimensional (3D) printing. Also in the field of functional printing, interest in inkjet printing technology during the last few years has been increasingly growing, outweighing other digital and conventional printing technologies. This growing can be demonstrated by numerous scientific publications on inkjet printing and by companies developing new printheads (e.g., Xaar with the 1003 AMp printhead[2]) and systems (e.g., Ceradrop[3], Notion Systems[4] or Ardeje[5]) dedicated to functional inkjet printing.

Two applications employing functional inkjet printing are the focus of this dissertation. The formation process of ejected droplets into functional deposits of a defined shape is of the highest interest in the field of functional printing. I propose an alternative understanding of the layer

formation process; namely, that inkjet printing is considered as a bottom-up manufacturing technology based on the principle of evaporation-driven self-assembly, or in general as evaporation-driven material flows (i.e., material transportation inside the deposited liquid films is initiated by convective flows as a result of evaporation). Under this scheme, an explanation of the different deposit morphologies obtained through inkjet printing and the evaporation-driven material transportation is given.

The aim of the dissertation is also to highlight the importance of the process chain in functional printing. Thus, a more general view of the entire functional inkjet printing process chain is presented, taking into account general considerations about fundamental layer formation processes based on a model ink suspension containing nanospheres, the relevance of print image preparation (i.e., prepress issues, such as image rasterization and the importance of the orientation of the digital print image related to the deposition process), and finally, the reliability of an up-scaled inkjet printing process for the manufacturing of transistor arrays.

Figure 2 depicts the main storyline and structure of this thesis. Functional inkjet printing is the basis and the subject of focus of this thesis. All the results will be discussed with reference to the inkjet printing process.

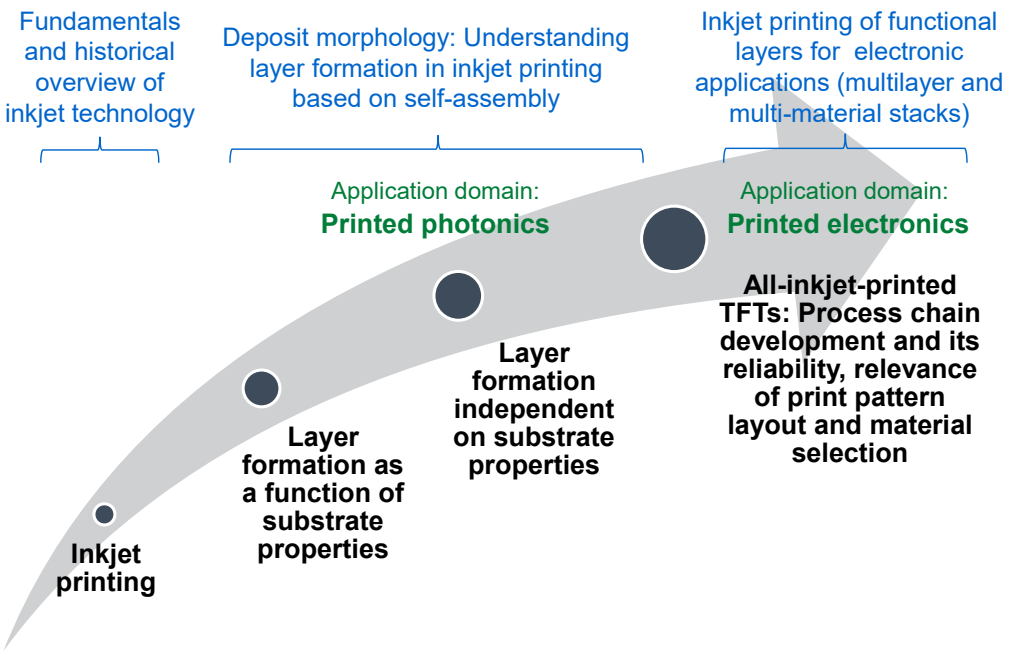

Figure 2: Overview of the main storyline and structure of the thesis

Fundamental aspects of inkjet printing are introduced in Chapter 2. The technological benefits and basic principles of piezoelectric droplet ejection are introduced. A historical literature overview of the inkjet technology development is presented focusing on scientific review articles. Basic print patterns and the process of pattern formation in inkjet printing is discussed.
An alternative way of understanding functional inkjet printing is proposed based on the bottom-up manufacturing approach and evaporation-driven self-assembly. Chapter 2 also provides basics of the interplay between substrate and ink. Further, Chapter 2 demonstrates that the bottom-up principle and self-assembly processes are inherent phenomena in inkjet printing, and that they determine the pattern (the term “pattern” is used in this thesis in general for printed deposits or print pattern files) and structure (the term “structure” is used in this thesis for printed deposits showing a clearly noticeable nano- or micrometer texture) formation of the printed deposits. The state-of-the-art of the two main applications domains of the thesis, (i) inkjet printing of colloidal nanospheres for the development of photonic structures and (ii) development of a manufacturing chain for all-inkjet-printed thin-film transistors (TFTs) is reviewed.

The experimental section in Chapter 3 briefly introduces the printers, printer accessories, inks and substrates, as well as analytical equipment and methods. It also provides a comprehensive summary of the characteristics of the employed colloidal suspensions as well as of the benchmarked silver ink formulations.

Chapter 4 is dedicated to the investigation of fundamental layer formation principles as a function of substrate properties and ink formulation. Model ink formulations consisting of spherical nanospheres, dispersed in aqueous fluids, are applied, and the interaction of substrate and ink is highlighted. The deposit morphologies obtained are discussed on the basis of evaporation-induced convective flows.

Chapter 5 presents the development of spherical colloidal assemblies of nanospheres using inkjet printing. These microscopic 3D spherical structures of varying size can be manufactured by the relocation of solvent evaporation from the sessile droplet on a substrate to the ejected droplet in flight. The remaining spherical assemblies of nanospheres can be prepared independently on substrate properties and have photonic characteristics.
This basic understanding about layer formation in inkjet printing as discussed in Chapters 4 and 5 is the key towards the development of complex multilayer and multi-material stacks, such as those forming TFTs or sensors.

The development of a manufacturing process chain for all-inkjet-printed TFTs is presented in Chapter 6. The focus is not on the electrical performance of the transistors (as it is usually the case in the literature), but rather on the development of the inkjet process chain for the manufacturing and its reliability. The generation of appropriate print pattern layouts and the influence of their orientation to the deposition process is shown within the process chain. The importance of the selection of suitable inks and materials for inkjet-printed TFTs is highlighted, and a benchmark for silver ink formulations that are used as electrodes is given. The influence of printing parameters and materials as well as the print pattern layout on morphological and functional characteristics of the layers and TFTs is discussed.

Finally, all the results of the thesis are briefly summarized and concluded in Chapter 7.

2 Fundamentals

2.1 Inkjet printing – an overview

The term “inkjet printing” encompasses a family of different digital non-contact direct writing technologies aimed at generating tiny, free-flying droplets of liquids ejected from a small nozzle in a defined manner. “Defined” refers, in this context, to the moment of droplet ejection, droplet volume, number of droplets, droplet repetition rate, droplet velocity and droplet impact position. For most of the applications in inkjet printing, the droplets will impact on a substrate. A larger pattern on the substrate can be obtained by progressively delivering further droplets in a droplet-by-droplet deposition approach, while moving either the printhead or the substrate relative to each other. In other words, inkjet printing can be considered as a bottom-up technology, since droplets are added as long as the desired pattern is generated. Thus, the working principle of inkjet printing consists generally of four process steps (which is also sometimes simplified into three process steps in the literature[6]):

(i) Positioning of printhead and substrate
(ii) Droplet formation and droplet ejection
(iii) Droplet impact on substrate: Spreading, contraction and/or coalescence of droplets
(iv) Solvent removal, formation of functionality (functionality forming)

These process steps are depicted schematically in Figure 3. After positioning the printhead and/or the substrate, the droplet formation process is initiated by electronic signals resulting in the ejection of droplets. The droplets impact on a substrate. This process of droplets impacting on the substrate is quite complex and the droplet will undergo – strongly depending on the substrate properties and its interaction with the liquid – several shape transitions (e.g., as a result of the kinetic energy of the ejected droplet) before it will find its equilibrium.[7–9] Right after the impact phase, further fluid dynamic phenomena will take place, such as wetting and spreading[10], or the contraction of the deposited fluid and droplet coalescence.

In graphics inkjet printing, droplet coalescence and further fluid dynamics are usually controlled by choosing appropriate absorbent substrates to prevent color bleeding or color blurring, because these effects result in reduced image quality.[11,12] In most of the applications of functional printing, non-absorbent substrates are used, and the interaction of spreading droplets forming defined beads, lines or more complex patterns is of the highest importance.[13] Droplet spreading or the deposition of overlapping droplets will lead to a continuous liquid film. The final step in the process

is the solvent removal and/or functionality forming. In some cases, solvent removal and functionality formation can be considered as two separate processes (i.e., drying to evaporate the solvent and oven sintering of metal nanoparticles to form a conductive film). In other cases, the functionality of the film is already formed when the solvent is removed (e.g., polymeric dielectric films). For ultra violet (UV) curable ink formulations, the process of solvent removal does not take place, because no solvent is used for such inks. They are cured by UV radiation. Apart from UV ink formulations, drying in the form of solvent evaporation is usually crucial for the inkjet process, since the amount of solvents in inkjet printing is relatively high compared to other printing methods.[14] Functionality forming refers mainly to functional printing, and describes any post-processing methods required to reveal the intended functionality of the deposits.

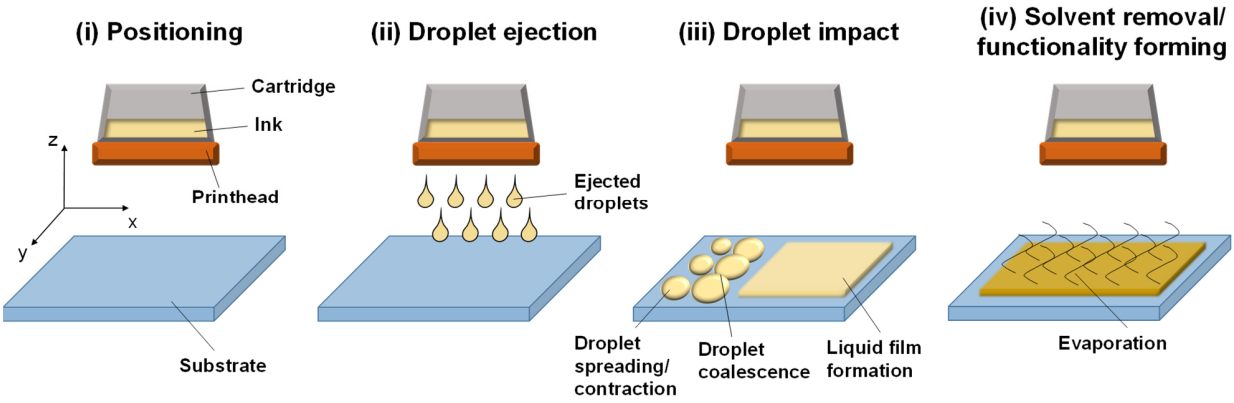

Figure 3: Working principle of the inkjet printing process system

The previously explained basic principle of inkjet printing is fundamentally different to conventional printing methods such as screen, gravure, flexographic or offset printing. Here, the print pattern is objectified in a physical form usually described as the “print master”. The pattern of the print master is directly or indirectly transferred to the substrate through direct contact, which is generally described as impact printing. Thus, the print master is decisive for the process, and a pattern change involves a print master change.[15,16]

Nowadays, inkjet printing is a mature technology achieving remarkable levels of print quality (e.g., Canon Pixma iP4700 with 9600 x 2400 dpi[17]), print speed (e.g., Kodak stream inkjet technology with up to about 15 m/s for monochrome imprinting systems (Kodak Prosper S30[18]) and about 5 m/s for full color printing (Kodak Prosper 6000P[19])), and efficiency. The main driver for the inkjet development was the small office home office market, making the technology familiar to the public. With the widespread use of computers, inkjet printing has started to attract increasing commercial interest, and most of the current relevant technologies were primarily developed from the 1980s

onwards. Therefore, inkjet printing is a relatively new technology in comparison to conventional printing technologies that have evolved over several centuries.[15]

Inkjet printing is a digital technology with many benefits over other printing technologies. In graphic printing, inkjet technology can best meet the requirements of variable data printing, personalization, customization, printing-on-demand with just-in-time delivery, and short (color) print runs.[20,21] The technology is also very popular in functional printing, especially in a laboratory environment. It is an additive technology that is both affordable in costs and that consumes less material (i.e., there is a low loss of ink due to low dead volume and low print waste). And since the technology is familiar to the public thanks to the home and office printer market, potential users in functional printing assume a similar intuitive and easy to use setup as they are accustomed to operate their desktop printers. This is one of the reasons why inkjet printing is used quite frequently in the area of printed functionalities, since the inkjet system is believed to be very easy in use, for example, compared to gravure or offset printing. Further reasons for the awakening interest in using inkjet printing for functional applications are high flexibility in terms of patterns (maskless) and materials, as well as the low cost approach, because only a small amount of materials is required in comparison to other solution-based deposition techniques.

Table 1 provides a brief summary of the main technology benefits of inkjet printing. A classification of benefits is done with regards to substrate, ink, print master, print file, press setup and deposit characteristics. Of course, inkjet printing technology has not only benefits but also some disadvantages and limitations. For instance, conventional printing methods with a print master are much more efficient for large print runs than inkjet printing. Furthermore, the discrete droplet-by-droplet nature of the inkjet process is challenging concerning the film homogeneity – especially for the field of printed electronics – as discussed more in detail in Chapter 6.1. However, based on the current market trends towards increasing product diversification, increasing product individualization, and thus decreasing batch sizes/shorter print runs, highly flexible technologies such as inkjet printing are more and more preferred over conventional printing technologies.

Table 1: Overview of technology benefits of the inkjet printing process based on different categories (information gathered from [16,20–24])

Substrate	▪ No contact between printhead and substrate, thus no touch, only soft droplet impact, low image distortion and no contamination ▪ Low forces required to hold the substrate ▪ Flexible and rigid substrates ▪ Flat and non-flat substrates ▪ Thin and highly delicate substrates ▪ Small substrate area size (in the range of µm²) up to ultra large area size (in the range of m²)
Ink	▪ Compatible with a high range of fluids: solvent-based, water-based, oil-based, UV inks, hot melt ▪ Dispersions and solutions ▪ Lower ink volumes are required compared to conventional technologies due to small dead volumes ▪ Usually less hazardous chemicals (depends on application, but most of the color inks are water-based, especially in small office home office market segment) compared to conventional printing methods
Print master	▪ No film, stencil, screen or plate masters required – low set-up time ▪ No typical printing process waste related to print masters and related chemistry ▪ No storage of physical print masters required (only digital) ▪ Maskless, direct writing deposition
Print file	▪ Minimal prepress (i.e., no development of physical print masters), fast processing ▪ Print file change and editing on the fly: variable data printing, customization, short print runs, prototyping, sampling, proofing ▪ No restriction to repeat patterns, less physical length limitation of patterns ▪ High web-to-print ability (print e-commerce, remote publishing)
Press setup	▪ Minimal press setup compared to conventional printing methods, and thus reduction of inventory, no large inking or dampening units ▪ Light-weight press materials (e.g., polymers) possible due to lesser impact compared to mainly metal materials applied in conventional printing presses ▪ Digital, built-in registration between colors or printheads (i.e., digitally controlled droplet jetting delays for registration adjustment in web-fed printing along web direction) ▪ Easily scalable, for example, in format (width)
Droplet and deposit characteristics	▪ Deposits have lower weight than, for example, in offset printing (color printing) ▪ High deposit height flexibility: From a few nm up to a few tens of µm with one printing pass ▪ High deposit surface smoothness flexibility: Highly smooth layer surfaces up to very rough surfaces ▪ Droplet volumina ranges from fL up to nL ▪ Droplet speed ranges from 3 m/s up to 20 m/s ▪ Droplet jetting frequencies from Hz up to several hundred kHz (e.g., drop-on-demand Fujifilm Dimatix Samba with 100 kHz and continuous systems > 250 kHz) ▪ Deposit structure size from sub-µm scale (electro-hydrodynamic inkjet) up to several hundreds of µm (continuous inkjet)

2.2 Piezoelectric inkjet technology and a historical overview of inkjet printing

Inkjet printing is usually classified by two widely-known mechanisms of drop generation: (i) continuous and (ii) drop-on-demand printing. The difference between the two mechanisms is the way in which the droplets are ejected. In continuous inkjet printing, a stream of usually uniformly-sized droplets is generated continuously and independently on the requirement of droplets for the print pattern. Droplets that are not required for the print pattern will be captured and recirculated, forming a circulation loop. Droplets that are required for the print pattern will be delivered to the substrate.[15,22,25] A change of the trajectory of the droplets can be initiated, for example, by electrical fields or airflows.[24] In drop-on-demand inkjet printing, droplets are ejected from the nozzle only when they are required for the print pattern. Thus, this technology is more economical than continuous inkjet systems. The droplets in drop-on-demand inkjet printing are usually generated thermally or piezo-electrically by digital signals referred to as thermal or bubble jet inkjet printing, and piezo inkjet printing, respectively.[26] There exist also further sub- or side-categories for both continuous and drop-on-demand inkjet printing that can be found in detail elsewhere[22,24,25,27–29].

Piezoelectric driving is the most popular actuation mode to eject droplets in the area of functional inkjet printing. It has been known for more than 20 years that the phenomena of droplet ejection in piezoelectric inkjet printing are mainly related to pressure waves.[30] The active element causing the pressure waves is a piezoelectric transducer located in the printhead. When voltage is applied to the piezoelectric transducer (i.e., inverse piezoelectric effect), a deformation (i.e., either an expansion or contraction) takes place, creating instantaneous mechanical vibrations and pressure waves, which propagate in the fluid. Depending on the deformation of the piezoelectric transducer, the actuation is classified in squeeze, bend, push or shear mode. These waves will be transmitted and reflected (e.g., at the walls of the printhead), and if a sufficiently high pressure peak arises at the nozzle, a strong acceleration of the fluid is caused, firing a droplet out of the printhead. The voltage signal applied to the piezoelectric transducer over a certain time is termed as waveform. The waveform has the most important impact on the drop ejection process, since it controls the size, speed, and shape of the droplets. Furthermore, the waveform is the most decisive parameter if the ink can or cannot be jetted out of the nozzle. Each ink requires a dedicated waveform for proper droplet ejection.[15,31–38]

The waveform applied to the piezoelectric transducers are usually unipolar or polar waveforms.[34] Figure 4 shows a scheme of a simple and a complex polar waveform as well as a unipolar

waveform with characteristic segments. Unipolar waveforms are, in the simplest case, single pulses, but can be further extended to more complex pulses depending on the driving electronics of the inkjet system.

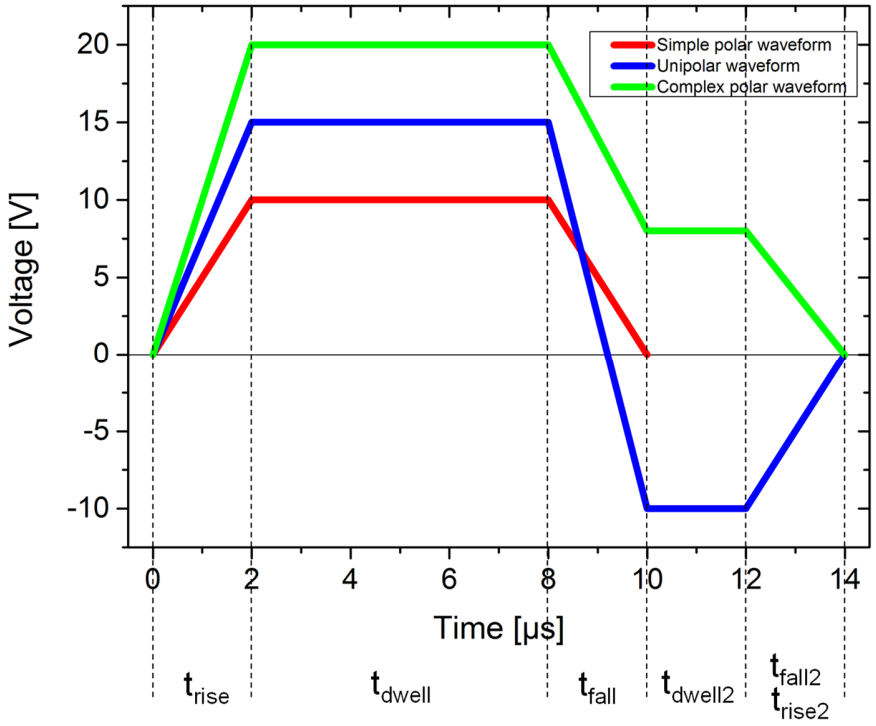

Figure 4: Simple and complex polar driving waveforms and unipolar driving waveform (adapted from Wu[39])

Depending on the printhead manufacturer, the printhead design, and the piezoelectric actuation mode, positive or negative voltages are applied to the transducer. For unipolar waveforms both positive and negative voltages are applied. Examples for such systems are usually dispenser inkjet systems (e.g., from Microdrop Technologies or Microfab Technologies). All the waveforms are characterized by the rise time t_{rise}, the dwell time t_{dwell} and the fall time t_{fall}. The maximum voltage at t_{dwell} is usually descried as the maximum jetting voltage. The maximum voltage value that can be applied to the piezoelectric transducer depends again on the printhead manufacturer, the printhead design, and the piezoelectric actuation mode. It usually ranges between a few 10 V up to several hundred volts. Both t_{dwell} and its voltage amplitude are the most important factors for the droplet ejection process. The negative trapezoidal pulse of the unipolar waveform is also called as a quenching pulse since it damps residual oscillations of the first pulse (resonating pulse) in the nozzle chamber. The two pulses – resonating and quenching pulse – can be also separated by a time interval.[40]

A negative pressure is initiated during the first rise time of the waveform t_{rise} upon a positive voltage step; as a consequence, the meniscus at the nozzle orifice retracts. The resulting pressure waves of t_{rise} are reflected at the printhead walls and turn into positives ones at t_{dwell}. The de-charging of the piezoelectric transducer initiated by t_{fall} should amplify the previously generated pressure waves by adding a new initial pressure distribution to the system. For the simple polar waveform depicted in Figure 4, this new initial pressure distribution is identical to the original initial pressure distribution at the beginning of the pulse, except for its sign. Finally, a droplet is fired when the amplified pressure waves reach at the nozzle orifice.[30,31,37]

The process is basically the same for the complex polar waveform and the unipolar waveform. But both the complex polar waveform and the unipolar waveform allow much more freedom to fine-tune the wave propagation and thus the droplet ejection. Particularly, the complex polar waveform is the standard for the laboratory Fujifilm Dimatix Materials Printer 2831 (DMP 2831). Simple polar waveforms are more frequently applied for the industrial deposition printheads of Fujifilm Dimatix, such as the QS256 printheads or Galaxy 256 printheads. Unipolar waveforms are used, for instance, to drive the piezoelectric transducer of the Microdrop Technology inkjet dispensers.

A proper drop formation process is the result and the overall aim of the waveform applied to the piezoelectric transducer. Usually, the waveform is optimized to allow the ejection of a single, spherical, regular droplet on a trajectory perpendicular to the nozzle plate. Commonly, each pulse of the firing signal generates one defined droplet in order to deposit it on a predetermined position of the substrate (an exceptional case is grey scale inkjet printing[31]). Figure 5 exemplarily shows a typical drop formation cycle captured with an imageXpert drop-watcher system on the basis of stroboscopic flashes.

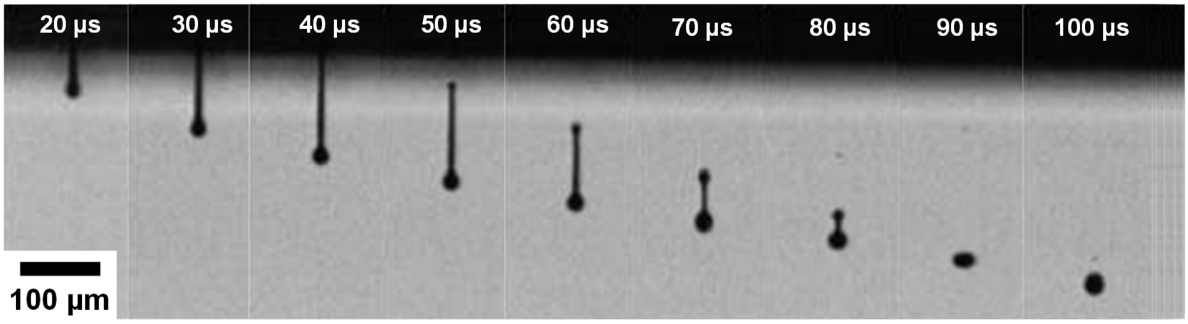

Figure 5: Drop formation cycle with 10 µs intervals after application of the waveform to the piezoelectric transducer (inkjet printhead: Fujifilm Dimatix QS256, ink: ANP DGP 40LT-15C)

Specifically, a Fujifilm QS256 AAA printhead with 10 pL nominal droplet volume and a silver nanoparticle ink from ANP (DGP 40LT-15C) were used. A simple polar trapezoid waveform was

employed as shown before in Figure 4. The t_{dwell} was about 10 µs and the maximum jetting voltage was about 55 V. According to Figure 5, a head droplet formation can be observed at 20 µs, and the droplet pinch-off (i.e., the time when the tail pinches off from the nozzle plate)[31] takes place between 40 µs and 50 µs. The droplet drags a tail, slowing down the average droplet speed which was determined to about 3.4 m/s. However, the tail formed due to capillary contraction of the ligament has a sufficiently high speed to merge with the main droplet before impacting on the substrate.[15]

The merge is between 80 µs and 90 µs. As a result of the collision of the tail with the head droplet, a strong deformation of the droplet shape takes place (see droplet at 90 µs). At 100 µs, the droplet shape is stabilized turning back to the nearly perfect spherical shape which is the energetically most stable state. The volume of the droplet was determined to be about 11 pL. The drop formation cycle displayed is free of satellite droplets, indicating a well-adjusted waveform. This can be considered as a desirable example of drop ejection in both color inkjet printing as well as functional inkjet printing.

Starting to develop after the mid-20th century, inkjet printing is a comparably young technology and has seen several development and application phases. The following anthology provides an overview of the scientific literature regarding the categorization of inkjet printing, the physics of the process related to different inkjet technologies and practical applications in a brief historical overview. The primary focus of this section is on scientific review articles. Review articles are summaries of the current state of research and understanding on a particular topic. They include relevant scientific literature and provide insights into previously published research, the latest developments in the field, and future directions. They are eminently suitable for a historical overview of the inkjet technology. A few books about inkjet printing are introduced as well. There are numerous excellent scientific articles and books available reviewing inkjet printing technologies and their applications. The number of articles increases each year. As shown in the next pages, many articles were published in the year 2015. However, one has to admit that the basic principles of inkjet printing are still the same, and that there are no groundbreaking new technological approaches described in the latest review articles compared to literature published 10 to 15 years ago. Since inkjet printing is also well-established in the home office market offering diverse consumer products, there is a very high number of popular science articles available at present, for example, comparing different currently available printer models or describing the basics of the technology.

1970s and 1980s: Continuous inkjet printing system for marking and coding applications, drop-on-demand inkjet printing development, and commercial success of thermal inkjet printing technology

Kamphöfner[41] published one of the first review articles on inkjet printing in 1972 focusing on continuous inkjet technology. In 1976, Keur et al.[42] described each step of the continuous inkjet printing process, at that time described as synchronous inkjet, in more detail. Continuous inkjet technology became attractive in an industrial context for coding and marking of products. One year later, Carnahan[43] reviewed the basic theory and principles of continuous inkjet, electrostatic inkjet, and drop-on-demand inkjet printing (at that time termed as impulse inkjet). In the 1980s, the drop-on-demand technology attracted increasing interest. Keeling[44] reviewed different inkjet technologies in 1981 and highlighted their characteristics. He also discussed further fields of application of the inkjet technology where the generation of small droplets with constant volume is of relevance. This can be considered as one of the first approaches towards functional printing. Bogy et al.[30] studied the physical phenomena underlying the operation of piezoelectric inkjet systems. Lee et al.[45] demonstrated the potential of the drop-on-demand inkjet technology for color printing. In 1985, Heinzl et al.[46] reviewed the state-of-the-art of inkjet printing technologies and Haysom[47] discussed the improvements in drop-on-demand printing over the last years.

In the mid 1980s, thermal inkjet printers from HP became attractive as portable consumer products due to the low costs and reasonable quality.[25] The thermal printhead technology from HP called ThinkJet was introduced in the Hewlett Packard Journal (Volume 36, Number 5) in 1985 with a couple of research articles about the technical details[48–51]. This was the starting point of a long period of success for the thermal inkjet technology, which clearly dominated the home and office inkjet market until the end of the 1990s.[22]

Already in 1987 and 1988, piezoelectric inkjet printing was being employed by Teng et al.[52–54] to deposit metallo-organic decomposition inks for microcircuits and photovoltaics. One year later, Kimura et al.[55] deposited enzyme droplets for a biosensor using piezoelectric inkjet printing. They also presented cross-sectional profiles of the droplets revealing the well-known coffee-ring effect (the authors do not refer to the coffee-ring effect, but instead describe the droplet profile as doughnut-like shape). These are a few of the first popular examples for the field of functional inkjet printing.

In 1988, Lee[56] provided a short review about inkjet printing focusing on piezoelectric actuation. Another review article was presented by Wehl[57] in 1989 which highlighted the drop-on-demand technologies. He also provided a classification of inkjet technologies, including a technical description of the piezoelectric and thermal printheads of different manufacturers. At this time, Wehl already claimed in his outlook a very promising future for inkjet printing, especially regarding

its use as a desktop publishing tool (DTP).[57] In the same year, Croucher et al.[58] presented an overview of design criteria for inkjet inks providing physiochemical ink properties.

1990s: Establishment of inkjet printing as a small office home office technology

At the beginning of the 1990s, the focus was on full color inkjet printing by developing new printers, new printheads and cartridge technologies, and inks – mainly driven by the continuing success of the thermal inkjet method. The number of inkjet product sales increased dramatically.[22] Also, piezoelectric printhead technologies again gained remarkable attention due to the introduction of Epson's Stylus printer family in 1993. It was the first piezoelectric drop-on-demand inkjet technology that was of great commercial interest for the home and office printer market. The printhead technology was based on the push-mode actuation.[25,59]

By end of the 1990s, several articles were published on thermal inkjet technology. In 1997, Chen et al.[60] investigated the bubble growth and the drop ejection in thermal inkjet printing, both numerically and experimentally. A performance overview of thermal printheads was provided in the same year by Peeters et al.[61] In 1998, Le et al.[25] published a review article about the main inkjet technologies. The authors presented a short overview of the history of inkjet printing, the well-known classification of inkjet technologies, and an introduction to selected technologies, mainly continuous inkjet, thermal inkjet, and piezoelectric inkjet technology. This article attracted remarkable scientific attention and has been cited several hundred times.

In the same year, Lemmo et al.[62] reviewed the use of inkjet technology for drug discovery applications. Interestingly, the term "inkjet dispensing" rather than "inkjet printing" is used in the article, clearly differentiating them from the traditional inkjet printers used primarily for texts and graphics. It was a relatively new field of application for the inkjet technology. According to Lemmo et al.[62], inkjet methods were mainly employed for high-throughput screening, genomics and combinatorial chemistry. However, the application of inkjet printing in the area of drug discovery was still in its infancy.

2000s: Towards industrial and functional applications

In 2000, Pond[22] published an educational and technological reference resource book describing the different inkjet methods and emerging trends in inkjet printing. In the 404 pages of texts and graphics, the history of inkjet printing, comparison to other non-impact technologies, and many further topics are presented. Interestingly, the majority of the references in the book is based on patent literature. This is unique compared to any other literature about inkjet printing and allows for some historical insight into the technological concepts of different inkjet companies.

In 2002, Brünahl et al.[35] provided an overview about piezoelectric inkjet printing with a particular focus on shear mode actuators applied in Xaar printheads. Still, however, the focus was set on traditional graphic applications.

From the year 2000 onwards, inkjet printing was exploited more and more as a deposition method in the field of functional printing. In 2001, Calvert[63] published a review about the application of inkjet printing for depositing functional materials and devices. In 2003, de Gans and Schubert[64] reviewed commercially available instrumentation for functional inkjet printing. They clearly identified the disadvantages of the use of standard color desktop inkjet printers in the area of functional printing and propose inkjet-technology-based dispensers (i.e., typically single nozzle systems), such as the Microdrop (Autodrop) or Microfab platforms. The application focus was on combinatorial polymeric materials research (and thus within the area of polymer materials chemistry).

Only one year later, a literature survey about inkjet printing of various polymer materials was provided by the same author (de Gans et al.[65]). The well-known principles of inkjet technologies were introduced, including the physical aspects of droplet formation as well as inkjet platforms for the area of functional material deposition, such as the Autodrop printer from Microdrop (similar to the publication of 2003 by de Gans and Schubert[64]). The authors concluded, that piezoelectric inkjet systems are the method of choice for polymer printing. The review article contains also novel developments such as inkjet printing of waxes (hot melt) and 3D powder bed inkjet using UV curable ink formulations.

In 2006, Boland et al.[66] reviewed the application of inkjet printing for the deposition of bio-inks containing cells towards organ printing. Interestingly, thermal inkjet technology from HP was employed rather than piezoelectric printheads, which are usually used in the field of biology and chemistry.[62]

Martin et al.[67] demonstrated in 2008 the importance of classical physics in the inkjet printing process to allow the controlled manipulation of liquid jets and droplets. He also introduced the evolution of inkjet applications until the 2020s in three generations: (i) marking and coding, (ii) home and office printing, and (iii) industrial printing and manufacturing. According to his prediction, the impact of generation (iii) - taking off at the end of the 2000s - will steadily increase during the 2010s and 2020s, outweighing the other two generations.

In 2008, Hon and Hutchings[26] reviewed direct writing technologies for manufacturing, including inkjet printing as the most mature form of direct writing. Thus, the particular focus of the article is on functional inkjet printing. The growing relevance of inkjet printing was demonstrated by the increasing number of scientific publications since 1990 based on the ISI Compendex database. Hon and Hutchings proposed categorizing inkjet printing under droplet-based methods next to

aerosol jet deposition. Different fields of application for inkjet printing were introduced, demonstrating its versatility in areas such as the micro-electronics industry, rapid prototyping for mechanical engineering, optics, and the biomedical and life sciences. Inkjet printing is described as the most established direct writing technology, followed by laser direct writing methods. The review article includes a summary of direct writing process characteristics and compares mechanisms, deposit feature sizes, process speeds and material aspects. Following the scheme of Hon and Hutchings[26], Zhang et al.[68] reviewed in a similar manner direct writing technologies for microelectronic applications one year later, including inkjet printing classified as a droplet-based direct writing method.

Since 2010: From digital manufacturing of text and graphics to functional electrical components, products, and applications in bioprinting

In 2010, Wijshoff published an excellent and detailed 100-page review article with 536 literature sources on piezoelectric inkjet printing (graphic inkjet), including the historical development of the inkjet technology, piezoelectric actuation details, fundamental considerations about channel acoustics and drop and fluid wetting dynamics. This is one of the fundamental research articles on inkjet printing, and complements the review article of Le et al.[25] and the book of Pond[22].

In the same year, Derby[13] reviewed the current state of understanding of drop formation in inkjet printing and the interactions between the deposited droplets and the droplets and the substrate. He also introduced the well-known major inkjet technologies and basic considerations about requirements for printable fluids.

Also in 2010, Yin et al.[69] reviewed the application of inkjet printing for flexible electronics. The authors focused on different materials and inks for flexible electronics. They also described the well-known inkjet printing methods. However, the review article highlights electro-hydrodynamic printing methods that use an electric field to eject droplets. This allows for deposits of much smaller droplets volumes compared to traditional piezoelectric and thermal inkjet printing. Yin et al.[69] introduced several ordinary desktop inkjet printers that were used for functional printing applications as well as dedicated functional inkjet printing systems.

Singh et al.[70] provided a progress report in 2010 on recent developments in inkjet printing technology for the manufacturing of electronic devices such as solar cells, transistors, memories and sensors. Film formation processes and film uniformity were addressed in the article as well. The authors predicted a strong future for inkjet printing as a flexible deposition process in the fields of applied science and engineering.

In 2012, Zhu et al.[71] presented recent advances in drug discovery, including assays of cells and proteins, microarrays, biosensors, tissue engineering, and basic biological and pharmaceutical

studies using inkjet dispensing. Here again, similar to the article by Lemmo et al.[62] published about 14 years ago, the term “dispensing” is used instead of “printing”.

Two books entitled *Inkjet Technology for Digital Fabrication*[72] and *Inkjet-based Micromanufaturing*[73] were issued in 2012, and summarized the latest developments in the field of functional printing. Cummins et al.[74] provided a detailed literature survey of inkjet-printed conductive materials for electronic applications. They demonstrated the application of various types of conductive inks in inkjet printing and explained fundamental aspects, for example, the basic principles of drop ejection modes and droplet impact and spreading.

Vaezi et al.[75] provided a survey on 3D micro-additive manufacturing technologies. The basic principles and the classification of inkjet printing was introduced. 3D printers and printed objects based on the inkjet principle were presented employing UV curable or metallic ink formulations.

Recent advances in organic transistor printing processes were reviewed by Kang et al.[76] in 2013. This review provides an overview of various deposition technologies for the development of transistors and does not specifically focus on inkjet printing. However, inkjet printing is introduced as a direct writing technology for the deposition of semiconductor ink formulations and the electrodes for transistors.

Komuro et al.[77] summarized recent advances of inkjet-printed bio(chemical) sensing devices. A variety of inkjet-printed sensor elements was introduced and advantages and challenges of the inkjet technology for bio(chemical) sensing applications were discussed in detail.

Basaran et al.[27] reviewed inkjet printing from a fluid mechanics perspective highlighting, as he described “nonstandard” inkjet technologies along with field- or flow-induced tip streaming (maybe better termed as “less common” technologies) and non-Newtonian fluids for printing.

In 2013, Castrejon-Pita et al.[24] reviewed the major as well as the less common inkjet technologies for the field of both graphical printing and functional printing. This review covered a wide range of current issues and highlights inkjet printing as emerging next generation manufacturing technique.

Bioprinting based on inkjet technology was detailed reviewed in 2014 by Saunders and Derby[78]. They showed that thermal inkjet printing has been extensively employed in the area of bioprinting despite the high operating temperature close to the heating element in the printhead. The printing process seems to have only a minimal impact on the cell activity. Beside the bioprinting topic, they also summarized fundamental aspects of inkjet printing. Seol et al.[79] and Dias et al.[80] published quite similar articles on bioprinting technology and its application. They introduced the general principles of the different bioprinting technologies including inkjet printing, and highlighted research on cardiothoracic surgery and tissue engineering. Murphy and Atala[81] also reviewed bioprinting of tissues and organs providing an overview about several manufacturing strategies. Inkjet printing was introduced as the main deposition and patterning technology for tissue

bioprinting. Kuang et al.[82] reviewed advances in precisely controlling droplets for high-resolution patterns and 3D structures. Specifically, they focus on formation mechanisms resulting in different droplet deposit morphologies, such as the well-known coffee-ring effect.

In 2015, a very high number of excellent review articles about inkjet printing was published, most of them in the area of bioprinting. Chen et al.[83] provided a recent overview of inkjet-printed conductive tracks for printed electrics. Daly et al.[84] introduced the main inkjet printing technologies and their application for pharmaceuticals, indicating a recurring trend of functional printing towards biotechnology and medicine. Ihalainen et al.[85] provided a literature survey on printing technologies for biomolecule and cell-based applications, specifically highlighting inkjet printing as one of the most frequently applied and most promising methods for biomolecule and cell deposition. Shirazi et al.[86] summarized advances in 3D inkjet printing for tissue engineering. Li et al.[87] provided a detailed literature survey on biosensor fabrication using inkjet printing technology. They introduced in brief the historical development of inkjet printing, its classification, and considerations about ink formulations. Knowlton et al.[88] reviewed bioprinting for cancer research, briefly introducing thermal and piezoelectric inkjet printing. Yamada et al.[89] discussed advances in the combination of inkjet printing and paper substrates for the development of microfluidic devices.

Liu et al.[90] reviewed inkjet printing synthesis of functional metal oxides and presented a variety of applications. The focus of this article is on inorganic metal ink formulations, such as precursor or nanoparticle systems. Choi et al.[91] reported on recent developments and directions in printed nanomaterials for a variety of applications. They demonstrated that inkjet printing has been used most frequently to deposit functional nanomaterials for wide-ranging applications. Sun et al.[92] summarized several strategies to control the deposit morphology in inkjet-printed droplets in the area of functional printing. The author highlighted the relevance of the deposit morphology for the final performance of the printed layer or device. Stüwe et al.[93] provided an overview on the application of inkjet technology in the field of silicon photovoltaics. Additionally, the authors listed suitable industrial inkjet printheads for this field as well as inkjet printers for functional materials deposition. Inkjet printing was used not only for the metallization, but also for the deposition of light trapping structures and for doping. Mattana and Briand[94] discussed recent advances in printed sensor devices on flexible polymer films such as inkjet-printed photodetectors, temperature sensors, IR detectors, accelerometers, humidity sensor, and many others.

The latest developments in inkjet printing as well as basics concerning the technology and related processes are summarized in the book *Fundamentals of Inkjet Printing*[15] issued in 2016.

In summary, this brief and certainly non-exhaustive historical overview of inkjet printing with a particular focus on review research articles, has described the development from a coding and

marking technology to a worldwide consumer market technology and finally to an industrial materials deposition technology for various fields of application, ranging from electronics to 3D printing and even to bioprinting. Inkjet printing is still increasingly attracting attention – not only in the field of functional printing, but also in traditional text and graphics printing. This is due to some key advantages of the inkjet technology over other printing methods and in particular traditional printing technologies that were explained in Chapter 2.1.

2.3 Pattern and film formation in inkjet printing under the scheme of self-assembly

In inkjet-printed electronics, mostly 1-bit images are used as print layout files. Greyscale is rarely used. Thus, the print pattern layout is defined by a grid of black and white pixels (px) in a defined print resolution (usually provided as dots per inch, or short dpi).[95] Each of the black pixels will result in a single droplet ejected from the nozzle orifice of the printhead. The individual print dots are arranged in a grid and usually have the same center-to-center distance (drop space s_{drop}), the same shape, and the same size.[95] Mainly standard image processing software well known from graphic industry and in a few cases also CAD software or specific manufacturer platform software are mainly employed for the preparation of print pattern layouts in the field of printed electronics.[95] The basic element in inkjet printing is a single droplet. It can be deposited simply by applying a suitable waveform to the piezoelectric transducer. The principle of droplet coalescence (the diameter on the substrate of the droplet $d_{drop} \geq$ drop space s_{drop}) is used for the development of continuous films based on single droplets. Printing single droplets with overlap next to each other allows for the formation of lines and rectangles or any other shape, termed as 1D or 2D films. 1D films are characterized as having exactly one droplet in width. If the width is larger than one droplet, 2D films are obtained.[96,97] These different classifications are shown schematically in Figure 6A-C. Figure 6D is a top view depicting the individual droplets of Figure 6A. The print origin is marked with ¤ and the deposition is performed in a line-by-line manner along the x-direction. Figure 6E differentiates between lines deposited along the printing direction and perpendicular to the printing direction, considering a sheet-fed mode. Assuming the usage of only one nozzle in the given example shown in Figure 6E, the main difference between both line types is the processing time and its influence on the deposit morphology. For example, printing a line unidirectionally perpendicular to printing direction results in more movements of the axis system, because a line feed is required for each droplet in y-direction. The deposition frequency between the individual droplets deposited in the printing direction will be much higher than the frequency of the droplets deposited perpendicular to the printing direction.[96]

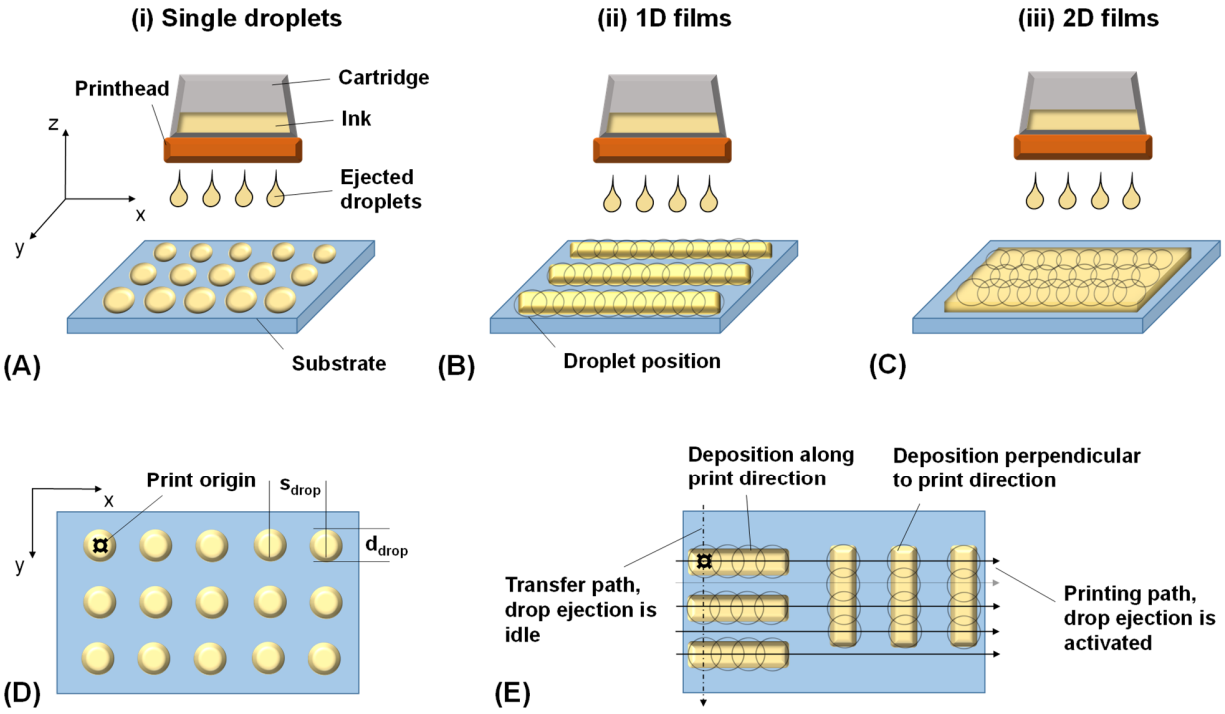

Figure 6: Overview and classification of print pattern elements; (A) deposition of single droplets without droplet coalescence, (B) lines upon droplet coalescence with one droplet in width termed 1D films and (C) 2D films consisting of deposited droplet with coalescence in x- and y-direction; (D) is a top view schematic of (A) indicating print origin, drop space s_{drop} and droplet diameter d_{drop}, (E) shows the formation of lines differentiating between lines deposited along the printing path and perpendicular to the printing path (unidirectional printing, for reasons of simplification a printhead with only one nozzle activated is assumed for (E))

Printing starts at the print origin and the deposition of the droplets takes place usually in a unidirectional manner by transferring the printhead over the substrate in x-direction. In y-direction, the substrate is positioned relative to the printhead without depositing any droplets. The printhead is in idle mode. Then, the deposition process starts again unidirectional in x-direction. Continuing in this line-by-line approach, the pattern is developed. This raster-scan-based unidirectional printing process is used frequently in functional printing (e.g., it is the standard of Fujifilm Dimatix Printers) as well as graphic printing. Vector-based processing is also sometimes used in inkjet printing, for example, in case of inkjet dispensers from Microdrop Technologies as well as Microfab. However, the standard is the raster-scan method. In graphic printing, bidirectional raster-scan printing is also sometimes applied to increase the process speed.[95–97]

All of the above mentioned patterns – single droplets, 1D films, and 2D films – were studied extensively in the field of functional printing. Most of the related research is based on simple rectilinear pattern layouts that are preferentially orientated exactly along the printing direction and/or perpendicular to the printing direction.

It was found that inkjet printing of precisely defined, smooth, uniform, and patterned layers in both small and large sizes is a big challenge for the field of printed functionalities.[95] Considerable research work has been done to study layer formation and influencing parameters in inkjet printing by focusing on the pattern elements (i) single droplets[98–104], (ii) lines[96,100,105–109], and (iii) rectangles[97,110–112]. Soltman et al. studied in detail inkjet-printed line morphologies[100] as well as morphologies of rectangles using a single nozzle inkjet printer[110]. The authors demonstrated the importance of process optimization in order to obtain smooth, narrow, and straight line characteristics by tuning the distance between neighboring droplets and the drop ejection frequency[100], or to obtain well-defined rectangular pattern shapes by a dedicated print layout development that includes an evaporative compensation[110]. Thus, the print pattern layout is of paramount importance for the inkjet printing process in functional printing.[95] It will not only influence the morphology of the deposits, but as a consequence also the functional performance of the layer or the device.[95,113]

The film formation of a printed droplet or layer is strongly influenced by the interaction between substrate and ink. As a result of intermolecular interactions between the ink and the substrate, a certain contact is formed between the liquid and the solid surface which is known as wetting.[114] How a printed liquid is wetting the surface of the substrate is usually characterized by its equilibrium contact angle θ, which is the characteristic angle between the liquid/vapor interface at the solid surface of the substrate (see Figure 7A).[15,114] The contact angle θ is described by Young's equation and a function of three interphase surface tensions as shown in Equation 1[115]:

$$\cos\theta = \frac{\sigma_{SV} - \sigma_{SL}}{\sigma_{LV}} \qquad \text{(Eq 1)}$$

The three interphase surface tensions are represented by σ and the subscripts SV, SL and LV correspond to the solid-vapor, solid-liquid and liquid-vapor interfaces. A perfectly smooth and flat surface is assumed. When a droplet of a liquid on a surface is sufficiently small, as in the case of inkjet printing, the surface tension dominates over gravity and the droplet forms a spherical cap shape.[116] Different wetting behaviors of droplets as a function of their contact angle on solid surfaces are schematically shown in Figure 7B. These different shapes will strongly influence the deposit morphology in inkjet printing. To change the wetting characteristics of a surface, physical or chemical substrate treatments methods can be applied.

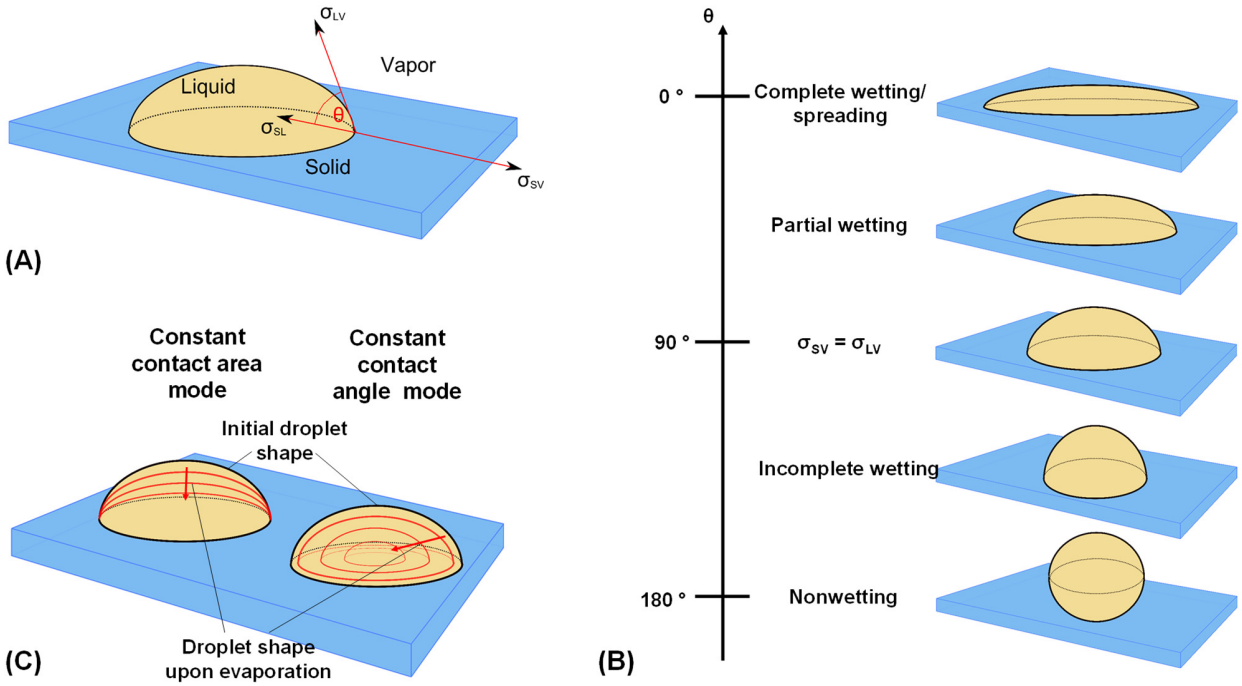

Figure 7: (A) liquid sessile droplet on a flat solid surface reaching its equilibrium contact angle θ at the three phase contact line, (B) different wetting behavior of droplets on solid flat surfaces according to the contact angle, (C) two basic evaporation modes – constant contact area and constant contact angle – for sessile droplets on solid surfaces (adapted and revised from Daly, Jung and Talbot[15])

Obviously, smaller contact angles result in larger contact areas but lower droplet heights, and vice versa. In addition, the droplets undergo different evaporation kinetics as a function of their surface area. The highest surface area appears for the droplets having a low contact angle, and the lowest for the spherical shape at high contact angles. As a consequence, evaporation processes of nonwetting liquids will take longer than for wetting liquids (assuming the volumes are the same).[116] Since the layer formation of a printed film is based on evaporation-driven material flows and self-assembly, a change of the evaporation kinetics causes a change of the film formation process and thus a change in overall film morphology and film functionality. The drying of a liquid is mainly a diffusion-controlled process and basically a natural phenomenon that can be observed in our everyday surroundings. It is also exploited in many technological applications such as inkjet printing.[15] The difference between the vapor pressure of the droplet liquid at the liquid/vapor interface and the surrounding atmosphere is the main driving force for the evaporation process. The liquid will evaporate when the ambient atmosphere is not fully saturated with the vapor of the liquid. Thus, the evaporation process will proceed as long as a balance between the vapor pressures is obtained. Since the surrounding air might be gradually saturated during the evaporation of the droplet[116], the process becomes quite complex, especially for the field of inkjet

printing where the deposition of the droplets takes place sequentially and in an space enclosed by the printing system.

There are basically three modes of evaporation: (i) the constant contact angle mode, (ii) the constant contact area mode, and (iii) the mixed mode where both contact angle and contact area change.[117] The two modes mentioned first are the pure modes of droplet evaporation, and are schematically shown in Figure 7C. The contact area between liquid and solid remains constant during evaporation, but the contact angle and thus the height of the droplets decreases for the constant contact area mode. On the other hand, the contact area decreases during evaporation of the droplets based on the constant contact angle mode, but the contact angle with the solid substrate remains constant. The different evaporation modes as well as the different wetting behaviors shown in Figure 7B and C will cause different transport mechanisms to assemble the particles or molecules contained in the liquid.[118,119]

There are two transport mechanisms that have been studied most frequently in the literature[98]: (i) Capillary flows transporting liquids and molecules or particles from the center of the deposited droplet towards the edge, where they accumulate due to a pinning of the three phase contact line, and (ii) inward flows from the droplet edge to the center usually leading to central bump deposits.[10,98,120] It has been demonstrated that these two transport mechanisms are of high relevance for inkjet printing as well as for other liquid direct writing technologies, since they define the morphology of the printed layer and thus also its properties.[98] Furthermore, these mechanisms can be actively exploited to control the morphology of deposits, for example, to enable high-resolution patterns.[82,108]

The first transport mechanism described above refers to the coffee-ring effect. It is one of the most prominent phenomena in film formation of inkjet printing. It causes ring-shaped stains remaining as deposits after solvent evaporation. They appear since the droplet solutes prefer to assemble along the three phase contact line. If a droplet wets a substrate well and is characterized by a pinned three phase contact line (corresponding to the constant contact area mode in Figure 7B), the evaporation flux is highest at the droplet edge. Capillary flows transport further solvent and solutes from the droplet center to the edge to replenish the lost solvent. The coffee-ring effect has been well-described, observed, simulated, and sometimes also exploited for certain applications many times in the literature[82,100,106,120–124]. However, most of the research in inkjet printing still focuses on a suppression of the coffee-ring effect because usually homogenous film morphology is desired rather than an inhomogeneous solute distribution. Strategies to suppress the effect include, among others, usage of incomplete or non-wetting substrates to initiate a de-pinning of the three phase contact line[98], cooled substrates[100], addition of co-solvents such as high-boiling

point solvents[98,125] and surfactants[116,126], change of particle shape[127], employment of evaporation control masks[128] and electrowetting[129].

The described transport mechanisms are in general not so important for the field of graphic printing, because porous substrates are usually applied, limiting these phenomena. In addition, the effect is mostly close to the resolution limit of the human eye. However, functional layers addressing more than only the human visual sense usually require both a microscopic or macroscopic texture and a well-defined nanoscopic structure at the same time. Whereas graphical printing does not consider structures smaller than the resolution limit of human recognition, structures on the micron and sub-micron scale are mostly essential for the performance of layers in functional printing. The micro- and nanoscopic order of the functional elements is important for the final functionality of the printed layer, and thus for the performance of the device, specifically in the field of printed electronics. In general, two basic principles are known to manufacture products, especially related to micro- and nanofabrication: Top-down and bottom-up.[130,131] Using the top-down method, a desired structure or shape is obtained by “sculpting” (i.e., removing physically or chemically piece by piece of a larger block of a base material).
Inkjet printing, however, is good example for bottom-up manufacturing. Small building blocks are added piece by piece until the desired shape or structure is obtained. The building blocks are on the one hand the droplets that are uniform and repeating, allowing one to print various patterns[15]. On the other hand, dispersed nano- and/or microscopic materials within the droplets can be considered as building blocks as well (see Figure 8). They appear in a disordered state with microscopic randomness, and usually represent the functional material that is required in functional printing for certain properties such as electrical conductivity, semi-conductivity or insulation. However, to form a certain functionality, the disordered state needs to change to a higher order, for example, by taking advantage of physicochemical interactions of molecules or particles. Finally, a macroscopic order originates from nano- and microscopic disorder.
The change from disorder to a higher order in inkjet printing is mostly based on the principle of evaporation-driven self-assembly, since the functional building blocks in the droplets autonomously and spontaneously organize themselves into patterns or structures upon solvent removal. The process is driven by the aim to minimize the energy of the system. Free movement of the particles is possible due to the ambient fluid. The assembly can be actively tailored by direct specific interactions (e.g., inter-particle forces) and/or through the environment (e.g., by usage of external fields, flows or templates). This allows a certain control over the process, and is usually known as directed self-assembly[124]. Intrinsic characteristics of nanoparticles can be tailored by varying, for example, their shape or surface charge, thus influencing the interactions between the

particles. On the other hand, external fields, such as magnetic or electrical fields, or flow fields (flow fields that are, for example, initiated by evaporation and capillary forces), can induce or guide self-assembly processes.[124]

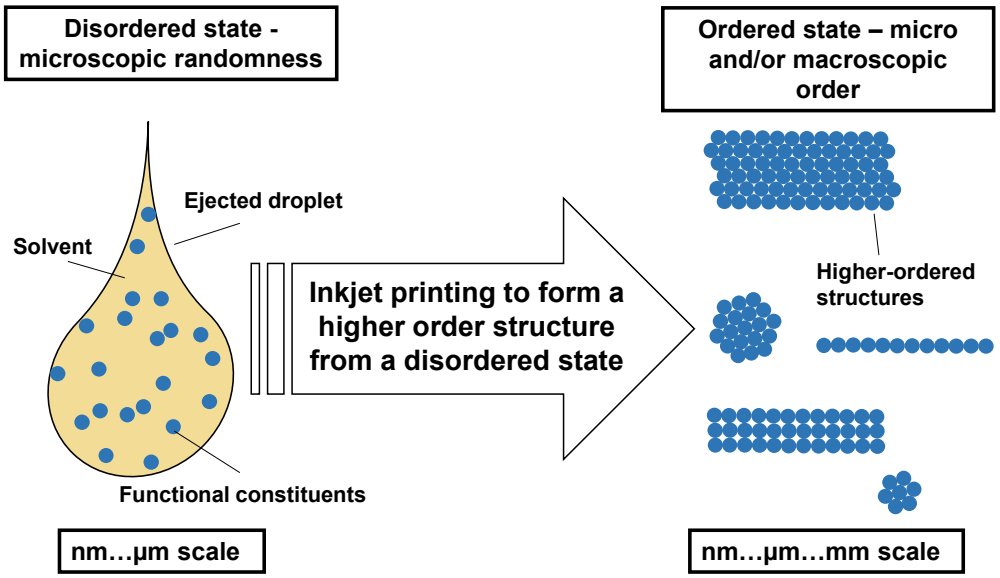

Figure 8: Utilization of inkjet printing and the principle of self-assembly to form from a disordered state with microscopic randomness of functional constituents deposits with higher order of the functional constituents

The concept of self-assembly has been well-known in different fields of science for several decades and has attracted increasing attention in nanoscience.[124,131–133] The term self-assembly has been also frequently used related to inkjet printing for specific applications. However, I propose a more global view regarding the understanding of functional inkjet printing. Functional inkjet printing is mostly carried out on non-absorbent substrates. The aim of functional inkjet printing is to deposit ordered patterns of molecular or nanoscopic building blocks which are dissolved or dispersed in fluids. The evaporation kinetics of the inkjet-printed droplets are critical for the film formation. The evaporation will define the position and assembly structure of molecules and nanoparticles. Evaporation kinetics depend on, among others, the interaction of substrate and ink. The interaction of substrate and ink will “shape” the deposit. Therefore, both evaporation kinetics and substrate-ink interaction influence the self-assembly of the functional material building blocks such as nanoparticles in the droplets. Different transport mechanisms will force nonvolatile molecules and particles within the evaporating droplet to certain positions, where they assemble and form in part rigid agglomerates.[98] The deposits formed by evaporating droplets which contain nanoparticles on non-absorbent and rigid surfaces are highly variable. This variability can range from uniform patterns[134] to ring-like patterns via the coffee-ring effect[122], central bumps[125], and

inner coffee-ring deposits[135], or a number of further patterns in between[116]. In most cases, uniform pattern deposits are preferred in functional printing.[98]

(Parts of this chapter are published in reference [96], reference [95], and reference [98])

2.4 Inkjet printing of colloidal nanospheres

Inkjet-printing of organic or inorganic colloidal spheres is a comparably young research discipline dating back to the early part of the last decade. The state-of-the-art is covered in substance by the research works of Jungho Park and Jooho Moon[134,136–138]. The colloidal spheres used are mostly in the range of 100 – 600 nm. They are termed differently in the literature, among others microspheres or nanospheres. Taking into account the size range, nanospheres is a more appropriate term that will be used in this thesis. In principle, two main strategies for the inkjet printing of nanospheres can be derived: (i) fundamental research to investigate determining factors of self-assembly processes, and (ii) application-driven research attempting to obtain highly defined colloidal assemblies with photonic properties.

In 2004, Ko et al.[138] did initial studies on inkjet printing of silica nanospheres using substrates with different wettabilities. Single droplets were deposited, serving as a template for the self-assembly of the contained nanospheres upon evaporation. They could develop colloidal deposits with hemispherical shape on substrates causing low wettability with the ink. In 2005, the photonic properties of the hemispherical deposits were investigated by Wang et al.[136]. Here, polystyrene (PS) nanospheres were employed. In 2006, Park et al.[134] studied the influence of the ink composition on the self-assembly of silica nanospheres by adding low boiling point solvents to the aqueous dispersion. Park et al.[137] also presented a detailed investigation on photonic properties of printed colloidal hemispherical assemblies as a function of the nanosphere size. In 2008, Perelaer et al.[123] reported on inkjet printing of silica nanospheres with an emphasis on the particular contact line behavior of the spheres as a function of their size. Cui et al.[139] demonstrated in 2009 for the first time large-area patterned inkjet-printed colloidal assemblies of nanospheres with photonic properties. Specialized core-shell nanospheres were developed. Upon evaporation of the solvent, self-assembly processes form ordered assemblies of nanospheres with very high packing densities due to the “paint-on effect” caused by the soft nanosphere shells. The application of different particle sizes resulted in patterned assemblies with different stop bands. In 2010, Biswas et al.[140] investigated in-situ the dynamics of inkjet-printed colloidal droplets on different substrates. PS nanospheres were used as a model system to simulate the behavior of quantum dots for application in photovoltaics. Already in 2012, responsive inkjet-printed photonic

layers in the centimeter scale were shown by Wang et al.[141] and microfluidic chips with inkjet-printed photonic crystals for protein detection by Shen et al.[142]. The hemispherical colloidal deposits initially developed by Ko et al.[138] in 2004 had a revival about one decade later due to the research by Kuang et al.[143]. They applied the inkjet-printed hemispherical crystals for wide viewing-angle displays in the centimeter range. Finally, multicolor vapor-responsive photonic crystal patterns by inkjet printing were demonstrated by Bai et al.[144] at the end of 2014.

As demonstrated by the state-of-the-art research works, printing of nanospheres can result in deposits with photonic properties. These deposits are called colloidal photonic crystals, and opals are considered to be their prototypes.[145,146] Colloidal photonic crystals are artificially structured objects consisting of periodically arranged nanospheres which result in repeating regions of low and high dielectric constants. These structures allow a modulation of electromagnetic waves which can be exploited to control the propagation of light. Photonic band gaps arise due to the periodically repeating regions of low and high dielectric constants leading to interference of electromagnetic waves from the dielectric lattice and prohibiting the propagation of certain electromagnetic wavelengths.[147] A theoretical approximation for the wavelength λ of the reflection peak of a photonic crystal (under normal incidence) can be made based on Braggs law with Equation 2[148–151]:

$$\lambda = \left(\frac{8}{3}\right)^{\frac{1}{2}} \cdot d_P \cdot (n_P{}^2 \cdot 0.74 + n_A{}^2 \cdot 0.26)^{\frac{1}{2}} \qquad \text{(Eq 2)}$$

In Eq 2, d_P is the diameter of the nanospheres, n_P is the refractive index of the nanospheres, n_A the refractive index of the voids (i.e., ambient air) between the nanospheres, and 0.74 and 0.26 are the assumed volume fraction values for the nanospheres and the voids, respectively. The volume fraction depends on the packing density of the nanospheres. Usually, a hexagonal or face-centered cubic (fcc) order is assumed for the self-assembled colloidal photonic crystal structures. The fcc order is considered to be the most energetically stable structure for colloidal crystals.[152] The packing density p_{D_fcc} of a fcc order is given in Equation 3[153]:

$$p_{D\_fcc} = \frac{\pi}{3 \cdot \sqrt{2}} \qquad \text{(Eq 3)}$$

The theoretical interplanar spacing D_{111} for the (111) planes in the fcc lattice (representing the lattice constant) of the colloidal photonic crystal can be calculated with Equation 4:

$$D_{111} = \sqrt{\frac{2}{3} \cdot d_P} \qquad \text{(Eq 4)}$$

(Parts of this chapter are published in reference [154] and reference [155])

2.5 Spherical colloidal assemblies

The development of assemblies with a spherical micro- or macroscopic morphology consisting of highly ordered spherical nanoparticles has progressed significantly during recent years.[156,157] After the pioneering work of Velev et al.[158] in 2000, many publications appeared using different methods to prepare spherical colloidal assemblies (SCAs). Figure 9A and B exemplarily show an inkjet-printed SCA of nanospheres from the top and as side view. The typical structure of the SCA with an fcc order of the nanospheres is shown schematically in the model of Figure 9C. The number of constituent nanospheres N in an fcc order of a SCA can be approximated with the Equation 5:

$$N = \left(\frac{d_S}{d_P}\right)^3 \cdot p_{D\_fcc} \qquad \text{(Eq 5)}$$

The quantity d_S represents the diameter of the SCA. SCAs became an interesting and promising topic of basic science and applied research, aiming for complex structures with high packing density and surface-to-volume ratio, as well as photonic components, especially in sensor applications.[154,159] Recently, two review articles about SCAs were published by Wang and Zhu[160] and Zhao[156]. They demonstrate the current interest for the topic and present the research progress made based on numerous fields of application, such as displays, sensors, barcodes and cell culture micro-carriers.

However, although there has been a significant progress due to the usage of microfluidics for the generation of droplet templates forming the SCAs, there is still a need for simple mass-production methods enabling a bulk generation of the SCAs.[154,156]

A variety of bottom-up approaches based on self-assembly for the preparation of the SCAs have been reported. They are considered to be the most simple and economical methods for the manufacturing of SCAs compared to top-down approaches.[156] Most of the bottom-up approaches based on self-assembly are emulsion-based processes where SCAs are formed by arrangement of particles inside droplets emulsified in liquid media. This class of approaches is called wet self-assembly (WSA) and shown schematically in Figure 9D. Besides WSA, dry self-assembly (DSA) methods are described, in which droplets with colloidal nanoparticles are dispensed on non-wetting solid surfaces.[161] The dispensed droplet forms a spherical shape, and the shrinking droplet

upon evaporation serves as a template confining the containing nanospheres.[154] Finally, the nanospheres are aggregated into a SCA due to symmetrically compressive capillary forces as depicted in Figure 9E.[161] This configuration is stabilized by van der Waals forces. The major drawback of the WSA methods is the long processing time that has been addressed by several researchers.[162,163] Although very fast consolidation times of colloidal nanoparticles inside droplet templates were reported recently by Gu et al.[164], the consolidation in WSA usually requires tens of minutes up to several hours.[165] In addition to the consolidation time, demulsification processes to extract the SCA out of the remaining liquid are considered to be quite challenging.[154,161]

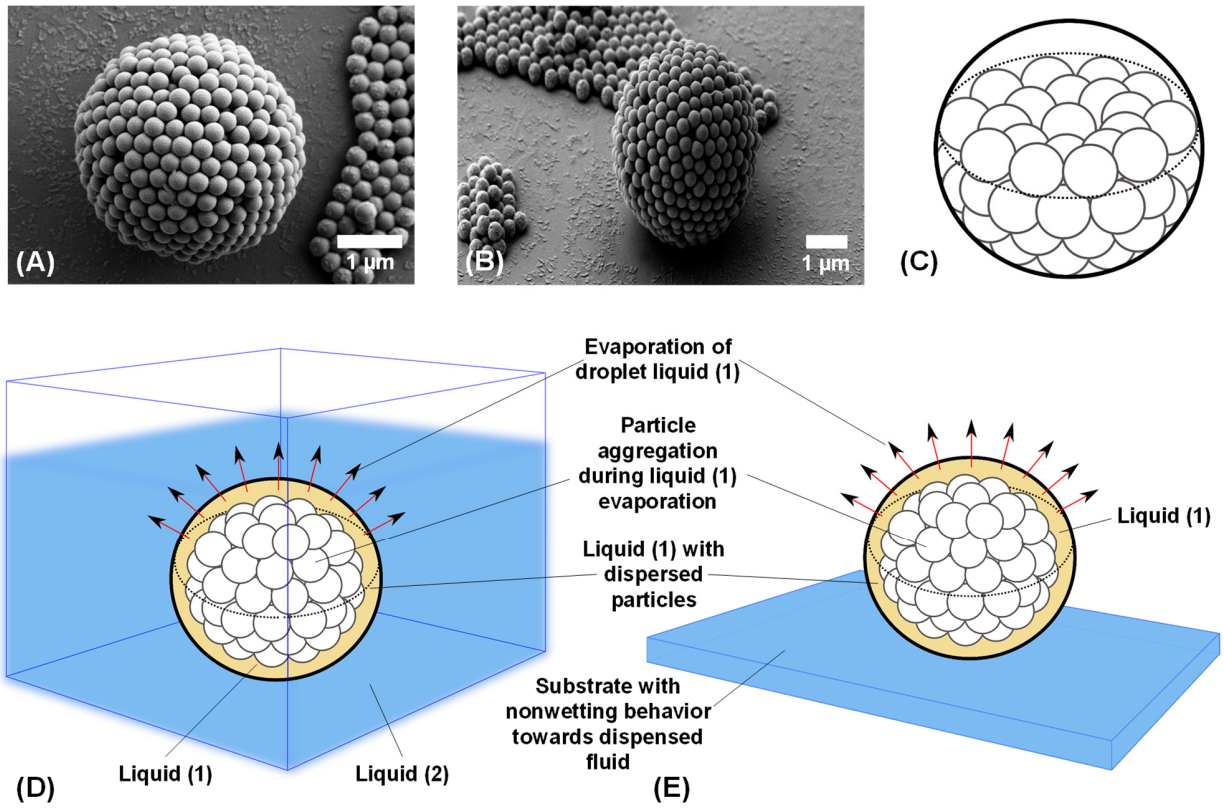

Figure 9: Examples of SCA by inkjet printing on solid substrates: (A) top view and (B) side view; (C) is a model of the SCA showing the arrangement of the nanospheres within the SCA; (D) and (E) depict schematically two basic concepts applied for the manufacturing of the SCA: (D) WSA method and (E) DSA method

WSA methods require an expensive experimental setup, for example, emulsion-assisted technologies and ultrasonic or microwave support to optimize and accelerate the particle consolidation.[154] With respect to industrial applications, DSA approaches are considered more promising.[161] The major disadvantage of the DSA methods is the strong dependence on the surface properties of the substrate on which the colloidal dispersion is dispensed. Basically, the interaction between the colloidal dispersion and the substrate defines the morphology of the

deposit and thus, whether or not SCAs can be prepared. However, DSA methods do not require ulterior process steps such as demulsification to extract the SCAs out of a liquid (see Figure 9D, liquid (2) in case of the WSA approach).[154] And DSA methods do not need any expensive experimental setup – for example, emulsion-assisted technologies and sometimes additional ultrasonic or microwave equipment to optimize the nanoparticle aggregation structure and to accelerate the nanoparticle consolidation.[154,166]

A few methods based on spray drying have been demonstrated as well.[167–171] In principle, these methods can be considered as DSA approaches (these methods are not considered in the WSA and DSA classification provided by Rastogi et al.[161]). However, there is no dependency anymore on the substrate since the evaporation takes place during the flight of the droplet. Interestingly, only a few publications are based on this simple approach. However, one has to admit that the droplet path length for the evaporation is usually quite long (e.g., about 2 m) as stated in the research work of Zhokhov et al.[169].

Inkjet printing technology was applied in 2009 for the first time to manufacture SCAs. Cho et al.[153] ejected toluene droplets containing PS nanospheres into an aqueous solution of emulsion stabilizer. The particles were self-assembled and consolidated inside the toluene droplet, and finally demulsified under stirring at 100 °C for 1 hour. Therefore, the basic method of this approach is WSA.[154] Similar procedures are reported by Zhao et al.[156] using microfluidic devices as a preparation method for SCAs. An ultra-micro pipette was utilized by Rastogi et al.[161] and Marin et al.[172] to dispense aqueous colloidal suspensions on superhydrophobic surfaces based on the principle of DSA. Anselmann et al.[173,174] applied a spray device in combination with a suitable (presumably hydrophobic) surface for developing SCA. However, inkjet printing of SCAs based on the DSA method has not yet been reported.

(Parts of this chapter are published in reference [166], reference [154] and reference [175])

2.6 All-inkjet-printed thin film transistors

Printing of organic TFTs has been one of the major research topics and drivers behind research in the area of printed electronics for many years.[76] One of the reasons is that transistors are basic components for integrated circuits and switches, and thus form the basis for most of the electronics (and especially consumer electronics) available today.[176] Transistors are considered to be one of the most important electronic devices and were the key enabler of the digital revolution.[76,176,177]

Most of the research in the field of printed electronics has been done on field effect transistors with organic semiconductors. Field effect transistors have a semiconductor layer separated by a

dielectric from the gate electrode. Source and drain (S-D) electrodes are separated from each other by a distance L, described as channel length. They are in contact with the semiconductor layer and inject and collect charges. The presence of an electric field controls and modulates the conductivity of the semiconductor layer in the channel between the S-D electrodes. By applying different voltages to the gate and the drain electrode, the electric field is generated, inducing and accumulating charge carriers at the semiconductor-dielectric interface and forming a conducting channel due to semiconductor band-bending. The number of charge carriers is a function of the voltage applied to the gate electrode and the capacitance of the transistor, which is mainly influenced by the dielectric thickness and dielectric constant. The type of charge carrier (electrons or holes) depends on the semiconductor material and whether the voltage applied to the gate is positive or negative. Thus, the transistor is "off" when no voltage is applied due to the low intrinsic conductivity of the semiconductor, and turns "on" upon voltage application.[178–180]

A TFT which is working well should have high output currents and low leakage currents, fast frequency of operation, and high ratio of currents between the on and off states. Leakage current is characterized as a small current flowing through the gate dielectric. Basically, this parameter defines the ratio of the current in the TFT "on" state (I_{ON}) and the TFT "off" state (I_{OFF}).[178] All of these desirable parameters are influenced by the mobility of the organic semiconductor, which is defined as the averaged charge carrier drift velocity per unit of electric field.[181]

It becomes clear from the provided basic description of the operation principle that organic TFTs based on the field effect are interfacial devices. Their performance strongly depends on the interplay between the dielectric and the semiconductor surface which is still – about three decades after the introduction of organic field effect transistors – not yet fully understood.[180] However, the intensive research during the last decades has contributed greatly to the scientific understanding of fundamental charge transport principles and the improvement of semiconductor materials, as well as their interface; which in turn has led to an improved device performance of organic transistors, sensor, solar cells and light-emitting devices.[182]

The idea behind manufacturing TFTs by means of printing technologies (and thus, based on solution-processing) has been attracting many researchers during the last decades.[76,176] Printing technologies are considered to be a promising alternative to conventional lithography due to their characteristics, such as high-throughput, large area, and low-cost production.[176] Among the different printing technologies, inkjet printing as a method with the highest degree of digitization dominates the research activities on printed TFTs.[183,184] There are numerous publications available on inkjet-printed TFTs using different materials, different architectures and different inkjet technology platforms.[176] However, in most of the publications only some of the layers are deposited by inkjet printing while others, such as the dielectric and/or the semiconductor, are spin-

coated, or electrode layers are evaporated.[101,176,185–200] In contrast, the number of scientific publications reporting about all-inkjet-printed TFTs and demonstrating the entire process chain is very low.[201–213]

Although all-inkjet-printed TFTs have been demonstrated for many years, the viability of the inkjet printing process for the manufacturing of printed electronics and specifically of TFTs was considered to be unclear and is still under discussion.[23,176,183] Several reasons for this uncertainty were identified, including (i) pixelation issues due to the inkjet-inherent droplet-by-droplet approach, (ii) complex drying phenomena, (iii) drop placement accuracy, and (iv) concerns about yield when doing up-scaling to allow higher printing speed, among others.[176] While many researchers have studied pixelation and drying effects in inkjet printing, the issues of drop placement accuracy and especially of yield for printed electronics remain poorly addressed. Pixelation issues in inkjet printing and corresponding effects of drying or post-processing were discussed by Diaz et al.[105], Soltman et al.[110], Ramon et al.[214], and Hammerschmidt et al.[215,216], among others.[176] The study of drying dynamics of inkjet-printed droplets on solid surfaces and the resulting deposit morphology has also been widely researched.[99,140,217–219] The improvement of droplet placement accuracy is an important task for printhead manufacturers.[176] Drop placement accuracies of less than 5 µm across the printhead were already reported in 2010 by Reinhold et al.[220], using Xaar 1001 piezoelectric inkjet printheads. The droplet placement accuracy depends on many parameters, such as nozzle straightness, jet-to-jet variation, droplet velocity, nozzle and surface wetting, ink formulation, and of course, largely on the distance between nozzle and substrate.[14,176] With regard to this last consideration, the lower the distance, the higher the accuracy.[15] In general, a 2 mm to 3 mm stand-off distance is used for piezoelectric and thermal inkjet printing in the area of graphic printing.[13,176] However, paper is usually applied as a substrate in the graphic industry. This is very rough on its surface compared to the plastic films that are mostly employed in printed electronics.[176] Therefore, the nozzle-to-substrate distance can be decreased remarkably in printed electronics to 1 mm or even less, as long as the substrate movement is sufficiently accurate.[176] This lower distance between printhead and substrate will increase the droplet placement accuracy. Concerns about yield when doing up-scaling in inkjet printing are probably the most important aspects to be discussed in the following. Up-scaling in inkjet printing is done by increasing the number of nozzles either (i) by using a printhead providing more nozzles, for example, due to the nozzle arrangement in multiple lines, or (ii) by forming arrays of multiple printheads.[176] However, increasing the number of nozzles makes the process even more challenging with respect to the process reliability.[24,176] Finally, this reliability will define if inkjet printing is a viable manufacturing process on an industrial scale for printed electronics, and specifically, TFTs. Up-scaling and reliability of the inkjet printing process for TFTs has been rarely

addressed in the literature.[176] Abbel et al.[221] demonstrated an up-scaling strategy for the inkjet deposition of silver lines, ranging from small-scale laboratory equipment to pre-industrial scale equipment. However, yield issues are not addressed.[176] Kim et al.[204] indicated that the manufacturing yield of the all-inkjet-printed TFTs with a simple one-channel layout is about 75 % for 160 TFTs deposited on 20 mm x 20 mm. The deposition was done with a single nozzle inkjet system. Recently, we have demonstrated the up-scaling of all-inkjet-printed capacitors and all-inkjet-printed TFTs.[212] Yields up to 70 % were obtained for the all-inkjet-printed TFTs. For the first time, industrial inkjet printheads were used along with laboratory printheads for the manufacturing of TFTs with a complex interdigitated S-D electrode design.[212]

In this respect, state-of-the-art of inkjet-printed TFTs is still the manufacturing of only a few TFTs with a very simplistic layout on small areas using laboratory-grade inkjet equipment.[176] An example is shown in Figure 10, which depicts five printed TFTs with a simple one-channel layout. This approach does not allow for the consideration of the process yield or any detailed statistical evaluation of the characteristics of the transistors.[176]

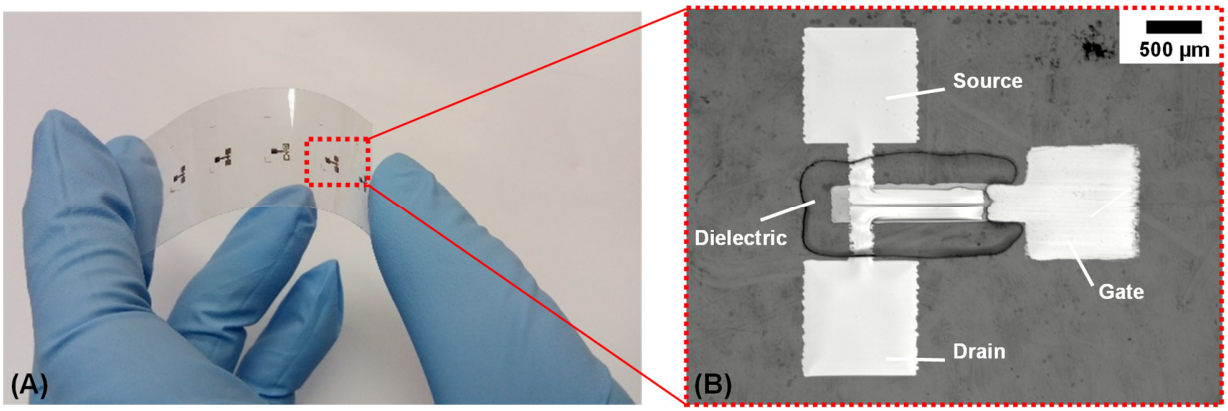

Figure 10: Image representing exemplarily the state-of-the-art of all-inkjet-printed TFTs: (A) photograph showing four printed TFTs on flexible polymer substrate and (B) is a magnified section depicting a TFT with a simple one-channel design (adapted from [176])

*(*Parts of this chapter are published in reference [176]*)*

3 Experimental section

3.1 Inkjet printing systems and accessories

Printed nanospheres and photonics

Deposition of the colloidal nanosphere ink formulations was carried out with a laboratory Dimatix Materials Printer 2831 (DMP 2831, Fujifilm Dimatix). The DMP 2831 was equipped with laboratory cartridge printheads with a 10 pL nominal droplet volume and a silicon nozzle plate with a non-wetting coating. Standard Dimatix Materials Cartridges (DMC) were employed as reservoirs for the ink formulations. The printheads have 16 square-shaped nozzles arranged in a single line, each with an edge length of about 21.5 µm (the commonly used term is nozzle diameter – although the nozzle has a square shape in this case). The center-to-center distance between the nozzles is 254 µm, resulting in a native print resolution of 100 dpi. The inside of the printer and details of the DMC are shown in Figure 11.

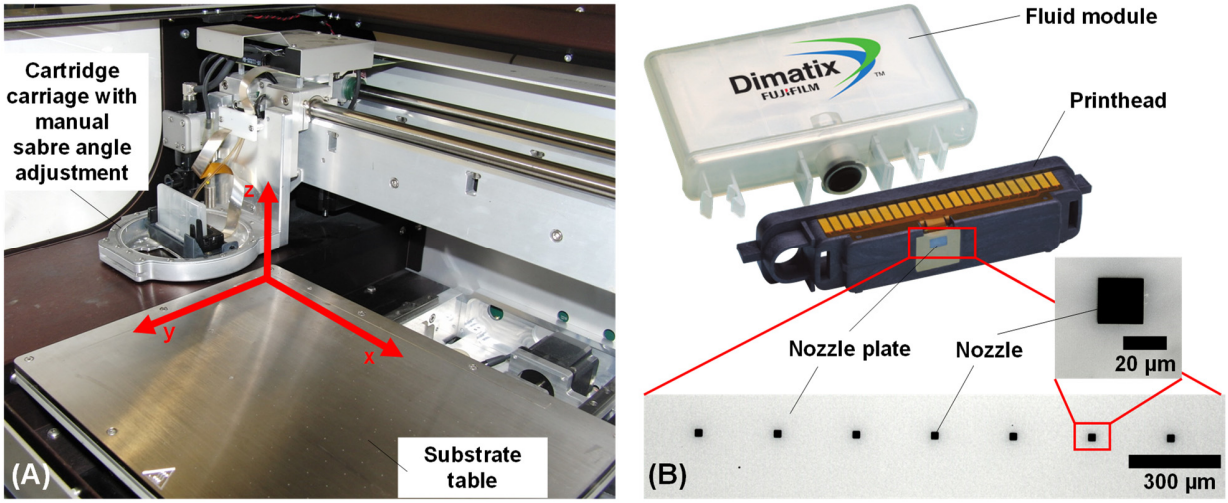

Figure 11: (A) image of the inside of the inkjet system DMP 2831 with installed DMC printhead and (B) the DMC consisting of fluid module and printhead (adapted from [222]); the insets are microscopic images of a section of the nozzle plate with the square-shaped nozzles

An increase of resolution can be done by changing the sabre angle of the printhead with regard to the deposition process. The DMP 2831 was applied in both single nozzle and multi nozzle mode. The distance between the nozzles and the substrate was maintained at 1 mm during printing. All printings were performed in ambient conditions (specifically, laboratory conditions

were 22.5 ± 0.8 °C room temperature and 22 ± 3 % relative humidity). The DMP 2831 has a built-in stroboscopic drop watcher to allow for the determination and optimization of the droplet formation process by adjusting the waveform applied to the piezoelectric transducer. The design of a complex polar waveform with the DMP 2831 is fully flexible due to the user-controllable variation of the pulse shape (i.e., voltage, time duration for dwell time, rise time and fall time) and frequency. By default, the printing process is unidirectional. The printhead is transferred over the substrate in x-direction (see Figure 11). Thus, deposition in x-direction is described as deposition in printing direction. The angle β defines the orientation of the print pattern towards the printing direction. For example, if the long edge length of a rectangle is oriented in printing direction, then β = 0 °. The substrate table of the printer transfers the substrate in y-direction and thus perpendicular to the printing direction in order to begin the deposition process on a new line. Therefore, if the long edge length of a rectangle is oriented perpendicular to the printing direction, then β = 90 °. The print image is built up drop-by-drop and line-by-line. The distance between substrate and printhead can be varied by moving the cartridge carriage in z-direction.

Printed electronics

Deposition of functional ink formulations for the manufacturing of TFTs was carried out with the DMP 2831 as previously described, as well as a Dimatix Materials Printer DMP 3000 (DMP 3000, Fujifilm Dimatix). Figure 12A shows the inside of the DMP 3000. The DMP 3000 was equipped with industrial Fujifilm Dimatix SE3, Fujifilm Dimatix SX3, and Fujifilm D-class D-128/10 DPN printheads, respectively. All the printheads have a silicon nozzle plate with a non-wetting coating. Standard DMC cartridges can be also used with the DMP 3000. The SE3 has 128 nozzles arranged in a single line with a nozzle diameter of 42 µm. The nominal droplet volume is 35 pL. 508 µm is the center-to-center distance between the nozzles, resulting in a native resolution of 50 dpi.[223] The SX3 has 128 nozzles arranged in a single line with a center-to-center distance of 508 µm as well, but a nozzle diameter of 27 µm. The nominal droplet volume is 8 pL.[224] The SX3 and SE3 printheads are designed for high throughput printing of functional fluids according to industrial inkjet standards. As shown in Figure 12B-E, the printheads were mounted on the main assembly plate which was built up on a printhead carrier and connected to a stainless steel ink development reservoir (capacity of about 9 mL) with a heater-thermistor assembly (all parts from Fujifilm Dimatix). Each printhead required its own printhead carrier. The D-128/10 printhead was mounted on an H-shaped D-class printhead latch assembly kit from Fujifilm Dimatix, also containing a reservoir and a built-in heater-thermistor assembly. The D-128/10 printhead has 128 nozzles and a center-to-center distance of 254 µm. The nozzle diameter is 21.5 µm, resulting in a

nominal droplet volume of 10 pL.[225] The DMP 3000 has relatively similar features as the DMP 2831, but of a higher quality and performance standard.[226,227]

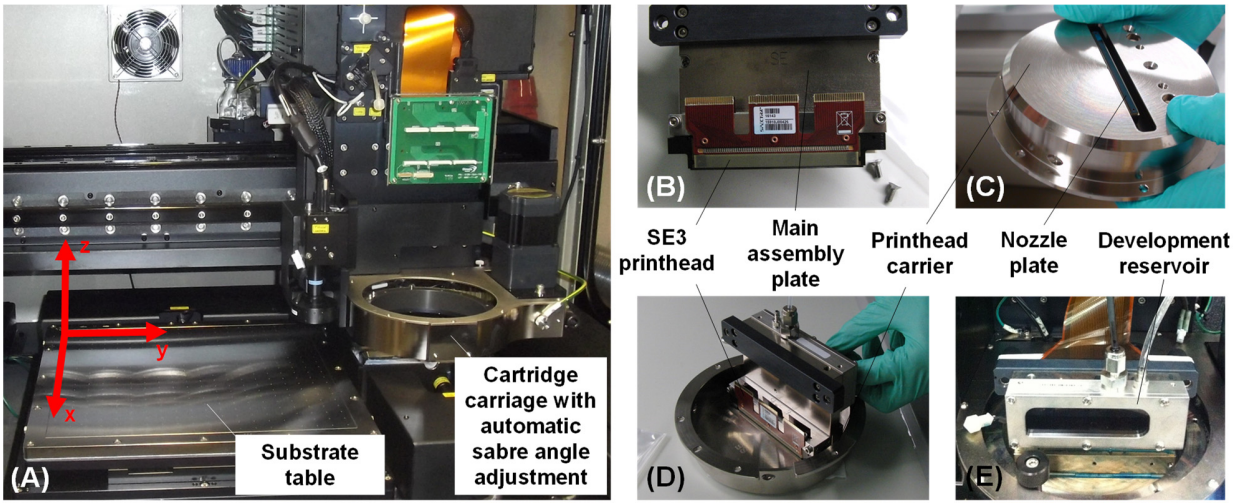

Figure 12: (A) image of the inside of the inkjet system DMP 3000; (B)-(E) show images of the printhead assembly required for the use with industrial inkjet printheads; (B) is the main assembly plate with the mounted printhead, (C) the printhead carrier with installed printhead as bottom view, (D) the printhead assembly with ink development reservoir on the back and (E) the installed printhead assembly in the cartridge carriage of the DMP 3000

Both DMC printheads and different industrial inkjet printheads can be used with the same printer, which is an important benefit for the development of printed TFTs. For example, it allows one to choose different droplet volumes according to the selected printhead. However, the assembly, installation, and preparation procedure of the jetting assemblies with industrial printheads is quite complex and time consuming compared to the simple handling of the DMC system.

The distance between the nozzles and the substrate was maintained at 1 mm during printing. All printings were performed in ambient conditions. The printing process is unidirectional. In contrast to the DMP 2831, the table with the substrate is transferred under the printhead in x-direction (i.e., printing direction, see Figure 12A) and the printhead is transferred perpendicular to the printing direction in order to start the deposition process on a new line. The print image is generated drop-by-drop and line-by-line in a similar manner as for the DMP 2831.

All the specifications of the printheads used are listed in Table 2.

Table 2: Specification overview for the used printheads based on Fujifilm Dimatix data sheets[222–226,228] and accessories price list from 2011[229]

Printhead	DMC-11610 printheads	SE-3	SX-3	D-128/10 DPN
Nominal droplet volume [pL]	10	35	8	10
Nozzle diameter [µm]	21.5	42	19	21.5
Number of nozzles [#]	16	128	128	128
Nozzle spacing [µm] / print resolution [dpi]	254 / 100	508 / 50	508 / 50	254 / 100
Maximum voltage [V]	40	138	138	40
Nozzle plate	Silicon with non-wetting coating	Silicon with non-wetting coating	Silicon with non-wetting coating	Silicon with non-wetting coating
Compatible jetting fluids	Water, organic solvents, UV inks, oil ink	Water, organic solvents, UV inks, oil ink	Water, organic solvents, UV inks, oil ink	Water, organic solvents, UV inks, oil ink
Optimal fluid viscosity range [mPa·s]	2 – 30	10 – 14	10 – 14	2 – 30
Dimatix printing system compatibility	DMP 2831 and DMP 3000	DMP 3000	DMP 3000	DMP 3000
Unit price [USD]	66.5 (including cartridge)	3000	7000	1950

3.2 Inks and substrates

Printed photonics

Different commercially available colloidal nanosphere suspensions were used as a base for inkjet inks. The commercial master suspensions contain (i) highly monodisperse organic PS nanosphere particles with anionic, hydrophobic surface or (ii) inorganic silica (SiO_2) nanospheres with non-functionalized polar hydroxyl surface groups (Si-OH) suspended in water. The colloidal inks were obtained from Polysciences (Warrington, PA, USA; abbreviated PSC221), BS-Partikel GmbH (Wiesbaden, Germany, abbreviated BS305), Duke Scientific (Palo Alto, CA, USA; abbreviated DS300) and Bangs Laboratories (Fishers, IN, USA; abbreviated: BL280). The colloidal ink BL280 containing 10 wt% SiO_2 nanospheres was diluted in deionized water (16 MΩ·cm) to 4 wt%, 2 wt% and 1 wt% solids content. A binary suspension in which SiO_2 and PS nanospheres were dispersed was prepared by mixing identical quantities of the 2 wt% BS305 PS suspension with the 2 wt% BL280 SiO_2 suspension under ultrasonic treatment. Formamide (boiling point: 210 °C, surface

tension: 58.9 mN/m, vapor pressure: 0.07 mmHg at 25 °C) and diethylene glycol (boiling point: 245 °C, surface tension: 44.4 mN/m, vapor pressure: 0.006 mmHg at 25 °C) were added to BS305 in different quantities to vary the boiling point of the suspension. The size of the nanospheres was provided by the manufacturers and was additionally proven by SEM. A DataPhysics OCA20 (DataPhysics Instruments GmbH, Filderstadt, Germany) contact angle measurement system in pendant-drop mode was applied to determine the surface tension of the suspensions. A Zetaview system from Particle Metrix[b] (Particle Metrix GmbH, Meerbusch, Germany) was employed to investigate the zeta potential ζ and the electrophoretic mobility μ_e of the nanospheres in the different ink formulation. The pH value was determined with universal indicator paper (Munktell, Bärenstein, Germany and Macherey Nagel, Düren, Germany). A summary of the used colloidal suspensions and their characteristics is provided in Table 3.[98]

Table 3: Characteristics of the colloidal nanosphere suspensions used for the experiments[98,154]

Manufacturer	**Polysciences**	**BS-Partikel**	**Duke Scientific**	**Bangs Laboratories**	**Custom-made binary mixture**
Abbreviation	PSC221	BS305	DS300	BL280	BS305 & BL280
Nanosphere material	PS	PS	PS	SiO_2	PS & SiO_2
Nanosphere diameter [nm]	221 ± 17	305 ± 8	300 ± 5	280 ± 7	305 ± 8 (PS), 280 ± 7 (SiO_2)
Nanosphere density [g/cm³]	1.05	1.05	1.05	1.96	1.05 (PS), 1.96 (SiO_2)
Refractive index (at 589 nm)	1.59	1.59	1.59	1.37 – 1.46	1.59 (PS), 1.37-1.46 (SiO_2)
Solids content [wt%]	2.6	2.0	0.1	10	2
Surface tension [mN/m]	44.1 ± 2.2	46.8 ± 0.8	57.3 ± 0.9	60.8 ± 1.3	56.2 ± 1.2
Electrophoretic mobility [(µm/sec)/(V/cm)]	-2.4 ± 0.9	-4.0 ± 1.2	Not available	-3.1 ± 1.5	-3.7 ± 1.1
Zeta potential (mV)	-34 ± 13	-51 ± 15	Not available	-39 ± 19	-47 ± 13
pH value	7.0 ± 0.2	7.0 ± 0.2	7.0 ± 0.2	7.0 ± 0.2	7.0 ± 0.2
Solids content used for printing [wt%]	2.6	1.5; 2	0.1	4; 2; 1	2
Development of SCAs	Yes	Yes	No	Yes	Yes

[b] The measurements with the Zetaview system were performed at the Department of Physical Chemistry at Technische Universität Chemnitz together with Dr. Steffen Hemeltjen (head of the department: Prof. Dr. Werner Goedel).

All the prepared inks were treated ultrasonically for about 3 – 15 minutes before printing. No further filtering process as it is usual for inkjet printing was carried out, since the particles are monodisperse and ultrasonic treatment was applied to re-disperse and re-agglomerate them.[98] Different waveforms were developed for each of the inks. The waveforms will be presented in the Chapter 5.2.

Coverslip glasses (18 mm x 18 mm and 20 mm x 20 mm; thickness 0.145 ± 0.015 mm, purchased from VWR Scientific, Dresden, Germany) served as substrates for the printing process and were treated with different methods. The following treatments were applied to vary the surface energy of the coverslip glasses, and thus the contact angle of a sessile droplet of water with the glasses: (i) "untreated", only cleaned with ethanol, (ii) hexamethyldisilazane (HMDS) treatment, (iii) octadecyltrichlorosilane (OTS) treatment[c], (iv) surfactant treated (based on anionic surfactants), and (v) corona treatment. The contact angle on all surfaces was determined with pure deionized water droplets (resistivity about 16 MΩ·cm) using the DataPhysics OCA20 system in sessile-drop mode. Table 4 summarizes the results of the measurement. The surfactant treatment and the silane treatments were done in a chemical bath according to known methods. A corona treatment was performed using an Arcotec corona generator CG061-2 (Arcotec GmbH, Mönsheim, Germany) with a high voltage discharge of 2.3 kV.[98]

Table 4: Measured contact angles of sessile deionized water droplets on the differently treated glass surfaces[166]

	Corona treatment	Surfactant treatment	untreated	HMDS treatment	OTS treatment
Contact angle [°]	< 10	< 10	67.7 ± 2.7	78.7 ± 1.5	100 ± 5

Printed electronics

Many commercially available silver ink formulations designed for inkjet printing were used. They are listed with their characteristic properties mostly provided from the product data sheets in Table 5. The costs were calculated based on quotes provided by the ink manufacturers to Technische Universität Chemnitz for 100 mL or 100 g of the inks. The main ink used is in this dissertation is Sun Chemical EMD5603. All the ink formulations except Jet-600C from KS Hisense are silver nanoparticle inks which are typically used in the field of printed electronics.

[c] The HMDS and OTS treatments were partially done at the Department of Physical Chemistry at Technische Universität Chemnitz by Dr. Susann Ebert (head of the department: Prof. Dr. Werner Goedel).

Table 5: Overview of the printed commercially available silver inks and their characteristics according to the corresponding product data sheets provided by the manufacturers; costs are calculated based on quotes provided to the Technische Universität Chemnitz for 100 mL or 100 g of the silver ink formulations

Manufacturer	Ink	Solids content [wt%]	Particle size [nm]	Viscosity [mPa·s]	Surface tension [mN/m]	Solvents	Costs [€/mL] or [€/g]*
Advanced Nano Product	ANP DGP 40LT-15C	30 – 35	≤ 50	10 – 17	35 – 38	Triethylene glycol monoethyl ether	7.5
Bando	OJ30-1	1 – 40	15 – 20	5 – 15	20 – 40	1,3-propanediol, glycol, glycerin, water	45
Bando	OJ31-1	35 – 45	15 – 20	6 – 10	25 – 30	Glycol, glycerin, water	45
Bayer	Bayink TPS C	~ 20	Not available	~ 10.6	~ 23.3	Water	11
Cabot	CSD-32	45 – 55	< 60	50 – 100		Ethylene glycol	6.5*
Fraunhofer IKTS	Ag-LT-20	~ 20	≤ 80	8 – 12	32 – 38	Water	16.5
Genes'Ink	CS01121	20	< 10	10 – 16	24 – 30	Alkane, alkohol	10
Harima	NPS-JL	~ 55	~ 7	~ 11	Not available	n-Tetradecane, petroleum hydrocarbon, napthen	6.6*
KS Hisense	Jet-600C	10 – 30	Not available	7 – 10	27 – 29	alcohol	2.6*
Methode	9102	-	-	~ 3.5	31 – 33	Water	9.1
Novacentrix	Metalon JS-B25HV	~ 25	~ 60	~ 8	30 – 32	Water	3.7
PVnanocell	I125EGE-100	20 – 30	70 – 115	Not available	Not available	Ethylene glycol, ethyl alcohol	5.3
PVnanocell	I125EGD-101	20 – 30	70 – 115	Not available	Not available	Ethylene glycol, dipropylene glycol methyl ether	5.3
PVnanocell	I30EG-1	~ 30	70 – 115	~ 28	~ 47	Ethylene glycol	5.3
PVnanocell	I30TD-102	28 – 32	70 – 115	Not available	Not available	Tripropylene glycol methyl ether, dipropylene glycol methyl ether	5.3
PVnanocell	I50T-11	48 – 50	70 – 115	~ 24	~ 28	Tripropylene glycol monomethyl ether	5.3
Sun Chemical	Suntronic EMD5603	~ 20	30 – 50	7 – 14	27 – 31	Ethanediol, ethanol	7
Sun Chemical	Suntronic EMD5730	~ 40	Not available	10 – 13	27 – 31	Ethanediol, ethyl (S) -2-hydroxypropionate	20.9
UTDots	UTDAgIJ1	55 – 60	~ 10	5 – 30	Not available	Hydrocarbons	12.7
Xerox	XCM-NS32	~ 32	< 12	~ 3	Not available	Decahydro-naphthalene	6.2*

Cross-linked poly-4-vinylphenol (cPVP, PVP ordered from Sigma Aldrich, Mw about 25000) was mainly applied as dielectric material. The ink formulation was prepared by dissolving 0.9 g of PVP in 10 mL of propylene glycol monomethyl ether acetate (PGMEA) at room temperature, supported

by magnetic stirring for 3 h. Poly(melamine-co-formaldehyde) methylated (PMFM, from Aldrich, Mn about 432, 84 wt% in 1-butanol) was added as a crosslinking agent by stirring for 2 h. The ratio of PVP to PMFM was 5:1. Before printing, the dielectric inks were filtered with a 0.2 µm syringe filter.[176]

Besides the cPVP, the following dielectrics were used:

- Sun Chemical EMD6415
- Tritron Hyperion Black ProWet
- Tritron V Photon Clear NonWet

Sun Chemical EMD6415 is a clear, UV curable dielectric ink based on acrylates designed to match up with the EMD5603 silver ink in terms of wetting and spreading when printing on top of each other. It was developed by Sun Chemical for applications in the field of printed electronics. The two Tritron ink formulations are also UV curable (based on the principle of radical polymerization), and mainly consist of acrylates. According to the datasheet, the Tritron Hyperion Black ProWet has a viscosity of about 24 ± 1 mPa·s and a surface tension of 23 ± 1 mN/m, and is black in appearance. The Tritron V Photon Clear NonWet is a clear ink formulation with a viscosity of 17.5 ± 1.5 mPa·s and a surface tension of 32 ± 1 mN/m. The different surface tensions correspond to the terms “ProWet” and “NonWet” in the names of the products. The inks by Tritron are reported by the supplier as having a good inkjet jetting behavior in conjunction with regular wetting properties for single-pass applications, enabling the deposition of patterns with good uniformity and a low surface roughness. In general, these inkjet ink are dedicated to graphic inkjet printing but have also been used for functional printing in the literature[201,215,216,230–232].

The ink formulation FS0096 provided by Flexink (Flexink, Southampton, UK) was employed as an organic semiconductor (OSC). It was specially designed for a fast inkjet printing process and consists of an amorphous, conjugated and aromatic-ordered p-type polymer (4 wt%) dissolved in mesitylene. Dedicated waveforms were developed for all of the different inks. The objective of the waveform design was to enable the ejection of a single spherical, regular droplet on a trajectory perpendicular to the nozzle plate.

Different materials were applied as substrates for the deposition of the inks for printed electronics. In most cases, the printing was performed on the PEN films Q65FA and Q65HA[d] (DuPont Teijin

[d] Teonex Q65FA and Q65HA are basically the same product. Q65FA has a one-side adhesion promoting chemical treatment while Q65HA has it on both sides. However, the manufacturing of Q65FA was stopped in 2015 and the product was substituted with Q65HA that has according to the manufacturer the same properties. The costs of these films are quite high with about 5 € per A4 sheet (low order quantities).

Films, Tokyo, Japan). These films have a thickness of about 125 µm and an area size of DIN A4 (210 mm x 297 mm), with a one-side or double-side adhesion-promoting chemical treatment. The average roughness was determined with the help of Atomic Force Microscopy (AFM), and was about 1 nm[e]. The surface energy of the films was measured to about 41.5 ± 4.5 mN/m. The ratio of disperse part to polar part was about 9:1.

In addition, standard float glasses with a thickness of 2 mm and an area size of 100 mm x 100 mm were used as substrates. There was no special coating on the glass. The glasses were cleaned before printing with acetone end ethanol. First, acetone-impregnated tissues were applied to wipe off dirt, dust and other debris from the glass surface. Second, an ultrasonic treatment of the glasses was performed in acetone and in ethanol, each for 3 min. Finally, the substrate was dried in a flow of nitrogen for a few seconds. The contact angle θ of deionized water on the cleaned glass substrates was determined to be about 58.3 ± 1.8 °. The contact angle of the silver inks Sun Chemical EMD5603 and UTDots UTDAgIJ1 on the cleaned glass substrate was determined to be 44.9 ± 1.7 ° and 9.0 ± 1.8 °, respectively. Also, RCA-cleaned silicon dioxide (SiO_2) wafers with a thickness of 600 µm were applied as substrates.

3.3 Print patterns

Printed photonics

Single droplets were deposited by designing lines each with a width of 1 px and a low print resolution (e.g., 100 dpi) to avoid droplet coalescence. 1D films were obtained by increasing the print resolution so that droplet coalescence can take place. For the SCAs, mainly simple rectangles with an area size of 0.35 mm² and 1 mm² and different print resolutions ranging from about 600 dpi – 5080 dpi were designed with the pattern editor software provided by Fujifilm Dimatix.

Printed electronics

A dedicated print pattern consisting of 3D films (macroscopic lines) by printing several lines next to each other was developed for studying the influence of the printing direction. The 3D films have different orientations with respect to the printing process. Basically, they are aligned along the printing (orientation angle β = 0 °) direction up to the counter printing direction (β = 90 °) in steps of 22.5 °. The design continuous from β = 90 ° up to β = 180 ° in steps of 22.5 °, aiming to increase

[e] The AFM measurement was carried within the project TDK4PE by Dr. Fulvia Villani from the Italian National Agency for New Technologies, Energy and Sustainable Economic Development (ENEA) in Portici, Naples.

the statistical relevance of the data obtained during the printing. This continuation represents the mirrored part of the lines from 0 ° to 90 °. Despite the different orientation angles, the mirrored counterparts are equal to their originals. The digital length and width of the films are 10 mm and 500 µm, respectively. A measurement pad is designed at line start and line end with a size of 2 mm x 2 mm.

Adobe Illustrator and Adobe Photoshop were employed for the design. Firstly, the required print patterns were designed in Adobe Illustrator, exported as grey-scale file with a resolution of 5080 dpi, and converted to a 1-bit bitmap file using Adobe Photoshop and a threshold of 50 %.[95] The resolution of 5080 dpi was chosen since it is the maximum print resolution of the employed inkjet printer. Secondly, a grid pattern consisting of single print dots with the resolution of 1270 dpi, 1016 dpi, and 847 dpi was overlaid on the previously prepared print pattern like a mesh. All the print dots of the grid pattern which were located directly on top of the firstly prepared print pattern were finally defined as the dots to be printed. All of the other print dots were deleted.[95] Finally, three print patterns were designed with the following print resolutions: 847 dpi, 1016 dpi, and 1270 dpi. The designed print pattern and a scheme of the different print resolutions is shown in Figure 13.[95]

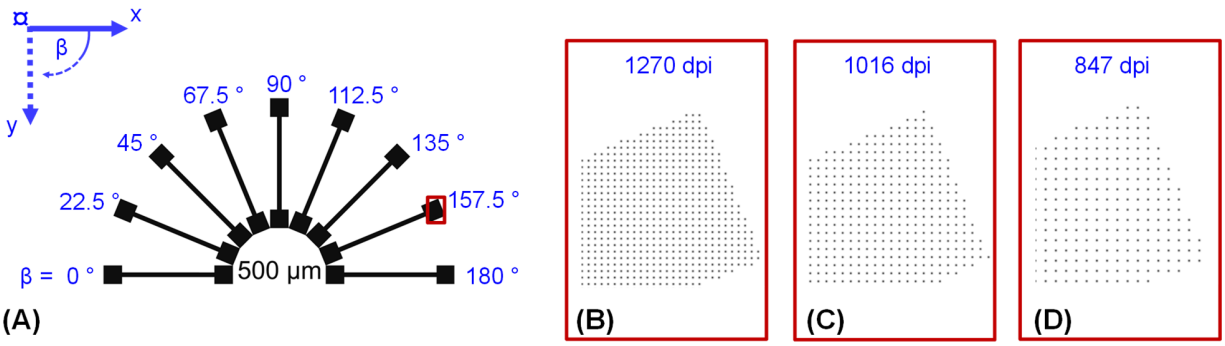

Figure 13: (A) print pattern layout (print areas are shown in black) consisting of lines with a line width of 500 µm at different orientation angles β (angles shown in °, blue color) to the printing process and with measurement pads; the coordinate axes at the top left indicate the print origin (¤), printing direction (x), and transfer direction (y); (B) – (D) are detailed images of the red-marked section in (A) depicting the digital pixel grid at the end of the designed line (adapted from [95])

A special test print pattern was designed to print conductive 1D films (i.e., lines with a width of 1 px). It consists of 15 horizontal line areas with different print resolutions starting from 182 dpi and ending with 5080 dpi (top to down). Since the pattern editor software of Fujifilm Dimatix does not allow the deposition of different print resolutions within one pattern, the design was developed with the help of Adobe Photoshop. The overall area size is about 2.5 mm x 2.9 mm. The distance between the lines is about 200 µm. A short section at the beginning of each line (about 140 µm long) was deposited with 5080 dpi to ensure proper nozzle operation and to simplify the

localization of the lines with a low print resolution. This kind of test pattern allows one to evaluate the line formation of the used silver inks as a function of print resolution. Furthermore, it provides a fast and simple indication about the wetting properties of the ink, and enables a comparison with other inks. A scheme of the print pattern is depicted in Figure 14A (not true to scale, number of droplets not representative). Figure 14B shows exemplarily the silver ink UTDAgIJ1 from UTDots deposited on a RCA-cleaned silicon wafer with the designed pattern. The surface of this silver ink is comparably rough with respect to other silver inks, especially for thick layers which are formed at higher print resolutions. Therefore, printed layers with a high print resolution appear black and layers at low print resolution appear white in Figure 14B. According to Figure 14B, single droplets are obtained reproducibly at a print resolution of 318 dpi and continuous 1D films until 635 dpi.

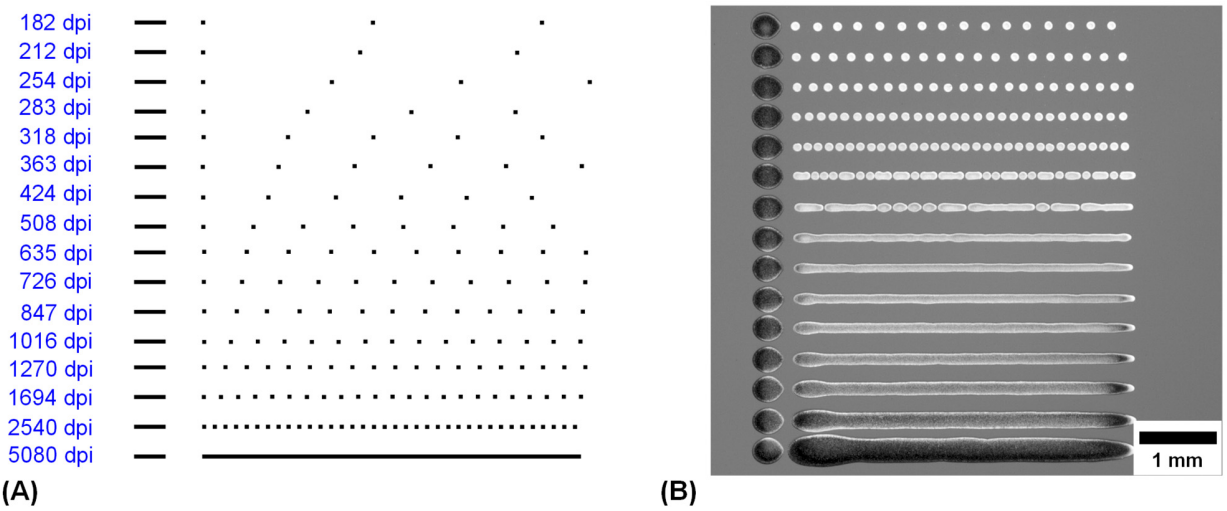

Figure 14: (A) scheme of the print pattern layout for the conductive ink formulations consisting of 13 lines (1D films) with different print resolutions (not true to scale, number of droplets not representative); (B) microscopic image of the ink UTDAgIJ1 from UTDots on silicon substrate printed with the line test layout shown in (A)

For the manufacturing of TFTs, the bottom-gate bottom-contact architecture was chosen. The software Clewin (WieWeb Software Inc., Netherlands) was employed for the development of the print pattern layout[f] consisting of four separated layers that were printed consecutively: (i) silver nanoparticle ink for the gate electrode, (ii) organic dielectric, (iii) silver nanoparticle ink for the S-D electrodes, and (iv) OSC. The layers were printed with different print resolutions, making it possible to control the amount of material deposited per area. For example, the silver as well as

[f] The design of the TFTs with the software Clewin was carried out within the project TDK4PE by the Printed Microelectronics Group at CAIAC, Universitat Autònoma de Barcelona, Bellaterra, Spain (Director: Prof. Dr. Jordi Carrabina; head of the group: Dr. Eloi Ramon).

the dielectric ink were deposited with 508 dpi, 564 dpi, 635 dpi and 726 dpi using the SE3 printhead with a nominal droplet volume of 35 pL. 1270 dpi with 10 pL nominal droplet volume printheads were applied for the OSC. The variation of print resolution of the S-D electrodes also results in a variation of the width of the fingers and thus in a variation of channel length of the transistor. The S-D electrodes were designed as interdigitated finger electrodes. The ratio of channel width W to channel length L (W/L) was varied to have different active area sizes and different numbers of finger electrodes. The following ratios were designed: 20, 40, 80, 100, 140, 180, and 240. Figure 15 shows a scheme of the architecture of the TFTs from (A) top view and as (B) cross-sectional view. The sizes are not true to scale. However, the dielectric layer area is by intention very large compared to the other areas, for example, compared to the OSC layer.

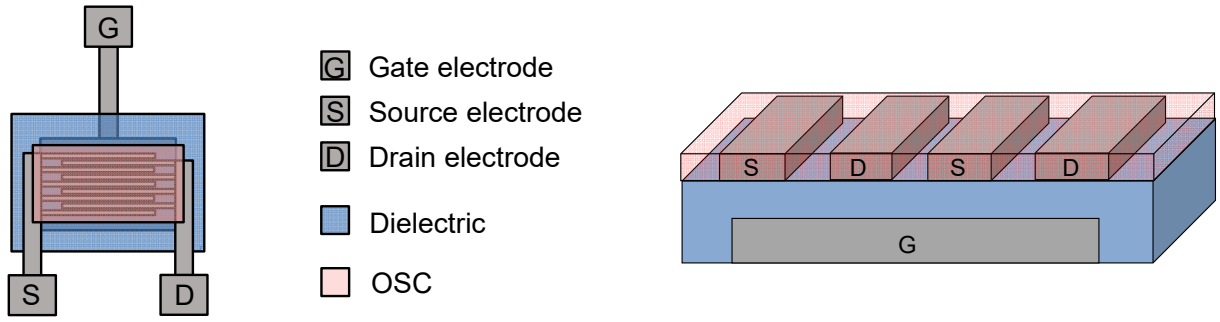

Figure 15: Architecture of the printed TFTs as (A) top view and (B) cross-sectional view; the electrodes are based on silver nanoparticles, the dielectric and the OSC are organic materials (adapted from [176])

3.4 Post-processing

For solution-based deposition technologies such as inkjet printing, post-treatment or post-processing plays an important role in obtaining deposits with the desired functionalities. These processes comprise, for example, the drying, curing, and/or sintering steps. Different tools are available to perform the post-treatment of the deposits.

No special post-treatment tool was required for the printed colloidal nanospheres. The ejected droplets dry either during their flight to the substrate or directly on the substrate. The water simply evaporates in ambient conditions and a stable nanosphere configuration remains due to strong van der Waals forces between the substrate surface and the nanospheres, as well as among the nanospheres themselves. Potentially remaining residual traces of water from the ink formulation itself or the ambient humidity in the menisci between adjacent nanospheres, as well as

nanospheres and substrate, contribute to an enhancement of these adhesion and cohesion forces.[154]

For the field of printed electronics, post-treatment methods are mostly essential to obtain the desired functionality of the layer. Drying and sintering of the silver nanoparticle deposits for the TFTs was done in an oven at 135 °C for 30 min. The cPVP dielectric films were dried inside a fume cupboard at room temperature for 20 min. Afterwards, the curing and crosslinking was performed at 150 °C for 40 min in a low vacuum. UV curing of the dielectrics Sun Chemical EMD6415, Tritron Hyperion Black ProWet and Tritron V Photon Clear NonWet was performed with a BlueWave 75 UV Curing Spot Lamp (Dymax, Torrington, USA) and a SubZero 085 ES system (Integration Technology, Upper Heyford, UK). The OSC film was dried at 100 °C for 20 min in an oven. Storage of the TFTs was done in dark and low vacuum (≤ 0.09 mbar). All printing and characterization steps were carried out in ambient conditions. Further or deviating process parameters are explained when necessary in Chapters 4 to 6.

3.5 Optical, morphological and functional characterization

The printed deposits were analyzed by scanning electron microscopy (SEM) using a Hitachi TM-1000 (Hitachi High-Technologies Cooperation, Tokyo, Japan), a Nova NanoSEM 200 (FEI, Hillsboro, USA)[g], and a Zeiss Auriga 60 (Zeiss AG, Jena, Germany)[h]. To avoid charging effects, most of the samples were coated with an approximately 18 nm thick layer of platinum by sputtering at 40 mA for 120 s using a BAL-TEC SCD 050 (formerly BAL-TEC AG, Balzers, Liechtenstein)[i] electron microscope preparation system. Optical microscopy analysis was carried out on a Leica DM 4000 M (Leica Microsystems CMS GmbH, Wetzlar, Germany) and a Zeiss Axio Imager M2m (Carl Zeiss Microscopy GmbH, Jena, Germany).

Microreflectance spectroscopy was performed using the mentioned Zeiss microscope coupled with a TIDAS S MSP 800 spectrometer (J&M Analytik AG, Esslingen, Germany). The light source of the microscope was used to illuminate the sample through the microscope objective lenses. The reflected light was collected by the same lenses and guided to the spectrometer by optical fibers. At the same time, the microscope is coupled to a CCD camera, making it possible to

[g] The SEM analysis with the Nova NanoSEM 200 was performed at the Department of Solid Surface Analysis at Technische Universität Chemnitz together with Torsten Jagemann (head of the department: Prof. Dr. Michael Hietschold).

[h] The SEM analysis with the Zeiss Auriga 60 was performed at the Micro Materials Center at Fraunhofer ENAS in Chemnitz together with Dirk Rittrich and Iris Höbelt (head of the department: Prof. Dr. Sven Rzepka, head of the institute: Prof. Dr. Thomas Gessner).

[i] The sputtering system was ceded for use by at the Department of Solid Surface Analysis at Technische Universität Chemnitz (head of the department: Prof. Dr. Michael Hietschold).

precisely define the measurement position. The measurement area for the spectroscopy is adjustable by a manual aperture. A wavelength range of 200 nm – 980 nm is detectable. However, due to the lenses, further microscope optics and the halogen light source, the reliably usable wavelength range is about 380 nm – 900 nm. The angle of incidence and measurement was kept constant for all the measurements with the spectrometer at 0 °. The consistent operation of the spectrometer was confirmed by spot checks with the same spectrometer coupled to the Leica DM 4000 M, and by using a similar spectrometer (A.S. & Co. GmbH, München, Germany) coupled with two different Zeiss microscopes. In some cases, the raw data of the measurement system was used to plot the graphs. However, the data of some samples showed clearly identifiable interference effects and noise. These data were smoothed with the Savitzky-Golay filter with a second-order polynomial considering a moving window of 100 data points.

To determine thickness and roughness of the printed deposits, profilometry scans were performed with a Dektak 150 (Veeco Instruments, New York, USA). In addition, the 3D laser scanning VK9700 (Keyence, Osaka, Japan)[j] was employed for profile scans and 3D profiles of deposits. Usually, the raw data from both measurement systems was used to plot the graphs. However, averages profiles of the inks EMD5603 and UTDAgIJ1 applied in Chapter 6.1 were normalized and equalized based on the simple moving average method using 300 neighboring values to smoothen the data.

Sheet resistance measurements were carried out according to the method of van der Pauw (by placing for point probes in the shape of a square (3 mm x 3 mm, 4 mm x 4 mm or 5 mm x 5 mm) with the manual probe system PM5 (Suess MicroTec, Garching, Germany) connected to a Keithley SourceMeter 2612 (Keithley Instruments, Cleveland, USA) on the layers.

Electrical characterization of the TFTs[k] was carried out with a semi-automatic Cascade Microtech Summit Series 12000 probe station (Cascade Microtech, Beaverton, USA) using a semiconductor parameter analyzer Keithley 4200 (according to the IEEE 1620 standard[233] for test methods) for the characterization of organic transistors and individual layers.

[j] The laser scanning system was provided by the Department of Conveyers at Technische Universität Chemnitz (head of the department: Prof. Dr. Klaus Nendel).

[k] The TFT characterization was done within the project TDK4PE by the Printed Microelectronics Group at CAIAC, Universitat Autònoma de Barcelona, Bellaterra, Spain (Director: Prof. Dr. Jordi Carrabina; head of the group: Dr. Eloi Ramon), by the Department of Integrated Circuits and Systems (ICAS) at the Institute de Microelectronica de Barcelona IMB-CNM (CSIC) (head of the department: Prof. Dr. Lluis Teres, director: Prof. Dr. Carles Cane) and by the Organic Electronics Group at Universidade do Algarve, Faro, Portugal (head of the group: Prof. Dr. Henrique Leonel Gomes). The semi-automatic characterization system is located in INB-CNM. Detailed studies on individual TFTs were performed by the Organic Electronics group in Portugal.

4 Inkjet printing of colloidal nanospheres: Evaporation-driven self-assembly based on ink-substrate interaction

The film formation of an inkjet-printed droplet or layer is determined by the interaction between substrate and ink, as well as by evaporation kinetics. The inkjet deposition of colloidal ink formulations with monodisperse dielectric nanospheres serves as a model system for understanding the film formation based on evaporation-driven self-assembly. In addition, one can obtain optically functional material structures with repeating regions of low and high dielectric constant, which are qualified to control the propagation of light.

4.1 Single droplet deposit morphology: Interaction of substrate and ink

The shape of the deposited liquid droplet and thus the morphology of the finally dry deposit depends on the interaction of substrate and ink as explained in Chapter 2.3. Inward- and outward-directed transport flows (mainly initiated by the evaporation of the solvent) cause an assembly and agglomeration of the nanospheres. The dry deposit morphology of inkjet-printed single droplets was studied as a function of substrate surface treatment method and ink/suspension composition. Figure 16A shows a plot of the measured water contact angle and droplet deposit diameters as a function of the differently treated substrates using the suspension DS300 (0.1 wt%) and BS305 (2.0 wt%).

As expected, the higher the water contact angle on the substrates, the lower the diameter of the resulting deposit. The different surface treatments also strongly affect the morphology of the deposits, as indicated in Figure 16C-G. At low water contact angles (i.e., higher surface energy of the substrate), capillary flows transport the nanospheres from the center of the evaporating droplet towards the edge where they agglomerate.[98] This phenomenon is described as the coffee-ring effect (see Chapter 2.4). At higher contact angles (i.e., lower surface energy of the substrate), no coffee-ring can be observed but the nanosphere particles are stacked in multilayers.[98,138] Even colloidal hemispheres (described as printed domes, as shown in APPENDIX A in Figure A1) can be obtained by printing or dispensing if the substrate has a very low surface energy, enabling a high receding contact angle and thus a freely sliding three phase contact line.[98,134,137,138,143]

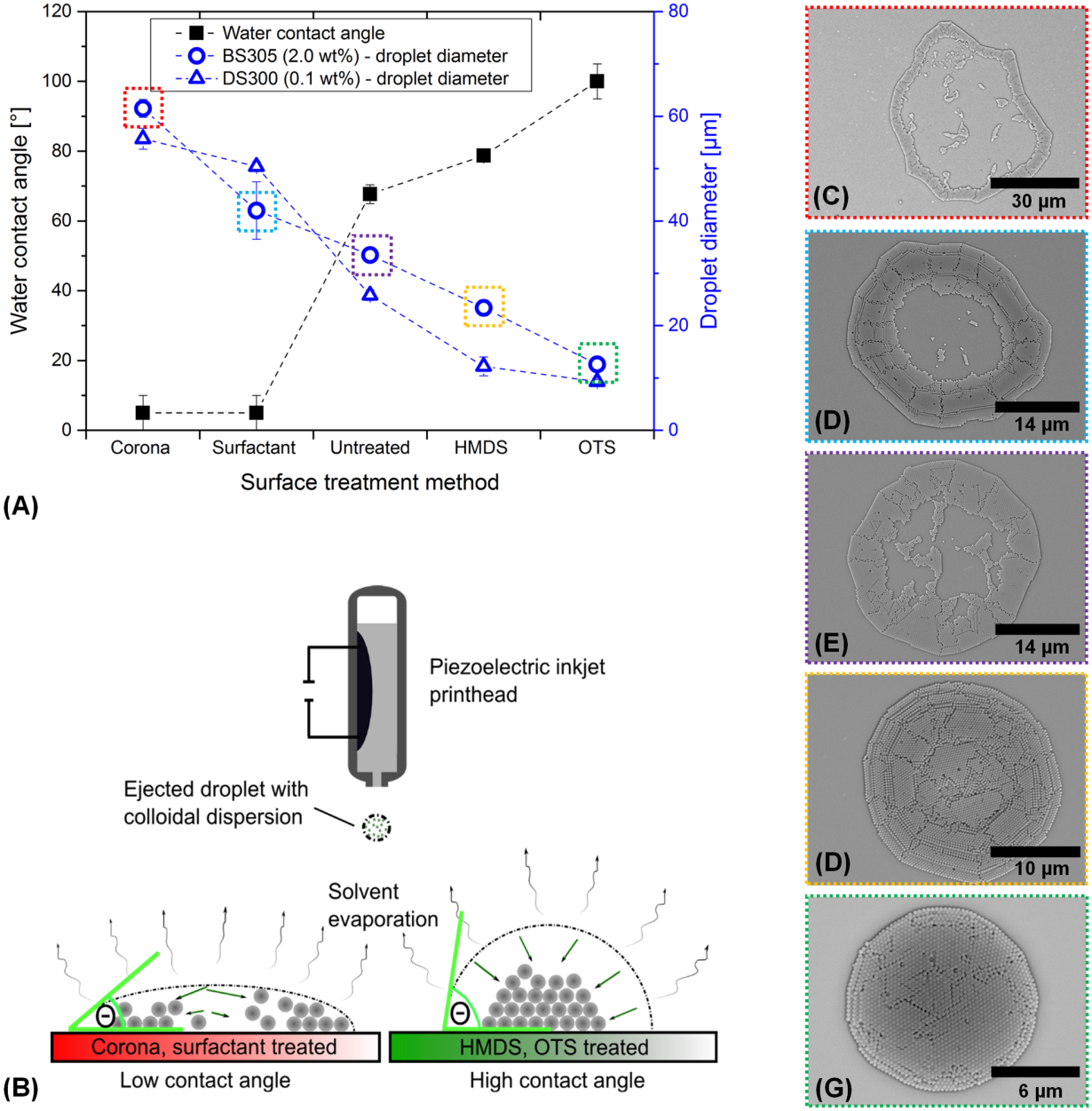

Figure 16: (A) measured water contact angle and measured droplet diameter of the inkjet-printed deposits of the suspensions BS305 and DS300 as a function of surface treatment method; (B) schematic cross-sectional view of the principle morphology of the inkjet-printed deposits; (C)-(G) are SEM images of typical deposits using the suspension BS305 of the highlighted (color code) data points of (A) (all adapted from [98])

The major principle of the formation of a droplet deposit as a function of the surface energy of the substrate, characterized by the static water contact angle, is shown in the scheme in Figure 16B. The area coverage with nanosphere particles of single, isolated inkjet droplets (determined on the basis of image processing by calculating the ratio of the number of pixels circumscribed by the deposited particles and the number of pixels making up the total droplet footprint marking the

deposit area) varies with the surface treatment.[98] The lower the water contact angle and the higher the spreading of the inkjet-printed droplet on the substrate, the lower the particle area coverage.[98] A coverage of 100 % was obtained for BS305 on HMDS- and OTS-treated substrates. Thus, a continuously covered area with at least one monolayer of nanospheres was achieved. The coverage decreases for BS305 to about 20 % to 40 % using corona-treated substrates.[98]

Obviously, the substrate properties also strongly affect the circularity of the deposits.[98] An almost ideal circularity with a very low eccentricity of about 0.2 µm (corresponding to about 1.6 % eccentricity) was obtained on OTS-treated substrates (see Figure 16D-G), whereas deviations from the circularity become more obvious for the deposits on corona-treated and surfactant-treated substrates. The drop-to-drop variation in diameter was determined for 20 sequentially printed droplets of BS305 on OTS-treated substrates. The drop diameter was about 12.6 µm and the drop-to-drop variation in diameter was about 4 %.[98,155]

The influence of the substrate treatment method on the morphology of the single droplet deposits is summarized qualitatively in Table 6.[98]

Table 6: Qualitative summary of main trends of single droplet morphology based on correlations between printing results and varying printing parameters[98]

Water contact angle	Diameter of the deposits	Circularity of the deposits	Number of stacked layers of nanospheres	Degree of manifestation of coffee-ring effect	Particle area coverage of the circumscribed deposit area
Low	High	Low	Low	High	Low
High	Low	High	High	Low	High

Deposits with multiple layers are obtained preferably on substrates that form a high contact angle with the deposited droplet. However, multilayer stacks can be also obtained on substrates that form a low contact angle with the droplet ,simply by inkjet printing a second droplet onto an already deposited and dried droplet deposit. These multilayer stacks are interesting for several reasons, specifically for the development of photonic crystals based on parallel stacks of layers of different dielectric constant, which in turn form a photonic band gap in a single direction.[98] These 1D photonic crystal structures can be applied as nanoparticle-based Bragg reflectors[98,234].

One further point of interest is the adhesion of the nanospheres to the substrate and among each other. If the adhesion is low, the solvent of the second droplet impinging in a wet-on-dry multi-pass printing set might re-disperse the deposited nanoparticles and rearrange them, perhaps into a different morphology.[98] Figure 17 shows deposits of this experiment of printing a second drop onto an already dried drop deposit. Figure 17A and Figure 17C represent single droplets printed

on cleaned glass with and without the coffee-ring morphology (BL280 was diluted to 2 wt% solids content and formulated with 60 wt% formamide to compress the coffee-ring effect).[98] After the deposition of the first droplet, the samples were kept on the substrate holder of the DMP 2831 for several minutes to allow for the evaporation of the solvent. Then, the same suspensions were printed as single droplets on top of the dried deposits (see Figure 17B and Figure 17D).[98]

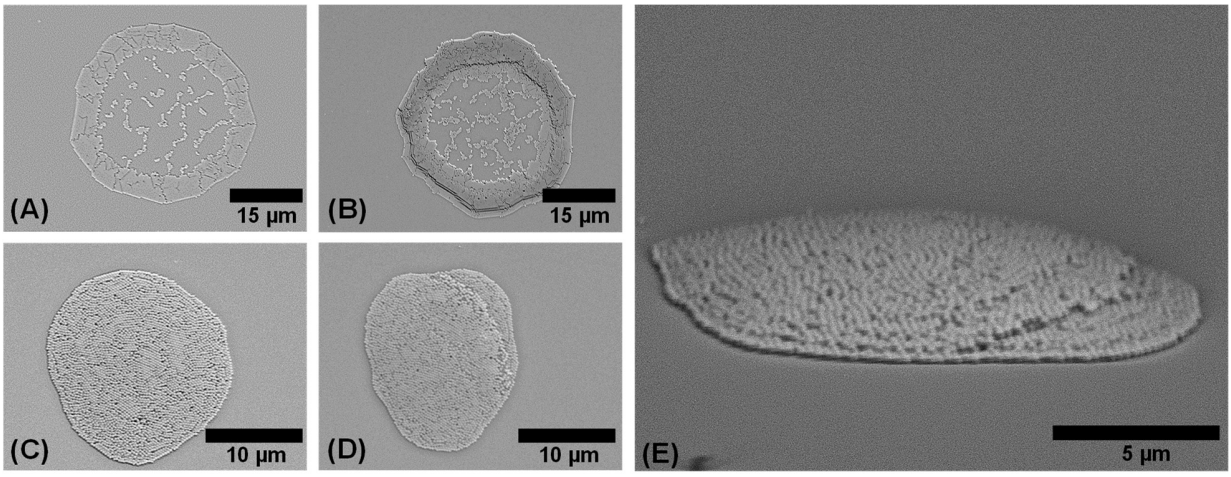

Figure 17: Deposits of inkjet-printed colloidal suspensions on cleaned glass slides; the deposit (A) was obtained with one droplet of the BS305 and (B) with printing two droplets of BS305 on top of each other; (C) was obtained with one droplet of BL280 diluted to 2 wt% and formulated with 60 wt% formamide and (D) with printing two droplets of this suspension on top of each other; (E) is a side-view of (D) at about 85° substrate inclination[98]

Figure 17E is a side-view of Figure 17D at about 85° substrate inclination. The second droplets do not seem to dissolve and re-disperse the underlying nanospheres.[98] However, a clearly distinguishable second layer on top of the first was established. The morphology of the second deposit follows the morphology of the first deposit quite well, and the coffee-ring becomes more pronounced in Figure 17B due to the assembly of most of the nanospheres of the second drop on top of the already existing coffee-ring deposit.[98] Although the evaporation time (and thus the available time for a re-dispersing of nanospheres) is increased for the suspension with formamide (as a consequence of a higher boiling point than water which results in longer evaporation time), the second drop seems to form a separate layer without dissolving the first deposit, as indicated in Figure 17D and Figure 17E.[98] Thus, the adhesion between the individual nanospheres as well as the adhesion between the nanospheres and the substrate can be considered to be very high.[98] Figure 18 provides an overview of the packing characteristics of the nanospheres in the deposits. Usually, the nanospheres are close-packed and highly ordered with some line and point defects, as demonstrated in Figure 18A-B and D. This close-packed arrangement of particles is both desired and beneficial for many applications in the field of photonics[235], such as for optical devices

(e.g., Bragg reflectors[234]) and coatings (one example is the application of ordered layers for enhanced light-trapping in solar cells[236]) or structural colors[148]. However, research on non-close-packed colloidal arrays[237,238] and disordered photonics[239] (e.g., photonic glasses) has also been attracting increasing interest over the last few years.[98] Here, a perfectly ordered arrangement of particles is not required but rather a completely random arrangement, making it possible to control the light scattering.[98] Diethylene glycol was employed as an evaporation agent to control the ordering process of the nanospheres in order to obtain a more random nanosphere arrangement.[98]

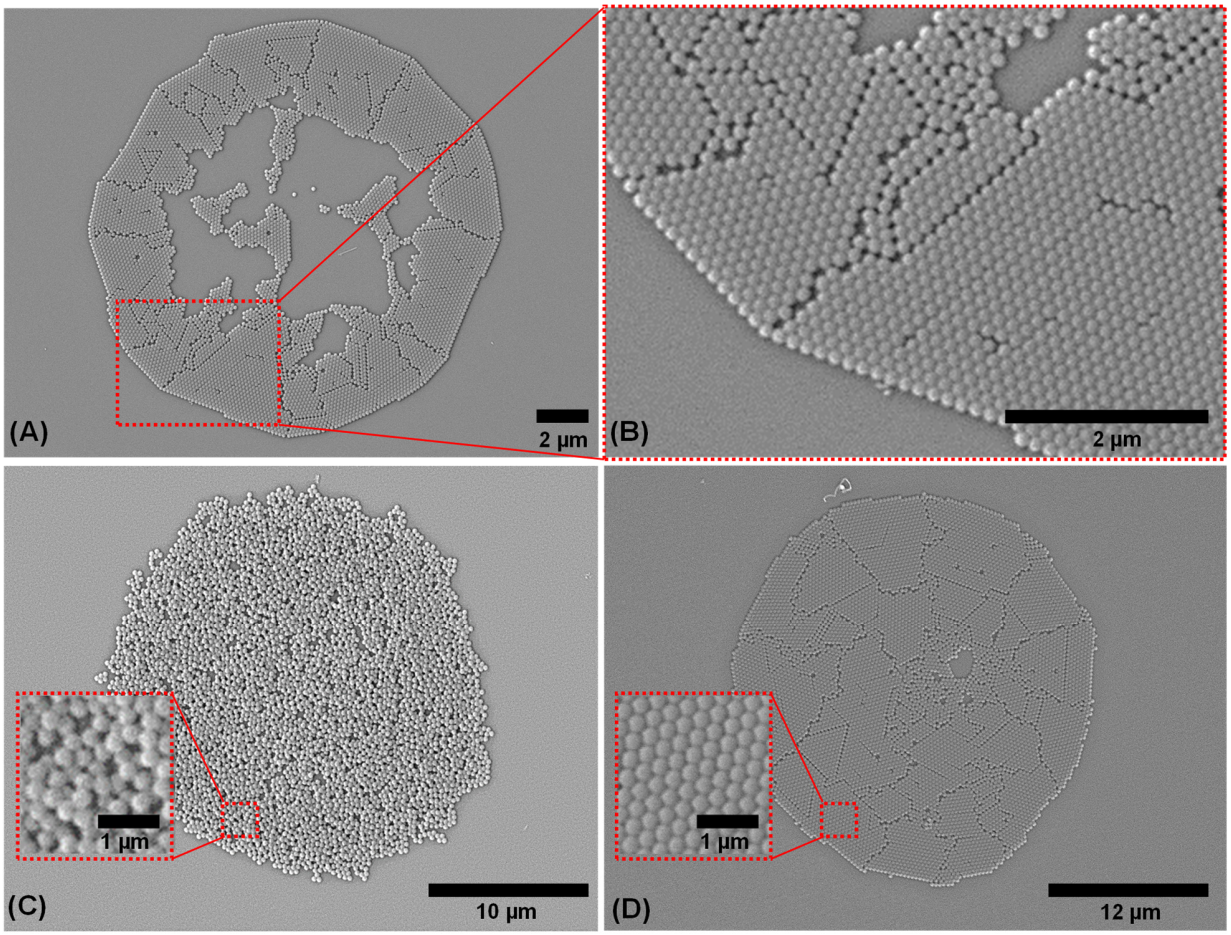

Figure 18: (A) single-droplet deposit using 2 wt% BS305 on cleaned glass, and (B) a detailed section of (A) showing the high ordering of the particles in hexagonal arrays with a few point and line defects; (C) shows an inkjet-printed deposit with randomly arranged nanospheres obtained by addition of 6.25 wt% diethylene glycol to the 1.5 wt% BS305 suspension; (D) close-packed two-dimensional colloidal array with hexagonal structure by addition of 2.5 wt% formamide (adapted from [98])

An aqueous suspension consisting of 1.5 wt% of PS particles of BS305 and 6.25 wt% diethylene glycol was inkjet-printed on HMDS-treated substrates as single droplets. Deposits with randomly arranged nanospheres, similar to the photonic glasses reported by Garcia et al.[239], were obtained

as shown in Figure 18C.[98] In contrast, deposits with arrays of remarkably high order in a hexagonally close-packed structure (see Figure 18C) were obtained by adding 2.5 wt% formamide to the aqueous suspension with 1.5 wt% PS particles of BS305.[98]

(Parts of this chapter are published in reference [155] and reference [98])

4.2 Optical properties of inkjet-printed single droplet monolayers and multilayers

The optical properties of the different colloidal inkjet-printed deposits based on microreflectance spectra are presented in Figure 19A-D. The spectra were measured for monolayers as well as multilayers of nanospheres. A typical measurement position for one of the deposits is shown in Figure 19E. Most of the measurements show specular reflectivity peaks which can be assigned to photonic stop bands. Figure 19E shows one of the single droplet deposits (BS305) discussed previously in Chapter 4.1 using reflected light microscopy. It appears in intense red coloration, indicating photonic properties due to the interaction of the ordered nanospheres with the light of the microscope. The crystal-like order of the nanospheres causes Bragg reflection of light with a wavelength defined by the nanosphere size and material. This is called structural color. Disorder of the nanospheres contributes to a non-resonant broadband scattering of light, appearing microscopically as bright whitish area (see Figure 19G and H).[159]

No individual nanospheres can be seen with light microscopy, but some line defects are already visible. The measurement area and position for the microreflectance spectroscopy is indicated in Figure 19E. A typical SEM image of the single droplet deposit is depicted in Figure 19F. It reveals that the color is a consequence of the highly-ordered particles arranged in a monolayer. A multilayer sample is presented in Figure 19G. A large number of stacked layers results in a bright white reflective color due to broadband scattering. There seems to be a shift from the red color of the monolayer area to a darker reddish-purple color for thicker layer of nanospheres to a white color for very thick layers. The multilayers are stacked on top of each other in a kind of terrace structure, as indicated in Figure 19G. Figure 19H is a magnified view of the section in Figure 19G using light microscopy and Figure 19J is a SEM image of the same section. The sample in Figure 19I was printed using PSC221 as colloidal suspension. A multilayer stack was obtained and a typical spectrometer measurement position and area for the multilayers is indicated. The color appears blue to green with some purple areas for PSC221, which is a noticeable contrast to the reddish color predominant when using BS305.

A theoretical approximation for the wavelength λ of the reflection peak of a photonic crystal can be made based on Braggs law using the Equation 2 provided in Chapter 2.4.

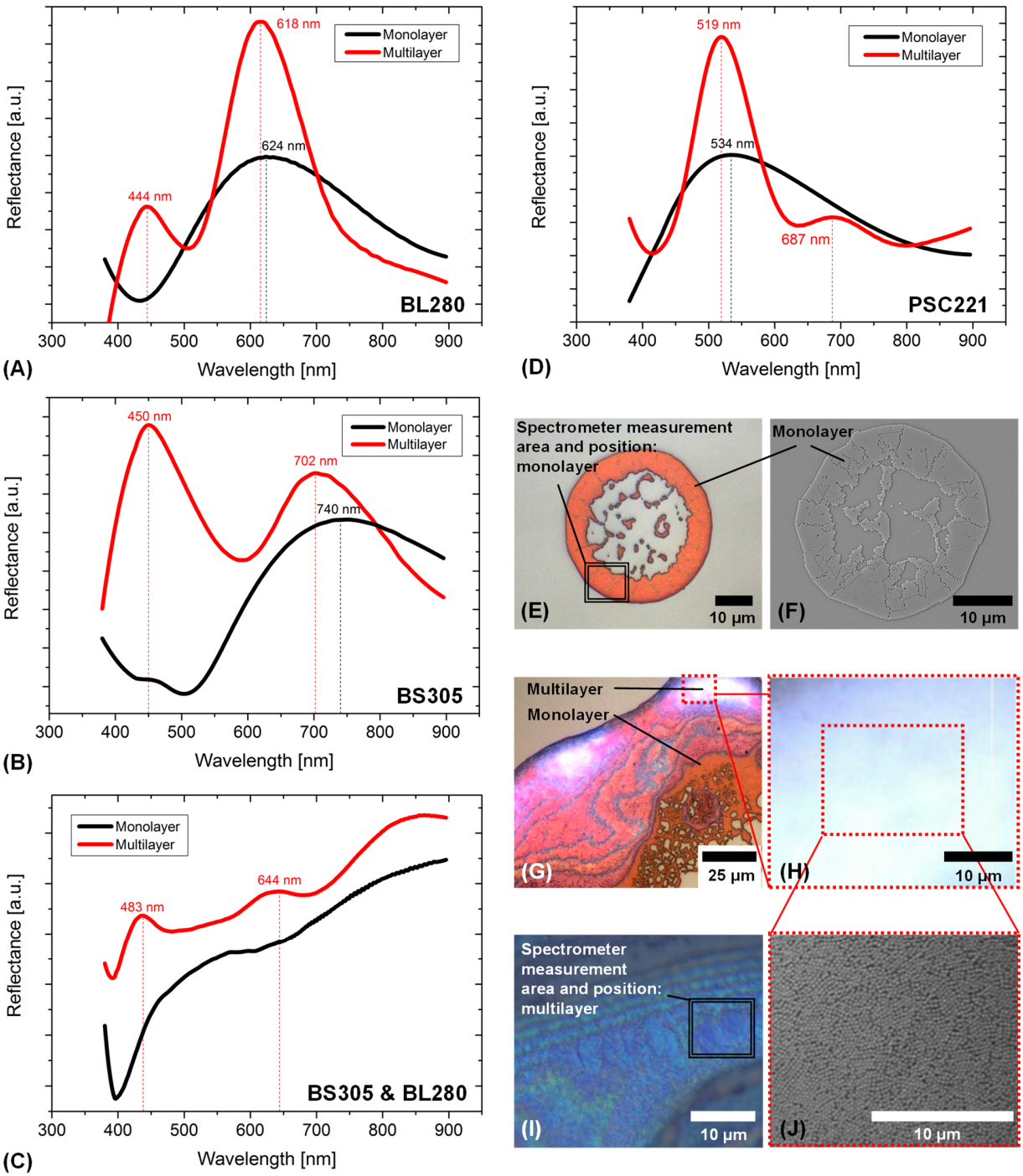

Figure 19: (A)-(D) are microreflectance spectra of the inkjet-printed deposits using (A) BL280, (B) BS305 (2 wt%), (C) BS305 & BL280 and (D) PSC221; (E) shows a single droplet deposit (BS305) with reflected light microscopy (the measurement position for the spectroscopy is indicated) and (F) a similar deposit by SEM; (G) shows a printed deposit comprising multilayers as well as a monolayers (BS305); the white bright part of the multilayer is shown in higher magnification in (H) and as SEM image in (J); (I) is a light microscopy image of a multilayer deposit using PSC221

The calculated wavelengths based on Equation 2 are 614 nm for BL280, 727 nm for BS305, and 526 nm for PSC221. The measurement data depicted in Figure 19A-D is generally in agreement with the calculated reflection peaks and the sample color appearing using light microscopy. The calculated peaks are in all cases within the wavelength range between the measured monolayer and multilayer peaks. Deviations might occur, for example, due to a certain disorder in the assemblies and due to the size distribution of the nanospheres.

The intensity of the reflectance of the multilayers is higher than the intensity of the monolayers, because multilayer samples consist of a higher number of repeating units. The wavelength gap or relative stop band width $\Delta\lambda/\lambda$, where λ corresponds to the maximum peak wavelength and $\Delta\lambda$ corresponds to the full-width at the half-maximum (FWHM) of the peak wavelength for the main peak within one spectra was calculated.[240] The multilayers using BL280, BS305 and PSC221 have a relative stop band width of about 19 % (second peak), 26 % (first peak) and 20 % (second peak) for BS305, and 18 % (first peak), respectively.

A second reflection peak is visible for most of the multilayer reflectance measurements. This can happen for different reasons, for instance, disorder in the crystal-like assembly, which results in unselective scattering of light or grating diffraction effects, or simultaneous Bragg diffraction from different crystal planes can cause an interference of waves and thus multiple Bragg peaks.[159,169] Other possible causes are discussed in further detail in Chapter 5.5.

The reflectance peak position shifts as a function of the size of the nanospheres. As the size of the nanospheres increases, the position of the reflectance peak shifts to longer wavelengths, implying that the photonic band gap shifts to lower energies.

There is no clear peak and thus no clear Bragg reflection for the samples with the binary suspension of BS305 & BL280 (Figure 19A-C), indicating too few repeating units with insufficient periodic refractive index variation. Although the layers deposited with the binary suspension have arrays of a remarkably high order and with a hexagonally close-packed structure, the different nanospheres consisting of PS and Si are not homogenously distributed. Moreover, they are randomly distributed in small array islands, as shown in SEM images obtained with back-scattered electron (BSE) mode in Figure 20. These deposits do not have a long-range order. The analysis of the deposits based on the BSE mode allows a visual indication of material properties since materials with a high atomic number will appear brighter than materials with a low atomic number. PS nanospheres have a lower density compared to the SiO_2 nanospheres. Dark and bright nanospheres can be easily distinguished in Figure 20A and in the contrast-enhanced image in

Figure 20B. Energy-dispersive X-ray (EDX)[1] analysis was performed (as shown in Figure 20C on the same position as in Figure 20A) to confirm that the grayscale (dark and bright) difference is a result of the nature of the nanosphere material. The blue color refers to SiO_2 and the red color to PS nanospheres. The measurement confirms that the greyscale difference in BSE mode can be employed to assign the corresponding material to the nanospheres.

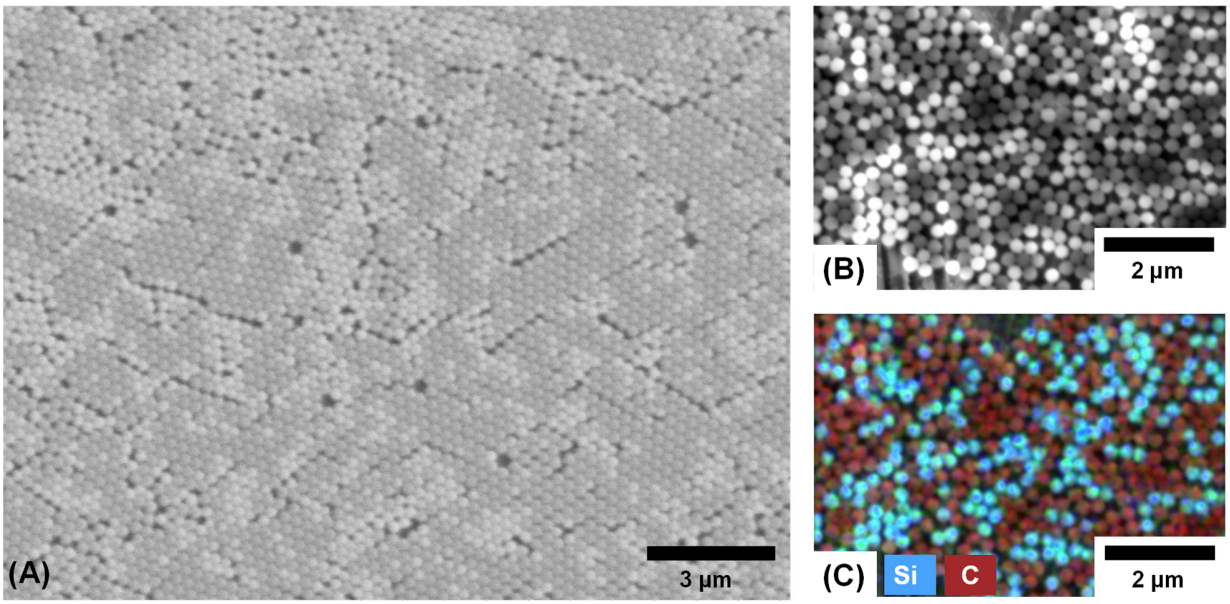

Figure 20: SEM images in BSE mode of deposits using the binary suspension BS305 & BL280, (A) monolayer with hexagonally close-packed structure, (B) enhanced contrast of the image obtained by the BSE mode and (C) EDX mapping of the same image position displayed in (B) (adapted from [154])

(Parts of this chapter are published in reference [154] and reference [98])

[1] The EDX analysis was performed in cooperation with Torsten Jagemann at the Department of Solid Surface Analaysis at Technische Universität Chemnitz (head of the department: Prof. Dr. Michael Hietschold).

5 Inkjet printing of colloidal nanospheres: Evaporation-driven self-assembly of SCAs independent on substrate properties

5.1 Inkjet printing of spherical colloidal assemblies and their identification

All of the printed deposits discussed previously have one characteristic in common: the morphology strongly depends on the interaction between substrate and ink (see Figure 16). As a consequence, ink/colloidal suspension and substrate need to be precisely geared to each other in order to obtain the desired size and structure of the deposit consisting of nanospheres. However, independence of the substrate-ink interaction in inkjet printing can be obtained by relocating of the evaporation-induced self-assembly process from the sessile droplet on a solid surface to the droplet in flight. Thus, the substrate properties do not affect the final morphology of the deposit anymore. However, the shape of the droplet will define the shape of the final deposit. Specifically, the shape of the final deposit is prescribed by the shape of the droplet in flight given by a spherical geometry (ball-shaped) due the comparable high surface tension of the suspensions (see Table 3). Thus, the air-ink interface directs the assembly and determines the final shape of the aggregation. The tiny droplets ejected by inkjet printing act as a confined geometry for the nanospheres inside. Due to the solvent evaporation, the nanospheres are self-assembled and consolidated during the flight upon shrinking of the droplet. The evaporation of the water in the droplet leads to a colloidal crystallization by a reduction of free volume. Finally, the nanospheres are packed into stable SCAs, and before the ejected droplets impinge on the substrate, most of the solvent will have evaporated.[154,166,241]

The only method to reliably differentiate SCAs from monolayer and other multilayer deposits on substrates was found to be a reliance on images captured by SEM. The sample to be investigated with SEM needs to be tilted. However, the procedure of sample preparation for SEM and the identification of the small features is challenging. Figure 21 particularly shows the procedure to identify SCA employed in this thesis.

Figure 21A is a top-view image captured with incident light microscopy in bright-field mode of a characteristic assembly of six SCAs. Figure 21B is the same assembly, but the top-view image was captured by SEM. At this moment there is still no clear indication that the deposits are SCAs. The sample under investigation needs to be tilted in the SEM (as depicted in Figure 21C) to about 60 °. The dimensionality of the deposits can be seen and the magnified image in Figure 21D confirms that SCAs were obtained. However, light microscopy can also be used for the

identification of SCAs to a certain extent. In incident light mode with bright-field activated, the SCAs are difficult to identify, but have a very characteristic spherical shape. In addition, there might be a slight coloration.

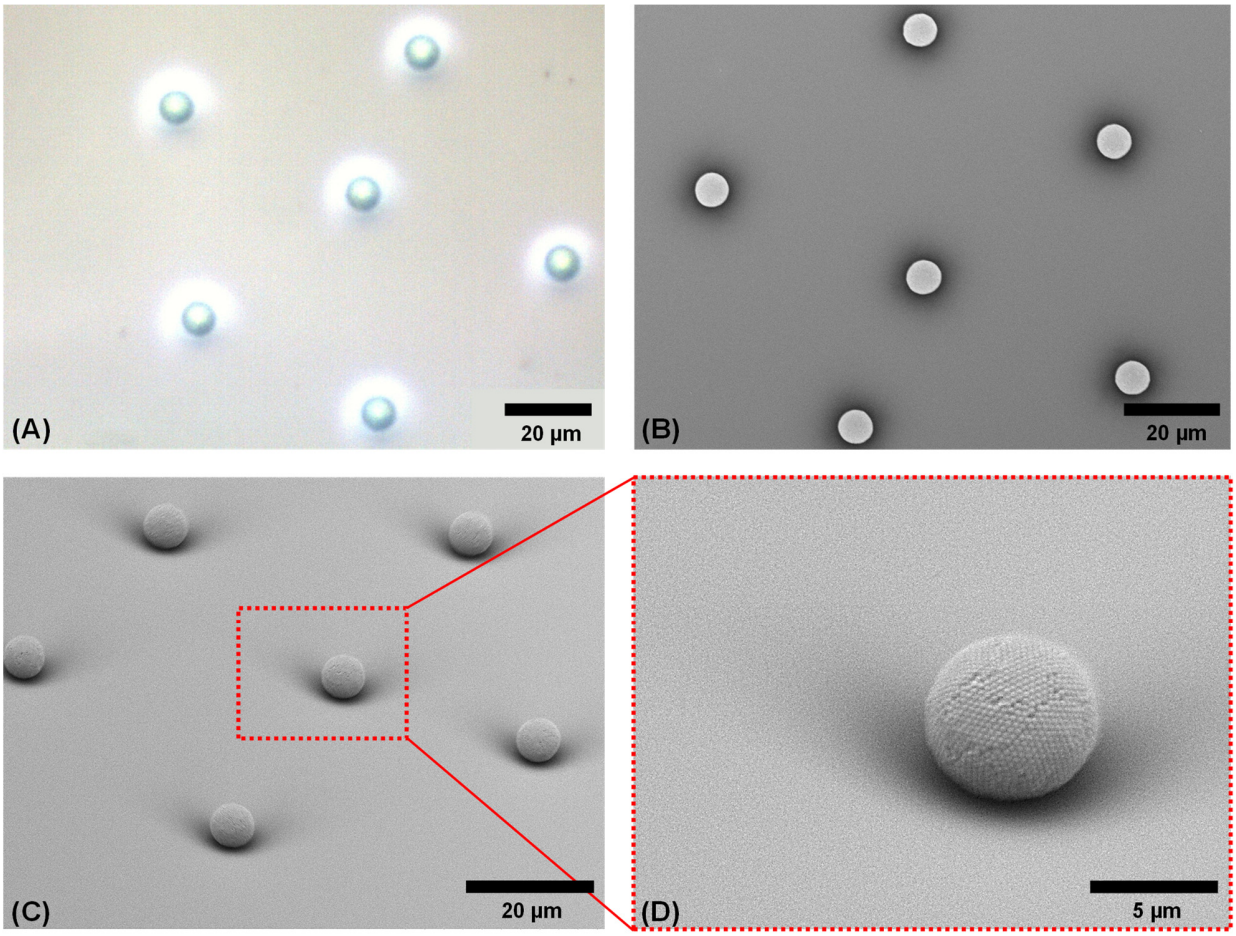

Figure 21: Inkjet-printed SCAs based on BS305 on cleaned glass substrates, (A) is a top-view incident light microscopy image in bright-field mode with a 50x magnification objective, (B) the corresponding top-view SEM image, (C) SEM image with tilted view (about 60 °) and (D) magnification of the centered SCA of (C) with 60 ° tilt

When changing the focus of the microscope a few µm, the monolayer and multilayer deposits become blurry. In contrast, SCAs do not change in their appearance since they are usually several µm in diameter.[154] These considerations are indicated in Figure 22A. The monolayer/multilayer deposit is blurry and hard to see while the SCAs have a clear reddish appearance. In dark field mode (incident light), the SCAs usually appear as bright white spherical spots due to diffraction of light, while monolayer deposits, for instance, show a characteristic color as result of Bragg reflection (see Figure 22B and C and see also Chapter 4.2).[154] The image section shown in Figure

22A is depicted in Figure 22B in dark field mode. Therefore, the bright-field mode in combination with the dark-field mode allow for a clear visualization of the SCAs.

As a result, optical microscopy can be employed to identify printed SCAs, and hence limits the efforts related to SEM sample preparation and SEM analysis. This procedure was applied for the identification of the SCAs and the statistical analysis introduced in the next chapters.

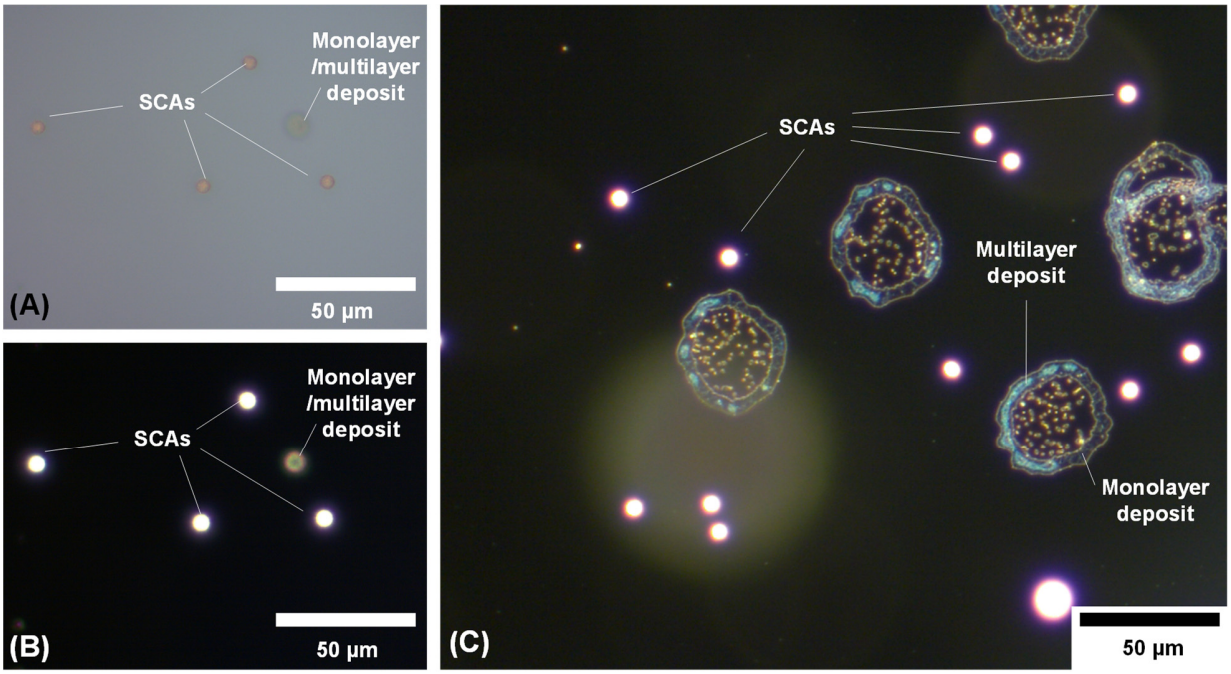

Figure 22: Light microscopy images of deposits obtained using BL280, (A) top-view with incident light mode, (B) the same sample position as (A) but in dark field mode; (C) shows the different appearance of SCAs and normal monolayer and multilayer deposits (adapted from [154])

5.2 Fine-tuning of the waveform applied to the printhead

As explained in Chapter 2.2, the waveform is one of the most important parameters to control the characteristics of the drop ejection, and hence the shape of the material deposits. The waveform is also most important in relocating the evaporation-induced self-assembly process from the sessile droplet on a solid surface to the droplet in flight. The relocation can be done by increasing the nozzle-to-substrate distance. However, depending on the solvent and the size of the ejected droplets, several meters of distance might be required[169]. A more convenient method is to fine-tune the waveform applied to the printhead. The aim is to generate tiny droplets with a high solids content thus decreasing the evaporation time. Then, a nozzle-to-substrate distance of about 1 mm was found to be sufficient for the generation of SCAs.[154]

Figure 23 shows the three differently designed complex polar waveforms (denoted as A, B, and C) which were applied to the printheads of the DMP 2831.

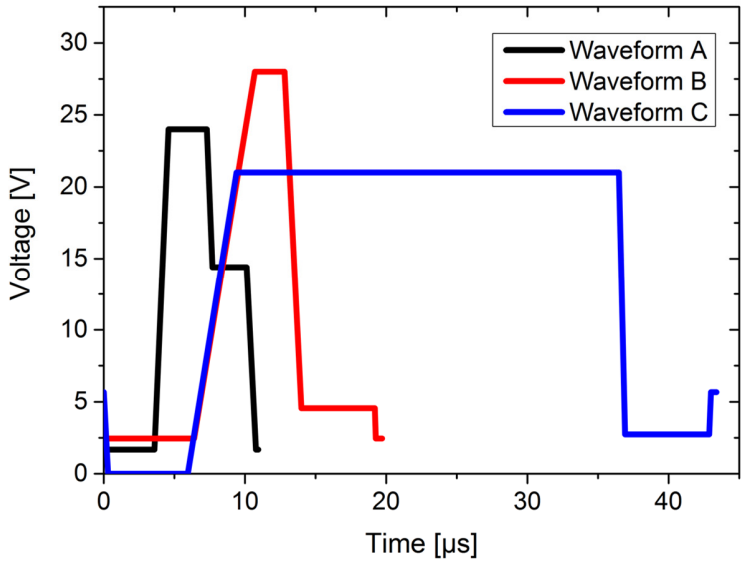

Figure 23: Three differently designed waveforms applied to the inkjet printheads for the deposition of the colloidal suspensions[154]

The three waveforms are completely different in terms of maximum voltages, rise times, dwell times, and fall times. The main differences between the waveforms are the time duration of the voltage signal, which was applied to the piezoelectric printhead, and the duration of the maximum voltage plateau indicating the highest deformation of the piezoelectric actuators.[154] Waveform C is characterized by a very long dwell time of the maximum voltage plateau and by the lowest jetting voltage compared to waveform A and B. Waveform A can be considered as a standard waveform, which is frequently used as a basis for the development of other waveforms for the DMP 2831. This waveform allows for the ejection of storybook inkjet droplets on a trajectory perpendicular to the nozzle plate and with a characteristic ball shape as shown in Figure 24A-C. Figure 24A depicts the waveform A, and Figure 24B is a scheme of the droplet ejection using waveform A. Figure 24C represent the droplet ejection captured with the drop-watcher camera of the DMP 2831 using BS305.[154]

The resulting deposit of such a droplet ejection on a glass substrate is shown in Figure 24D. The nanospheres form a coffee-ring deposit as a result of the interaction between the surface energy of the substrate and the surface tension of the suspension according to the theoretical basics given in Chapter 2.3 and the experimental findings presented previously in Chapter 4.1. Therefore, the properties of the substrate are a major influencing factor on the final structural architecture of the deposit when applying waveform A.[154]

In contrast, a completely different morphology was obtained by applying waveform B, as presented in Figure 24H (waveform C results in similar deposits as waveform B). Here, SCAs appeared, despite the fact that the same substrate (glass) and suspension (BS305) was employed.[154] This indicates that the waveform is the determining factor for the different deposit morphologies. The waveform was configured contrary to the usual goal in inkjet printing to generate a satellite-free single droplet with a controlled trajectory and shape.[154] Satellite drops or droplet mists are generally not intended in graphical as well as functional inkjet printing due to droplet placement accuracy issues and thus quality aspects in printed patterns.[154] Consequently, most previous research efforts on droplet formation in inkjet printing were aimed at avoiding satellite drops and droplet mists, and improving the droplet generation process towards creating a well-defined, single and stable ball-shaped droplet ejection.[242–244] According to my knowledge, the exploitation of usually unintended satellite droplets or a mist of droplets in inkjet printing has not yet been reported in the literature.[154]

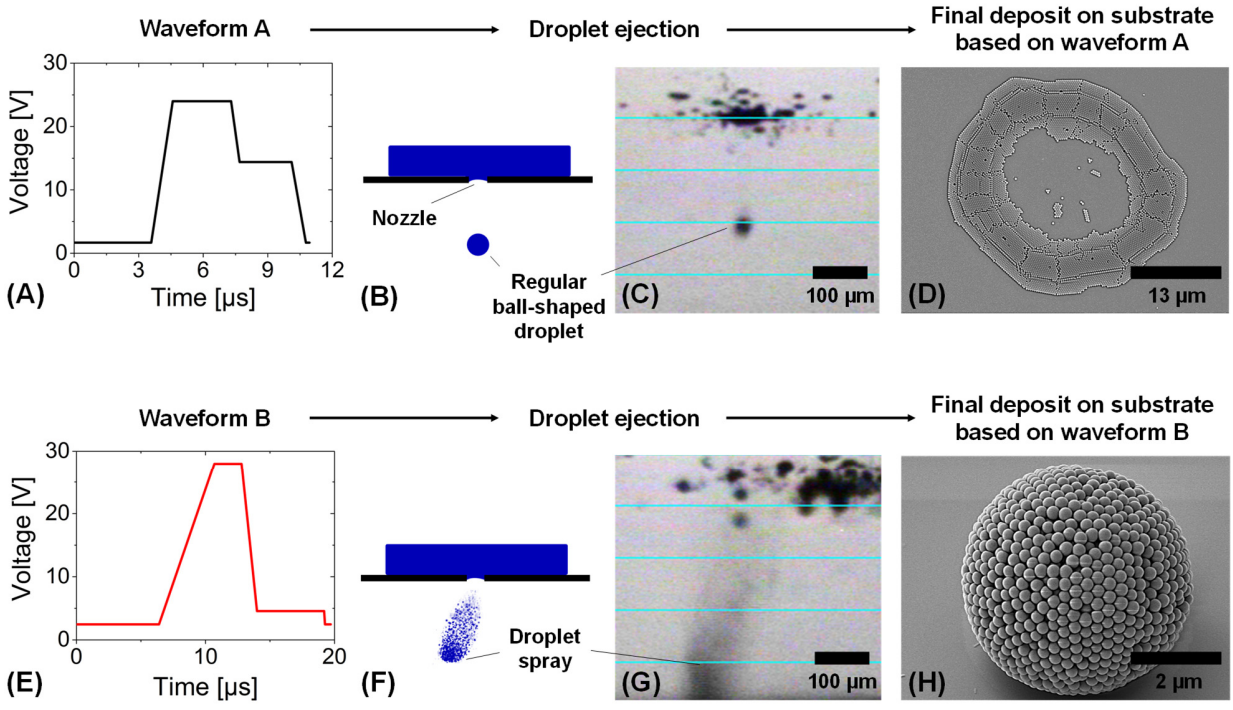

Figure 24: Influence of the waveform applied to the inkjet printhead on the droplet ejection and the resulting deposit on the substrate; (A) and (E) depict two classes of waveforms (both driven with a frequency of 3 kHz), (B) and (F) are schematics of the basic principle of the droplet ejection based on waveform A and B (waveform C shows similar drop ejection as Waveform B); (C) and (G) show the droplet ejection captured with the DMP 2831 built-in drop watcher camera corresponding to the two different waveforms; (D) and (H) are SEM images showing the different final deposit morphologies obtained on the substrate as a result of waveform A and B (adapted from [154])

When applying waveform B (or C), no primary droplet can be identified using the built-in stroboscopic drop watcher camera of the DMP 2831, but a large number of small droplets with similar sizes – all ejected by a single firing pulse (Figure 24G).[154] Phenomena such as satellite droplet formation in inkjet printing have been extensively investigated by Wijshoff[31]. Wijshoff[31] classified satellite droplet formation into (i) mist of droplets, (ii) Rayleigh breakup, (iii) fast satellites, and (iv) slow satellites.[154] However, the droplet formation process presented here using waveform B or C does not match any of these types of satellites, because Wijshoff considered satellite drops as additional droplets in close vicinity to a main droplet.[154]

Obviously, the image of the drop watcher camera in Figure 24G and the scheme in Figure 24F do not show a clearly distinguishable main droplet, but rather a mist or spray of small droplets characterized by a higher material concentration at the front of the fluid ejection than at its back.[154] It must be mentioned that the scheme in Figure 24F is idealized, and a very intense mist ejection has been selected as image for representation. Indeed, much less intense mists can be generated with a much lower amount of material.[154] However, these smaller mists are already close to the resolution limit of the built-in drop-watcher camera, and are difficult to identify when capturing the image.[154]

Song et al.[245] also studied different phenomena in inkjet printing with a focus on droplet ejection. Song et al. described one of the observed effects as ink spray, which is very close to the effect that I observed with the drop watcher upon application of waveform B or C. Song et al.[245] assumed that partially clogged nozzles either by (i) an emerging dried deposit build-up of ink adhering to the nozzle orifice, or by (ii) particle agglomerations and larger particles cause the observed spray or mist of droplets in inkjet printing.[154] However, partially clogged nozzles might be a reason for a mist of droplets ejected by inkjet printing that takes place suddenly, undesirably, and also uncontrollably from a formerly regular jetting and non-clogged nozzle.[154] This is a big difference to the approach introduced here, because the mist of droplets can be induced intentionally using a fine-tuned waveform in a controlled and reproducible manner.[154] The novel method for the manufacturing of SCAs is a contrasting approach to the previously reported manufacturing of dome-shaped colloidal assemblies using inkjet printing[134,137,138,143,246], or SCAs using a ultra-micropipette and superhydrophobic substrate surfaces[161]. In these cases, the self-assembly process takes place on the substrate and the shape of the droplet template is a result of the surface energy of the substrate.[154] Only a high contrast between the surface energy of the substrate and the surface tension of the droplet liquids will lead to dome-shapes or spherical assemblies.[154] The newly developed method using inkjet printing relocates the self-assembly process from the substrate to the free-flying droplet, so that the interaction between the liquid droplet and the ambient gas phase becomes decisive.[154]

The reliability of the developed process for the manufacturing of the SCAs was studied in detail, specifically using the suspension BL280 with varying solids contents (1 wt%, 2 wt% and 4 wt%).[154] The other suspensions behave similarly.[154] The focus was set on the influence of the different waveforms on the process. SCAs were obtained only with waveform B and C. Waveform A did not result in any SCA.[154] I found that a solids content of 4 wt% of the nanospheres with a diameter of about 280 nm is an upper limit for the inkjet printing process.[154] The relatively high concentration of nanospheres in conjunction with their size results in limited jetting performance, such as frequently interrupted droplet jetting due to clogged nozzles.[154] The dynamic viscosity of BL280 was determined to about 1 mPa·s for all three solids contents, and the surface tension of BL280 decreased with an increasing solids content.[154] Both physical ink parameters are basically within the range of inkjet-printable ink formulations. Thus, the comparatively large nanosphere diameter and the solids content are the major reasons for the problematic jetting behavior. Therefore, BL280 with 4 wt% solids content was not considered for the detailed reliability study.[154]

Figure 25 presents data regarding the reliability of the developed manufacturing process for SCAs using inkjet printing as a function of the applied waveform and solids content of the suspension.[154]

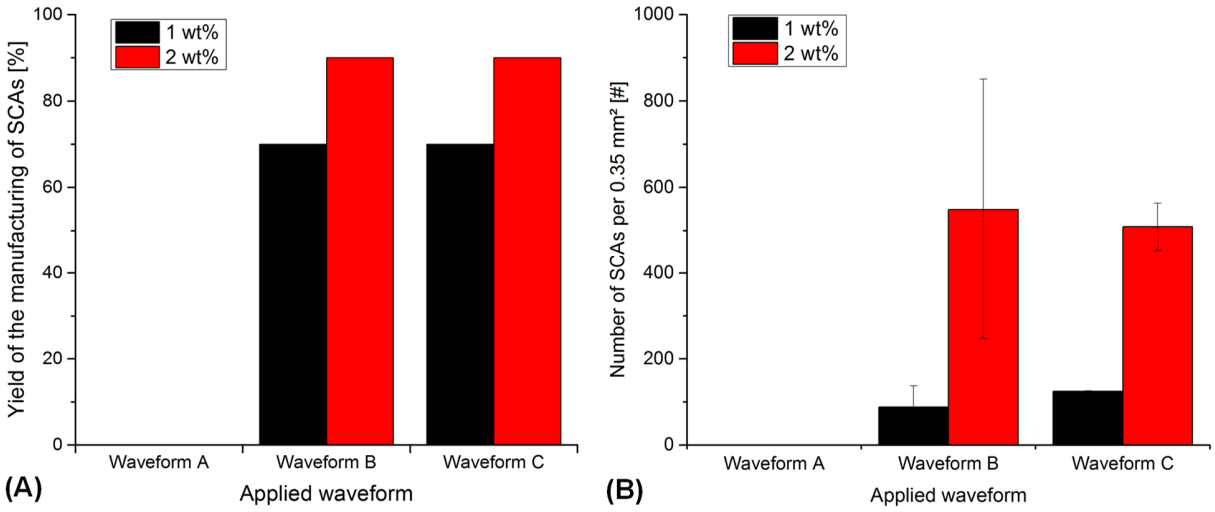

Figure 25: Reliability of the manufacturing method of SCAs using the DMP 2831 represented by (A) the manufacturing yield, and (B) the number of manufactured SCAs per area as a function of applied waveform and solids content of the suspension; the print pattern was defined as rectangle with an area of 0.35 mm² at 5080 dpi (adapted from [154])

The yield of the manufacturing process is shown in Figure 25A. The yield was determined by printing 10 rectangular areas each of 0.35 mm² in size with a print resolution of 5080 dpi per suspension formulation and per waveform, on cleaned glass substrates, and by counting the number of samples on which SCAs were obtained.[154] The number of SCAs was determined by

using light microscopy and calculating the average of the counted assemblies per suspension and applied waveform. If SCAs were found in all 10 rectangles, the yield is rated as 100 %. If no SCAs were found in the 10 rectangles, the yield is 0 %.[154] The higher the solids content, the higher the yield of the manufacturing process, and also the higher the number of SCAs. In total, 10 rectangles were printed with waveform A. However, no SCAs were found in any of the 10 rectangular areas.[154] In all cases, mono- or multilayer deposits appeared but no colloidal assemblies with spherical shape were observed. As a consequence, the manufacturing yield for SCAs is 0 % when using waveform A. SCAs were achieved with a high yield for waveform B and C. The yield obviously depends on the solids content, since 1 wt% results in a manufacturing yield of about 70 % and 2 wt% in a manufacturing yield of about 90 %.[154] The number of manufactured SCAs per 0.35 mm² was about five times higher using the 2 wt% solids content suspension compared to the 1 wt% suspension, as indicated in Figure 25A. Waveform B results in a higher number of SCAs, but also a much higher standard deviation compared to those obtained with waveform C.[154] The number of assemblies for waveform C was about 510 ± 60 for an area of 0.35 mm², deposited with a print resolution of 5080 dpi.[154] This implies a quite stable and reproducible manufacturing process, which I found quite similar for the other suspensions as well. Thus, it is indeed possible to exploit unintended droplet formation in inkjet printing for the stable manufacturing of SCAs.[154]

The developed process is highly productive because several hundreds of SCAs with a similar size can be manufactured within some seconds on any substrate, as demonstrated in Figure 26.[154] Figure 26 shows a light microscopy image (bright field mode, incident light) of manufactured SCAs based on BS305 & BL280.

Each of the small dark round dots represents one SCA. Larger dots are most probably dust and dirt particles or normal monolayer or multilayer deposits. Figure 26B is a magnified image section of A. Some of the SCAs are marked for indication. However, nearly all of the dots are SCAs. This was confirmed by spot-checks using SEM.

I could not observe any clear influence of the applied waveform on the size of the SCAs. However, the solids content has a very strong influence on the size.[154] For instance, the average diameter of the SCAs using the suspension with 1 wt% solids content was about 5.0 ± 0.3 µm, and the average diameter with 2 wt% was about 8.2 ± 0.6 µm. Thus, a higher solids content clearly results in larger SCAs since the number of nanospheres per ejected droplet increases with the solids content of the suspension.[154]

The major drawbacks of this process developed are the SCA placement accuracy, and that there are not only SCAs but usually also some planar deposits. As indicated in Figure 24F and G, the spray ejection trajectory is not oriented orthogonally to the nozzle plate. Consequently, the droplet

position is difficult to predict and depends strongly on the direction of the spray. Surprisingly, however, the spray direction was the same in most of the more than 200 hundred printing experiments. The direction was either 10 o'clock and/or 2 o'clock with respect to the printed rectangle. It is difficult to determine the positioning accuracy; however, it was roughly approximated to be about ± 1200 µm. In some tests the displacement was on average up to about ± 2500 µm.

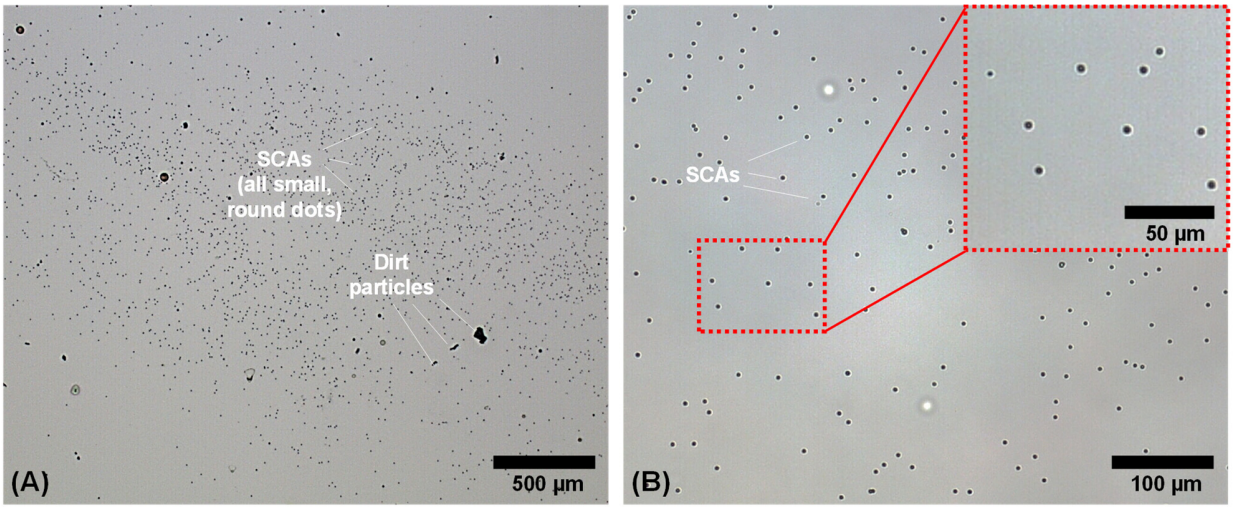

Figure 26: (A) large field with small dark dots, each of the dots represents an SCA; (B) is a magnified section of (A), some of the SCAs are marked and presented in the inset at higher magnification – in general most of the dots shown here are SCAs

(Parts of this chapter are published in reference [154], reference [166] and reference [175])

5.3 Interaction of substrate and ink

The process developed for the manufacturing of SCAs is independent of substrate properties. This is a key finding of this thesis, because film formation in inkjet printing is usually based on the interaction of substrate, ink and printhead – the so called inkjet triumvirate[22]. In this research work, I demonstrate that the substrate has no influence on the formation of the SCAs due to the relocation of the self-assembly process from the substrate to the droplet in flight.

Glass substrates with different surface treatments were applied to prove the substrate-independent formation of SCAs. The measured water contact angles on these treated substrates are shown in Table 4. Since the contact angles were measured with deionized water that has a surface tension of about 72 mN/m, the contact angles expected to be formed with the colloidal

suspension will be much lower as a consequence of their lower surface tension (as listed in Table 3) compared to deionized water.

Figure 27A is a scheme indicating the expected shape of a sessile droplet of the colloidal suspensions (here BS305) on the differently treated substrates. The lower the contact angle of the droplet with the substrate, the larger the droplet diameter and the lower the height of the droplet will be. Without fail, the development of SCAs is not possible based on the DSA process (as introduced in Chapter 2.5) when taking into account these different droplet shapes. These droplet shapes are not qualified for the development of SCAs. However, as shown in Figure 27B-F, SCAs were obtained on all the substrates with the developed in-flight self-assembly process based on inkjet printing.[166]

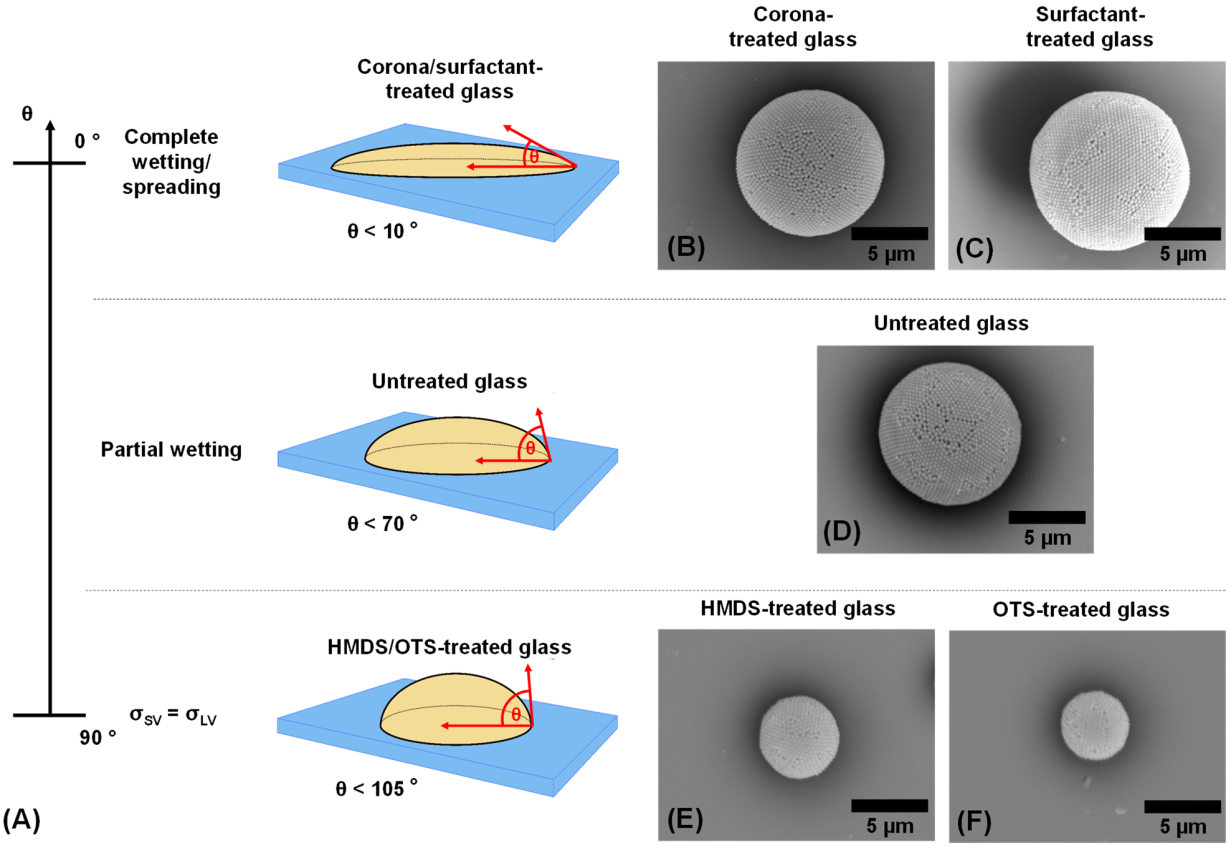

Figure 27: Development of SCAs based on BS305 independent on substrate surface properties; (A) is a scheme indicating the expected wetting states formed by sessile droplets of the colloidal suspensions with the differently treated substrates; (B)-(F) are top-view SEM images of SCAs obtained on the differently treated substrates proofing that the formation of SCAs is independent on the substrate properties (adapted from [166])

The decrease in size of the SCAs from top to down in Figure 27B-F could indicate a certain dependency, but in fact, this is not the case, because the selection of images was done haphazardly, and both larger as well as smaller SCAs were found on all of the substrates. The

selection of the images displayed in Figure 27B-F was mainly done with regard to the image quality.

Although the expected shape of a sessile droplet is similar to a flat disc for the corona- and surfactant-treated substrates, SCAs were still obtained; this indicates that the formation of SCAs is independent of any surface properties.[166] Due to the in-flight formation of the SCAs based on evaporation-driven self-assembly, the particular wettability and surface morphology of the substrate no longer influences the morphology of the deposits. SCAs were also developed on further substrates with a different surface energy compared to the treated glasses employed in Figure 27.[166] Among others, silicon wafers, aluminum, PTFE, glasses coated with gold, and silver were applied as substrates as well. SCAs were observed on all of these substrates.

The major disadvantage of the DSA methods for the preparation of SCAs is the strong dependence on surface properties of the substrate as well as the interaction of the colloidal suspension and the substrate. The method presented in this thesis makes it possible to use any kind of substrate, and thus increases the flexibility regarding the solvent and the materials used for the colloidal suspensions.[166]

(Parts of this chapter are published in reference [166])

5.4 Structures, morphologies and materials of SCAs

According to the literature[153,247], SCAs can be divided into three categories depending on the number of constituent nanospheres forming the SCA: (i) high-order clusters (N < 100), (ii) supraparticles (N > 100), and (iii) supraballs (N → ∞).[154] Figure 28 shows the size variety of the SCAs manufactured by inkjet printing using exemplarily BS305. Figure 28A is an example close to the category of higher-order clusters (see APPENDIX B, Figure A2 for a higher-order cluster with larger image magnification), Figure 28B an example of a supraparticle, and Figure 28C a typical example of a supraball.[154]

Larger SCAs have a very regular hexagonal ordering of the nanosphere particles at the surface comparable to the surface of SCAs as reported in the literature[153,172,174,247–259], which are based on other manufacturing methods. However, there are also some point and line defects, such as grain boundary scars[260,261], visible at the surface of the spheres.[154] A deviation from the spherical shape can also be observed, indicating a high influence of defects for SCAs with smaller diameters in the range of 1 µm (e.g., Figure 28A).[154] Defects are intrinsic for colloidal assemblies with spherical shapes due to their surface curvature.[156,262] I could not derive any influence of printing parameters on the formation of the above-mentioned defects.[154] A reduction of defects might be obtained in

principle by two approaches: (i) usage of smaller nanosphere particles and their assembly to larger SCAs, and (ii) the application of specially designed nanosphere particles with soft shells, facilitating a crystal structure formation with low defect density in a very short time (e.g., as reported by McGrath et al.[263] and Cui et al.[139]).[154] As shown in Figure 28, some of the SCAs are surrounded by planar assemblies of nanospheres (monolayers or multilayer), as already explained previously. This demonstrates that usually both types planar as well as 3D assemblies exist simultaneously due to the manufacturing process based on inkjet spray.[154]

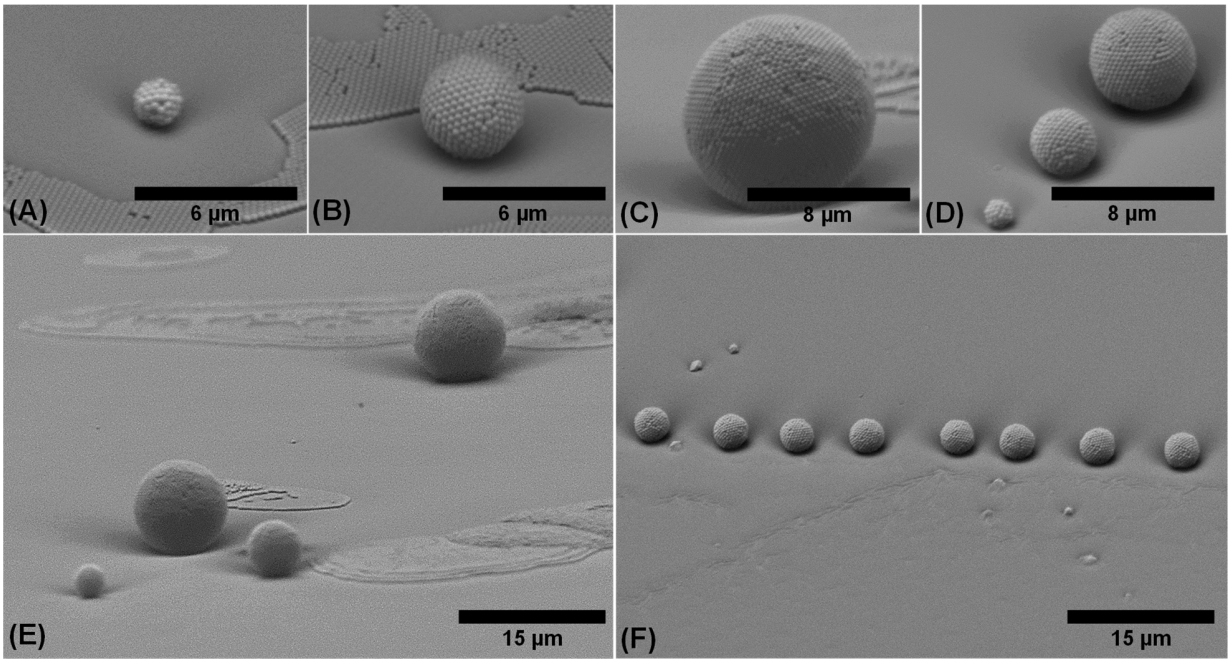

Figure 28: Tilted view by SEM of SCAs based on BS305 with changing number of constituent nanospheres: (A) N ≈ 140, (B) N ≈ 1900, (C) N ≈ 31800; (D) and (E) show variable sizes of the assemblies obtained in a line arrangement as well as randomly distributed as a result of one individual droplet spray signal, (F) presents the line-up of particles with similar size[154]

The number of constituent nanospheres was calculated with Equation 5, assuming a hexagonal or face-centered cubic order of the nanospheres with a packing density of about 74 %.[153] Since the fcc order is considered to be the most energetically stable structure for colloidal crystals, I assume that the manufactured SCAs exhibit the fcc structure or a mixture of fcc and hexagonal order.[152,154] According to the results shown in Figure 28, a broad variety of SCA sizes can be manufactured depending on (i) the volume of the ejected droplets in the droplet spray, and (ii) the number of nanosphere particles contained in a single ejected droplet.[154] The droplet volume is correlated with the waveform and frequency applied to the printhead, while the number of particles is mainly a function of ink formulation.[154] However, SCAs with a changing number of constituents

also appear sometimes without any alteration of the waveform signal or ink formulation based on a single driving pulse, as depicted in Figure 28D and E.[154]

The droplet spray can contain droplets of different volume, and more importantly, with different numbers of nanospheres depending on the drop formation dynamics.[154] Reasons for the different sizes could be also build-ups of dried deposits of nanoparticles adhering to the nozzle tip or particle agglomerations that temporarily clog the nozzle, as observed by Song et al.[245] Although similar SCAs have been demonstrated using other preparation methods, the development of monodisperse, micro-scale small and uniform SCAs (as shown in Figure 28F) is still a challenge.[254,259] The highly monodisperse SCAs can be obtained by repetition of the voltage signal to the piezoelectric transducer, resulting in the formation of similar droplet sprays with droplets having similar volumes and a similar number of constituent nanospheres (see APPENDIX B, Figure A3).[154]

Other colloidal suspensions (e.g., BL280) were tested as well, and show very similar behavior concerning the formation of SCAs.[154] Suspensions with smaller particle sizes using PSC221 were also printed and SCAs of a similar shape were obtained (see APPENDIX B, Figure A3).[154]

Interestingly, the manufacturing concept developed for SCAs based on dielectric materials can be transferred to other classes of materials as well. For instance, printing tests with dedicated waveforms enabling a spray ejection were performed with silver nanoparticle inks such as Harima NPS-JL. This ink formation contains silver nanoparticles with an average size of about 7 nm. The shape of the nanoparticles is spherical; thus, they are similar to the PS or SiO_2 nanospheres, but with a lower circularity. Figure 29 presents SCAs developed based on silver nanoparticles. Obviously, the characteristic spherical shape is obtained also for other material classes and particles sizes, proving the flexibility and applicability of the developed method for various materials and ink formulations.

The SCA shown in Figure 29A was printed with the DMP 2831 and dried at 60 °C for several hours to remove the solvent. The surface of the SCA seems to be very homogeneous as a result of the low silver nanoparticle size. In addition, soft organics used to stabilize the ink (with the aim to avoid agglomeration and fast sedimentation) might still be located on the surface of the nanoparticles, contributing to a high packing which in turn leads to a homogeneous and smooth surface appearance. Figure 29B depicts a SCA after a sintering process of 200 °C for 20 min. The smooth surface changes to a furrowed topology as a result of the sintering process initiating a volume loss, as well as a particle grain growth by neck formation. However, the spherical shape remains.

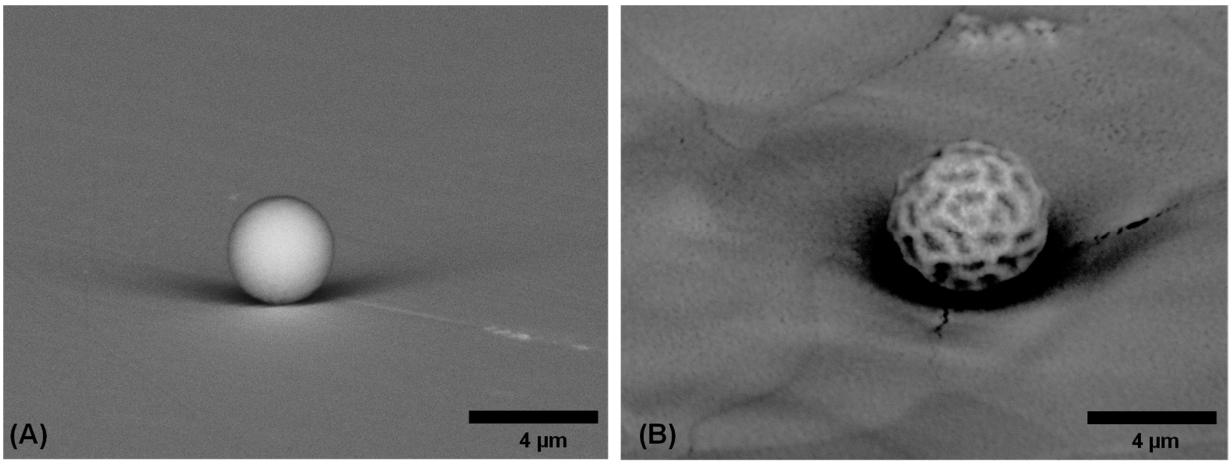

Figure 29: SCAs based on silver nanoparticles using the ink NPS-JL from Harima; (A) is a SCA which was inkjet-printed and subsequently simply dried at 60 °C for several hours; (B) is a SCA which was dried at 60 °C and subsequently sintered on hot plate at 200 °C

The same ink was used with another waveform to print planar layer deposits, for instance for electrodes of TFTs (see Chapter 6.2). I could not observe any SCA. This example is a proof of the concept that the developed process based on waveform-engineering and in-flight self-assembly can be applied to various materials, various ink formulations and various nanoparticle sizes – perhaps even for nanoparticles with shapes strongly deviating from spheres, such as wires, tubes, cuboids and others.[154]

The previously shown images of the SCAs consisting of PS or SiO_2 nanospheres (e.g., shown in Figure 28), do not reveal the internal structure. However, given the visible surface, one can assume that the SCAs are completely filled with nanospheres.[154] This is in contrast to the hollow assemblies of nanoparticles described in the literature as capsules or colloidosomes[264,265]. Some of the printed SCAs were broken by a simple micro-force apparatus consisting of two plates with plane surfaces, one of which contained the SCAs on its interior.[154] These plates were supplied with a low manual force directed vertically. Thus, the SCAs were clamped in between the two plates; the aim was to break them up to reveal the inside structure.[154] It turned out that the SCAs were either deformed or broken in a few big parts, as it is indicated in Figure 30.[154,166]
They were usually not completely destroyed by disordering all constituent nanospheres.[154] These observations assume strong van der Waals forces among the nanospheres. The relatively high stability of the SCAs is interesting for biomedical applications, such as drug delivery or biomolecular screening and detection.[154,253,266,267]
As shown in Figure 30, the inside of the SCAs (here based on BS305) is completely filled with nanospheres.[154,166] However, it is difficult to derive any order from the broken areas of the SCAs in Figure 30. Therefore, some of the SCAs were cut to obtain a cross-sectional image of the

resulting hemisphere. The cutting was performed using a focused ion beam (FIB)[m] of a gallium source within an evacuated SEM chamber. Platinum was deposited locally by means of an electron beam and assisted by an ion beam as a protection layer.[154] The angle of the SCAs relative to the electron and ion beam source was varied during the platinum deposition in order to ensure proper embedding of the SCAs.[154] One of the SCAs is depicted in Figure 31A as the top-view and Figure 31B as the side-view before the FIB process was carried out. The diameter of the SCA is approximately 10 µm.

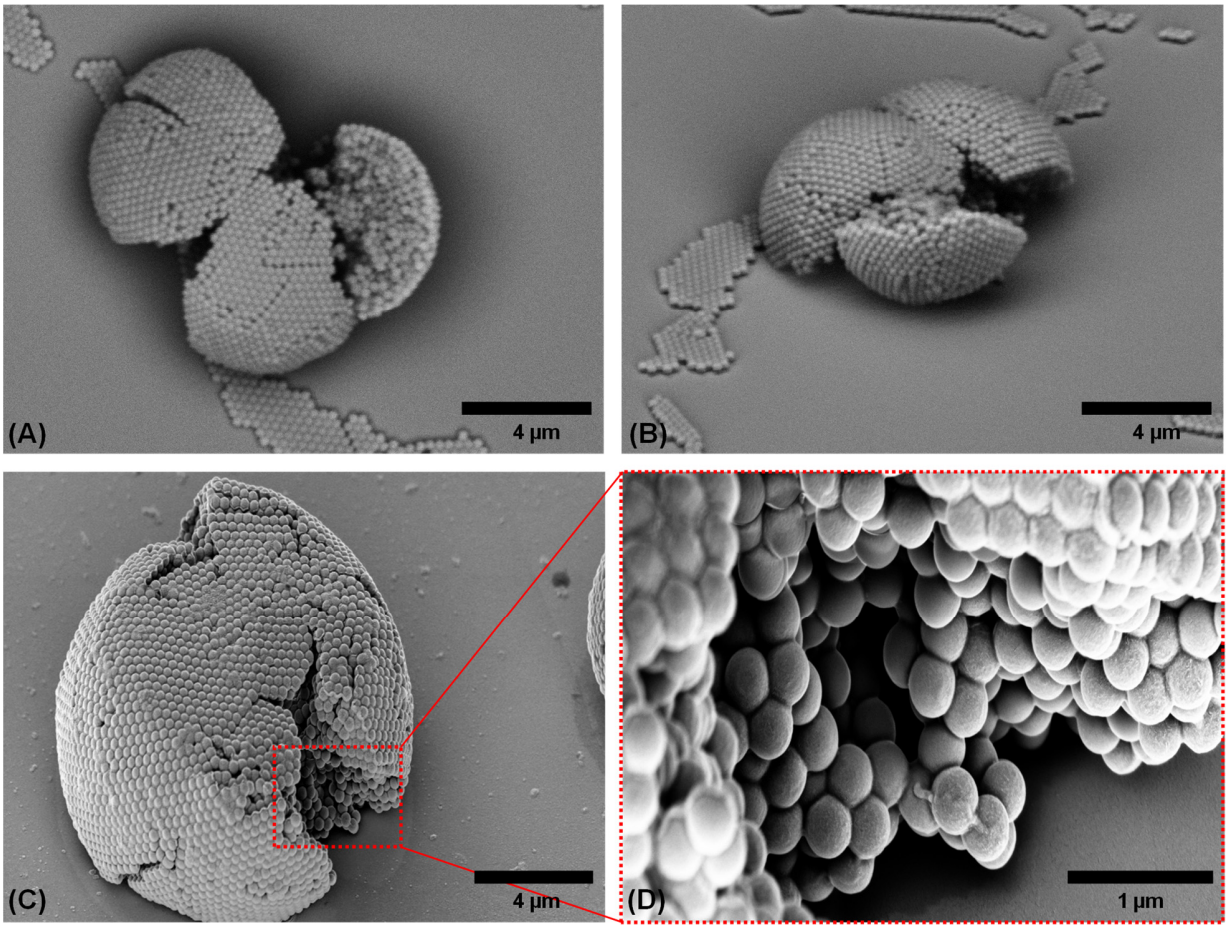

Figure 30: Internal structure of SCAs based on BS305 revealed by the micro-force apparatus; (A) top-view of a broken SCA, and (B) side-view at 60 ° substrate tilt of the SCA of (A); (C) is a deformed SCA, the opened area is shown with higher magnification in (D) (adapted from [154,166])

Figure 31C is a magnified section of the surface of the SCA showing a well-ordered hexagonal packing structure of the nanospheres with uniform pores between the nanospheres, as well as

[m] The FIB cut and the SEM analysis was performed at the Micro Materials Center at Fraunhofer ENAS in Chemnitz by Dirk Rittrich (head of the department: Prof. Dr. Sven Rzepka, head of the institute: Prof. Dr. Thomas Gessner).

some line and point defects as a result of the spherical shape.[154] The FIB cut was performed in a plane close to the center of the SCA.

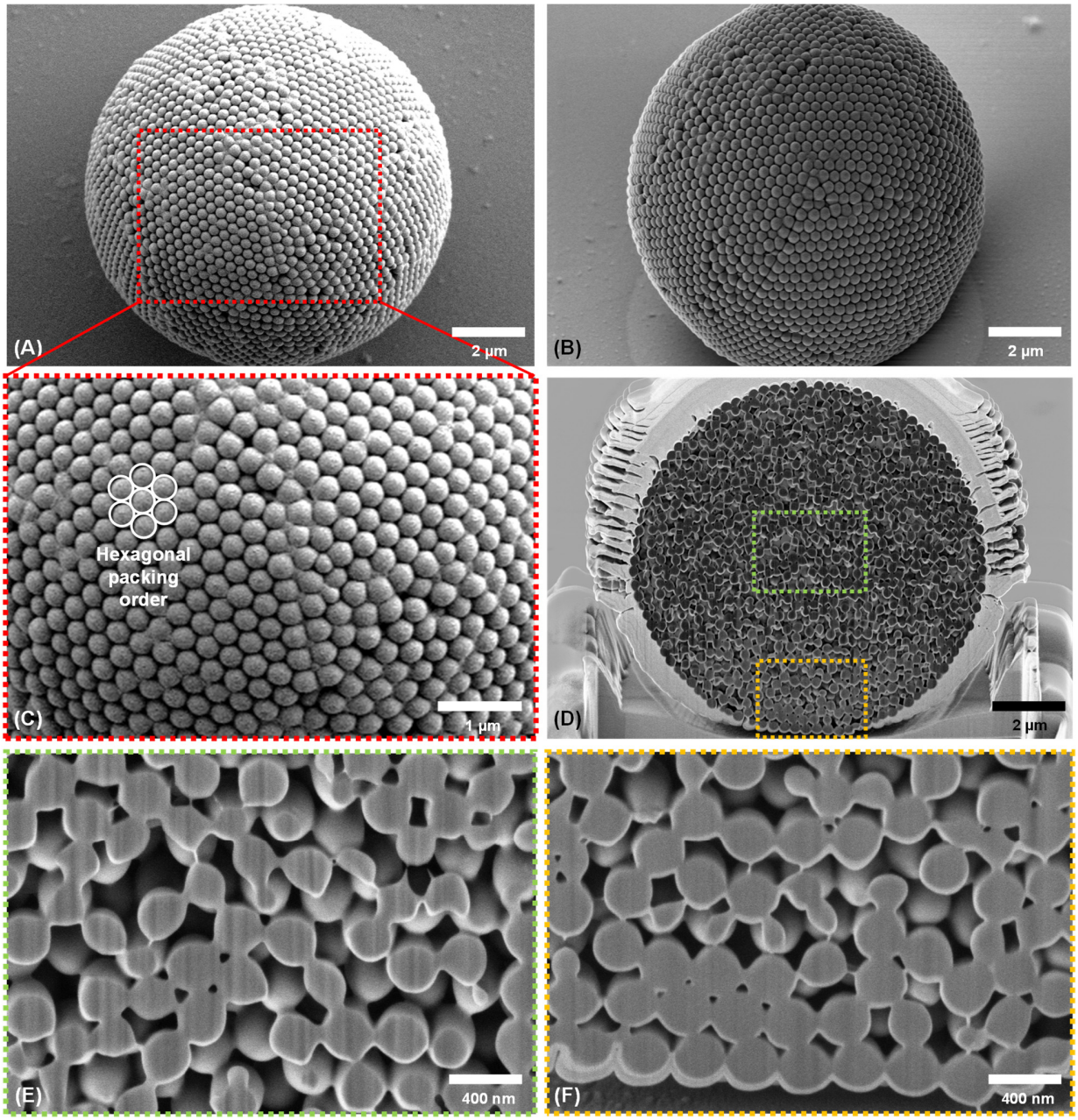

Figure 31: Structure of an inkjet-printed SCA based on BS305; (A) is a top-view and (B) a side-view of a SCA that was cut by FIB; (C) is a magnified section of (A) highlighting the hexagonal packing order of the nanospheres on the surface of the SCA; (D) is a cross-section view on the hemispherical area resulting from the FIB cut, the marked rectangles are depicted with higher magnification in (E) and (F) (adapted from [154])

The cross-section of the resulting hemispherical area with the build-up of the platinum protection layer at its outside is shown in Figure 31D.[154] Figure 31E and F are magnified sections of Figure

31D. The surface texture at the cut plane is depicted clearly, but the inner structure is a little blurry due to charging effects.[154] The FIB cuts the nanosphere particles at different positions so that cross-sections of the nanospheres appear with different cross-sectional area.[154] Indeed, this makes it difficult to derive any order from the images. However, in combination with the images of Figure 30, it can be concluded that the printed SCAs are completely filled with nanospheres and that the nanospheres are most probably arranged in a mixture of close-packed fcc and hexagonal structure.[154] Considering the *convective assembly hypothesis* of Norris et al.[152] (although the hypothesis is based on planar opal growth), I assume that the fcc order outweighs the hexagonal order in the inner part of the SCAs.[154] The theoretical interplanar spacing D_{111} for the (111) planes in the fcc lattice was determined for the SCAs in Figure 30 and Figure 31 with Equation 4 to about 249 nm.[154]
Figure 31F depicts a cross-sectional image of the outside area of the SCA. The arrangement of the lower nanospheres directly at the interface of the SCA is especially interesting, since they are more or less in one plane.[154] According to the image, there seems to be a slightly higher order at the shell than in the center of the SCA.[154] This was also confirmed for further SCAs prepared by inkjet printing, and is in general in agreement with findings reported in the literature[159].

The mechanical stability of the SCAs is remarkable as indicated with Figure 30, which depicts the broken SCAs. The adhesion of the SCAs to the substrate was tested by two simple abrasive micro-mechanical methods.[154] Rinsing with deionized water (moderate rinsing with standard narrow neck dash bottle for up to 5 seconds) and purging with compressed air (1 bar for up to 5 seconds) were used to invoke a detachment of the SCAs from the substrates.[154] Some of the SCAs were perhaps removed. However, upon further study with light microscopy, most of them remained on the substrates after the treatments, indicating a good level of adhesion.[154] This can be explained by the fact that the SCAs are attached to the glass substrate via strong van der Waals forces.[156,253]
Aside from inkjet-printing of SCAs consisting of only one specific nanosphere material, such as PS, SiO_2, or silver, one can also manufacture SCAs composed of two and potentially even more types of nanosphere materials. The suspension BS305 & BL280 was inkjet-printed using waveform B and C as driving signals to develop binary SCAs composed of organic and inorganic nanospheres.[154] The deposition of monolayers and multilayers with waveform A based on this binary suspension has already been discussed in Chapter 4.2 (e.g., see Figure 20). The binary suspension showed stable jettability because both kinds of nanospheres SiO_2 and PS exhibit a negative charge, indicated by the zeta potential measurement (see Chapter 3.2).[154] The zeta potential value of the binary suspension indicates nearly equal proportions of SiO_2 and PS nanospheres. For monolayer and multilayer deposits, the two different nanosphere materials were

randomly ordered without any preferential arrangement.[154] Using SEM in BSE mode allows one to differentiate between the two materials by the different brightness of the nanospheres.
Figure 32 depicts a top-view image obtained by SEM in BSE mode of a close-packed SCA with a diameter of about 6 µm, containing both SiO_2 and PS particles.[154]

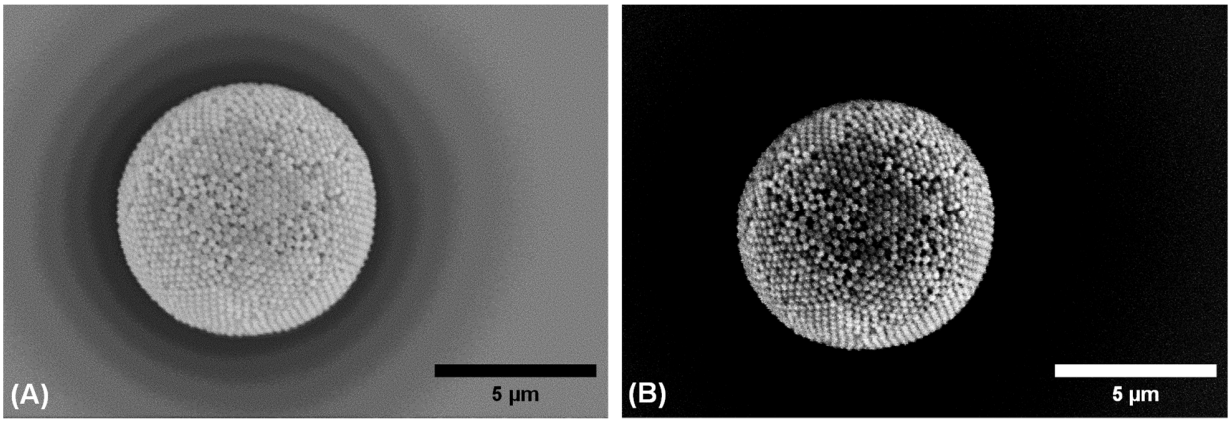

Figure 32: Top-view images of inkjet-printed SCAs based on the binary suspension BS305 & BL280 imaged by SEM in BSE mode; (B) is the same SCA as shown in (A) but with intensified contrast to indicate the distribution of PS and SiO_2 nanospheres (adapted from [154])

The packing quality seems to be similar to the SCAs that are composed of one type of nanosphere material only.[154] Figure 32B is a contrast-intensified version of Figure 32B by image processing, indicating the distribution of the particles on the surface of the SCA. There is also no preferential order visible.[154] EDX analysis of the SCA was performed, but did not gave results since the SCAs were displaced by a few tens of micrometers due to the intense electron beam. However, the displacement did not result in any obvious damage to the SCAs.[154] Some samples of the binary SCAs were heated in a furnace at 300 °C for 5 h with the aim of removing the PS nanospheres. A scheme of the preparation concept is displayed in Figure 33A.
A depolymerisation process of the PS is initiated, resulting in styrene and finally in the thermal decomposition of the organic materials.[154] Afterwards, the samples were sputtered with platinum and characterized by SEM in order to analyze the SiO_2 nanosphere arrangement of the formerly binary SCAs in more detail.
The images in Figure 33B-D show the skeletons of the remaining SiO_2 nanospheres after removal of the PS nanospheres from the SCAs.[154] The sizes of the depicted SCAs correspond to the classification given before of higher-order clusters, supraparticles, and supraballs. Again, the stability of the assemblies is remarkable.[154] Although the PS nanopsheres are removed and only the skeleton of SiO_2 particles remain, they are still stable without any obvious nanosphere distortion. This observation implies a well-mixed architectural structure of the nanospheres. Upon

removal of the PS nanospheres, the porosity increases dramatically. This could potentially qualify these structures for applications such as drug delivery.[154]

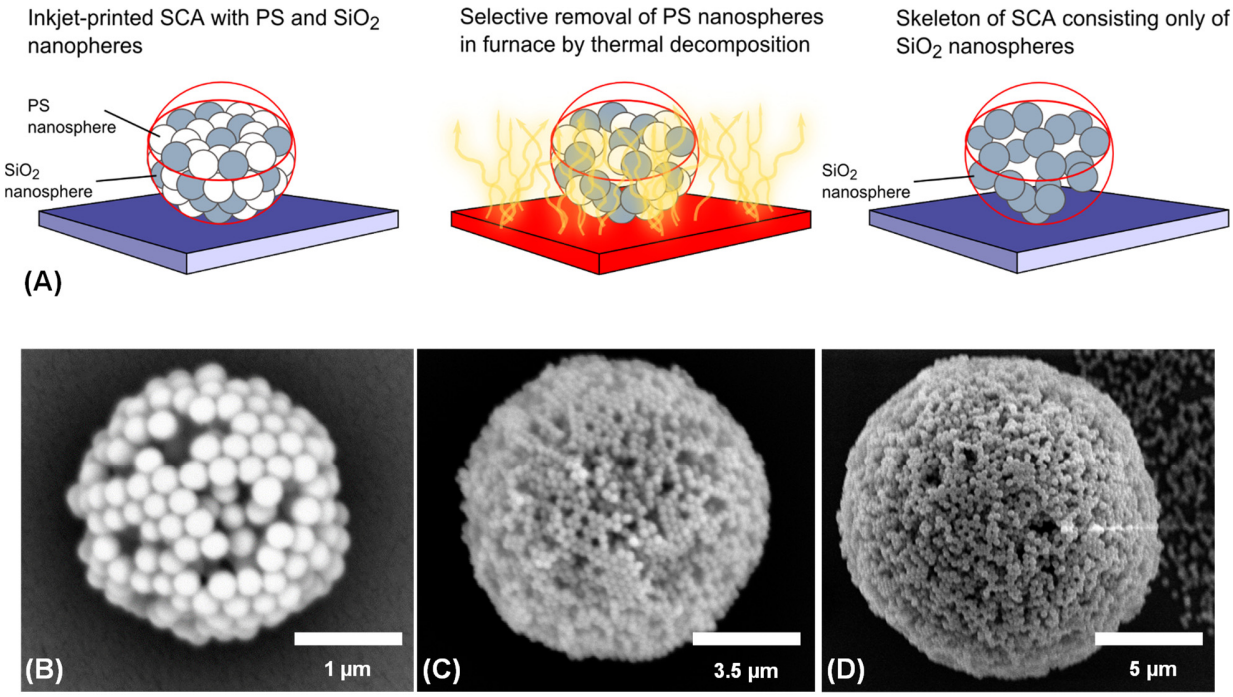

Figure 33: (A) scheme of the selective removal of PS nanospheres from the initially binary SCAs by heating in a furnace; (B) to (D) are spherical skeletons of SiO_2 nanospheres obtained by the removal of PS from the inkjet-printed SCAs with different numbers of constituent nanospheres representing initially (B) higher-order clusters, (C) supraparticles and (D) supraballs[154]

(Parts of this chapter are published in reference [154] and reference [166])

5.5 Optical properties of SCAs

The previously presented ordered packing of the nanospheres within the SCAs results in periodic refractive index variation, resulting in photonic properties. Microreflectance spectroscopy was carried out to investigate the optical properties of the SCAs and to determine the photonic stop bands. Figure 34 shows the UV-VIS reflectance spectra of SCAs based on BL280, BS305 and PSC221. The spectra were normalized and smoothen with the Savitzky-Golay filter for better visibility and comparability. A comparison of raw data plot, a smoothen plot and a normalized plot is provided in APPENDIX D in Figure A4.

The spectra clearly show reflectivity peaks, which can be assigned to photonic stop bands. These peaks correspond to the Bragg reflection resulting mainly from the (111) planes of the SCAs.[154]

The SCAs printed with BL280 and PSC221 have one characteristic stop band at about 623 nm and about 530 nm, respectively. The measured stop bands are within the expected wavelength regimes calculated with Equation 2 (Chapter 2.4). The calculated wavelength for BL280 is 614 nm and 526 nm for PSC221.[154] Thus, the measured reflection peaks are in good agreement with the calculation. The reflectance spectrum of the SCAs of BS305 show two significant peaks, hypsochromically and bathochromically shifted with respect to the theoretically expected peak position at 727 nm based on Equation 2.[154] Thus, the calculated peak position for the SCAs of BS305 corresponds quite well with the measured second peak of the reflection spectrum, but not with the first peak.[154]

The spectra of the SCAs in Figure 34 are also quite similar to the spectra of the multilayers presented in Figure 19A-D. The relative stop band width of the SCAs was determined based on the non-normalized data. The SCAs using BL280, BS305 and PSC221 have a relative stop band width of about 20 % (second peak), 19 % (first peak) and 14 % (second peak) for BS305, and 31 %, respectively.[154] The intense peaks and relative band widths confirm the interaction of the SCAs with light. They can be considered as indicators for the high ordering of the particles within the SCAs.[154]

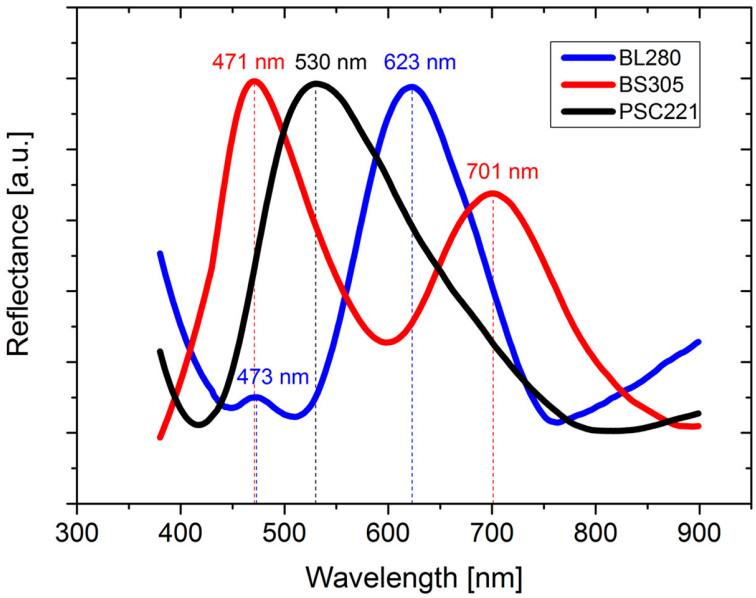

Figure 34: Normalized microreflectance spectra of representative SCAs based on BL280, BS305 and PSC221 (adapted from [154])

Based on the reflectance spectrum of SCAs of BS305, it seems that there are two stop bands.[154] A very small second peak also appears for BL280. However, this one is not as significant as the one for BS305. There are only a few examples in the literature available which discuss SCAs with

a comparable reflectance spectra having two significant reflectance peaks.[154] In general, if one kind of material with the same size is used for the constituent nanospheres, only one reflection peak occurs. Multiple peaks might be a consequence of multiple materials, for instance arranged in a core-shell structure of the SCAs based on different nanosphere diameters.[154,253]
Liu et al.[268] prepared core-shell SCAs consisting of PS particles used for the core and SiO_2 for the shell. They detected a spectra similar to the spectra shown here with BS305, having two significant stop bands as a result of the material architecture of their SCAs.[154] However, the suspension BS305 consists of only one material and the nanospheres are highly monodisperse. However, two significant reflection peaks were clearly obtained, as displayed in Figure 34. As discussed before in Chapter 4.2, this can be because of many different reasons, and mostly heuristic explanations are given in the literature. For example, the two peaks can appear due to a disorder in the crystal-like assembly, causing unselective scattering of light or grating diffraction effects as well as simultaneous Bragg diffraction from different crystal planes. This in turn could cause an interference of waves and thus multiple Bragg peaks. Mechanical deformation and/or compression of the soft, non-cross-linked PS nanospheres might appear as a result of strong capillary forces during the solvent evaporation. This can lead to an alternation of the volume ratio between PS and voids, and possibly to a variation of the dielectric constant, resulting in different reflectance peaks. All these possible reasons are partially addressed in the literature[137,157,159,169,269]. The identification of the causes for the two detected peaks with BS305 as shown in Figure 34 is beyond the scope this thesis.

The wavelength of the reflection peaks for the SCAs based on BS305 varied during several measurements. The spread was approximately 480 ± 25 nm for the first peak and 670 ± 45 nm for the second peak. The peak reflection wavelength as well as the reflectance intensity is a function of the number of constituent nanospheres of the SCAs. Figure 35 shows the spectra of three SCAs with different numbers of constituent nanospheres to be categorized as higher-order clusters, supraparticles and supraballs.
The higher the number of constituent nanospheres (and thus, the larger the diameter of the SCAs), the higher the reflection intensity. According to Figure 35, both the first peak and the second peak shift to slightly shorter wavelengths as the size of the SCAs decreases. The reason for these shifts is not yet clear, but I suppose a decrease in packing quality along with the decreasing size on account of the increased importance of surface effects. This causes a lower volume fraction of particles, and thus a shift of the reflectance peak to lower wavelengths. A lower packing quality with a decreasing diameter of SCAs was also observed by Marin et al.[172] A perfect close-packed

arrangement with a volume fraction of 0.74 was found for very large assemblies, and a volume fraction of less than 0.64 was found for smaller ones.

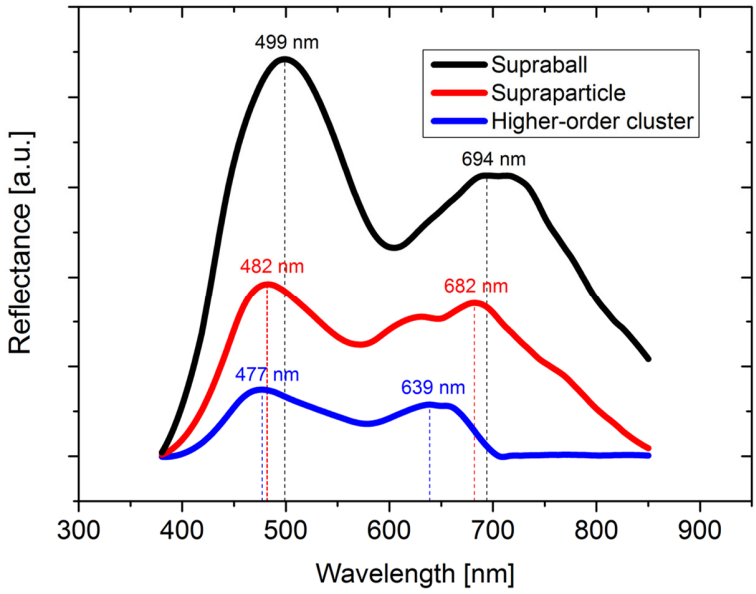

Figure 35: Reflectance spectra of SCAs based on BS305; SCAs with different number of constituent nanospheres were measured representing the three categories higher-order cluster, supraprticle, and supraball

(Parts of this chapter are published in reference [154])

6 Inkjet printing of TFTs: Process development and process reliability

6.1 Influence of print layout design

The influence of different printing parameters on morphological properties of printed deposits has been demonstrated many times before in the literature using model inks consisting of dissolved polymers. However, a change of morphology also usually causes a change in performance of the layer, for example, in terms of electrical conductivity. The print layout has a strong influence on the morphology of printed deposits, and thus on the functionality of the layer. In standard inkjet printing, all print patterns are deposited in a line-by-line raster-scan process.[95] This is the inherent principle of inkjet printing.[96] Regardless of the orientation of the pattern to be printed, the printing process will be performed in all cases in this line-by-line manner.[95] This procedure presents challenges, since the overall printing time for a pattern element of the same size (assuming a print pattern size larger than the print swath width) will depend on its orientation angle to the printing process. In addition, prepress issues such as pixelation (which are well known from traditional graphic industries), will come into play, and impose challenges when deviating from simple orientation angles β such as 0 ° (along the printing direction) and 90 ° (perpendicular to the printing direction).[16,95] These challenges will be investigated by inkjet printing of silver lines with a varying orientation angle β to the deposition process.[95] Specifically, two commercially available silver nanoparticle inks were employed for the study: (i) Sun Chemical EMD5603), and (ii) UT Dots UTDAgIJ1 (see Table 5 of Chapter 3.2 for further information). Sun Chemical EMD5603 is a well-known and well-established ink formulation in the field of inkjet-printed electronics and has been used by many researchers, for instance in the references [210,231,270–273]. The solvent is mainly based on ethanol and ethylene glycol. Therefore, the nature of the ink is hydrophilic. The UTDots ink is less common in the field of printed electronics, and the solvent is based on hydrocarbons that have generally hydrophobic characteristics.[95]

The print layout introduced in Figure 13A was printed with both of the inks using the DMP 2831 on cleaned float glasses at a print resolution of 847 dpi, 1016 dpi, and 1270 dpi, respectively. The waveform and images of the droplet ejection, as well as a photograph of the printed patterns, can be found in the APPENDIX E in Figure A5 and Figure A6. After the deposition process, the layers were dried and sintered at 180 °C for 30 min in an oven.[95] Both the morphological characteristics as well as the electrical conductivity of each line were studied. As an outcome of the study, I found three main parameters that influence the morphology and the electrical performance of inkjet-

printed silver line deposits as a function of their orientation angle to the deposition process: (i) variation of number of pixels in the print layout file, (ii) number of droplets per printing pass, and (iii) pixelation at the edge of the print pattern.[95]

Variation of number of pixels

Bitmap files are required for the printing process. The bitmap data format is a pixel-based format. Problems such as pixelation issues arise in the digital prepress of the printing workflow when the printed line orientation angle $\beta \neq 0\,°, 90\,°$.[95] This is mainly caused by the fixed cell grid pattern, which is constant for each orientation angle of the elements.[95] The schematic in Figure 36A particularly represents this problem. Figure 36A shows a rectangular print element with $\beta = 0\,°$ (= 180 °). The pixel grid is indicated in the left part of the scheme in the color yellow. The print element consists of 85 px to be printed. As shown exemplarily in Figure 36B, the number of pixels to be printed reduces to 77 for $\beta = 22.5\,°$.[95] The print pattern area and the pixel grid remain constant as before in Figure 36A. Obviously, depending on the orientation angle β, the number of pixels can vary.[95] This variation depends on the overall number of pixels for a defined pattern element, the pattern shape, and the method used for preparing the print pattern, for example breaking a vector graphic down to pixels. The variation of the number of pixels results in a variation of the number of droplets, and thus in a variation of the volume of material deposited. As a result, the printed patterns show a variation in morphology, and for conductive materials, a variation of electrical performance.[95] The graph in Figure 36C displays the determined number of pixels for the lines of the print pattern layout as defined in Figure 13A as a function of orientation angle and print resolution. The higher the print resolution, the higher the number of pixels will be.[95] The horizontal lines marked in green indicate the reference which is the number of pixels for $\beta = 0\,°$ for each print resolution. Thus, the distance of the data points to the horizontal lines show the deviation. As expected, 0 °, 90 ° and 180 ° line orientations result in the same number of pixels.[95] The maximum deviation is obtained for $\beta = 45\,°$ and $\beta = 135\,°$ with a print resolution of 1270 dpi and 1016 dpi and for $\beta = 22.5\,°$, 67.5 °, 112.5 ° and 157.5 ° with a print resolution of 847 dpi. Interestingly, the deviation of the two line patterns with 1270 dpi and 1026 dpi is positives while the line pattern with 847 dpi causes a negative deviation.[95] The reason for this is the low print resolution and the method of preparation of the print layout file using the mesh as explained in Chapter 3.3. A smaller print resolution results in a higher distance between pixels to be printed, and depending on the threshold value set for the transfer of an n-bit image file format to a 1-bit image file format (default: 50 %), dots are considered to be outside of the print element more frequently.[95] A different method or a different pattern size might result in another deviation. Due to

the specific algorithms of each software, this deviation might differ from the deviation shown here. However, in any case a deviation will result.[95]

The deviations displayed in Figure 36C seem to be quite high, especially for the highest print resolution of 1270 dpi. But taking into account the entire number of pixels to be printed, the relative deviations are < 3 % per orientation angle β.[95]

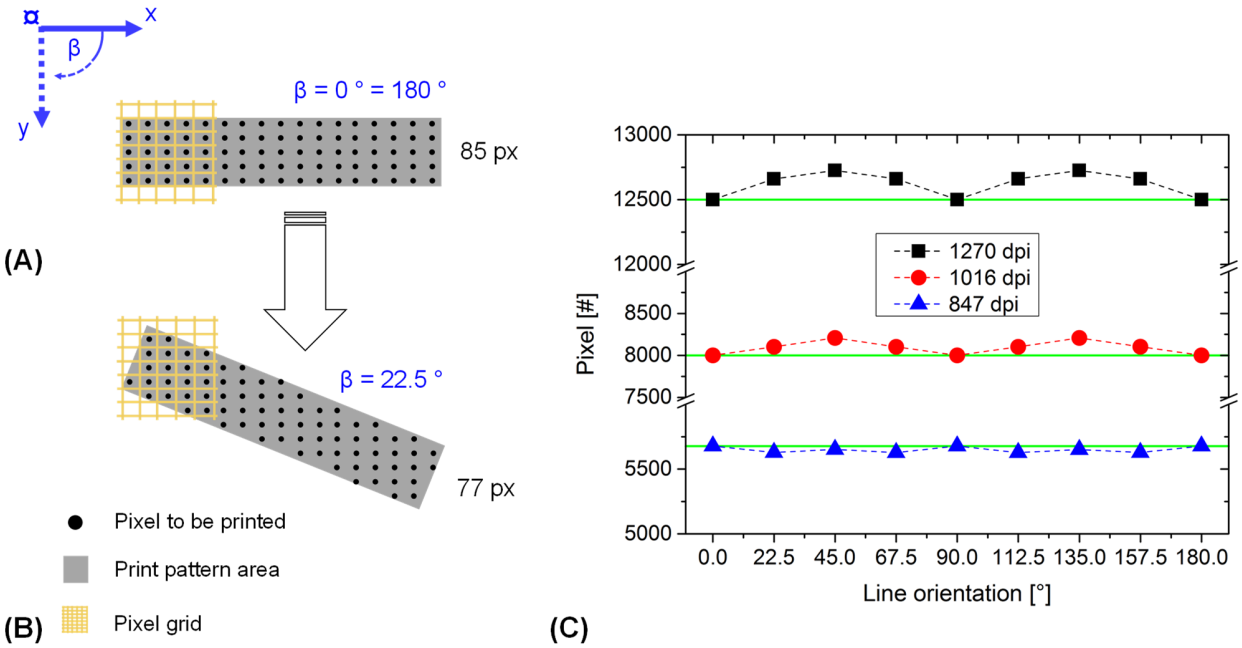

Figure 36: (A) and (B) are schematics showing exemplarily the influence of the orientation of a line pattern on the number of pixels; as indicated in the scheme, the angle of the pixel grid is constant, as well as the desired print pattern area which corresponds to the line area; (A) represents a print pattern element with a fixed print resolution and an orientation angle β = 0 ° consisting of 85 px; (B) shows the same line element having exactly the same area size and the same pixel grid but with β = 22.5 °, here the number of pixels reduced to 77; (C) is a graph with the calculated number of pixels for the print pattern layouts at different print resolutions of Figure 13A (only the line elements are considered, not the measurement pads), green horizontal lines in the graph indicate the reference which is the defined number of pixels for β = 0 ° for each print resolution (adapted from [95])

Number of droplets per printing pass

Another important factor that dramatically influences the deposit morphology is the number of droplets deposited per printing pass.[95] The number of droplets deposited per printing pass is a function of the orientation angle β.[95] The dramatic influence of the printing direction in inkjet printing on the morphology of the 1D film deposits (lines with a width of 1 px) is demonstrated in Figure 37 for β = 0 ° and β = 90 °.[96] The measured line widths and line peak heights of the ink CSD-32 from Cabot are plotted. The deposition was done with laboratory cartridge printheads on

silicon wafers with a print resolution varying between 508 dpi and 5080 dpi, with β = 0 ° and β = 90 °. As shown in Figure 37A, the line width increases and the peak height decreases with increasing drop space. Figure 37B depicts lines with a different print resolution printed at β = 0 ° (first row) and β = 90 ° (second row).

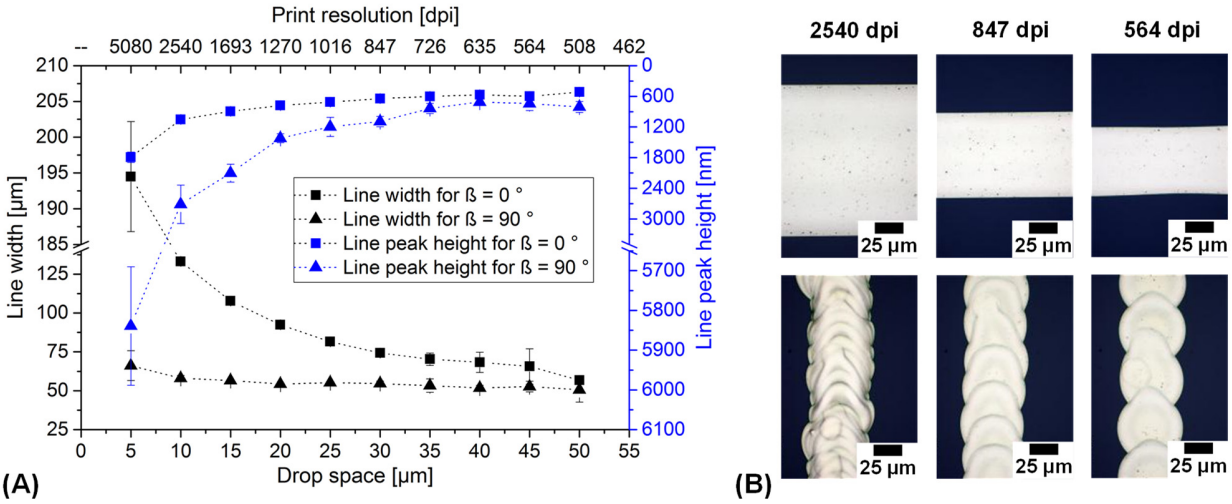

Figure 37: (A) average line widths and line peak heights of inkjet-printed 1D film deposits as a function of print resolution and orientation angle β (please note: the axis for the line peak height is inverted to avoid overlaying of the data plots); (B) exemplarily depicts microscopic images of the printed lines with a print resolution of 2540 dpi, 847 dpi and 564 dpi at β = 0 ° (first row) and β = 90 ° (second row) (adapted from [96])

The morphology of the lines printed at β = 90 ° is described by Soltman and Subramanian[100] as stacked coins. Obviously, the line widths are quite comparable, and remain nearly constant at the different print resolutions. However, the peak heights of the lines show a dramatic decrease as the print resolution decreases. The opposite appears for β = 0 °.[95] The peak height values remain comparably constant while the values for the line width undergo a large variation. The smaller the drop space, the higher the line width will be. It was assumed, that the droplets deposited at β = 90 ° start to dry before subsequent drops can coalescence with the already deposited droplets, as in the case of lines printed at β = 0 °. Many more axis movements of the printer and thus a much longer time duration is required to print the lines oriented at β = 90 ° than at β = 0 °. Therefore, the time delay between subsequently deposited droplets and as a consequence the evaporation dynamics were found to be the major parameter causing the differences in morphology. Based on these finding, further investigations were performed to study the influence of the orientation angle on much larger 2D films, which are more frequently applied in the field of printed electronics. The question was whether layers with a higher number of droplets follow the trend found for 1D films.[95]

The influence of the number of deposited inkjet droplets per printing pass on the time duration is illustrated schematically in Figure 38. To simplify the illustration, one printing pass will result in a deposition of two droplets in width.[95] It becomes obvious that the number of printing passes is much higher for the line with an orientation of β = 90 ° (Figure 38B) than β = 0 ° (Figure 38A). As indicated in Figure 38, with one printing pass, about 40 % of the droplets of the line element oriented along the printing direction are deposited, while only 12 % are deposited for the element oriented at 90 °.[95] Thus, the deposition process will take more time for lines with a 90 ° orientation and the number of droplets deposited per printing pass is lower.[95] Of course, the movement of the printhead is much shorter for the lines oriented at β = 90 ° compared to the lines with β = 0 °. However, this shorter movement is of little account in terms of time compared to the movement required for another printing pass (e.g., due to acceleration distance and stopping distance of the printhead).[95]

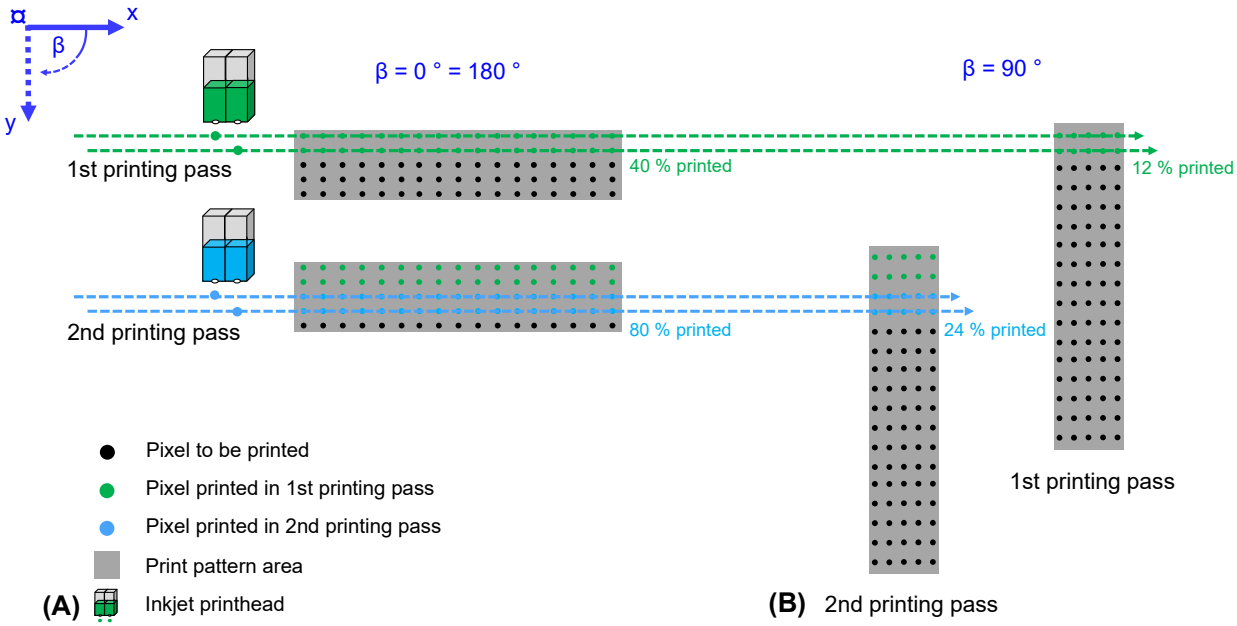

Figure 38: Schematic illustration of the influence of the pattern orientation angle β for exemplarily (A) β = 0 ° and (B) β = 90 ° on the deposited number of droplets per printing pass; the number of droplets per printing pass is much higher for the line pattern element with β = 0 ° than β = 90 °; therefore, the deposition of the print pattern element in (B) requires much more printing passes and thus longer time duration than in (A) (adapted from [95])

Since the formation of the final deposit morphology in inkjet printing of solvent-based inks on non-absorbent substrates is a result of the evaporation processes[98], the number of droplets per printing pass is of high relevance.[95] The higher the number of droplets, the higher the volume and the higher the duration of the evaporation. This leads to a longer “open time” duration, allowing the deposited liquid to spread and to reach its equilibrium state of spreading based on the surface

energy of the substrate and the surface tension of the liquid.[95] After deposition of the droplets, they are far from their equilibrium state, and the droplet will move until the equilibrium contact angle between the liquid and the substrate is reached.[10,95] According to the spreading law, also known as Tanner's law, the radius of a droplet on a solid substrate is a function of time.[10,274] On the other hand, the evaporation-induced volume loss is a function of the liquid volume and the surface unit area that is wetted by the liquid.[97,275,276]

As a result, the evaporation time for the deposited droplets per printing pass for line elements oriented at β = 0 ° will be much higher than for β = 90 °, which in turn leads to a higher droplet spreading and thus to a higher line width.[95]

Pixelation at the edge of the print pattern

A change of the orientation angle β can result in a change of the drop space directly along the edge of a printed line element. This can cause pixelation issues of the print pattern edges.[95] The schematics in Figure 39A and C indicate a variation of the edge shape formed by the outer pixels (marked in red) of the line element upon a change in β.[95]

For β = 0 °, a perfect rectangle is formed with a constant drop space at each position when connecting the outer pixels with a straight red line (Figure 39A). Deviation from the perfect rectangular shape becomes obvious when connecting the outer pixels with straight lines for β = 22.5 ° (Figure 39B).[95] Here, the distance of the pixels located directly at the edge of the line element (s_e) is different from s_{drop}. For β = 0 °, 90 °, 180 °, s_e is constant and corresponds to the drop space s_{drop} of the pixel grid. For β = 45 ° and 135 °, s_e can be determined by multiplying the drop space of the grid s_{drop} with $\sqrt{2}$. [95]

The determination of s_e of the printed line element for other orientation angles is much more complex.[95] However, in all cases $s_e > s_{drop}$, and the lower the print resolution, the higher the value of s_e. The microscopic images in Figure 39B and D demonstrate the previously explained edge effect for the printed patterns (Sun Chemical EMD5603, DMP 2831).[95] Obviously, smooth line edges appear for β = 0 °, while rough line edges (i.e., edges with pixelation) appear for β = 22.5 °.[95] This finding is of high relevance for the area of printed electronics, for instance, when designing layouts for devices such as thin-film transistors. Rough and wavy edges (e.g., in the case of S-D electrodes), will dramatically increase the risk of short circuits.[95] Furthermore, the edge roughness can influence the performance of printed devices.[113] According to these results, it is advisable to orient the source-drain electrode print pattern along the printing direction.[95] Different orientations might cause device performance problems or even a performance breakdown of the transistors due to open or short circuits.[176]

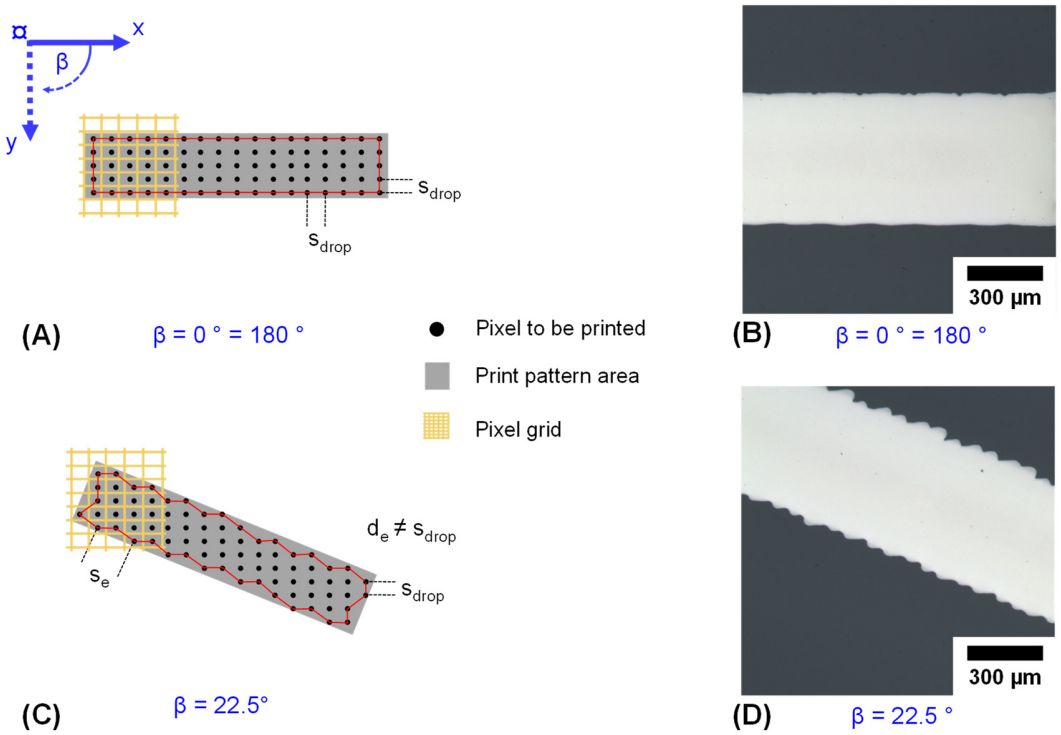

Figure 39: (A) and (C) are schematics showing exemplarily the influence of the orientation angle β on the shape of the edges (marked red) of the printed elements; (B) and (D) are the corresponding microscopic images of the lines printed using EMD5603 from Sun Chemical at a print resolution of 847 dpi (adapted from [95])

Influence of β on layer morphology and layer resistance

Figure 40 presents the measured line widths and line profiles of the silver inks EMD5603 and UTDAgIJ1 as a function of the orientation angle β (profiles were smoothen as described in Chapter 3.5, since the UTDAgIJ1 ink formulation resulted in a very rough surface morphology; further details are found in APPENDIX F, Figure A7). The line width data displayed in Figure 40A and B has a very high symmetry between the data points from β = 0 ° to β = 90 ° and β = 90 ° to β = 180 °, indicating high accuracy of the printing process and the measurement procedure.[95]

The print resolution has a strong influence on the line width. As expected, the higher the print resolution, the higher the line width.[95] Interestingly, both ink formulations result in lines within a similar line width range, despite the contrasting nature of the solvents.[95] The standard deviations for the lines printed with EMD5603 are much higher than for UTDAgIJ1, and they scale approximately with the print resolution. Larger standard deviations were obtained at high print resolutions, for instance, due to bulging effects[13,100,108]. The digital print pattern was initially designed with a line width of 500 µm for both of the inks. Obviously, higher line widths were

obtained in both cases due to ink spreading.[95] Line patterns with β = 90 ° which were printed with 847 dpi conform best to the digital print pattern size.[95]

As shown in Figure 40A and B, the line width usually decreases from β = 0 ° to β = 90 °, and then increases from 90 ° to 180 °. The lowest line width was obtained for β = 90 °, although the number of pixels and therefore the number of deposited droplets is equal for β = 0 °, 90 ° and 180 ° (see Figure 36C).[95] This result is in line with the result for 1D films (see Figure 37). Taking into account the distribution of the pixels as indicated in Figure 36C, one would expect a similar shape in the graph, since there should be a correlation between the number of pixels and the line width.[95] Surprisingly, this is not the case. Many more droplets are deposited next to each other within one printing pass of the printhead for the lines with β = 0 ° than for the lines with β = 90 °.[95] Specifically, the ratio of deposited droplets per printing pass for a print resolution of 1270 dpi is about 1000 droplets for β = 0 ° to 50 droplets for β = 90 ° (assuming the usage of two nozzles for the deposition, as depicted in Figure 38). This results in a ratio of approximately 20:1. Depositing 1000 droplets next to each other will lead to a fast droplet coalescence (see Chapter 2.1) and to a comparable high volume of ink.[95] Mainly the interaction between the surface energy of the substrate and the surface tension of the deposited ink defines the spreading of the ink, and thus also the lateral and vertical size of the deposit[98] (see also Chapter 4.1). Firstly, the evaporation of the solvent of a deposited volume of 1000 droplets requires a much longer duration of time than for 50 droplets.[95] Thus, spreading of the deposit with higher ink volume can proceed more extensively with time according to Tanner's law[10,274] than the deposit with lower ink volume. Secondly, the deposition will result in a cylindrical bead morphology of the ink with the substrate for contact angles θ < 90 °.[95] The cross-section of the cylindrical bead is equal to a spherical cap shape as long as the surface tension dominates over gravitational forces.[276] The increase in height of the spherical cap is more limited (e.g., by gravitational force and the interaction with the surface of the substrate) than the increase of the diameter (e.g., limited by the pinning of the ink at the three phase contact line), which corresponds to the width of the wetted area, and thus finally to the line width.[95]

In other words, printing hundreds or thousands of droplets on top of each other on a fixed area will not result in a continuous growth in height of the layer for the partial wetting state. At a certain point, gravitational force and the spreading tendency of the ink will become more dominant, resulting in a larger wetted area.[95]

The two previously explained dependencies, (i) higher ink volumes require longer time duration to evaporate than lower ink volumes, and (ii) higher spreading tendency of the higher volume deposits compared to smaller ones due to more limitation to increase in height such as gravitational force), clearly dominate the line width formation presented in Figure 40A and B over

the entire number of droplets deposited per line pattern as indicated in Figure 36C.[95] The data set of EMD5603 printed with 847 dpi is obviously an exceptional case, since it behaves differently (Figure 40A). Here, the line widths for β = 0 °, 90 ° and 180 ° are quite similar. I assume that a critical limit related to the number of droplets for this specific ink formulation has been reached.[95] Non-continuous film formation was obtained for patterns printed with lower print resolution (e.g., 726 dpi). Therefore, a print resolution of 847 dpi is a threshold for droplet coalescence. The low print resolution of 847 dpi results in less spreading and bulging of ink, since also much less volume of ink compared to higher print resolutions is deposited.[95] These liquid films are much closer to their equilibrium contact angle with the substrate directly after the deposition than the films deposited with a higher print resolution. The layers will evaporate faster, avoiding excessive spreading, and the drop coalescence might result in a slight contraction of ink, thus equalizing the line widths for β = 0 °, 90 ° and 180 °.[95]

Figure 40C and D show the averaged surface profiles obtained by profilometry of the inkjet-printed silver lines with a print resolution of 1016 dpi as a function of orientation angle β. The profiles of the EMD5603 ink formulation are very smooth, forming a nice plateau at the center, and can be considered as an excellent example for printed electronics applications, such as for the manufacturing of multi-layer stacks, as required for capacitors or transistors.[95] The profiles of the ink UTDAgIJ1 are characterized by a high layer thickness at the edges compared to the center part, and by high surface roughness in general (see APPENDIX F, Figure A7 for raw data profiles for a better comparison).[95] Figure 40E and F present the maximum heights of the averaged surface profiles in Figure 40C and D using the same color code for better visualization.[95] The lowest average profile height is obtained for both ink formulations at β = 0 ° and β = 180 °. The highest average profile height was determined at β = 90 ° for EMD5603 and β = 135 ° for UTDAgIJ1.[95] However, one would expect in both cases at 90 ° orientation the maximum layer height. The deviations can be explained in terms of the roughness of the UTDAgIJ1 layers and the more complex, not completely symmetrical shape of the profiles, and the averaging of the profile heights done for both of the inks, as well as the height measurement at the exact same middle position. One must also note that the difference in height of the ink UTDAgIJ1 between β = 90 ° and β = 135 ° is only about 30 nm. Overall, the values of the line height in Figure 40E and F could be roughly correlated with the line width displayed in Figure 40A and B. This is not true in all cases – there are obviously deviations that I consider as measurement uncertainty; however, generally if the line width is high, the line height is usually low and vice versa.[95]

As expected, the print resolution also has a strong influence on the average height of the lines. The higher the print resolution the higher the average line height will be. Further details about the line heights and line profiles as a function of print resolution are found in APPENDIX F, Figure A8.

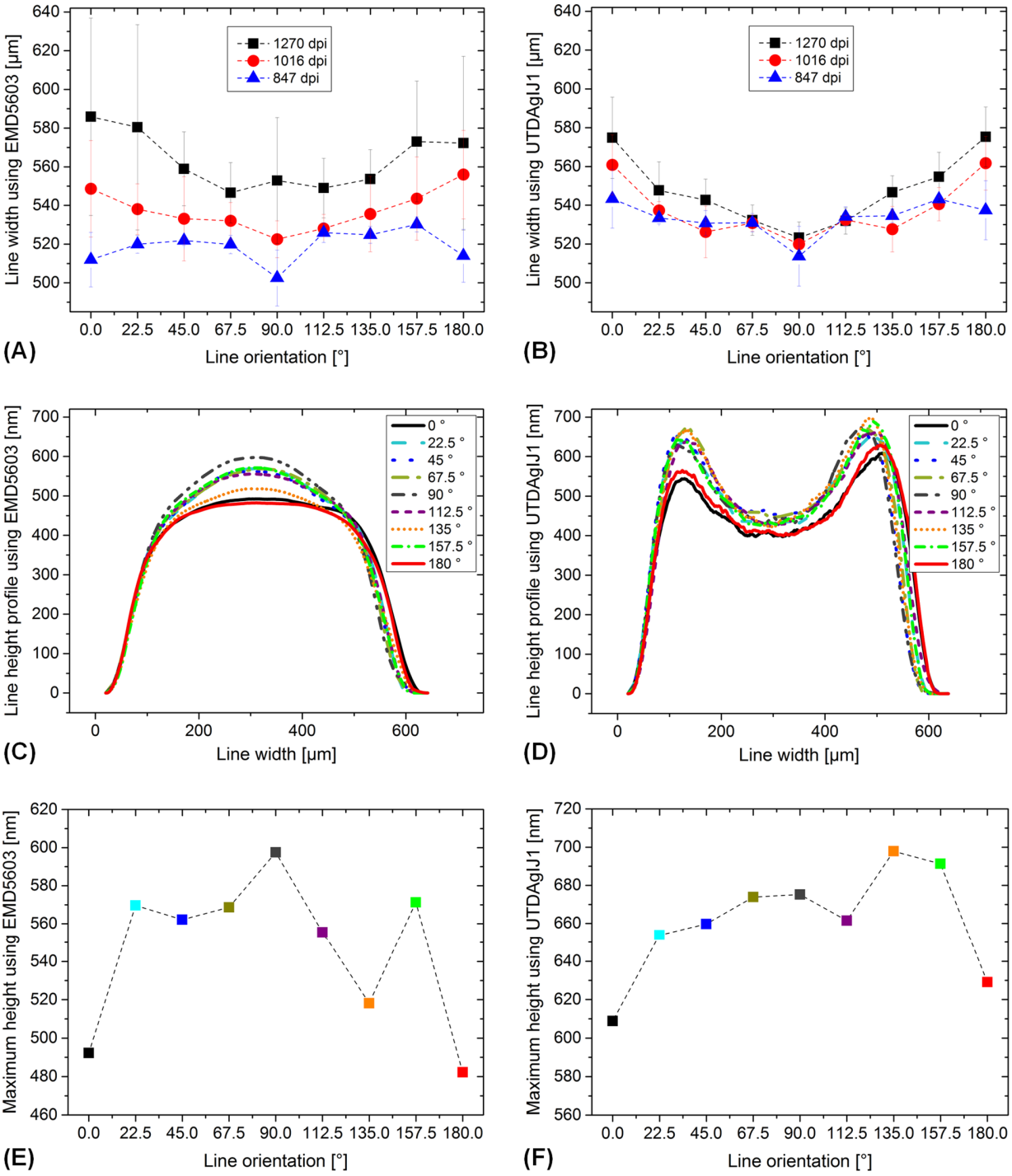

Figure 40: Average line widths of inkjet-printed lines (2D films) of (A) EMD5603, and (B) UTDAgIJ1 as a function of orientation angle β and print resolution; layer profiles obtained with profilometry of (C) EMD5603 and (D) UTDAgIJ1 at a print resolution of 1016 dpi (adapted from [95]); (E) and (F) present the maximum heights for EMD5603 and UTDAgIJ1 of the profiles of (C) and (D) as a function of orientation angle β

Figure 41A and B show the measured average line resistance. Obviously, the line resistance varies with the changing line orientation angle β for the EMD5603 ink formulation, while the resistance is relatively constant for the UTDAgIJ1 ink.[95] It is difficult to derive any trend for lines printed with the UTDAgIJ1 ink shown in Figure 41B.[95] The average line resistances are more or less constant – though somehow independent of the line orientation angle β – and have very high standard deviations in the range of 20 % to 30 %. The average resistances taking into account all orientation angles β for 1270 dpi, 1016 dpi, and 847 dpi are 4.28 ± 0.12 Ω, 4.62 ± 0.09 Ω, and 5.66 ± 0.16 Ω, respectively.[95] The overall highest resistance was obtained for lines using the EMD5603 ink with a print resolution of 874 dpi, and the lowest with EMD5603 deposited with 1270 dpi. As expected, the higher the print resolution, the lower the line resistance.[95] This is because more ink volume and thus more conductive silver is deposited at higher print resolutions.[95] The standard deviations increase as the print resolution decreases for both of the inks. However, the effect is more pronounced for the EMD5603 ink. The data plots of the EMD5603 ink show a very clear trend that is exactly the mirrored counterpart of the number of pixels per line orientation angle β (see Figure 36C).[95] This result is comprehensive, since the number of pixels defines the amount of silver to be deposited on the substrate, and the higher the amount of silver, the lower the resistance.[95] Only the resistance of EMD5603 with a print resolution of 847 dpi behaves again differently. Here, the graph is not the mirrored counterpart of the graph with the number of pixels in Figure 36C, but it shows the same trends. However, it corresponds well with the line width plot in Figure 40A. I explain this difference due to the fact that the print resolution of 847 dpi is – as already explained – very low, and at a lower limit to obtain continuous lines.[95]

Taking into account the cross-sectional areas determined by calculating the integral of the determined line profile graphs (see Figure 40C), a conductivity of up to 20 % of bulk silver for the lines with the UTDAgIJ1 ink and about 15 % conductivity of bulk silver for the lines printed with EMD5603 ink can be approximated.[95] Figure 41C is an idealized comparison of the line parameters as a function of the orientation angle β of all the printed lines investigated in this contribution. The color code qualitatively indicates a range from low (light colors) to high (dark colors) with respect to the parameters under comparison.[95] Although it is idealized and not absolutely reliable in all cases, it summarizes the main results of the influence of β on line width, line edge roughness, line height, and line resistance. These results demonstrate that the orientation angle is of high importance in inkjet-printed electronics.[95]

The discrete droplet-by-droplet nature of the inkjet printing process imposes challenges on the control of printed patterns such as the simple lines (2D films). The film formation process of inkjet-printed materials is inherently different from many other liquid deposition methods.[95] Therefore, designing devices for inkjet-printed electronics requires a detailed understanding about the

process and all parameters that influence morphological or functional characteristics of the deposits, such as orientation of the print layout pattern to the deposition process.[95]

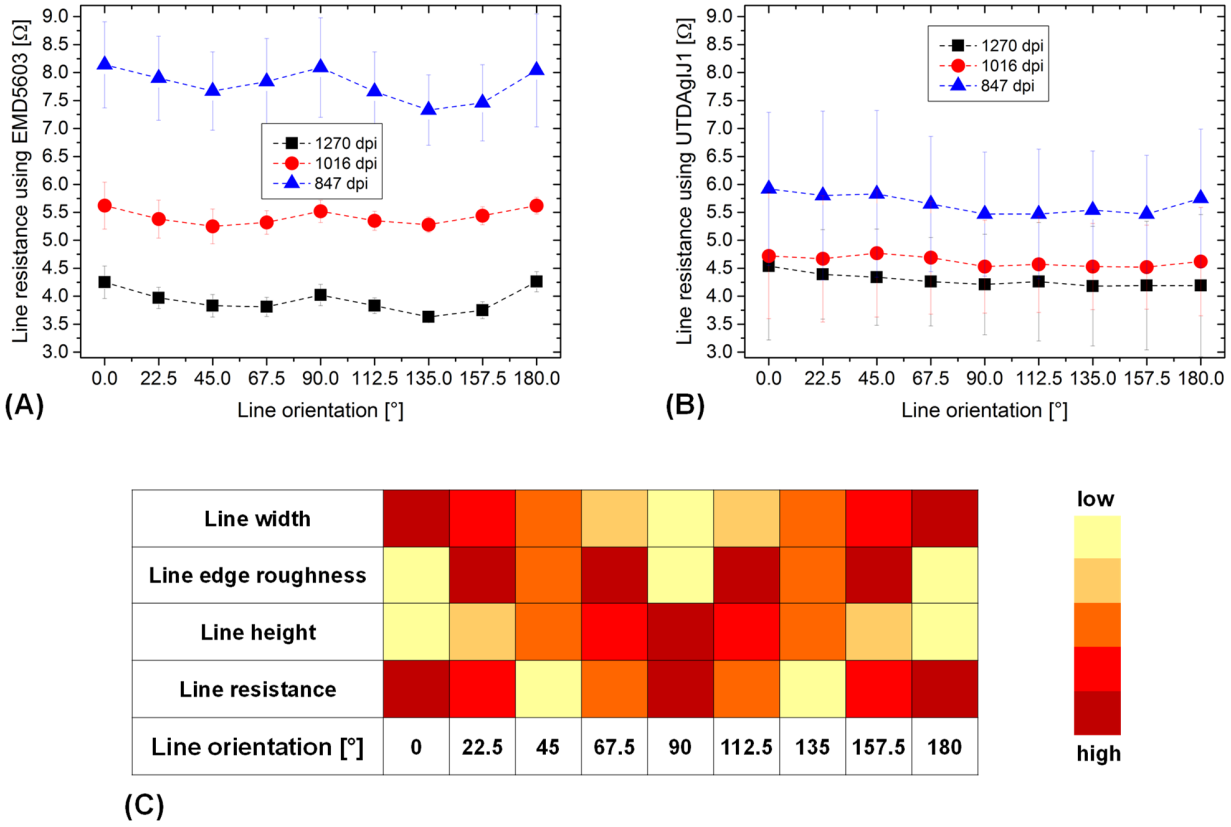

Figure 41: Average line resistance of lines inkjet-printed with (A) EMD5603, and (B) UTDAgIJ1 as a function of print resolution and line orientation β; (C) is an idealized comparison of the main parameters investigated as a function of line orientation, the color code indicates qualitatively a range from low to high with respect to the parameters under comparison (adapted from [95])

These investigations of both morphological and functional characteristics of inkjet-printed silver lines with different orientation angles β can be considered as a basic contribution allowing design and printing engineers to deposit desired, optimized and arbitrarily shaped, complex pattern features. This can finally lead to an improvement of printed electronic devices.[95]

(Parts of this chapter are published in reference [95] and reference [96])

6.2 Selection of materials and inks

TFTs consist of (i) three electrodes separated from each other, (ii) a semiconductor, and (iii) a dielectric layer (see Chapter 2.6 and Chapter 3.3). S-D electrodes are separated from each other, thus forming the active TFT channel due to the contact with the semiconductor layer. S-D

electrodes are separated from the gate electrode due to the dielectric layer. Therefore, functional and morphological requirements exist for each of the components of the TFT, along with processing requirements for the ink formulations. For instance, the electrodes need to have a certain conductivity to transport charges. A certain work function is required for the S-D electrodes in the interplay with the OSC to efficiently inject and collect charges. On the other hand, the dielectric layer should have a high dielectric constant, and the OSC a low amount of dopants to limit current flow of the TFT when it is in off-mode. The surface energy of the deposited and solid layers should be adequate to allow the deposition of further layers on top, which are required to complete the TFT stack. This presupposes that the deposited layers do not get dissolved in contact with the inks deposited on top of them. For this reason, a high compatibility between the different layers is required. In addition, comparable smooth layer surfaces (preferably average roughness < 200 nm) without high spikes (preferably < 300 nm) are required to avoid connections between the different layers (values are derived from experience). If layers are desired to be continuous, they should be continuous after printing without any areas uncovered, for instance, to avoid open circuits or short circuits. Since the deposition is done on flexible PEN substrates, there are also limitations in temperature. All these issues (along with many others) have to be considered for the selection of the materials and inks, if the aim is to develop a process for the manufacturing of TFTs based entirely on inkjet printing. Different studies and general considerations will be presented in the following section for each component of the TFTs, indicating the selected materials and inks; and the importance of the selection process will be also considered.

Substrate

Flexible plastic substrates are preferred in the field of printed electronics in order to meet the growing demand for flexible, light-weight, large area, and shapeable electronic devices. There are many polymer materials available that are discussed in detail by MacDonald et al.[277], Choi et al.[278], and Zardetto et al.[279]. Polymers, such as polypropylene (PP), polyvinylchloride (PVC), polyether sulfone (PES), polyimide (PI), polycarbonate (PC), polyethylene terephthalate (PET), and polyethylene naphthalate (PEN) are the most frequently used.[280] Without a doubt, the last two polymers mentioned are the major materials used nowadays as substrates for printed and flexible electronics.[279]

Despite the high transparency of PET and PEN substrates employed in printed electronics, PET and PEN are classified as semi-crystalline thermoplastic polymers substrates, and thus have high resistance against solvents.[278] The main issue of PET, PEN, and in general low cost polymer substrates in printed electronics is their low glass transition temperature T_g. The value or the range

of T_g defines the feasible post-treatment methods and treatment temperatures, and thus helps to identify the materials that can be deposited and post-treated on the substrate. PEN (T_g of about 120 °C) shows a higher temperature stability than PET (T_g of about 78 °C), but at the same time a lower UV stability due to the presence of naphthalene rings instead of benzene rings.[278,279] Both PEN and PET are also available as heat-stabilized substrates with T_g > 140 °C, allowing the deposition or post-treatment processes at temperatures up to 200 °C or even higher as demonstrated by Zardetto et al.[279] for heat-stabilized PEN[278].

Superior thermal properties, excellent surface smoothness, and well-defined surface energy due an adhesion-promoting chemical treatment are the major reasons that the heat-stabilized Teonex Q65FA/Q65HA PEN films were chosen as substrates for the development of the TFT manufacturing process.

Electrodes

Conductive materials required for the creation of electrodes are the basis for all electronic devices. Organic as well as inorganic materials for the electrodes of printed TFTs have been used. The organic conductors usually have comparably low conductivities (< 1500 S/cm; also sometimes higher values up to 3400 S/cm are reported in the literature[281,282]). Additionally, especially polymeric conductors such as poly(3,4-ethylenedioxythiophene) polystyrene sulfonate (PEDOT:PSS) have a high sensitivity, for instance towards humidity, UV light and oxygen, and thus suffer from performance degradation over time. However, the benefit of the organic materials is that the post-processing of the deposited layers is quite simple (e.g., hot plate drying to remove the solvents). Furthermore, they are usually cheaper than metal inks and easier to handle and to print.[83,111,281–285]

Organic conductors based on carbon, such as carbon nanotubes with metallic conducting behavior (CNTs), graphene, or simply carbon black, are very interesting materials. However, there are still major challenges in implementing them in printed TFT devices. Carbon black is a very cheap material and is already used in conventional pigmented printing inks for graphic application.[286] Recently, there have also been inkjet ink formulations with carbon black nanoparticles available, which are dedicated to the area of printed electronics.[287] However, the electrical conductivity of the layers is very low (usually < 100 S/m), and not well-suited to TFT electrodes. The liquid deposition of graphene or CNTs usually results in nano- or even micro porous layers characterized by a percolation network structure of individual graphene flakes or CNTs.[108,288] While the intrinsic transport of charge carriers within single CNTs or graphene flakes is highly efficient, the charge carriers undergo a hopping mechanism from one individual CNT or

graphene flake to the other. In this case, the charge carrier transport efficiency is limited, resulting in an decrease of conductivity.[289] Furthermore, the deposition of homogeneous layers of preferably aligned graphene flakes or CNTs using printing technologies is a big challenge.[83,290–292]

Inorganic materials based on metal nanoparticles or metal-organic decomposition inks have significantly higher conductivities than that of organic materials and have been widely studied.[14,292] Silver nanoparticle inks have been, and still remain, the most commonly used conductive material in printed (and especially inkjet-printed) electronics.[293] However, copper as metal deposited by inkjet printing is attracting increasing attention.[293–295]

Today, there is a large amount of commercialized silver nanoparticle inks for inkjet printing available. Many of the available inks are listed in Table 5 in Chapter 3.2. Obviously, there is no standard concerning the ink formulation chemistry since different solvents, particle sizes, and particle wt% are used. As a consequence, each of the inks will behave differently during the jetting process and on the substrate. The development of a dedicated waveform is required for each of the inks. It is assumed that each of the inks show different spreading behavior and film formation behavior as a result of their different composition. The different spreading behavior will result in different line widths. However, the geometric line width is of high importance in printed electronics; for instance, for the deposition of S-D electrodes. Here, the line width should be as low as possible to allow a high integration of finger electrodes per area. In addition, the edge sharpness of the lines should be as high as possible to prevent short circuits. All of the inks listed in Table 5 were inkjet-printed with the DMC printheads, which eject droplets with a nominal volume of 10 pL. A dedicated waveform was developed for each of the inks and the print pattern presented in Figure 14 was employed (all the lines are 1D films with the print pattern orientation angle $\beta = 0$ °). The print pattern makes is possible to determine the line width of the inks at different print resolutions. The obtained line width can be considered as a qualitative parameter for the spreading of the ink, and the standard deviation acts as a parameter for the edge sharpness. All prints were done on Teonex Q65FA and Q65HA, which was heated to about 50 °C to ensure stable conditions. However, one must note that the inks are made by the manufacturer for different applications, and that they maybe recommend different substrates and different substrate temperature. The substrate Teonex Q65FA and Q65HA and the substrate temperature of 50 °C were chosen as a reference standard, which meets the processing recommendations of most of the ink formulations quite well.

Figure 42A shows the results by plotting the measured line width of each of the ink formulations listed in Table 5 in Chapter 3.2 as a function of print resolution. Figure 42B is a sectional view of Figure 42B from a line width of 0 µm up to 140 µm to improve the readability. Obviously, there is a clear trend which is already visible in the exemplarily depicted image in Figure 14B. The higher

the print resolution, the higher the line width, because more droplets are deposited per length. Most of the inks have a line width in the range of 30 µm to 140 µm. ANP DGP 40LT-15C, PVnanocell I50T-11, PVnanocell I30TD-102, Bando OJ30-1 and Harima NPS-JL show a higher spreading, and line widths close to 700 µm were obtained at 1693 dpi. These ink formulations are not suitable for the development of highly integrated S-D electrodes. The Bando OJ30-1 has an especially high standard deviation, indicating high edge roughness, and thus a high probability of causing short circuits if applied as ink for S-D electrodes with short channel length.

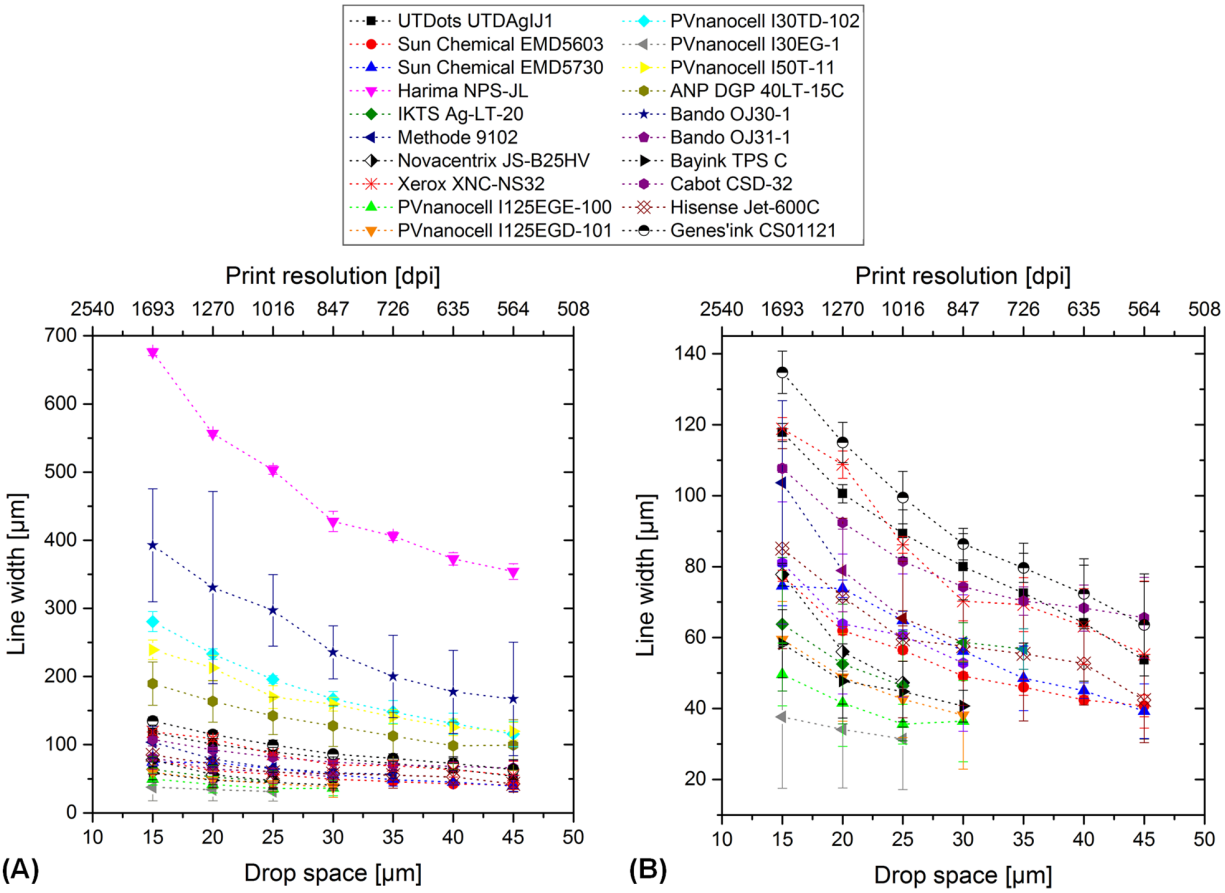

Figure 42: (A) measured line widths of commercially available silver ink formulations as a function of print resolution and drop space; (B) is a sectional view of (A) up to a line width of about 140 µm; all of the inks were printed with the Fujifilm Dimatix DMC printheads (10 pL nominal droplet volume) on PEN substrates which were heated to about 50 °C

In some cases, continuous line formation did not occur at a certain print resolution. The surface tension of the ink dominated over wetting forces and prevented the formation of continuous lines at a lower print resolution. For example, the ink PVnanocell I30EG-1 and Novacentrix JS-B25HV can be used only up to a print resolution of 1016 dpi. Lower print resolutions will result in non-continuous line formation (i.e., non-continuous area coverage). Bayink TPS C, PVnanocell

I125EGD-101 and PVnanocell I125EGE-100 can be used up to 847 dpi before interruptions in the lines appear.

The ink formulation Harima NPS-JL is clearly very different to other inks. It shows intense spreading on the PEN substrate, resulting in an area increase which strongly deviates from the digital print layout. The lowest line width obtained was about 400 µm, which is approximately 10 times higher than other silver ink formulations. This has to be considered when designing TFTs for inkjet printing. The area increase as a function of print resolution is proportional to the number of deposited droplets. Further information can be found in APPENDIX G in Figure A9.

For the application of the silver inks as S-D electrodes in TFTs, the standard deviations given in the data points in Figure 42 are the most important. The standard deviation is the square root of the average of the squared deviations from the mean value, and thus is a measure for the spread of values in a certain value distribution. As mentioned before, the standard deviation can be considered qualitatively as a parameter for edge sharpness. Edge sharpness is basically a roughness of the edge profile of a line that can be calculated, for example, as average roughness or root mean square roughness (i.e., square root of the sum of the squares of the individual minima and maxima of the mean). Therefore, the higher the standard deviation, the higher the deviation from a straight line edge, and thus the higher the degree of roughness. A high roughness in turn indicates a higher risk of short circuits between the S-D electrodes. The bar chart in Figure 43 shows the average standard deviation per ink formulation.

The average standard deviation was determined by taking into account the standard deviation of each line at each print resolution for the individual silver inks and calculating their average, and then again by taking the standard deviation of the standard deviation. Thus, the bar chart is an indicator for the edge sharpness and the homogeneity of the printed silver ink lines. The standard deviations of the average standard deviation in Figure 43 represent the spread between the different print resolutions. This graph was chosen in order to assess the edge sharpness, allowing for the selection of appropriate ink formulations, which are qualified for the development of homogenous and straight S-D electrodes. The lowest average standard deviations were obtained for the inks Sun Chemical EMD5603, Cabot CSD-32, Sun Chemical EMD5730, and Genes'ink CS01121. As a result, Sun Chemical EMD5603 was preferred as a silver ink formulation for the development of the S-D electrodes of the TFT manufacturing process. After all of the silver inks listed in Table 5 in Chapter 3.2 were inkjet-printed, a pre-selection was done based on the line width measurements, the average standard deviation of the line widths, and on the jettability and layer formation properties of the different ink formulations.

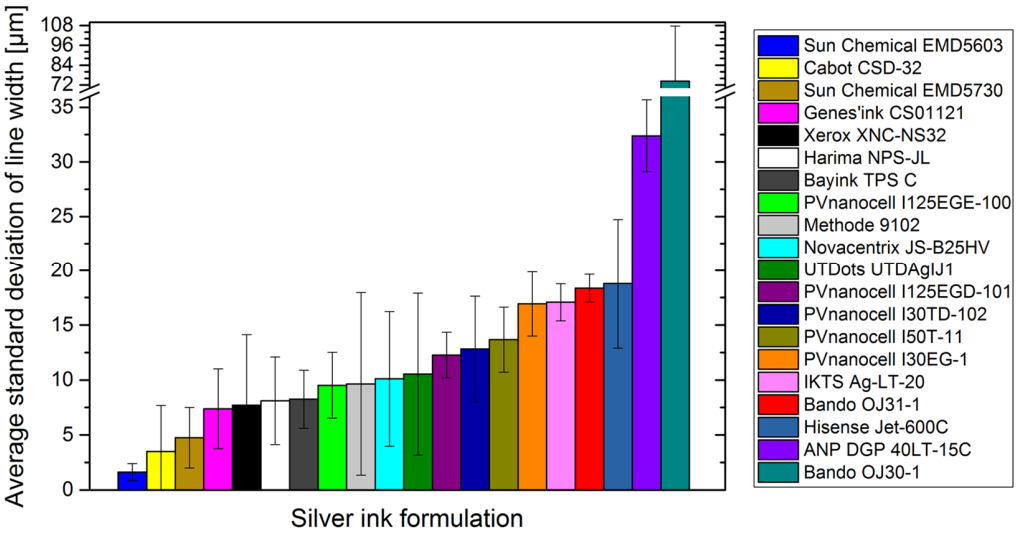

Figure 43: Average standard deviation of the line width measurements of the inkjet-printed silver inks as indicator for the edge sharpness of the lines; all of the inks were printed with the Fujifilm Dimatix DMC printheads (10 pL nominal droplet volume) on PEN substrates heated to about 50 °C

The layer formation is influenced by many parameters, and can be considered as evaporation-driven self-assembly (or in general, evaporation-driven material transportation) as discussed in Chapter 2.3. Several examples of influencing factors were given in Chapter 4.1 and Chapter 6.1. The final layer morphology is of high interest, especially if it is necessary to print something on top of this layer (e.g., a dielectric as separator to further electrodes). Most of the inks show comparable layer deposit morphologies that are, in principle, qualified for the development of TFTs. However, it was found that the layer morphology strongly depends on the area of the deposited layer, despite the fact that all the printing parameters remained constant.

One example is shown below in Figure 44, using the ink formulation PVnanocell I30EG-1. Figure 44A is a photograph of printed gate electrode metal patterns on PEN films which were partially covered with the dielectric cPVP. Figure 44B and D are detailed microscopic images of sections having a small area printed of about 750 µm x 750 µm and a larger area of about 1000 µm x 1200 µm. The surface of both of the rectangles is obviously quite different, although the same printing system and the same print settings were used. The small rectangle in Figure 44B appears homogeneous and the surface profile obtained with the laser microscope in Figure 44C confirms this assumption. The edges have a slightly higher thickness, with a peak height up to 5 µm, indicating the occurrence of the coffee-ring effect. However, overall it is sufficiently homogeneous. In contrast, the larger rectangle shows a high inhomogeneity in its center. There are even holes in the layer. The 3D scan in Figure 44D reveals high peaks in the center and a ring-like structure. These peaks were found to have thicknesses of up to 20 µm. It is an extreme example for counter coffee-ring effects (i.e., inward-directed convection flows), since a lot of

material is accumulated in the center of the pattern. The preparation of a bottom gate TFT with this rough layer is not possible due to the formation of short circuits as a result of the silver peaks.

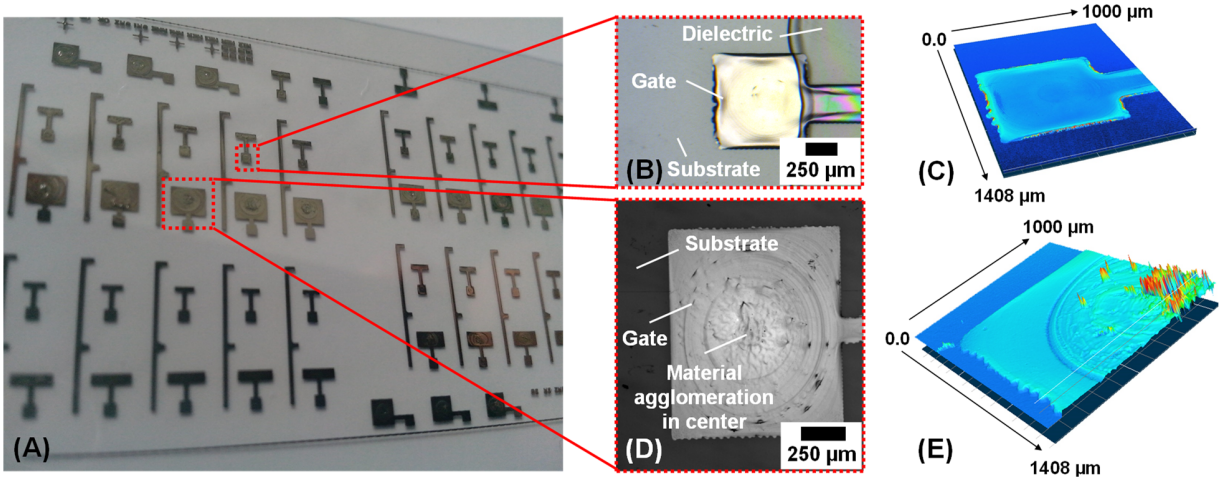

Figure 44: (A) inkjet-printed silver gate electrode pattern using PVnanocell l30EG-1, (B) and (D) are detailed microscopic images of different rectangles having an area of 750 x 750 µm² and 1000 µm x 1200 µm, (C) and (E) are 3D profiles done by laser microscopy

Finally, the 14 most promising inks were used to print squares with 1270 dpi for the measurement of sheet resistance. Drying and sintering of the printed silver inks were carried out in an oven at a temperature of 160 °C for 30 min. It is important to note that a drying and sintering in oven at 160 °C for 30 min was used as a reference parameter to allow better comparability. However, the recommendations of the ink manufacturers might deviate.

The measured sheet resistances of the inks are shown in Figure 45. One must note that the inks have different silver nanoparticle sizes and different wt% of silver which affects the result. In this sense, the sheet resistance is not normalized to the obtained thickness of the layers. Based on layer thickness data obtained by cross-sectional SEM images and profilometry measurements on silicon or glass, an average layer thickness range for all of the inks between 300 nm – 1200 nm can be assumed. Given this assumption, the layer thickness among the silver inks can be quite different up to a factor of four. Table 5 might also provide indications for the varying layer thicknesses, since the solids content and the size of the nanoparticles is given for most of the inks. Determining the layer thickness after the drying and sintering on the polymer substrate was quite difficult due to the waviness of the substrate. Therefore, Figure 45 is not normalized to the thickness, since the measured thicknesses of the silver layers were not reliable.

Moreover, I consider the print resolution to be one of the most important parameters in inkjet printing. Inkjet printing is performed based on the parameter print resolution rather than on layer

thickness. Thus, I selected the print resolution as a parameter of interest for the comparison of sheet resistance.

Most of the ink formulations have a sheet resistance lower than 0.1 Ω/□. However, two inks from PVnanocell have a much higher sheet resistance (i.e., they required higher sintering temperature). The previously chosen ink formulation Sun Chemical EMD5603 has a sheet resistance of about 0.3 Ω/□, which is definitely sufficient for the development of TFTs.

In general, the sheet resistance strongly depends on the print resolution as well as on the temperature and time duration of the drying and sintering process.[176] The higher the print resolution, the lower the sheet resistance. This is due to the increase in cross-section available for the charge carrier transport. The higher the drying and sintering temperature, the lower the sheet resistance. This is as consequence of a more intense, and thus more efficient sintering process. These already well-known dependencies are displayed in APPENDIX G in Figure A10, particularly for the ink formulations Sun Chemical EMD5603 and Harima NPS-JL.

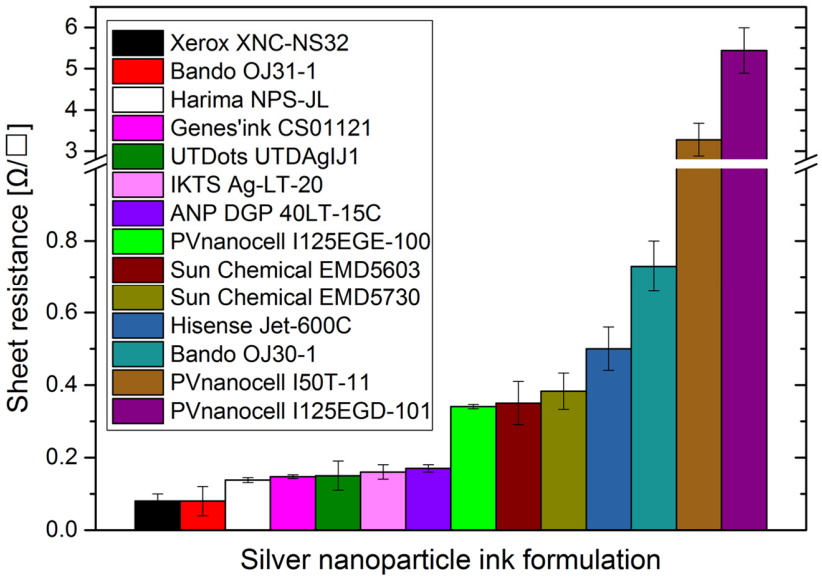

Figure 45: Comparison of sheet resistance of the inkjet-printed silver ink formulations; printing was done at 1270 dpi (corresponds to 20 µm drop space) on PEN substrate and drying and sintering at 160 °C for 30 min (sheet resistance not normalized to layer thickness)

Dielectric

The main question of this chapter is which kind of dielectric ink is more useful for application in TFTs: UV curable or solvent-based ink formulations? There are many nanoparticle inkjet inks available to form conductive electrode patterns as presented in the section before. However, there are rarely dielectric inkjet inks available designed for use in printed TFTs. Dielectric layers are

large band gap materials characterized by the absence of charge carrier transportation, which results in insulation against electrical conduction.[178] To obtain a stable, thin and smooth inkjet-printed dielectric layer with a high dielectric constant (relative permittivity) is considered to be one of the biggest challenges in forming an operating inkjet-printed TFT. The dielectric ink and the layers formed with it using inkjet printing are very critical to the operational performance of the TFT. The following bullet points indicate the major challenges of dielectric inks and the dielectric layer that were identified during my doctoral research, based on printing tests with several dielectrics:

- Difficult processing of existing dielectric inks with inkjet printing, for instance, limited jettability due to high viscous ink formulations (most of the dielectrics were designed for spin coating and are adapted to inkjet printing by dilution)
- Bad dielectric layer formation, for instance, due to wetting and de-wetting problems or issues related to convectional material transportation flows
- High dielectric layer thickness (e.g., > 3 µm, based on UV curable inks) which decreases the TFT performance
- Difficulty to print on top of the dielectric, for instance, due to low surface energy of the dielectric layer but usually the high polarity of the solvents of the conductive inks
- Chemical nature of the dielectric, for instance, hydrophilic or acid groups that limit the TFT performance due to charge trapping
- High leakage current (e.g., > 50 nA) due to inhomogeneous dielectric morphology or material properties after the printing
- Stability and compatibility of the dielectric layer, including dissolubility in solvents used for ink formulations printed on top of the dielectric

UV curable dielectrics are usually preferred in inkjet printing. In comparison to dielectric ink formulations based on solvents, UV curable inks result in layers with homogeneity and smoothness. Furthermore, a fast curing process at low temperature is possible which is attractive for web-fed processing. The application of solvent-based dielectric inkjet inks on nonabsorbent substrates leads in most cases to inhomogeneous layers due to convectional flows during the solvent evaporation. The film formation is mainly determined by evaporation kinetics and the interaction of the ink with the substrate (see Chapters 2.3 and 4.1). For UV curable inks, no evaporation takes place, and therefore convectional flows have no effect on layer formation.[201] Nonetheless, the layer formation process can undergo several wetting and spreading dynamics, although no convectional flows take place. One example is shown in Figure 46.

Here, the dielectric ink Sun Chemical EMD6415 was deposited as a square pattern with a size of 2 mm x 2 mm on the gate electrode (dried and sintered Sun Chemical EMD5603 silver layer). The size of the square is chosen to fit to the minimum magnification level of the optical microscope Leica DM 4000 M. Figure 46A shows the percentage area coverage of this layer as a function of time passed after its deposition using the DMP 2831 with six nozzles activated. The graph indicates an area decrease, and thus a lateral shrinkage of the layer from about 100 % coverage to about only 30 % coverage after 3.5 min.

Obviously, a strong de-wetting takes place and most of the deposited ink material contracts to less than half of the initially designed area. Figure 46B depicts the de-wetting processing as a function of time. For the measurement of the area increase, the darker part of the ink was considered as edge and the circumventing area was subtracted from the 2 mm x 2 mm area to obtain the decrease. The images are displayed such that printing started at the top left corner and proceeded down to the bottom right corner. De-wetting starts at the top of the rectangle and generally follows the printing process. A very thin film of the ink maintains the original shape. However, this part of the film is very thin, not continuous and inhomogeneous. This thin film does not provide sufficient dielectric properties when applied in a TFT stack. Most of the dielectric material contracts to a hemispherical shape at the bottom right corner of the print patterns. These effects result in very thick and inhomogeneous layers which are not suitable for the development of inkjet-printed TFTs.

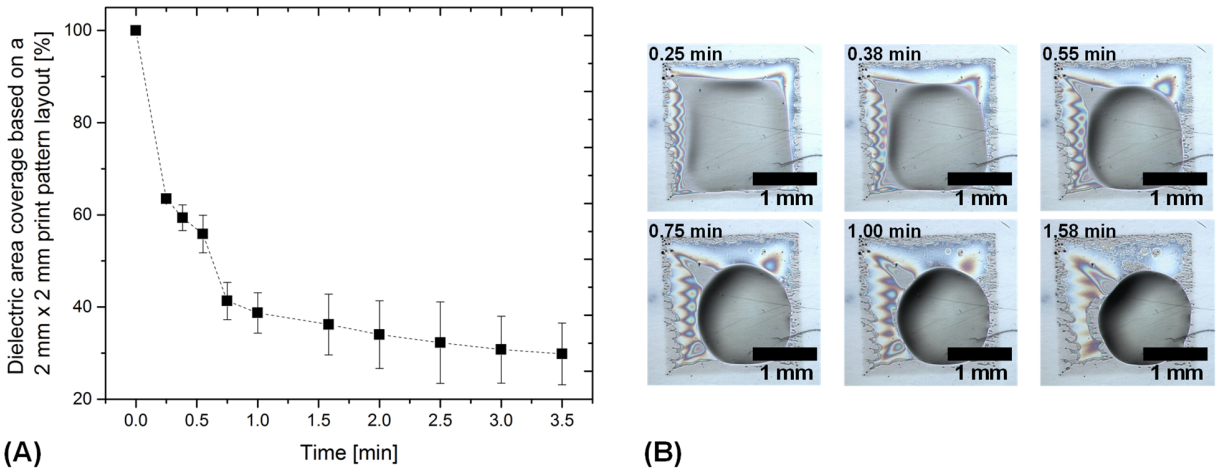

Figure 46: (A) percentage area coverage of Sun Chemical EMD6415 printed as 2 mm x 2 mm square on Sun Chemical EMD5603 silver layer indicating decrease/lateral shrinkage due to ink contraction; (B) microscopic images showing the inkjet-printed layer and the contraction at different time periods after the deposition

A representative cross-sectional view of a TFT stack with a very thick dielectric layer using Sun Chemical EMD6415 is shown in APPENDIX H in Figure A11. A very fast deposition and curing might mitigate the effect of ink contraction and thus the increase in thickness. However, this is

difficult to achieve in the batch process with the DMP 2831. There are of course other UV curable dielectric ink formulations, such as the inks from Tritron, which behave differently. These inks form smooth layers and very homogeneous and continuous films. However, they also have a big disadvantage, which they share with all UV curable inks without volatile components. The thickness of the printed layers is very high compared to solvent-based ink formulations. Figure 47A shows the average thickness of layers with an area of 15 mm x 15 mm using the dielectric ink Tritron V Photon Clear NonWet. A further decrease in print resolution towards 508 dpi results in inhomogeneous and non-continuous films. The calculated thickness was determined by dividing the droplet volume by the drop space squared. The droplet volume was determined to be about 8 pL with the installed drop watcher camera. The measured layer thickness is in good agreement with the calculation. Most remarkable is the very high thickness of more than 35 µm obtained with inkjet printing, depositing one layer only at 1693 dpi. Any other UV curable ink formulation will behave similarly, and the layer thickness will be in a similar micrometer range. This might be a disadvantage for usage as a gate dielectric, but the high layer thickness is perfect for applications such as reinforcement patterns for microsieves[215,296], as well as encapsulation or passivation[297].

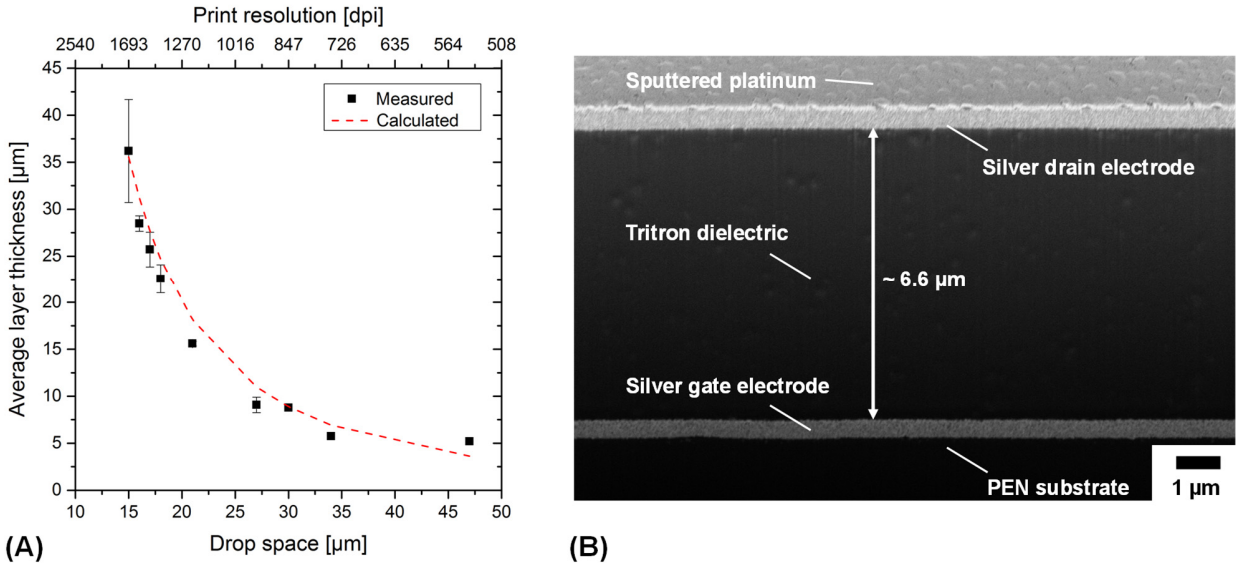

Figure 47: (A) average layer thickness of the dielectric ink Tritron V Photon Clear NonWet as a function of print resolution/drop space; inkjet printing of squared print patterns with 15 mm x 15 mm area size was performed with the SX3 printhead and the DMP 3000; (B) Cross-sectional view of the dielectric layer embedded between silver gate and silver drain electrode (adapted from [201])

Figure 47B shows a cross-sectional view of the Tritron dielectric layer, printed with a print resolution of about 726 dpi and embedded between silver gate and silver drain electrode. The

cross-section was obtained by a FIB cut[n]. The entire sample was sputtered with a 40 µm-thick layer of platinum in order to avoid charging effects. The cross-section confirms the range of the measured and calculated average layer thickness. The dielectric layer is very continuous and smooth, without any obvious defects. It is about 20 times thicker than the silver electrode layers. This ratio is well represented in Figure 47B. A high thickness of the dielectric layer causes high operating voltages for TFT devices, and thus limitations if they are used in integrated circuits.[201] Usually, high gate capacitances are desired in TFTs because higher charge densities are induced at lower voltages.[178,298,299] For instance, with the dielectric ink formulation from Tritron, capacitances > 550 pF/cm² were obtained for layers with about 6 µm thickness. The approximated dielectric constant is 3.8. As expected, a very high gate voltage up to hundred volts is required to modulate the current between the S-D electrodes.[201]

Thinner dielectric layers with higher dielectric constants are needed to increase the capacitance, and thus to decrease the threshold voltage and operating voltage of TFTs. However, another important parameter comes into play for dielectrics with low thickness: leakage current. The challenge is that leakage currents scale exponentially with the layer thickness. The thinner the dielectric layer, the higher the leakage current. These considerations imply that both the (i) thickness as well as the (ii) material properties themselves – especially towards the parameter leakage current – must be precisely defined and controlled.[178]

Printing of very thin and at the same time homogenous, uniform, continuous, and defect-free layers is one of the major visions in inkjet printing, and in general in the field of functional printing. However, it is also one of the major challenges experienced by many researchers during the past decade.[300] Solvent-based ink formulations with high dilution were applied to obtain thin layers using polymers such as PVP, polyimide, or poly(methyl methacrylate). The final shape of the printed layers is mainly determined by evaporation kinetics, which induce material flows within the films due to the high solvent content. Layer morphologies ranging from ring-like patterns via the coffee-ring effect, central bumps, or a number of further deposit patterns in between have been demonstrated, and were found to be problematic for the development of TFTs. In the literature, many researchers aimed to suppress the effects responsible for the non-uniform layer formation by optimizing the ink formulation, the deposition methodology and/or the post-processing.[92] However, another approach is to design the layers in such a way that the inhomogeneous parts of the dielectric layer arising from evaporation kinetics are located outside of the active area of the

[n] The FIB cut and the SEM analysis was performed at the Micro Materials Center at Fraunhofer ENAS in Chemnitz by Iris Höbelt and Dirk Rittrich (head of the department: Prof. Dr. Sven Rzepka, head of the institute: Prof. Dr. Thomas Gessner).

TFTs.[301] This is a quite simple and ingenious approach. Additionally, evaporation effects can contribute to thin and homogeneous layer morphologies. The idea is to take advantage of the coffee-ring effect to reduce the dielectric layer in the center area of the deposit.[301] This approach has also been recently applied by Graddage et al.[300] The center of the dielectric layer will be designed in the region of the active area, whereas the coffee-ring is located outside the active TFT area. Thus, the coffee-ring does not affect the performance of the TFT.[301] The challenge of this idea is to precisely control the coffee-ring effect aiming to allow a high reliability and to "scale-up" the coffee-ring effect from single droplets and lines (1D films) to areas of several millimeters consisting of thousands of inkjet-printed droplets (2D films).[301]

For the ink formulation, the solvent PGMEA was chosen, since it has a high boiling point of about 145 °C which allows all droplets to coalescence into a film on the substrate over time. Furthermore, PGMEA dissolves PVP and the crosslinker PMFM, and was found to work well with the inkjet printheads. Printing was performed mainly with the SE3 printhead with as many nozzles as possible, and at jetting frequencies > 5 kHz using the DMP 3000. The dielectric layer was designed as a very large print pattern of about 3700 µm x 3750 µm to ensure that the coffee ring edge is outside the active area (see also Figure 15A).[301]

Figure 48A shows the obtained dielectric layer as part of the layer stack of the TFT (only the OSC is missing for better visibility). As explained, the dielectric layer has a very large area so that the coffee ring does not affect the active area.[301]

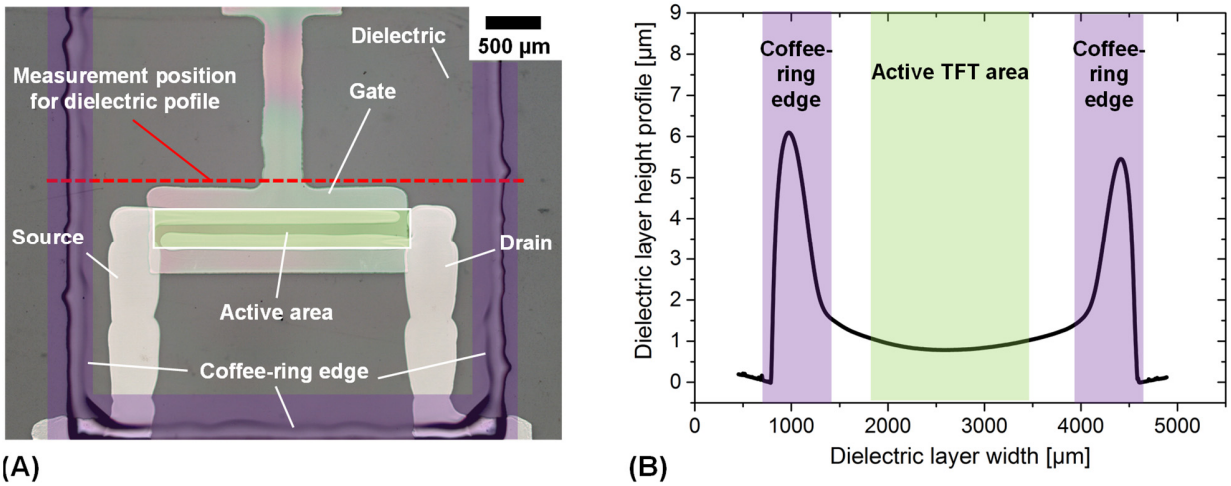

Figure 48: (A) layer stack of silver gate electrode, dielectric cPVP layer and silver S-D electrodes; the dielectric is designed such that the coffee ring is outside the active TFT area; (B) is a profile of the dielectric layer morphology nearby the measurement position indicated in (A) (adapted from [301])

From the microscopic image, the dielectric layer appears quite homogeneous in its center area. This is a result of the optimization of several printing parameters, mainly the deposited material per area and timeframe, and the temperature of the substrate.[301] Further information can be found in APPENDIX I in Figure A12. Figure 48B shows the surface profile of the dielectric layer measured close to the indicated measurement position in Figure 48B. The surface profile implies a strong coffee-ring effect during the evaporation process of the volatile ink components.[301] The valley area, with an average height of about 1 µm, is comparably uniform, and its center part is used for the active area of the TFT.[301] The coffee-ring edges are significantly higher with peak heights of about 6 µm.[301] However, due to their height and width they contribute to the reduction of the layer thickness in the center area. With this approach, smooth layers with a thickness of down to 300 nm were successfully and reliably printed.[301] This is only a fraction of the layer thickness obtained with the UV curable ink formulation. Therefore, the solvent-based ink formulation resulting in a thin cross-linked cPVP layer was preferred over the UV curable dielectrics.

A cross-sectional view of the TFTs (obtained by a FIB cut[o]) based on the dielectric cPVP is shown in Figure 49. All layers were printed with the DMP 2831. Sun Chemical EMD5603 was used for gate as well as S-D electrodes with a print resolution of 847 dpi. cPVP was employed as dielectric and printing at 1270 dpi. The OSC was also printed with a print resolution of 1270 dpi.
Figure 49A depicts a section of the TFT with a single drain electrode. The width of the electrode is about 40 µm, and the electrode profile shows a coffee-ring shape. The dielectric of this section is very homogeneous in thickness, but has some nanometer-sized defects in form of inclusions which are most probably simple voids (i.e., gas bubbles). These defects are located in all images very close to the gate electrode. In all cases, they also have the size range which is indicated below in Figure 49A. These bubbles might be caused by the drying and curing process, which takes place at a relatively high temperature of 150 °C for 40 min inside the hot plate oven. The cross-sectional images confirm the smoothness of the dielectric layer in the center area of the TFT as it was already determined by profilometry in Figure 48B.
Figure 49B is a magnified section of Figure 49A showing the edge of the drain electrode and the structure of the silver layers. Obviously, the drying and sintering process forms a nano-porous silver layer structure. The porosity is a function of the drying and sintering process conditions, and was studied elsewhere for copper[293,295] and silver[302] ink formulations more in detail. A S-D electrode height profile was obtained by profilometry. It is presented in Figure 49C with a scheme

[o] The FIB cut and the SEM analysis was performed at the Micro Materials Center at Fraunhofer ENAS in Chemnitz by Iris Höbelt and Dirk Rittrich (head of the department: Prof. Dr. Sven Rzepka, head of the institute: Prof. Dr. Thomas Gessner).

indicating the measurement direction. The S-D electrodes have a thickness of approximately 300 nm, which is confirmed by the SEM images as well. The coffee-ring shape appears more pronounced here as a result of the scale of the x-axis.

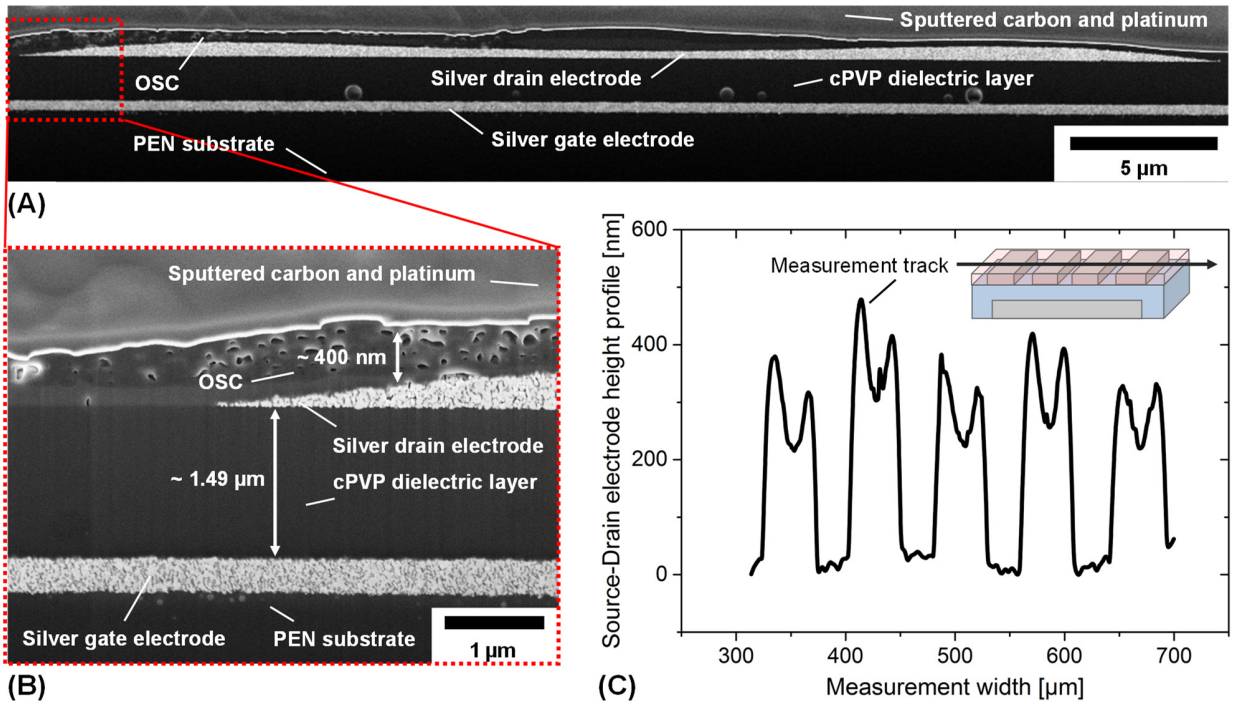

Figure 49: Inkjet-printed TFT using cPVP as dielectric; (A) cross-sectional view on the TFT layer stack; (B) is a magnified image section of (A) and (C) is the surface profile of the S-D electrodes printed on top of the cPVP dielectric, the schematic inset shows the measurement direction

OSC

The OSC ink formulation FS0096 from Flexink consists of a p-type conjugated aromatic ordered polymer dissolved in mesitylene. Mesitylene was chosen instead of tetralin or toluene, because it was reliably jettable. The deposition of the OSC was performed with 16 nozzle laboratory cartridge printheads in order to reduce material waste, since the dead volume of the laboratory DMC printheads is much smaller than that of the industrial SE3 or SX3 printheads.[176]

The development process from an irregular OSC layer shape up to a continuous and comparable regular OSC layer is shown in Figure 50.[176] Only the substrate temperature was varied to improve the layer morphology. All other parameters remained constant (print resolution 1270 dpi, 16 nozzles with 5 kHz jetting frequency). The print pattern was designed as a square with 3 mm edge length (see white dotted line in Figure 50). Figure 50A depicts the printed OSC layer on PEN at a substrate temperature of about 20 °C (room temperature).[176] Obviously, the shape of the printed

layer deviates largely from the designed layer shape (i.e., white dotted line). The deposited ink contracts and forms a bulge due to the movement of the receding contact line during solvent evaporation.[176] The contact angle hysteresis is close to zero and contributes to the formation of a circular planform droplet shape.[176] Soltman et al.[110,303] investigated the phenomenon of layer formation for squared shapes in detail. Methods such as fine-tuning of the print layout or application of substrates with rough surfaces are presented to compensate the contraction of the inkjet-printed ink formulations. Here, a very simple alternative approach was chosen by heating the substrate to compensate the contraction of the ink.[176]

In Figure 50B, the substrate was heated to about 30 °C contributing to a remarkable reduction of the contraction. Nearly no contraction takes place when the substrate is heated to 60 °C as shown in Figure 50C.[176] Figure 50D depicts the transfer of the OSC layer to the final TFT layer stack. The OSC layer was printed on the cPVP layer with the S-D electrodes patterned on top at a substrate temperature of 60 °C.[176] The obtained layer shape improved a lot compared to Figure 50C. The shape is close to a square with comparable tight corners. However, the thickness of the OSC layer is obviously not very homogeneous. The center appears a little darker in color, indicating a higher layer thickness.[176]

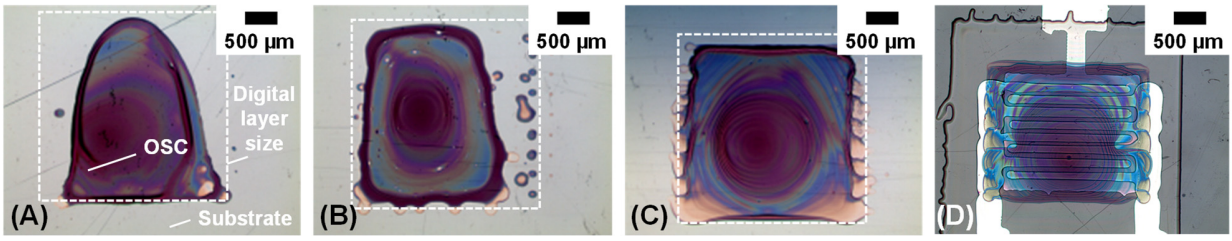

Figure 50: Inkjet-printed OSC layers with a print resolution of 1270 dpi on PEN substrate at (A) 20 °C substrate temperature, (B) 30 °C substrate temperature, (C) 60 °C substrate temperature and (D) at 60 °C substrate temperature deposited directly on the Gate/dielectric/S-D electrode layer stack to complete the TFT (white dotted lines indicate the designed layer size for the OSC layer)[176]

Further optimization can be done by adjusting the ink formulation. However in general, the ink can be printed with inkjet printing and shows a very good and stable jetting performance. Layers with adequate quality are formed and since it is a p-type OSC, the handling is much simpler compared to an n-type OSC.[176]

The FS0096 is not considered as a high performance OSC, but it is quite stable in ambient conditions over several weeks. After a couple of months in ambient conditions, the OSC degrades resulting in an increase of the TFT threshold voltage.[213] The long time period where the OSC is stable makes it possible to process the ink by inkjet printing in ambient conditions, and furthermore

to perform an adequate electrical and morphological characterization of the TFTs in ambient atmosphere.[176]

(Parts of this chapter are published in reference [176], reference [201] and reference [301])

6.3 Manufacturing workflow and electrical TFT parameters

A manufacturing workflow for the all-inkjet-printed TFTs was developed under consideration of the influence of the print layout design (see Chapter 6.1) and by using the inks, materials, and equipment which were previously defined (see Chapter 3 and Chapter 6.2.). A scheme of the workflow is shown in Figure 51.

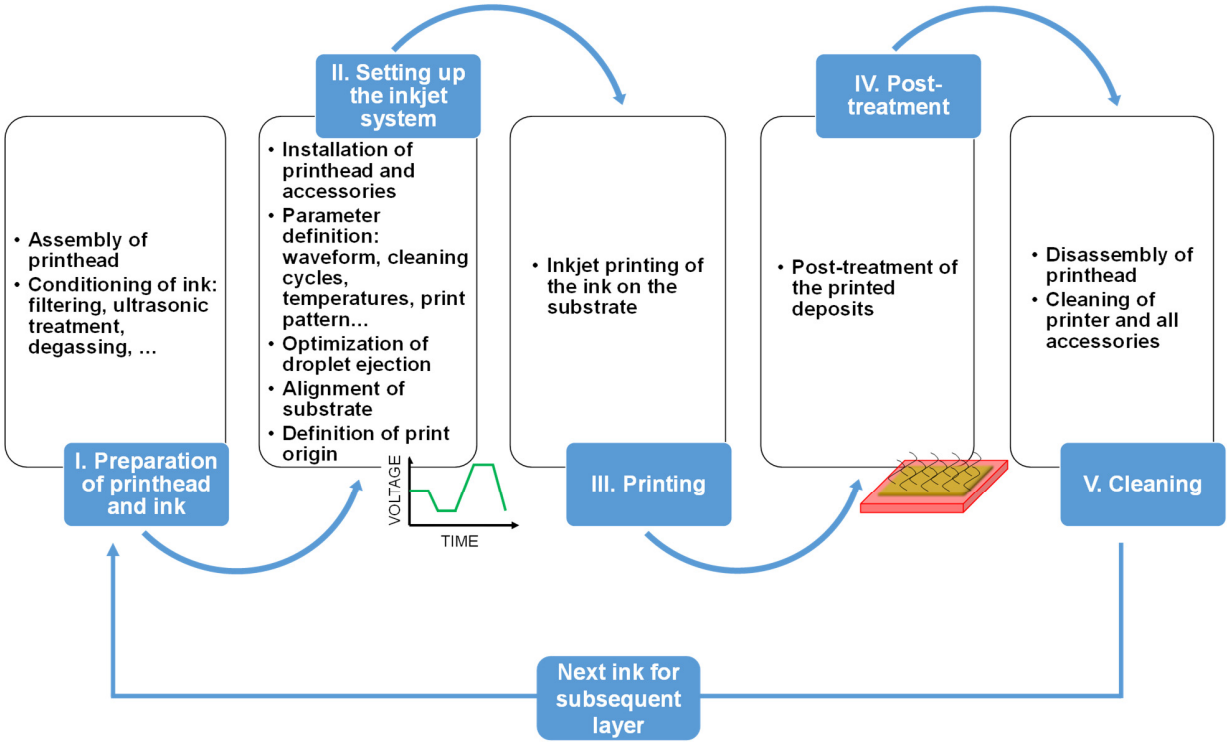

Figure 51: Scheme of the developed manufacturing workflow for all-inkjet-printed TFTs

The deposition of each of the layers of the TFTs consists of five consecutive process steps. Process step I. and II. require about 2.5 h – 8 h when using the DMP 3000 equipped with industrial inkjet printheads. If all the printing parameters are known, a time duration of 2.5 h is feasible for the preparation. If one starts from scratch with a new ink, it might take 8 h or even longer depending on the efforts to optimize the entire process. The time duration of the printing process itself (III.) depends mainly on the desired printing area, print resolution, jetting frequency and

number of activated nozzles. However, compared to the process steps I. and II., it is much faster. For instance, printing an area of about DIN A4-size (i.e., 924 TFTs) with a print pattern resolution of 635 dpi using 50 activated nozzles jetting at 5 kHz will take about 12 min. The post-treatment method employed was a simple thermal treatment in an oven. The time duration depends on the printed ink and ranges between 20 min – 40 min. Cleaning of industrial printheads in the field functional printing usually requires a disassembly of all parts in order to avoid contamination of other inks used with the same printhead or printhead parts. The complete disassembly and cleaning is quite time consuming (2 h – 4 h) since it should be carried out carefully and in a clean environment, similar to the assembly of the printhead in order to prevent dust and dirt particles from clogging the nozzles of the printhead. For each subsequent ink (and thus, for the deposition of a subsequent layer), each of the process steps have to be carried out again.
The printing needs to be performed for each of the inks repetitively on a large area to increase the efficiency of the manufacturing process. As a result, the most elaborated process steps I., II., and V. are minimized proportionally to the printing process (III.).

Figure 52 shows further details of the developed manufacturing process. Figure 52A is a photograph of 924 TFTs arranged in six arrays printed on a PEN DIN A4 sheet.[176] The sequential layer-by-layer approach of the explained manufacturing workflow is presented in Figure 52B-E. The silver gate electrode (Sun Chemical EMD5603) depicted in Figure 52B was deposited directly on the PEN substrate. The layer thickness on average ranges from 600 nm – 900 nm (564 dpi, SE3 printheads with 35 pL nominal droplet volume).[176]
After the post-treatment of the deposited silver layers in an oven, the sheet resistance was determined to be about 0.35 Ω/□, which corresponds to about 4 % - 6 % of the conductivity of bulk silver.[176] The dielectric layer in Figure 52C was printed as a large rectangular pattern on top of the gate electrode. The coffee-ring effect was exploited to obtain a smooth layer with low thickness, as explained before in Chapter 6.2. The S-D layer is, next to the dielectric layer, the most critical one.[176] Figure 52D shows the formation of well-defined interdigitated S-D electrodes on top of the cPVP layer. The electrodes were deposited along the printing direction ($\beta = 0\ °$), taking into account the considerations about the print pattern orientation of Chapter 6.1. The challenges for an optimal deposition of the S-D electrodes are (i) a good alignment accuracy with respect to the gate electrode (preferred accuracy ± 10 µm), (ii) a smooth dielectric cPVP layer, (iii) a well-adjusted interaction of surface energy of cPVP and surface tension of the silver ink, and (iv) well-adjusted printing parameters.[176]

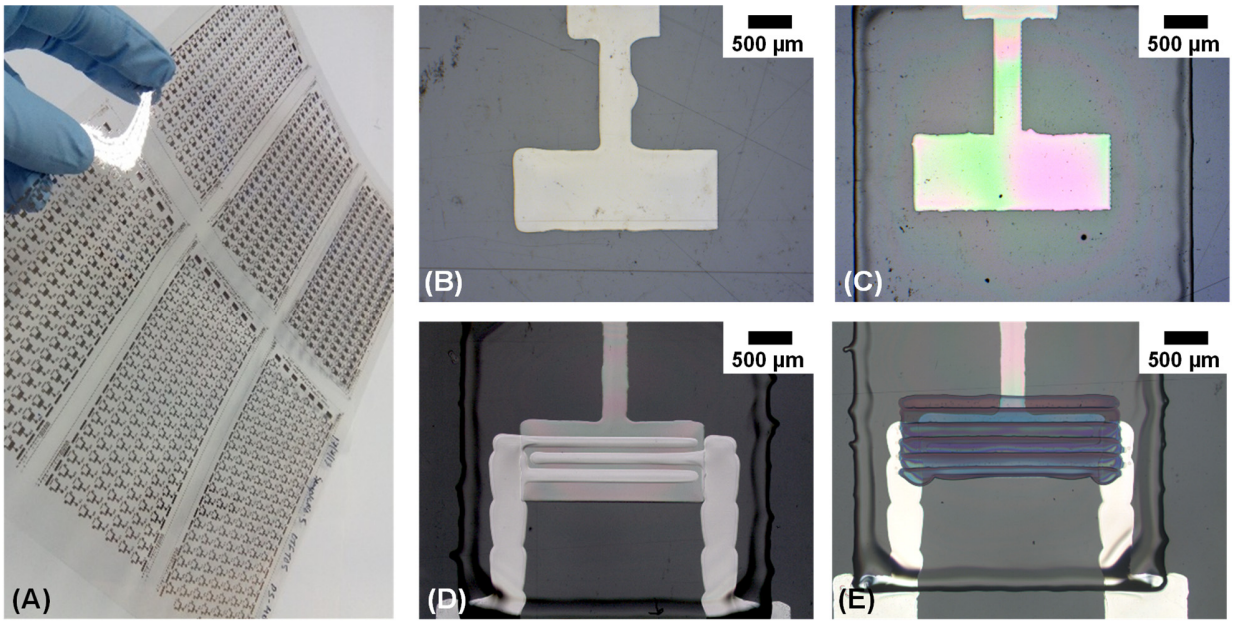

Figure 52: (A) 924 all-inkjet-printed TFTs arranged in six pattern arrays on a PEN DIN A4 sheet, (B)-(E) layer-by-layer manufacturing approach for the all-inkjet-printed TFTs: (B) silver gate electrode, (C) cPVP dielectric layer deposited on gate electrode, (D) silver S-D electrodes printed on the cPVP dielectric with overlap to the gate electrode and (E) OSC printed as last layer to complete the TFT (adapted from [176])

Even small changes of printing parameters for the S-D electrodes can result in defective TFT devices, for instance, due to short circuits or open circuits.[176] Short circuits can appear when the contact line of the deposited liquid ink is allowed to move due to spreading (e.g., when bulging of the ink appears). The substrate was heated to 50 °C to counteract excessive spreading and bulging of the deposited ink. Open circuits can easily appear due to jetting problems. The finger electrodes are designed as 1D films, thus having a width of one droplet only. A missing droplet will inevitably result in a non-continuous film formation and hence to an open circuit. Figure 52E shows the deposited OSC layer on top of the pre-printed layer stack. The printing direction was along the S-D electrodes ($\beta = 0$ °) with the optimized procedure discussed before in Chapter 6.2.[176]

All of the TFT arrays were manufactured on PEN films with a maximum processing temperature of 150 °C. All deposition processes were carried out in a standard laboratory in ambient conditions.[176] A low vacuum was applied only for storing of the samples in the time between the deposition of the individual layers or shipping to project partners, and for the drying and curing of the cPVP dielectric layer to improve the interface of dielectric and OSC due to the reduction of surface charge traps.[176]

The electrical properties[p] of the TFTs depend strongly on the ink materials and printing parameters used. Most of the electrical properties are summarized in references [176,201,202,213,301]. However, these references also include materials which are not considered in this thesis. The main results of the electrical TFT performance based on the materials and printing parameters explained in this thesis are listed here:

- Threshold voltage of about -14 V
- I_{ON}/I_{OFF} of about 10^2 to 10^3
- Field effect mobility up to 0.02 cm²/(V·s)
- Drain-source current I_{DS} up to 3 µA

Figure 53 shows the electrical performance of the printed TFTs. A typical transfer curve and output current-voltage characteristics measured in the saturation regime of a TFT with a W/L of 140 are plotted. The S-D electrodes were deposited with a print resolution of 508 dpi, and the dielectric cPVP layer with 564 dpi.[176] The data plots in Figure 53C-F are based on about 400 functional TFTs. The field effect mobility shown in Figure 53C is about 0.02 cm²/(V·s) with a very slight decrease with increasing W/L ratio.[176] In addition, the standard deviations seems to decrease with increasing W/L. At a W/L of 240, the variation in mobility was found to be about 30 %, which is comparable to values reported recently by Fukuda et al.[189] for fully solution-processed TFT arrays (among others, spin-coating is used). The decreasing standard deviation with increasing W/L can be explained by the area of the OSC layer.[176]

The number of interdigitated electrodes is increased in order to increase W/L. Therefore, the influence of some process failures are much more significant if only a relatively low number of droplets is deposited.[176] A higher number of droplets, and thus a large and/or thick layer, will allow one to compensate for process failures better than for smaller-sized and/or thinner layers.[176,301] The reduction of the field effect mobility with increasing W/L ratio was also found in other printing trials performed within the project TDK4PE. Defects in the OSC forming boundaries for the electrons are possibly one of the major reasons for this trend.[176]

[p] The TFT characterization was done within the project TDK4PE by the Printed Microelectronics Group at CAIAC, Universitat Autònoma de Barcelona, Bellaterra, Spain (Director: Prof. Dr. Jordi Carrabina; head of the group: Eloi Ramon), by the Department of Integrated Circuits and Systems (ICAS) at the Institute de Microelectronica de Barcelona IMB-CNM (CSIC) (head of the department: Prof. Dr. Lluis Teres, director: Prof. Dr. Carles Cane) and by the Organic Electronics Group at Universidade do Algarve, Faro, Portugal (head of the group: Prof. Dr. Henrique Leonel Gomes). The semi-automatic characterization system is located in INB-CNM. Detailed studies on individual TFTs were performed by the Organic Electronics group in Portugal.

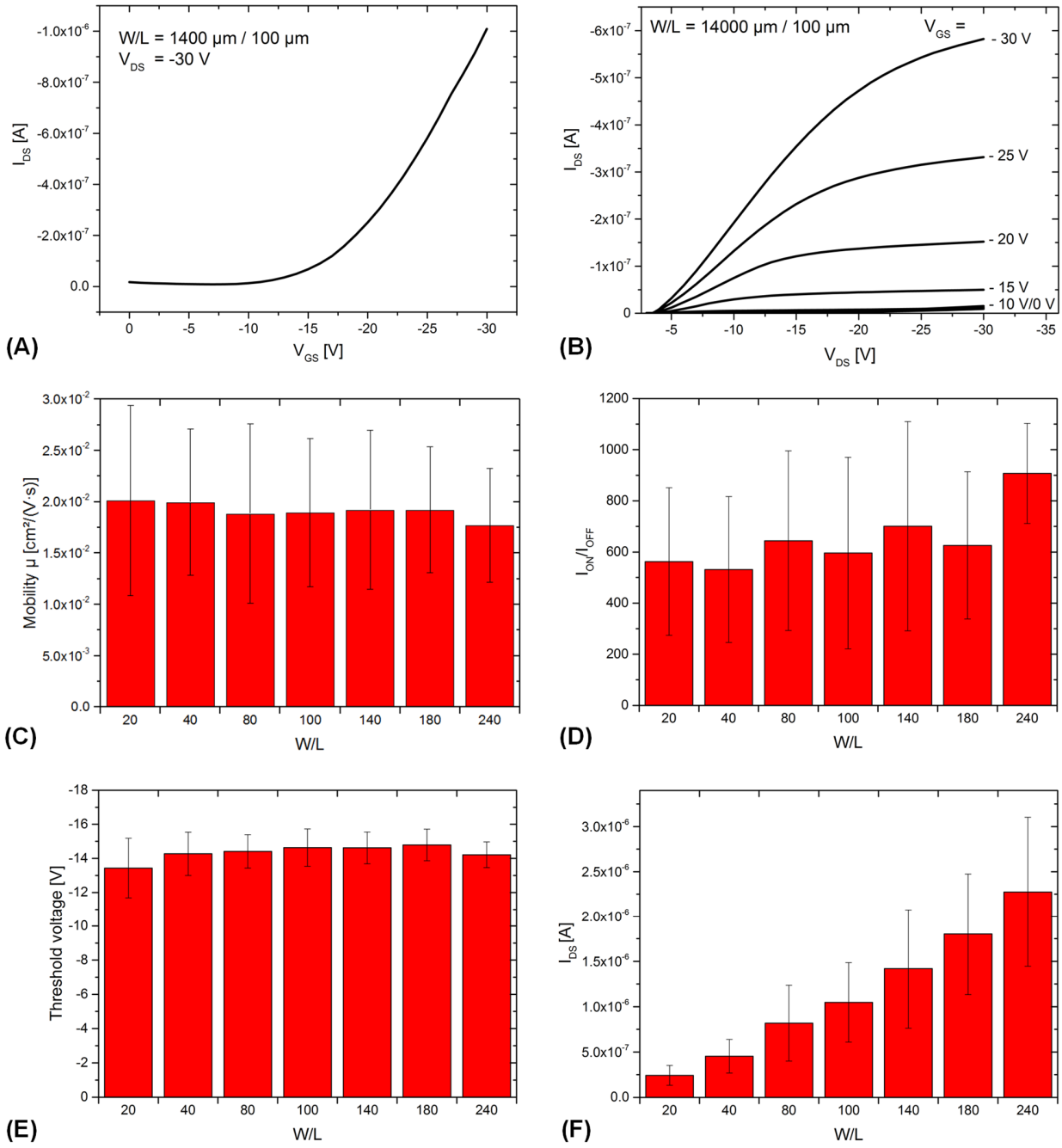

Figure 53: Typical (A) transfer characteristics and (B) output characteristics, exemplarily for a TFT with a designed channel length of about 100 µm (W/L = 140) using 508 dpi print resolution for the S-D electrodes and 564 dpi print resolution for the cPVP dielectric layer; (C)-(F) Electrical characteristics of about 400 functional TFTs: (C) charge carrier mobility, (D) I_{ON}/I_{OFF}, (E) threshold voltage and (F) maximum drain-source current as a function of W/L (adapted from [176])

The plot in Figure 53D shows the current ratio of I_{ON} and I_{OFF} (I_{ON}/I_{OFF}). The on-current is defined as the drain-source current (I_{DS}) measured in the saturation region (V_{DS} = -30 V and V_G = -20 V),

and the off-current as the current passing through the TFT without any applied gate voltage (V_{DS} = -20 V and V_G = 0 V). I_{ON}/I_{OFF} seems to increase as W/L increases.[176]
Here, we can also see a high variation in the currents. The lowest variation can be determined to be about 20 % for the TFTs with a W/L of 240. However, the on-current increases nearly linearly with the W/L ratio. The off-current, which should be ideally as low as possible, is therefore one of the major reasons for the data variation.[176]
The threshold voltage is shown in Figure 53E and is on average about -14.3 ± 1.1 V, with a slight positive drift (towards 0 V) at the W/L of 20 and 240. The variation is about 8 %.[176]
Figure 53F depicts the maximum drain-source current as a function of W/L. There is a clear, near linear, trend. As expected, the higher the value of W/L, the higher the maximum current due to an increase of the active TFT area.[176]

(Parts of this chapter are published in reference [176] and reference [213])

6.4 Manufacturing yields and failure origins

The manufacturing yield depends on many parameters, but particularly on the print layout and on the printing parameters. A few influencing parameters will be presented here.
The print resolution has a strong influence on the morphology of the deposits. This was demonstrated, for instance, in Figure 37 and Figure 42 for 1D films. The higher the print resolution, the higher the width of the lines. The same strategy was applied for the S-D electrodes of the TFTs. For this reason, TFTs with a varying print resolution of the S-D electrode layer (Sun Chemical EMD5603) were designed. All other parameters were kept constant.[176]
Figure 54 shows the result of this investigation considering 616 TFTs. The percentage of short-circuited S-D electrodes and the measured channel length are shown as a function of print resolution in Figure 54A.[176]
The higher the print resolution, the lower the channel length and the higher the amount of short-circuited S-D electrodes.[176] Figure 54B-E show microscopic images of the S-D electrode layers (printed on top of the dielectric and gate electrode) with the different print resolutions under consideration. Figure 54B corresponds to 726 dpi.[176] Obviously, there are no individual electrode fingers visible. The high print resolution causes coalescence of the finger electrodes so that a rectangular block is obtained, short-circuiting the S-D electrodes. All S-D electrodes printed with 726 dpi were short-circuited independent of the number of fingers.[176] Decreasing the print resolution to 635 dpi results in a channel length of close to 40 µm with about 70 % of short-circuited S-D electrodes.[176] One of the functional S-D electrodes printed with 635 dpi is depicted in Figure

54C. All the fingers are separated from each other. The print resolutions 564 dpi and 508 dpi behave similarly, and the channel length increases accordingly, which limits the risk to create short circuits. Figure 54A indicates that the lowest channel length obtained is just below 40 µm. This is not true, since the graph considers only four different print resolutions.[176] There is no further differentiation between 635 dpi and 726 dpi which could result in a further channel length reduction. Shorter channels can be also obtained by fine-tuning the print pattern layout, for instance, by a reduction of the channel length in the design.[176] This will result in a channel length of just below 10 µm. Further information is found in APPENDIX J in Figure A13. A similar strategy was applied in references [201,202], for the manufacturing and electrical characterization of all-inkjet-printed TFTs with a channel length in the range of 10 µm.

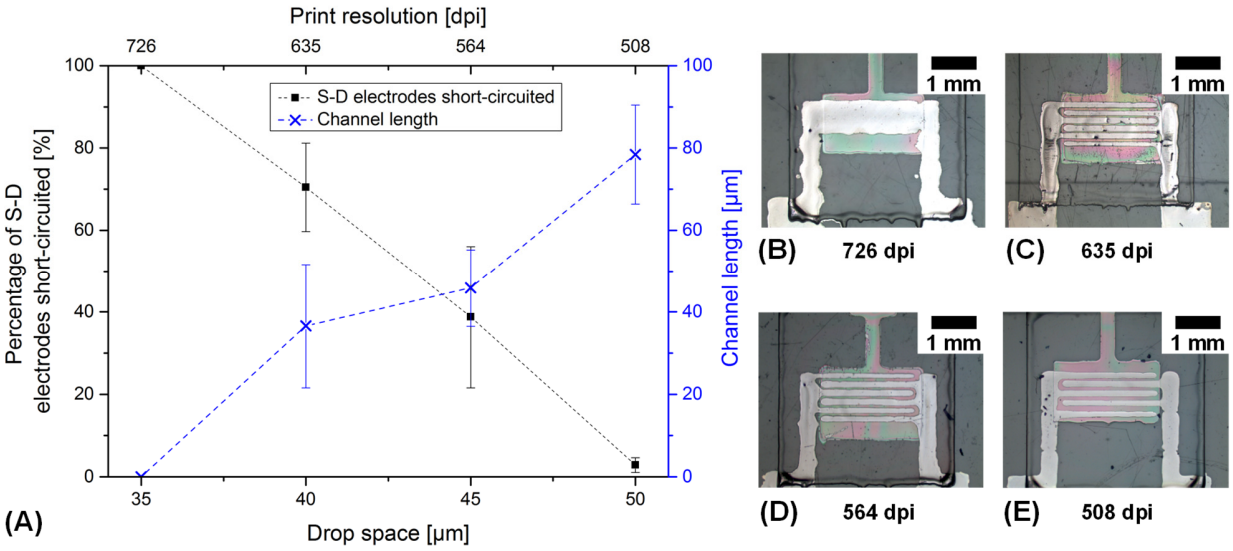

Figure 54: (A) percentage of S-D electrodes short-circuited and measured channel length as a function of print resolution; (B)-(E) are microscopic images of the TFT S-D electrodes for each print resolution considered in the graph (A) (adapted from [176])

The yield of the inkjet-printed S-D electrodes does not depend only on the print resolution, but also on their size represented by the ratio of channel width W to channel length L (W/L).[176] Each of the manufactured TFT arrays consists of TFTs with seven different sizes due to a variation of W. For this investigation, L was kept constant at about 80 µm since the S-D electrodes were deposited with a print resolution of 508 dpi.[176]

Figure 55A shows the percentage of functional (i.e., not short-circuited) S-D electrodes as a function of W/L and Figure 55B-H microscopic images of TFTs with the corresponding W/L.[176]

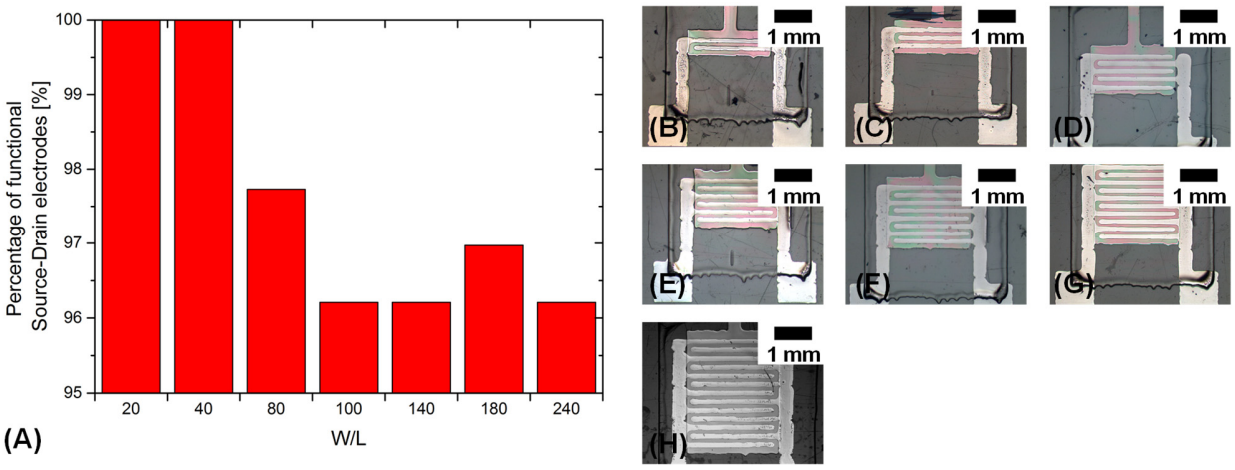

Figure 55: (A) percentage of functional S-D electrodes as a function of W/L (about 132 TFTs were considered per W/L); (B)-(H) are microscopic images showing the inkjet-printed layer stack of gate electrode, cPVP dielectric and S-D electrodes with varying W/L: (B) 20, (C) 40, (D) 80, (E) 100, (F) 140, (G) 180, (H) 240 (adapted from [176])

132 S-D electrodes were considered for each W/L ratio in this graph. The lower the size of the TFTs the, higher the manufacturing yield. One of the reasons for this trend is the increasing number of pixels, and therefore the increasing number of droplets with increasing W/L.[176] The higher the number of droplets, the higher the risk of creating short circuits, for instance, due to jet straightness/droplet placement accuracy or inhomogeneous cPVP layer behavior.[176] As shown in Figure 55A, 100 % of the S-D electrodes with a W/L of 20 and 40 were functional. Starting with a W/L of 80, the percentage of functional S-D decreases, but remains at a relatively high value of close to 98 %.[176]

The dielectric layer imparts the highest risk to obtain non-functional TFTs. Usually, about 10 % of the TFTs are short-circuited between the gate and the source and/or drain electrodes.[176] Thicker dielectric layers result in higher dielectric resistance, and thus in a lower probability of short circuits. Similar to the S-D electrodes, the dielectric layer was printed with different print resolutions (726 dpi, 635 dpi, 564 dpi, and 508 dpi). These print resolutions resulted in a layer thickness in the center area of approximately 950 nm, 760 nm, 570 nm, and 620 nm, respectively.[176] The leakage current for the highest layer thickness was in the range of 5 ± 2 nA and the lowest thickness results in about 27 ± 3 nA.[176] Thus, the leakage current is a function of print resolution, and subsequently, the leakage current is a function of layer thickness of the dielectric. It was found that the higher the W/L, the higher the probability of short circuits through the dielectric layer.[176]

The process yield for 924 all-inkjet-printed TFTs (print resolution of S-D electrodes was 508 dpi and for the dielectric 635 dpi) was determined and is shown as a function of W/L in Figure 56.[176]

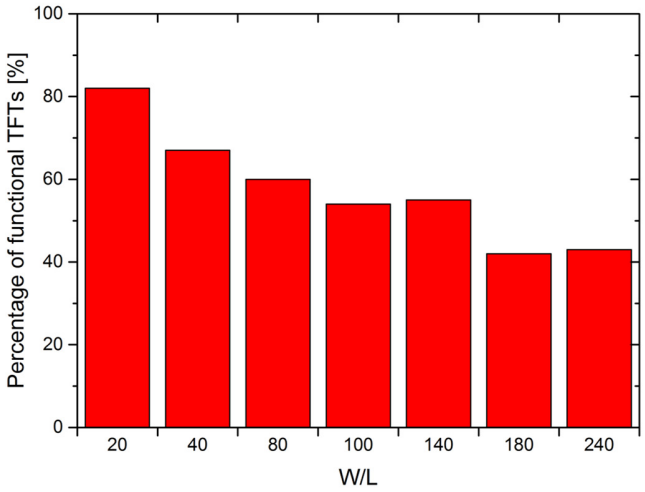

Figure 56: Yield of 924 all-inkjet-printed TFTs indicated by the percentage of functional TFTs as a function of W/L[176]

TFTs were classified as functional based on the following criteria: (i) no short circuits between S-D electrodes, (ii) no short circuits between gate and S-D electrodes (resistance > 1 GΩ), (iii) no open circuits in S-D layers (measurement of S-D current at -30 V; open circuit if current in the range of nano to pico ampere and no proportional to the resistance of the OSC), (iv) transfer curve of the TFTs have a monotonic behavior and a positive slope, and (v) ratio of I_{ON}/I_{OFF} > 20.[176,301] Obviously, the trend is quite similar to the data presented previously. The number of functional TFTs decreases with increasing W/L, because larger active areas imply a higher amount of deposited droplets with a higher risk of layer problems.[176,301]

The highest process yield for the developed all-inkjet-printing process in ambient conditions is about 82 % for the devices with a W/L ratio of 20.[176] Process yields > 90 % were obtained through further process optimization, such as simply printing the dielectric layer twice. This high yield is remarkable, taking into account that all TFTs were manufactured entirely by inkjet printing on flexible PEN substrates, on a relatively large area (DIN A4), and in ambient conditions without a cleanroom environment.[176]

Examples of defective TFTs having failures related to the printing process are depicted in Figure 57. They can be classified in five different failure categories: (i) wetting issues (Figure 57A-C), (ii) satellite droplets (Figure 57D-E), (iii) droplet jetting oddness (Figure 57F-G), (iv) dirt and dust particles (Figure 57H-I), and (v) missing droplets (Figure 57J-L).[301] The digital, idealized layout is depicted in the middle as a reference (see also Figure 15).

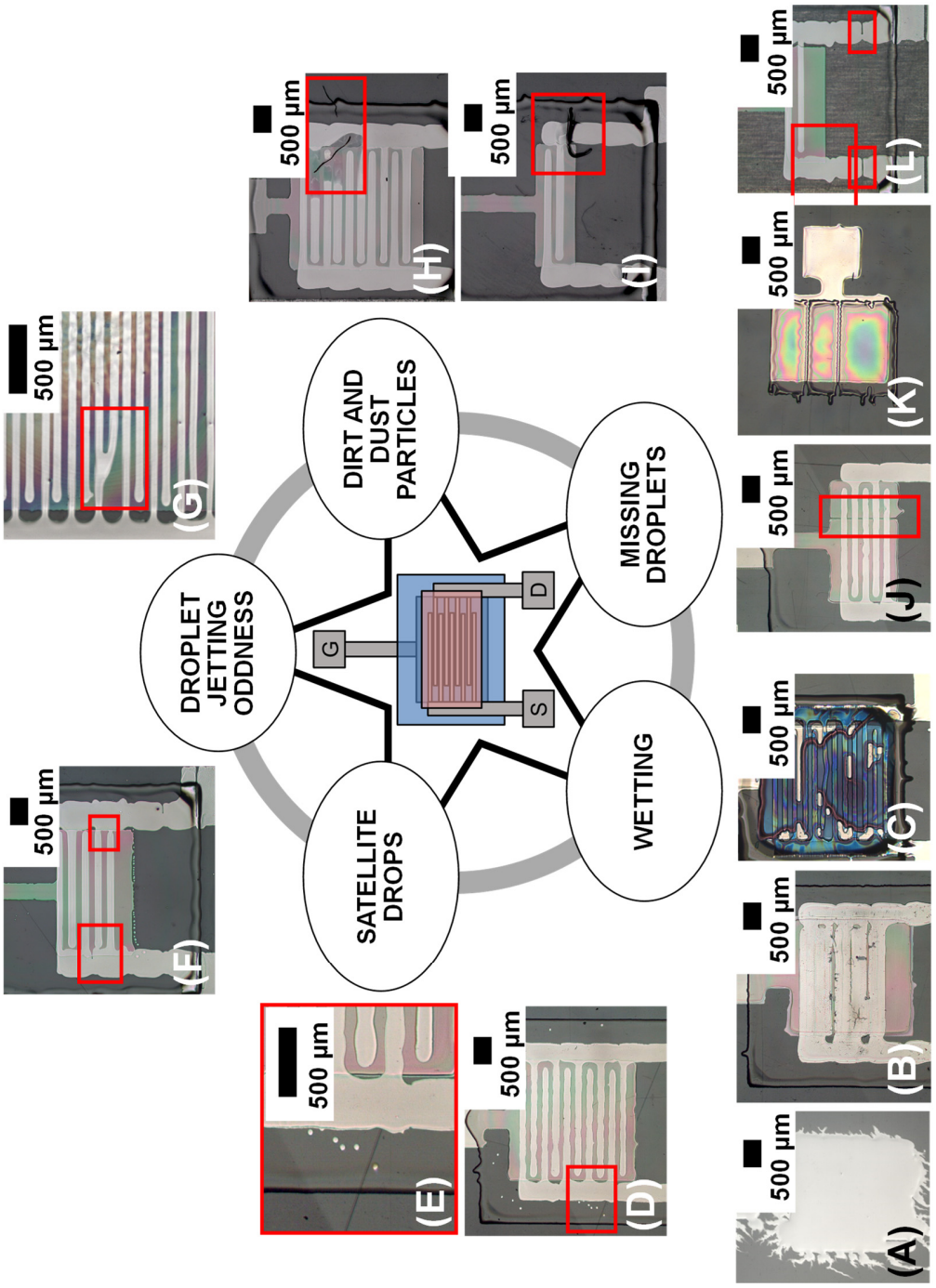

Figure 57: Overview of failures detected in inkjet-printed layers of the all-inkjet-printed TFTs; (A)-(C) are failures due to wetting properties of the deposited ink on the printed surface, (A) depicts a printed gate electrode with intense spreading on PEN, (B) shows intense ink spreading of the S-D electrodes on cPVP resulting in a short-circuit and (C) depicts inhomogeneous layer formation of the OSC due to the surface energy contrast between cPVP layer and S-D silver electrodes; (D) shows satellite droplets of silver ink and (E) is a magnification of the marked area in (D); (F) and (G) represent short-circuited S-D electrodes due to odd droplet jetting; (H) is an example of a short circuit between S-D and (F) between drain and gate electrode due to dirt and dust particles; (J) and (L) present TFTs with an open circuit due to missing droplets in the gate and the S-D layer, and (K) shows the dielectric layer with missing lines due to inkjet nozzle clogging (adapted from [301])

Wetting issues can appear for all the layers of the TFT. However, they are most critical for the S-D electrodes. Wetting issues of the silver ink on the dielectric layer can cause an intense spreading of the S-D electrodes and a short circuit, as shown in Figure 57B.[301] The reason is largely due to the interaction of the surface energy of the cPVP layer and the surface tension of the silver ink. Of course, wetting problems can also appear for the gate electrode and the OSC layer.[301]

Some of the printed silver gate electrodes have intense, irregular lateral spreading, as shown in Figure 57A. The reason might be a locally high hydrophilicity of the substrate attracting the highly polar silver ink – for instance, due to electrostatic charging.[301] Figure 57C shows dewetting of the OSC due to the surface energy contrast between S-D silver electrodes and the dielectric cPVP. This results in a non-continuous layer formation.[301]

I also found several TFTs that were classified as functional, but have satellite droplets close to the printed pattern. The satellites appeared mostly for the silver ink, as shown in Figure 57D-E. These occasionally generated extra droplets can have a negative impact on the printed layers by, for example, forming short circuits between the S-D electrodes.[301] However, there was rarely any influence of the satellite drops on the functionality or performance of the TFTs, since the satellites were mostly located outside the active area.[301]

Droplet jetting irregularity, also called droplet jetting oddness, is another issue in inkjet printing resulting in droplet placement errors that can cause short circuits as shown in Figure 57F-G.[301] The short circuits can appear directly between the S-D finger electrodes or at the electrode busbars, depending on the direction of the jetting oddness.[301] Droplet jetting oddness resulting in droplet placement errors is one of the main reasons for the short circuits. A droplet trajectory orthogonal to the nozzle plate is preferred in inkjet printing, typically within a 0.6 ° accuracy[31]. However, the 0.6 ° angle accuracy strongly depends on the printhead as well on the interplay between printhead and ink, and is usually according to my experience difficult to obtain in printed electronics.[301] Droplet jetting oddness can be caused, for instance, by air bubbles or particle agglomeration in the ink, or material build-ups of the ink on the nozzle plate or at the nozzle orifice, causing unstable droplet break-off.[301] Other influencing factors for jetting oddness are electrostatic charges or aerodynamic effects, such as soft draughts resulting from the movement of the printhead, the movement of the droplets or from the exhaust system, or printhead defects/nozzle failures in general.[15,301] Based on observations with the drop-watcher, it was found that the silver ink was mostly affected by jetting oddness – although new printheads were used for its deposition. An example of intense jetting oddness is shown in Figure 58. The dotted blue lines indicate the droplet trajectory, the red lines the optimal droplet trajectory orthogonally to the nozzle orifice, and the green lines different vertical positions. The distance between the nozzle and the substrate is usually about 1 mm and indicated with the solid green lines. For the given example, the jetting

oddness causes in the worst case a droplet displacement > 100 µm. Taking into account the dimensions of the TFTs (e.g., the S-D electrodes), a placement error of 100 µm will most probably cause a short circuit as shown in Figure 57F-G. Thus, a lot of efforts were focused on the optimization of the jetting behavior by, for instance, frequent application of cleaning cycles, filtering and degassing of the inks, priming of the printheads, etc.

Inkjet printing was performed in a standard laboratory in ambient conditions without a high level of cleanliness.[301] The handling of the substrate and the printed samples, such as positioning in the printer, or removal of the substrate after the ink deposition and its transportation to the oven under a change of the laboratory, was also carried out in a standard laboratory environment without facilities for improved cleanliness. Dirt and dust particles were recognized frequently on the PEN substrate.[301] These particles in the µm range were found to be an important reason for short circuits between the S-D electrodes as shown in Figure 57H.[301] Here, a fiber-like dirt particle connects S-D due to the intense coalescence of silver ink along the particle. Particles can also short circuit the gate electrode with the S-D electrodes as it is shown in in Figure 57I.[301]

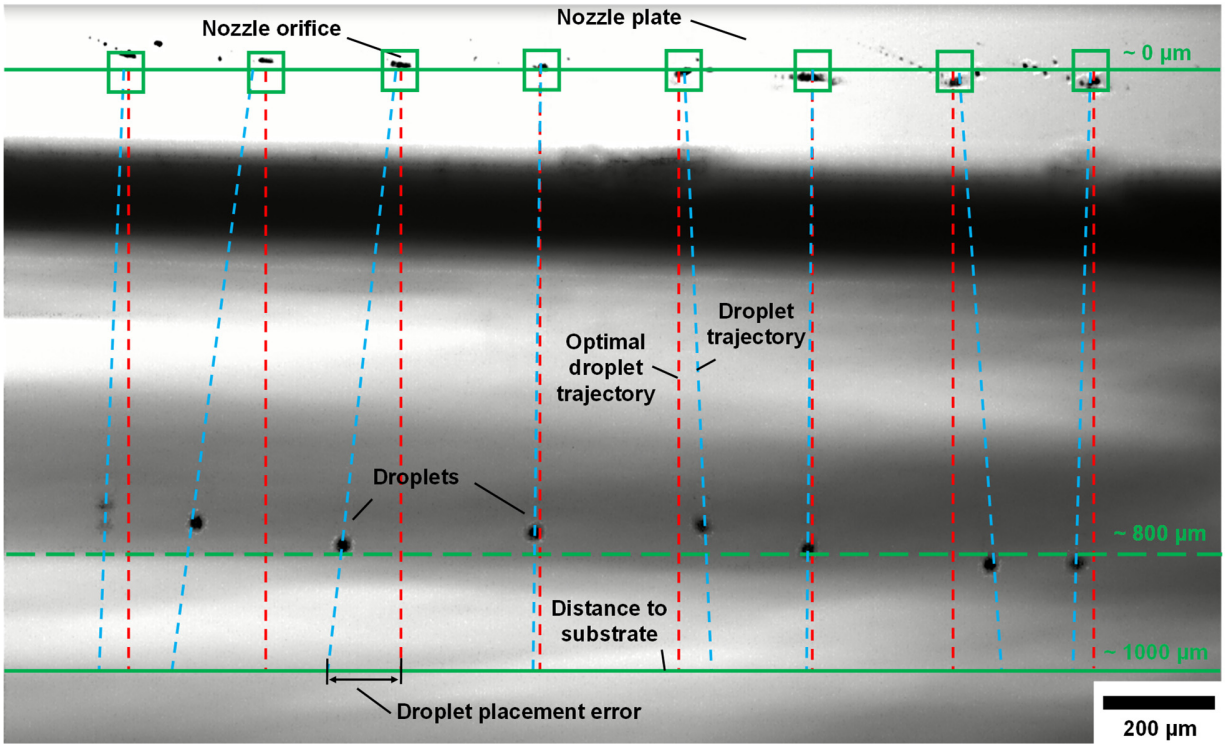

Figure 58: Example of jetting oddness of Sun Chemical EMD5603 using a D128/10 DPN printhead in the DMP 3000, the image was obtained with the build-in drop-watcher camera, the colored lines were added to make the different droplet trajectories and distances more clear

However, the most prominent device failures appeared to be due to missing droplets.[301] Usually, simple nozzle clogging due to solvent evaporation causes a complete breakdown of the jetting,

and thus results in missing droplets on the substrate.[301] There could be many further reasons, such as air bubbles in the ink, which promote missing droplets. Figure 57J shows a missing line in a printed gate electrode, and Figure 57L a TFT with missing lines in the S-D electrode contact pads.[301] Both result in open circuits. The missing lines appeared most frequently for the electrode layers. For only a few devices, missing lines appeared in the dielectric layer causing a short circuit.[301] It is much more difficult to identify missing droplets by one or more nozzles appearing irregularly somewhere in the printed layer. No missing lines can be observed in these cases, but the layer thickness could vary laterally.[301] For the dielectric layer, a low thickness due to missing droplets causes a high probability of pinholes, and ultimately results in low dielectric resistance, high gate leakage currents under device operation, or even short circuits between the gate and source or/and drain electrodes.[301]

The local distribution of different failures of the all-inkjet-printed TFTs on the DIN A4 substrate was investigated. The following failures were considered:

- Short circuits of S-D electrodes
- Short circuits of gate and source and/or drain electrodes
- Open circuits in the S-D electrodes
- High leakage current through the dielectric

The first three failures are caused by physically defective regions. These failures are usually clearly related to the printing process. They are caused by, for instance, missing nozzles, wetting issues of the ink, dirt and dust particles, and other environmental impacts as previously explained.[301] High leakage current can be caused as well by a physically defective region. However, this defect can be also be described as an operational instability of the TFT.[301] Tunneling currents or soft-dielectric breakdowns across thinner or structural defective dielectric regions lead to leakage currents.[301] The currents leaking through the dielectric layer might be tolerable to a certain extent, and do not result into a total device failure.[301] The leakage current is determined by the measurement of the gate leakage current from the transfer characteristics. The current between gate-drain at a voltage of -30 V is compared to the current between S-D electrodes at the same voltage.[301] If the gate-drain current is higher than the S-D current, the TFT is classified into the high leakage current category, and thus marked as defective. Short circuits appear due to electrical contact between any of the electrodes.[301] This defect is detected by measuring the current between the S-D and gate and the source and/or drain electrodes under a fixed bias of - 10 V.[301] If the measured current exceeds 10 mA, the TFT is classified into the short circuit category and thus marked as defective. Open circuits are defined by measuring the S-D current from the transfer characteristics, similar to the procedure for leakage currents but instead using a

voltage of -30 V.[301] TFTs with currents in the range of nano- to pico ampere are classified into the open circuit category.[301]

Figure 59A shows the distribution of the mentioned defects for 942 TFTs in a position map. The basis of the map is an optical scan using a standard flat-bed office scanner of the DIN A4 substrate with all the inkjet-printed TFTs.[301] Thus, the printed silver layers appear dark-green to black due to the high reflectance of their surface. Next to the TFTs, small test areas, alignment marks, and other test patterns, as well as an indication of the print origin and the printing direction, are shown in Figure 59A.[301] The scan also makes it possible to identify the spatial uniform size distribution of TFTs within the six arrays that are marked with frames and grids, which have been laid on top of each of the arrays.[301]

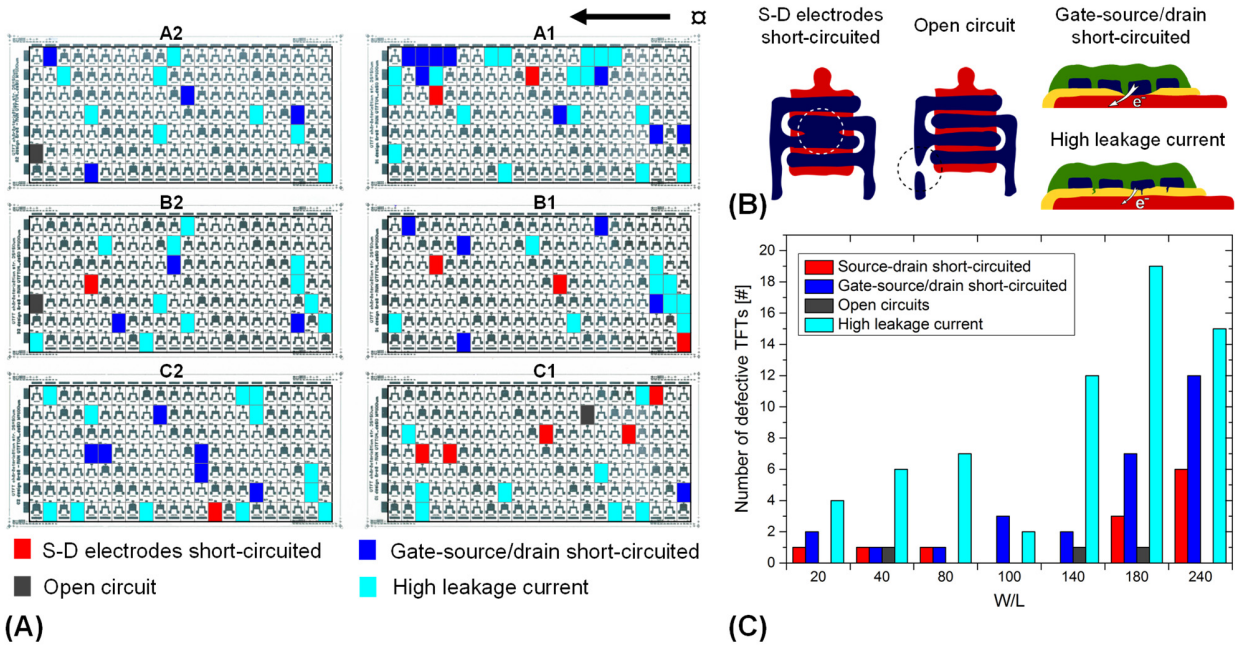

Figure 59: (A) position map of inkjet-printed TFTs; each color pixel represents the position of a defective TFT: the red pixels indicate TFTs with S-D short circuits, the blue pixels TFTs with gate-source and/or drain short circuits, grey pixels open circuits and cyan pixels high leakage currents through the dielectric; (B)[q] is a schematic of the different defects under consideration, and (C) is a histogram based on the position map showing the number of defective TFTs as a function of W/L (adapted from [301])

Based on the grids, the defective TFTs can be marked by coloration of the respective pixel in the grid. Thus, a colored pixel represents the position of a defective TFT. Here, pixels that are marked

[q] The schemes in Figure 59B were prepared by Carme Martinez-Domingo from the Department of Integrated Circuits and Systems (ICAS) at the Institute de Microelectronica de Barcelona IMB-CNM (CSIC) (head of the department: Prof. Dr. Lluis Teres, director: Prof. Dr. Carles Cane) in the frame of the preparation of a joint manuscript for publication.

red represent TFTs that have short-circuited S-D electrodes, blue pixels represent TFTs with short-circuited gate-source/drain electrodes, grey pixels are TFTs with open circuits, and cyan pixels are TFTs with high leakage currents.[301]

Obviously, the arrays A1, B1 and C1 are more affected than the areas A2, B2 and C2.[301] In addition, most of the failures appear in A1. Several DIN A4 substrates using the same TFT design, as well as other TFT designs, were manufactured using similar printing parameters to confirm this behavior. I found that the trend is highly reproducible and similar every time.[301] Most of the failures are located in A1, B1 and C1, each time. In the arrays A1, B1 and C1, the printing process starts moving to A2, B2 and C2, and finally moving back and restarting. Thus, A1, B1 and C1 represent the parts that are printed first (before A2, B2 and C2) after a longer period of non-jetting when the printhead is moving back from the end of the substrate to the starting point. This period of non-jetting causes instabilities in the droplet formation process. Some of the droplets are not formed at all, or are not formed properly.[301]

Volatile ink components will start to evaporate at the nozzle orifice during the non-jetting period. The evaporation process will be supported by the heated substrate table, causing an increased evaporation rate.[301] This can result in an increase of viscosity and a difference in surface tension at the nozzle orifice and its close proximity. However, the energy level of the acoustic pressure waves generated by the piezoelectric transducer of the inkjet printhead that is required for drop ejection strongly depends on the viscosity of the fluid.[301]

The higher the viscosity of the fluid, the higher the energy required to eject a droplet.[301] Therefore, a higher driving amplitude of the waveform is usually applied to the piezoelectric printhead if inks with higher viscosities are used.[301] Since the maximum driving amplitude of the jetting waveform remains constant during the deposition process, the generated acoustic pressure waves might be not be powerful enough to eject the droplets, due to the increasing viscosity of the ink at the nozzle orifice when the printhead returns to the idle state at the printing start position.[301] Nanoparticles will undergo agglomeration during the evaporation of the solvent. That is why the application of nanoparticles in the ink formulation, such as silver nanoparticles, additionally contributes to nozzle failures. The evaporating solvent causes material buildup in the printhead, especially at the nozzle orifice and nozzle plate, negatively influencing the drop ejection.[301]

This phenomena is described in the literature as the “first drop problem”.[301] It has been well-known in the field of inkjet printing for many years and has already been addressed by several researchers in review articles or experimental studies[63,69,74,84,242,304–307]. The duration of an ink remaining idle at the nozzle orifice of a printhead before droplet ejection is no longer possible is termed as latency[14]. It has been reported that even for short non-jetting periods of about 1 s a droplet speed degradation and thus a negative influence on droplet jetting can occur for water-

based ink formulations.[15] The first ejected droplets of an inkjet deposition sequence were in detail investigated by Famili et al.[306] and Verkouteren et al.[307]. They observed significant differences in terms of droplet shape and volume as well as droplet velocity and trajectory for the first ejected droplets compared to those droplets that follow later in the sequence.[301] Besides evaporation effects at the nozzle orifice or on the nozzle plate, acoustic and fluid resonances causing acoustic instability[306,307] in the printhead can contribute to the first drop problem.[301] Thus, according to the literature the first drop problem is a result of a combination of different effects.[301] For graphic inkjet applications, the first drop problem has been reduced to a minimum nowadays. The inks are usually ready to be printed at all times in high quality.[301] The printheads, inks, waveforms applied in jetting and idle state, and cleaning procedures are perfectly coordinated with each other and standardized as a result of many years of development and optimization works by several companies.[301] However, in the field of functional inkjet printing and especially in the field of printed electronics, these components and parameters need still to be harmonized, because they are usually not intentionally designed for each other.[301] Printhead manufacturers very recently developed printheads designed specifically for applications in the field of printed functionalities.[2] Most functional fluids for printed electronics are still under development and are quite complex, for instance, due to their chemical and rheological properties combined with functional nanoparticle ingredients.[301] Many of the ink manufacturers aim for high functional performance of the layer, such as high conductivity for metal inks. However, reliable jettability with long-term stability should also be a future focus of the ink manufacturers.[301]

The histogram in Figure 59C shows the defective TFTs as a function of the TFT size given by W/L. As shown before (see Figure 56), TFTs with larger W/L are more frequently affected by defects than TFTs with smaller W/L.[301] The probability of defects increases with the size of the TFT, because larger TFTs have (i) a higher number of finger electrodes, which increases the risk of a short circuit between them, and have (ii) larger overlapping electrode areas that should be separated by the dielectric, increasing the risk of short circuits through the dielectric.[301] Overall, the number of devices with short circuits, open circuits and high leakage current is reasonably low and other failures related to the operational performance dominate. These failures are not the scope of this thesis, but are reported in detail in reference [301].

(Parts of this chapter are published in reference [176] and reference [301])

7 Summary and conclusion

Inkjet printing technology evolved from a technology initially geared towards simple one-color coding and marking to a worldwide consumer market technology, and ultimately to an industrial graphic and functional printing technology for the deposition of versatile materials for various fields of applications.

This thesis addressed functional inkjet printing based on two focus topics: (i) inkjet printing of colloidal suspensions to study the fundamental principles of deposit formation and to develop deposits with photonic properties, and (ii) the development of a reliable manufacturing process for TFTs highlighting the importance of materials and inks, prepress (digital print pattern layout preparation), and the interplay between ink, substrate and printing conditions.

This thesis emphasized an alternative understanding of functional inkjet printing based on the bottom-up manufacturing approach and evaporation-driven self-assembly – generally termed evaporation-driven material transportation. The work presented within this thesis demonstrates the value of approaching functional inkjet printing from the perspective of evaporation-driven self-assembly. The interplay between substrate, ink and inkjet process was highlighted, and printed deposits of different materials were studied to explain the processes leading to their formation. It was demonstrated that evaporation-driven self-assembly processes and evaporation-driven material transportation in general are inherent phenomena in inkjet printing, and that they determine the pattern and structure formation of the printed deposits.

Inkjet printing of colloidal nanospheres

Colloidal suspensions were applied as a model ink to study the layer formation processes of inkjet-printed deposits on non-absorbent substrates. It was found that desired droplet deposit morphologies can be obtained, for instance, deposits with a coffee-ring shape, highly ordered monolayer deposits with close-packed colloidal arrays, randomly arranged particles, multilayer stacks, and even SCAs. Is was demonstrated that inkjet printing can lead to micro- and nanoscopically engineered morphologies of deposited layers.

The presented findings highlight the importance of a tuned interaction between ink, ink ingredients and inkjet printing process parameters, such as the waveform applied to the piezoelectric printhead, or specific process conditions, such as the orientation angle of the print pattern layout related to the printing process.

The control signal for the piezoelectric printhead was found to be one of most important parameters influencing the final morphology of the printed deposits. Based on sophisticated control signals, SCAs were successfully and reliably manufactured. Thus, the thesis demonstrates a novel and alternative process for the manufacturing of SCAs. The manufacturing process is based on inkjet printing, and turned out to be highly productive as well as applicable for other nanomaterials and potentially different particle shapes. SCAs can be assembled “ready-to-use” in dry environments and ambient conditions within seconds. In contrast to other methods, the developed approach is completely independent of the surface properties, and does not require pretreated substrates or ordinarily essential subsequent processes (e.g., demulsification or liquid elimination). The formation of the SCAs takes place in flight. As a consequence, the particular wettability and surface morphology of the substrate does not influence the formation mechanism of the SCAs.

Based on the developed method, finite, ordered SCAs were manufactured in a reproducible manner with variable diameters, and thus different number of constituents, using both SiO_2 and PS nanospheres. The SCAs exhibit a well-ordered packing of nanospheres which qualifies for photonic properties. I could confirm the theoretical stop bands by performing microreflectance measurements of the SCAs. The size of the nanospheres and their periodical arrangement, which was mainly caused by the evaporation-driven self-assembly process, are compatible for future photonic applications in optoelectronics, photovoltaics, and sensors, as well for biomedical applications and microfluidics.

Inkjet printing of TFTs: Process development and process reliability

This thesis describes the successful development of a deposition process for the manufacturing of TFTs based entirely on inkjet printing. For the first time, industrial relevant printheads were applied for the manufacturing process. The amount of printed devices and their analysis based on the developed and up-scaled process is an important achievement, and allowed the investigation of process yields and origins of device failures, as well as to perform a statistical analysis.

The influence of different parameters such as the print layout design, the selected inks and printing process settings on the morphology and/or performance of the printed functional layers was demonstrated. The importance of the orientation angle of the print pattern layout related to the deposition process was introduced. Geometrical as well as functional variations were found as a function of the orientation angle. This finding is a basic contribution not reported before in the literature, and will allow design and printing engineers to deposit desired, optimized and arbitrarily shaped, complex pattern features for the field of functional printing such as printed electronics. I was introducing different examples to demonstrate that the discrete droplet-by-droplet nature of

the inkjet printing process imposes challenges in the control of printed patterns. As a result, designing devices for inkjet-printed electronics requires a detailed understanding of the process and all parameters that influence morphological or functional characteristics of the deposits, such as the selection of appropriate materials.

The future application of inkjet printing technology for the manufacturing of electronics has great potential. This thesis demonstrated the successful development of a batch to batch process based on inkjet printing for TFTs. All printing processes were performed in ambient conditions, and flexible polymers were applied as substrates. Finally, it was demonstrated that the technology is able to obtain quite high manufacturing yields (> 90 % for TFTs with low W/L ratio).

The important role of evaporation-driven material transportation within the liquid deposits was presented, for instance for the electrode layer and for the dielectric layer of the TFTs. The electrical and morphological analysis of the TFTs revealed several device failures, which arise from the manufacturing process itself, or from the materials used. Different origins for these failures, mainly related to the inkjet printing process, were introduced and discussed in detail. This will allow for the optimization of the process in the future in order to obtain even higher manufacturing yields.

References

1. Gilboa, R. I. The Functional & Industry Printing Opportunity. *InfoTrends* (2014). at <http://www.infotrends.com/public/Content/Services/FIPS/fips.html>
2. Xaar plc. Xaar 1003 AMp. *Manuf. Prod. Website* (2016). at <http://www.xaar.com/en/products/xaar-1003amp>
3. Ceradrop. Ceradrop - Our products. *Manuf. Prod. Website* (2016). at <http://www.ceradrop.com/en/our-products/>
4. Notion Systems GmbH. Notion Systems GmbH - Inkjet. *Manuf. Prod. Website* (2016). at <http://www.notion-systems.com/inkjet.html>
5. Cruickshank, C. Ardeje launches OriginD100 digital printing platform. *OSA-Direct Newsl.* (2015). at <http://www.osadirect.com/news/article/1522/ardeje-launches-origind100-digital-printing-platform/>
6. Burgués-Ceballos, I., Stella, M., Lacharmoise, P. & Martínez-Ferrero, E. Towards industrialization of polymer solar cells: material processing for upscaling. *J. Mater. Chem. A* **2,** 17711–17722 (2014).
7. van Dam, D. B. & Le Clerc, C. Experimental study of the impact of an ink-jet printed droplet on a solid substrate. *Phys. Fluids* **16,** 3403–3414 (2004).
8. Yarin, A. L. DROP IMPACT DYNAMICS: Splashing, Spreading, Receding, Bouncing…. *Annu. Rev. Fluid Mech.* **38,** 159–192 (2006).
9. Rioboo, R., Marengo, M. & Tropea, C. Time evolution of liquid drop impact onto solid, dry surfaces. *Exp. Fluids* **33,** 112–124 (2002).
10. Bonn, D., Eggers, J., Indekeu, J. & Meunier, J. Wetting and spreading. *Rev. Mod. Phys.* **81,** 739–805 (2009).
11. Shi, J., Schuman, T. P. & Stoffer, O. Ink-jet printing paper with improved waterfastness. *J. Coatings Technol. Res.* **1,** 225–234 (2004).
12. Varela, F., Armendáriz, E. & Wolluschek, C. Inkjet printed electronics: The wet on wet approach. *Chem. Eng. Process. Process Intensif.* **50,** 589–591 (2011).
13. Derby, B. Inkjet Printing of Functional and Structural Materials: Fluid Property Requirements, Feature Stability, and Resolution. *Annu. Rev. Mater. Res.* **40,** 395–414 (2010).
14. *The Chemistry of Inkjet Inks*. (World Scientific Publishing Co. Pte. Ltd., 2009). doi:10.1142/9789812818225
15. *Fundamentals of Inkjet Printing*. (Wiley-VCH Verlag GmbH & Co. KGaA, 2016).

doi:10.1002/9783527684724

16. *Handbook of Print Media*. *Handb. Print Media* (Springer Berlin Heidelberg, 2001). doi:10.1007/978-3-540-29900-4
17. Canon. *Canon Pixma iP4700 Datasheet*. (2014). at <https://www.canon-europe.com/images/PIXMA iP4700_Specifications Sheet_tcm13-672710.pdf>
18. Eastman Kodak. *Kodak Prosper S30 Imprinting System Datasheet*. (2012). at <http://graphics.kodak.de/KodakGCG/uploadedFiles/Products/Printers_and_Presses/High_Volume_Inkjet/PROSPER/PROSPER_S_SERIES/S30/Tab_Contents/ProsperS30_SellSheet_US_Mar2012_Lo.pdf>
19. Eastman Kodak. *Kodak Prosper 6000P Press Datasheet*. (2014). at <http://graphics.kodak.com/KodakGCG/uploadedFiles/Products/Printers_and_Presses/High_Volume_Inkjet/Prosper/PROSPER_PRESS/6000/6000P Press Datasheet.pdf>
20. Romano, F. J. *Inkjet!: History, Technology, Markets, and Applications, Volume 1*. (Digital printing Council, PIA/GATFPress, 2008).
21. Cahill, V. Introduction to Digital Printing Technology. *SGIA J.* **2,** 1–11 (1998).
22. Pond, S. F. *Inkjet technology and product development strategies*. (Torrey Pines Research, 2000).
23. Subramanian, V., Cen, J., de la Fuente Vornbrock, A., Grau, G., Kang, H., Kitsomboonloha, R., Soltman, D. & Tseng, H.-Y. High-Speed Printing of Transistors: From Inks to Devices. *Proc. IEEE* **103,** 567–582 (2015).
24. Castrejon-Pita, J. R., Baxter, W. R. S., Morgan, J., Temple, S., Martin, G. D. & Hutchings, I. M. Future, Opportunities and Challenges of Inkjet Technologies. *At. Sprays* **23,** 541–565 (2013).
25. Le, H. P. Progress and trends in ink-jet printing technology. *J. Imaging Sci. Technol.* **42,** 49–62 (1998).
26. Hon, K. K. B., Li, L. & Hutchings, I. M. Direct writing technology-Advances and developments. *CIRP Ann. - Manuf. Technol.* **57,** 601–620 (2008).
27. Basaran, O. A., Gao, H. & Bhat, P. P. Nonstandard Inkjets. *Annu. Rev. Fluid Mech.* **45,** 85–113 (2013).
28. Onses, M. S., Sutanto, E., Ferreira, P. M., Alleyne, A. G. & Rogers, J. A. Printing: Mechanisms, Capabilities, and Applications of High-Resolution Electrohydrodynamic Jet Printing. *Small* **11,** 4412–4412 (2015).
29. Raje, P. V. & Murmu, N. C. A Review on Electrohydrodynamic-inkjet Printing Technology. *Int. J. Emerg. Technol. Adv. Eng.* **4,** 174–183 (2014).
30. Bogy, D. B. & Talke, F. E. Experimental and Theoretical Study of Wave Propagation

Phenomena in Drop-on-Demand Ink Jet Devices. *IBM J. Res. Dev.* **28,** 314–321 (1984).

31. Wijshoff, H. The dynamics of the piezo inkjet printhead operation☆. *Phys. Rep.* **491,** 77–177 (2010).
32. Kim, B.-H., Kim, S.-I., Lee, J.-C., Shin, S.-J. & Kim, S.-J. Dynamic characteristics of a piezoelectric driven inkjet printhead fabricated using MEMS technology. *Sensors Actuators A Phys.* **173,** 244–253 (2012).
33. Chen, A. U. & Basaran, O. A. A new method for significantly reducing drop radius without reducing nozzle radius in drop-on-demand drop production. *Phys. Fluids* **14,** 18–22 (2002).
34. Gan, H. Y., Shan, X., Eriksson, T., Lok, B. K. & Lam, Y. C. Reduction of droplet volume by controlling actuating waveforms in inkjet printing for micro-pattern formation. *J. Micromechanics Microengineering* **19,** 55010 (2009).
35. Brünahl, J. & Grishin, A. M. Piezoelectric shear mode drop-on-demand inkjet actuator. *Sensors Actuators A Phys.* **101,** 371–382 (2002).
36. Kim, B.-H., Kim, T.-G., Lee, T.-K., Kim, S., Shin, S.-J., Kim, S.-J. & Lee, S.-J. Effects of trapped air bubbles on frequency responses of the piezo-driven inkjet printheads and visualization of the bubbles using synchrotron X-ray. *Sensors Actuators A Phys.* **154,** 132–139 (2009).
37. Kwon, K.-S. & Kim, W. A waveform design method for high-speed inkjet printing based on self-sensing measurement. *Sensors Actuators A Phys.* **140,** 75–83 (2007).
38. Herran, C. L. & Huang, Y. Alginate microsphere fabrication using bipolar wave-based drop-on-demand jetting. *J. Manuf. Process.* **14,** 98–106 (2012).
39. Wu, C.-H. & Hwang, W.-S. The effect of the echo-time of a bipolar pulse waveform on molten metallic droplet formation by squeeze mode piezoelectric inkjet printing. *Microelectron. Reliab.* **55,** 630–636 (2015).
40. Khalate, A. a., Bombois, X., Babuška, R., Wijshoff, H. & Waarsing, R. Performance improvement of a drop-on-demand inkjet printhead using an optimization-based feedforward control method. *Control Eng. Pract.* **19,** 771–781 (2011).
41. Kamphoefner, F. J. Ink jet printing. *IEEE Trans. Electron Devices* **19,** 584–593 (1972).
42. Keur, R. I. & Stone, J. J. Some Effects of Fluid Jet Dynamics on Ink Jet Printing. *IEEE Trans. Ind. Appl.* **IA-12,** 86–90 (1976).
43. Carnahan, R. D. & Hou, S. L. Ink Jet Technology. *IEEE Trans. Ind. Appl.* **IA-13,** 95–104 (1977).
44. Keeling, M. R. Ink jet printing. *Phys. Technol.* **12,** 196–203 (1981).
45. Lee, F. C., Mills, R. N. & Talke, F. E. The Application of Drop-on-Demand Ink Jet Technology to Color Printing. *IBM J. Res. Dev.* **28,** 307–313 (1984).

46. Heinzl, J. & Hertz, C. H. in *Adv. Electron. Electron Phys.* **65,** 91–171 (Elsevier, 1985).
47. Haysom, P. Improvements in ink-jet technology. *Data Process.* **27,** 31–33 (1985).
48. Nielsen, N. J. History of ThinkJet printhead development. *Hewlett Packard J.* **36,** 4–10 (1985).
49. Katen, C. V. & Braun, T. R. An inexpensive, portable ink-jet printer family. *Hewlett Packard J.* **36,** 11–20 (1985).
50. Bhaskar, E. V. & Aden, J. S. Development of the thin-film structure for the ThinkJet printhead. *Hewlett Packard J.* **36,** 27–33 (1985).
51. Allen, R. R. Thermodynamics and hydrodynamics of thermal ink jets. *Hewlett Packard J.* **36,** 21–27 (1985).
52. Teng, K. & Vest, R. Liquid Ink Jet Printing with MOD Inks for Hybrid Microcircuits. *IEEE Trans. Components, Hybrids, Manuf. Technol.* **10,** 545–549 (1987).
53. Teng, K. F. & Vest, R. W. Application of ink jet technology on photovoltaic metallization. *IEEE Electron Device Lett.* **9,** 591–593 (1988).
54. Teng, K. F. & Vest, R. W. A microprocessor-controlled ink jet printing system for electronic circuits. *IEEE Trans. Ind. Electron.* **35,** 407–412 (1988).
55. Kimura, J., Kawana, Y. & Kuriyama, T. An immobilized enzyme membrane fabrication method using an ink jet nozzle. *Biosensors* **4,** 41–52 (1989).
56. Lee, F. C. PZT printing applications, technologies, new devices. in *IEEE 1988 Ultrason. Symp. Proceedings.* 693–697 (IEEE, 1988). doi:10.1109/ULTSYM.1988.49467
57. Wehl, W. R. Ink-jet printing: the present state of the art. in *Proceedings. VLSI Comput. Peripher. COMPEURO 89* **1992,** 2/46-2/52 (IEEE Comput. Soc. Press, 1989).
58. Croucher, M. D. & Hair, M. L. Design criteria and future directions in ink-jet ink technology. *Ind. Eng. Chem. Res.* **28,** 1712–1718 (1989).
59. Tang, H. K., Kuek, W. H., Gozali, R. & Liew, R. Ink jet printer pioneers and competitors. in *Proc. 2000 IEEE Int. Conf. Manag. Innov. Technol. ICMIT 2000. 'Management 21st Century' (Cat. No.00EX457)* **1,** 94–98 (IEEE, 2000).
60. Chen, P.-H., Chen, W.-C. & Chang, S.-H. Bubble growth and ink ejection process of a thermal ink jet printhead. *Int. J. Mech. Sci.* **39,** 683–695 (1997).
61. Peeters, E. & Verdonckt-Vandebroek, S. Thermal ink jet technology. *IEEE Circuits Devices Mag.* **13,** 19–23 (1997).
62. Lemmo, A. V, Rose, D. J. & Tisone, T. C. Inkjet dispensing technology: applications in drug discovery. *Curr. Opin. Biotechnol.* **9,** 615–617 (1998).
63. Calvert, P. Inkjet Printing for Materials and Devices. *Chem. Mater.* **13,** 3299–3305 (2001).
64. de Gans, B.-J. & Schubert, U. S. Inkjet Printing of Polymer Micro-Arrays and Libraries:

Instrumentation, Requirements, and Perspectives. *Macromol. Rapid Commun.* **24,** 659–666 (2003).

65. de Gans, B.-J., Duineveld, P. C. & Schubert, U. S. Inkjet Printing of Polymers: State of the Art and Future Developments. *Adv. Mater.* **16,** 203–213 (2004).
66. Boland, T., Xu, T., Damon, B. & Cui, X. Application of inkjet printing to tissue engineering. *Biotechnol. J.* **1,** 910–917 (2006).
67. Martin, G. D., Hoath, S. D. & Hutchings, I. M. Inkjet printing - the physics of manipulating liquid jets and drops. *J. Phys. Conf. Ser.* **105,** 12001 (2008).
68. Zhang, Y., Liu, C. & Whalley, D. Direct-write techniques for maskless production of microelectronics: A review of current state-of-the-art technologies. in *2009 Int. Conf. Electron. Packag. Technol. High Density Packag.* 497–503 (IEEE, 2009). doi:10.1109/ICEPT.2009.5270702
69. Yin, Z., Huang, Y., Bu, N., Wang, X. & Xiong, Y. Inkjet printing for flexible electronics: Materials, processes and equipments. *Chinese Sci. Bull.* **55,** 3383–3407 (2010).
70. Singh, M., Haverinen, H. M., Dhagat, P. & Jabbour, G. E. Inkjet Printing-Process and Its Applications. *Adv. Mater.* **22,** 673–685 (2010).
71. Zhu, X., Zheng, Q., Yang, H., Cai, J., Huang, L., Duan, Y., Xu, Z. & Cen, P. Recent advances in inkjet dispensing technologies: applications in drug discovery. *Expert Opin. Drug Discov.* **7,** 761–770 (2012).
72. Hutchings, I. M. & Martin, G. *Inkjet Technology for Digital Fabrication*. (John Wiley & Sons, Ltd, 2012). doi:10.1002/9781118452943
73. *Inkjet-Based Micromanufacturing*. (Wiley-VCH Verlag GmbH & Co. KGaA, 2012). doi:10.1002/9783527647101
74. Cummins, G. & Desmulliez, M. P. Y. Inkjet printing of conductive materials: a review. *Circuit World* **38,** 193–213 (2012).
75. Vaezi, M., Seitz, H. & Yang, S. A review on 3D micro-additive manufacturing technologies. *Int. J. Adv. Manuf. Technol.* **67,** 1721–1754 (2013).
76. Kang, B., Lee, W. H. & Cho, K. Recent advances in organic transistor printing processes. *ACS Appl. Mater. Interfaces* **5,** 2302–2315 (2013).
77. Komuro, N., Takaki, S., Suzuki, K. & Citterio, D. Inkjet printed (bio)chemical sensing devices. *Anal. Bioanal. Chem.* **405,** 5785–5805 (2013).
78. Saunders, R. E. & Derby, B. Inkjet printing biomaterials for tissue engineering: bioprinting. *Int. Mater. Rev.* **59,** 430–448 (2014).
79. Seol, Y.-J., Kang, H.-W., Lee, S. J., Atala, A. & Yoo, J. J. Bioprinting technology and its applications. *Eur. J. Cardio-Thoracic Surg.* **46,** 342–348 (2014).

80. Dias, A. D., Kingsley, D. M. & Corr, D. T. Recent advances in bioprinting and applications for biosensing. *Biosensors* **4,** 111–136 (2014).
81. Murphy, S. V & Atala, A. 3D bioprinting of tissues and organs. *Nat. Biotechnol.* **32,** 773–785 (2014).
82. Kuang, M., Wang, L. & Song, Y. Controllable Printing Droplets for High-Resolution Patterns. *Adv. Mater.* **26,** 6950–6958 (2014).
83. Chen, S.-P., Chiu, H.-L., Wang, P.-H. & Liao, Y.-C. Inkjet Printed Conductive Tracks for Printed Electronics. *ECS J. Solid State Sci. Technol.* **4,** P3026–P3033 (2015).
84. Daly, R., Harrington, T. S., Martin, G. D. & Hutchings, I. M. Inkjet printing for pharmaceutics - A review of research and manufacturing. *Int. J. Pharm.* **494,** 554–567 (2015).
85. Ihalainen, P., Määttänen, A. & Sandler, N. Printing technologies for biomolecule and cell-based applications. *Int. J. Pharm.* **494,** 585–592 (2015).
86. Shirazi, S. F. S., Gharehkhani, S., Mehrali, M., Yarmand, H., Metselaar, H. S. C., Adib Kadri, N. & Osman, N. A. A. A review on powder-based additive manufacturing for tissue engineering: selective laser sintering and inkjet 3D printing. *Sci. Technol. Adv. Mater.* **16,** 33502 (2015).
87. Li, J., Rossignol, F. & Macdonald, J. Inkjet printing for biosensor fabrication: combining chemistry and technology for advanced manufacturing. *Lab Chip* **15,** 2538–2558 (2015).
88. Knowlton, S., Onal, S., Yu, C. H., Zhao, J. J. & Tasoglu, S. Bioprinting for cancer research. *Trends Biotechnol.* **33,** 504–513 (2015).
89. Yamada, K., Henares, T. G., Suzuki, K. & Citterio, D. Paper-Based Inkjet-Printed Microfluidic Analytical Devices. *Angew. Chemie Int. Ed.* **54,** 5294–5310 (2015).
90. Liu, X., Tarn, T.-J., Huang, F. & Fan, J. Recent advances in inkjet printing synthesis of functional metal oxides. *Particuology* **19,** 1–13 (2015).
91. Choi, H. W., Zhou, T., Singh, M. & Jabbour, G. E. Recent developments and directions in printed nanomaterials. *Nanoscale* **7,** 3338–3355 (2015).
92. Sun, J., Bao, B., He, M., Zhou, H. & Song, Y. Recent Advances in Controlling the Depositing Morphologies of Inkjet Droplets. *ACS Appl. Mater. Interfaces* **7,** 28086–28099 (2015).
93. Stüwe, D., Mager, D., Biro, D. & Korvink, J. G. Inkjet technology for crystalline silicon photovoltaics. *Adv. Mater.* **27,** 599–626 (2015).
94. Mattana, G. & Briand, D. Recent advances in printed sensors on foil. *Mater. Today* **19,** 88–99 (2016).
95. Sowade, E., Polomoshnov, M. & Baumann, R. R. The design challenge in printing devices and circuits: Influence of the orientation of print patterns in inkjet-printed electronics. *Org. Electron.* **37,** 428–438 (2016).

96. Seifert, T., Sowade, E., Roscher, F., Wiemer, M., Gessner, T. & Baumann, R. R. Additive Manufacturing Technologies Compared: Morphology of Deposits of Silver Ink Using Inkjet and Aerosol Jet Printing. *Ind. Eng. Chem. Res.* **54,** 769–779 (2015).
97. Belgardt, C., Sowade, E., Blaudeck, T., Baumgärtel, T., Graaf, H., von Borczyskowski, C. & Baumann, R. R. Inkjet printing as a tool for the patterned deposition of octadecylsiloxane monolayers on silicon oxide surfaces. *Phys. Chem. Chem. Phys.* **15,** 7494–504 (2013).
98. Sowade, E., Blaudeck, T. & Baumann, R. R. Inkjet Printing of Colloidal Nanospheres: Engineering the Evaporation-Driven Self-Assembly Process to Form Defined Layer Morphologies. *Nanoscale Res. Lett.* **10,** 362 (2015).
99. de Gans, B.-J. & Schubert, U. S. Inkjet Printing of Well-Defined Polymer Dots and Arrays. *Langmuir* **20,** 7789–7793 (2004).
100. Soltman, D. & Subramanian, V. Inkjet-Printed Line Morphologies and Temperature Control of the Coffee Ring Effect. *Langmuir* **24,** 2224–2231 (2008).
101. Lim, J. A., Lee, W. H., Kwak, D. & Cho, K. Evaporation-Induced Self-Organization of Inkjet-Printed Organic Semiconductors on Surface-Modified Dielectrics for High-Performance Organic Transistors. *Langmuir* **25,** 5404–5410 (2009).
102. Lee, M. W., Ryu, G. S., Lee, Y. U., Pearson, C., Petty, M. C. & Song, C. K. Control of droplet morphology for inkjet-printed TIPS-pentacene transistors. *Microelectron. Eng.* **95,** 1–4 (2012).
103. James, D. T., Kjellander, B. K. C., Smaal, W. T. T., Gelinck, G. H., Combe, C., McCulloch, I., Wilson, R., Burroughes, J. H., Bradley, D. D. C. & Kim, J.-S. Thin-Film Morphology of Inkjet-Printed Single-Droplet Organic Transistors Using Polarized Raman Spectroscopy: Effect of Blending TIPS-Pentacene with Insulating Polymer. *ACS Nano* **5,** 9824–9835 (2011).
104. Lee, D. J. & Oh, J. H. Shapes and morphologies of inkjet-printed nanosilver dots on glass substrates. *Surf. Interface Anal.* **42,** 1261–1265 (2010).
105. Diaz, E., Ramon, E. & Carrabina, J. Inkjet patterning of multiline intersections for wirings in printed electronics. *Langmuir* **29,** 12608–12614 (2013).
106. DUINEVELD, P. C. The stability of ink-jet printed lines of liquid with zero receding contact angle on a homogeneous substrate. *J. Fluid Mech.* **477,** 175–200 (2003).
107. Stringer, J. & Derby, B. Formation and Stability of Lines Produced by Inkjet Printing. *Langmuir* **26,** 10365–10372 (2010).
108. Dinh, N. T., Sowade, E., Blaudeck, T., Hermann, S., Rodriguez, R. D., Zahn, D. R. T., Schulz, S. E., Baumann, R. R. & Kanoun, O. High-resolution inkjet printing of conductive carbon nanotube twin lines utilizing evaporation-driven self-assembly. *Carbon* **96,** 382–393

(2016).

109. Wang, T., Roberts, M. a, Kinloch, I. a. & Derby, B. Inkjet printed carbon nanotube networks: the influence of drop spacing and drying on electrical properties. *J. Phys. D. Appl. Phys.* **45,** 315304 (2012).
110. Soltman, D., Smith, B., Kang, H., Morris, S. J. S. & Subramanian, V. Methodology for Inkjet Printing of Partially Wetting Films. *Langmuir* **14,** 15686–93 (2010).
111. Singh, A., Katiyar, M. & Garg, A. Understanding the formation of PEDOT:PSS films by ink-jet printing for organic solar cell applications. *RSC Adv.* **5,** 78677–78685 (2015).
112. Teichler, A., Eckardt, R., Hoeppener, S., Friebe, C., Perelaer, J., Senes, A., Morana, M., Brabec, C. J. & Schubert, U. S. Combinatorial Screening of Polymer:Fullerene Blends for Organic Solar Cells by Inkjet Printing. *Adv. Energy Mater.* **1,** 105–114 (2011).
113. Noh, J., Jung, M., Jung, Y., Yeom, C., Pyo, M. & Cho, G. Key Issues With Printed Flexible Thin Film Transistors and Their Application in Disposable RF Sensors. *Proc. IEEE* **103,** 554–566 (2015).
114. Förch, R., Schönherr, H. & Jenkins, A. *Surface Design: Applications in Bioscience and Nanotechnology*. *Nanotechnology* (Wiley-VCH Verlag GmbH & Co. KGaA, 2009). doi:10.1002/9783527628599
115. Kettle, J., Lamminmäki, T. & Gane, P. A review of modified surfaces for high speed inkjet coating. *Surf. Coatings Technol.* **204,** 2103–2109 (2010).
116. Yildirim Erbil, H. Control of stain geometry by drop evaporation of surfactant containing dispersions. *Adv. Colloid Interface Sci.* **222,** 275–290 (2015).
117. Doganci, M. D., Sesli, B. U. & Erbil, H. Y. Diffusion-controlled evaporation of sodium dodecyl sulfate solution drops placed on a hydrophobic substrate. *J. Colloid Interface Sci.* **362,** 524–531 (2011).
118. Uno, K., Hayashi, K., Hayashi, T., Ito, K. & Kitano, H. Particle adsorption in evaporating droplets of polymer latex dispersions on hydrophilic and hydrophobic surfaces. *Colloid Polym. Sci.* **276,** 810–815 (1998).
119. Joshi, A. S. & Sun, Y. Numerical Simulation of Colloidal Drop Deposition Dynamics on Patterned Substrates for Printable Electronics Fabrication. *J. Disp. Technol.* **6,** 579–585 (2010).
120. Bhardwaj, R., Fang, X., Somasundaran, P. & Attinger, D. Self-assembly of colloidal particles from evaporating droplets: Role of DLVO interactions and proposition of a phase diagram. *Langmuir* **26,** 7833–7842 (2010).
121. Layani, M., Gruchko, M., Milo, O., Balberg, I., Azulay, D. & Magdassi, S. Transparent conductive coatings by printing coffee ring arrays obtained at room temperature. *ACS Nano*

3, 3537–3542 (2009).

122. Deegan, R. D., Bakajin, O., Dupont, T. F., Huber, G., Nagel, S. R. & Witten, T. a. Capillary flow as the cause of ring stains from dried liquid drops. *Nature* **389,** 827–829 (1997).
123. Perelaer, J., Smith, P. J., Hendriks, C. E., van den Berg, A. M. J. & Schubert, U. S. The preferential deposition of silica micro-particles at the boundary of inkjet printed droplets. *Soft Matter* **4,** 1072 (2008).
124. Grzelczak, M., Vermant, J., Furst, E. M. & Liz-Marzán, L. M. Directed self-assembly of nanoparticles. *ACS Nano* **4,** 3591–3605 (2010).
125. Hu, H. & Larson, R. G. Marangoni effect reverses coffee-ring depositions. *J. Phys. Chem. B* **110,** 7090–7094 (2006).
126. Still, T., Yunker, P. J. & Yodh, A. G. Surfactant-induced Marangoni eddies alter the coffee-rings of evaporating colloidal drops. *Langmuir* **28,** 4984–4988 (2012).
127. Yunker, P. J., Still, T., Lohr, M. A. & Yodh, A. G. Suppression of the coffee-ring effect by shape-dependent capillary interactions. *Nature* **476,** 308–311 (2011).
128. Harris, D. J., Conrad, J. C. & Lewis, J. a. Evaporative lithographic patterning of binary colloidal films. *Philos. Trans. R. Soc. A Math. Phys. Eng. Sci.* **367,** 5157–5165 (2009).
129. Eral, H. B., Augustine, D. M., Duits, M. H. G. & Mugele, F. Suppressing the coffee stain effect: how to control colloidal self-assembly in evaporating drops using electrowetting. *Soft Matter* **7,** 4954 (2011).
130. Velev, O. D. & Gupta, S. Materials Fabricated by Micro- and Nanoparticle Assembly - The Challenging Path from Science to Engineering. *Adv. Mater.* **21,** 1897–1905 (2009).
131. Ozin, G. a., Hou, K., Lotsch, B. V., Cademartiri, L., Puzzo, D. P., Scotognella, F., Ghadimi, A. & Thomson, J. Nanofabrication by self-assembly. *Mater. Today* **12,** 12–23 (2009).
132. Whitesides, G. M. & Grzybowski, B. Self-Assembly at All Scales. *Science* **295,** 2418–21 (2002).
133. Maenosono, S., Okubo, T. & Yamaguchi, Y. Overview of nanoparticle array formation by wet coating. *J. Nanoparticle Res.* **5,** 5–15 (2003).
134. Park, J. & Moon, J. Control of Colloidal Particle Deposit Patterns within Picoliter Droplets Ejected by Ink-Jet Printing. *Langmuir* **22,** 3506–3513 (2006).
135. Nguyen, T. A. H., Hampton, M. a. & Nguyen, A. V. Evaporation of Nanoparticle Droplets on Smooth Hydrophobic Surfaces: The Inner Coffee Ring Deposits. *J. Phys. Chem. C* **117,** 4707–4716 (2013).
136. Wang, D., Park, M., Park, J. & Moon, J. Optical properties of single droplet of photonic crystal assembled by ink-jet printing. *Appl. Phys. Lett.* **86,** 241114 (2005).
137. Park, J., Moon, J., Shin, H., Wang, D. & Park, M. Direct-write fabrication of colloidal photonic

crystal microarrays by ink-jet printing. *J. Colloid Interface Sci.* **298,** 713–719 (2006).

138. Ko, H.-Y., Park, J., Shin, H. & Moon, J. Rapid Self-Assembly of Monodisperse Colloidal Spheres in an Ink-Jet Printed Droplet. *Chem. Mater.* **16,** 4212–4215 (2004).
139. Cui, L., Li, Y., Wang, J., Tian, E., Zhang, X., Zhang, Y., Song, Y. & Jiang, L. Fabrication of large-area patterned photonic crystals by ink-jet printing. *J. Mater. Chem.* **9428,** 1–6 (2009).
140. Biswas, S., Gawande, S., Bromberg, V. & Sun, Y. Effects of Particle Size and Substrate Surface Properties on Deposition Dynamics of Inkjet-Printed Colloidal Drops for Printable Photovoltaics Fabrication. *J. Sol. Energy Eng.* **132,** 21010 (2010).
141. Wang, L., Wang, J., Huang, Y., Liu, M., Kuang, M., Li, Y., Jiang, L. & Song, Y. Inkjet printed colloidal photonic crystal microdot with fast response induced by hydrophobic transition of poly(N-isopropyl acrylamide). *J. Mater. Chem.* **22,** 21405 (2012).
142. Shen, W., Li, M., Ye, C., Jiang, L. & Song, Y. Direct-writing colloidal photonic crystal microfluidic chips by inkjet printing for label-free protein detection. *Lab Chip* **12,** 3089 (2012).
143. Kuang, M., Wang, J., Bao, B., Li, F., Wang, L., Jiang, L. & Song, Y. Inkjet Printing Patterned Photonic Crystal Domes for Wide Viewing-Angle Displays by Controlling the Sliding Three Phase Contact Line. *Adv. Opt. Mater.* **2,** 34–38 (2014).
144. Bai, L., Xie, Z., Wang, W., Yuan, C., Zhao, Y., Mu, Z., Zhong, Q. & Gu, Z. Bio-Inspired Vapor-Responsive Colloidal Photonic Crystal Patterns by Inkjet Printing. *ACS Nano* **8,** 11094–11100 (2014).
145. Marlow, F., Muldarisnur, Sharifi, P., Brinkmann, R. & Mendive, C. Opals: Status and Prospects. *Angew. Chemie Int. Ed.* **48,** 6212–6233 (2009).
146. Fleischhaker, F. & Zentel, R. Photonische kristalle: Opale. *Chemie Unserer Zeit* **41,** 38–44 (2007).
147. Joannopoulos, J. D., Meade, R. D. & Winn, J. N. *Photonic Crystals: Molding the Flow of Light*. (Princeton University Press, 1995).
148. Sato, O., Kubo, S. & Gu, Z.-Z. Structural Color Films with Lotus Effects, Superhydrophilicity, and Tunable Stop-Bands. *Acc. Chem. Res.* **42,** 1–10 (2009).
149. Yin, S.-N., Wang, C.-F., Liu, S.-S. & Chen, S. Facile fabrication of tunable colloidal photonic crystal hydrogel supraballs toward a colorimetric humidity sensor. *J. Mater. Chem. C* **1,** 4685 (2013).
150. Yu, Z., Chen, L. & Chen, S. Uniform fluorescent photonic crystal supraballs generated from nanocrystal-loaded hydrogel microspheres. *J. Mater. Chem.* **20,** 6182 (2010).
151. Parker, A. R., Welch, V. L., Driver, D. & Martini, N. Structural colour: Opal analogue discovered in a weevil. *Nature* **426,** 786–787 (2003).

152. Norris, D. J., Arlinghaus, E. G., Meng, L., Heiny, R. & Scriven, L. E. Opaline Photonic Crystals: How Does Self-Assembly Work? *Adv. Mater.* **16,** 1393–1399 (2004).
153. Cho, Y.-S., Kim, S.-H., Yi, G.-R. & Yang, S.-M. Self-organization of colloidal nanospheres inside emulsion droplets: Higher-order clusters, supraparticles, and supraballs. *Colloids Surfaces A Physicochem. Eng. Asp.* **345,** 237–245 (2009).
154. Sowade, E., Blaudeck, T. & Baumann, R. R. Self-Assembly of Spherical Colloidal Photonic Crystals inside Inkjet-Printed Droplets. *Cryst. Growth Des.* **16,** 1017–1026 (2016).
155. Sowade, E., Hammerschmidt, J., Blaudeck, T. & Baumann, R. R. Inkjet Printing of Polymer Microspheres. in *Proceeding 25th Int. Conf. Digit. Print. Technol. NIP 25 Digit. Fabr. 2009* 788–790 (2009).
156. Zhao, Y., Shang, L., Cheng, Y. & Gu, Z. Spherical colloidal photonic crystals. *Acc. Chem. Res.* **47,** 3632–3642 (2014).
157. Phillips, K. R., England, G. T., Sunny, S., Shirman, E., Shirman, T., Vogel, N. & Aizenberg, J. A colloidoscope of colloid-based porous materials and their uses. *Chem. Soc. Rev.* **45,** 281–322 (2016).
158. Velev, O. D., Lenhoff, A. M. & Kaler, E. W. A Class of Microstructured Particles Through Colloidal Crystallization. *Science* **287,** 2240–2243 (2000).
159. Vogel, N., Utech, S., England, G. T., Shirman, T., Phillips, K. R., Koay, N., Burgess, I. B., Kolle, M., Weitz, D. A. & Aizenberg, J. Color from hierarchy: Diverse optical properties of micron-sized spherical colloidal assemblies. *Proc. Natl. Acad. Sci.* **112,** 10845–10850 (2015).
160. Wang, J. & Zhu, J. Recent advances in spherical photonic crystals: Generation and applications in optics. *Eur. Polym. J.* **49,** 3420–3433 (2013).
161. Rastogi, V., Melle, S., Calderón, O. G., García, A. a., Marquez, M. & Velev, O. D. Synthesis of Light-Diffracting Assemblies from Microspheres and Nanoparticles in Droplets on a Superhydrophobic Surface. *Adv. Mater.* **20,** 4263–4268 (2008).
162. Xu, K., Xu, J. H., Lu, Y. C. & Luo, G. S. Extraction-derived self-organization of colloidal photonic crystal particles within confining aqueous droplets. *Cryst. Growth Des.* **13,** 926–935 (2013).
163. Hu, Y., Wang, J., Wang, H., Wang, Q., Zhu, J. & Yang, Y. Microfluidic fabrication and thermoreversible response of core/shell photonic crystalline microspheres based on deformable nanogels. *Langmuir* **28,** 17186–17192 (2012).
164. Gu, H., Rong, F., Tang, B., Zhao, Y., Fu, D. & Gu, Z. Photonic Crystal Beads from Gravity-Driven Microfluidics. *Langmuir* **29,** 7576–7582 (2013).
165. Sun, C., Zhao, X. W., Zhao, Y. J., Zhu, R. & Gu, Z. Z. Fabrication of colloidal crystal beads

by a drop-breaking technique and their application as bioassays. *Small* **4,** 592–596 (2008).
166. Sowade, E., Hammerschmidt, J., Blaudeck, T. & Baumann, R. R. In-Flight Inkjet Self-Assembly of Spherical Nanoparticle Aggregates. *Adv. Eng. Mater.* **14,** 98–100 (2012).
167. Moon, J. H., Yi, G.-R., Yang, S.-M., Pine, D. J. & Park, S. B. Electrospray-Assisted Fabrication of Uniform Photonic Balls. *Adv. Mater.* **16,** 605–609 (2004).
168. Hong, S.-H., Moon, J. H., Lim, J.-M., Kim, S.-H. & Yang, S.-M. Fabrication of spherical colloidal crystals using electrospray. *Langmuir* **21,** 10416–10421 (2005).
169. Zhokhov, A. A., Masalov, V. M., Sukhinina, N. S., Matveev, D. V., Dolganov, P. V., Dolganov, V. K. & Emelchenko, G. A. Photonic crystal microspheres. *Opt. Mater.* **49,** 208–212 (2015).
170. Cho, Y. S., Yi, G. R., Chung, Y. S., Park, S. Bin & Yang, S. M. Complex colloidal microclusters from aerosol droplets. *Langmuir* **23,** 12079–12085 (2007).
171. Lenggoro, I. W., Xia, B., Okuyama, K. & De la Mora, J. F. Sizing of colloidal nanoparticles by electrospray and differential mobility analyzer methods. *Langmuir* **18,** 4584–4591 (2002).
172. Marin, A. G., Gelderblom, H., Susarrey-Arce, A., van Houselt, A., Lefferts, L., Gardeniers, J. G. E., Lohse, D. & Snoeijer, J. H. Building microscopic soccer balls with evaporating colloidal fakir drops. *Proc. Natl. Acad. Sci.* **109,** 16455–16458 (2012).
173. Kursawe, M., Anselmann, R., Hilarius, V. & Pfaff, G. Nano-particles by wet chemical processing in commercial applications. *J. Sol-Gel Sci. Technol.* **33,** 71–74 (2005).
174. Anselmann, R. & Winkler, H. Ordered Structures from Nanoparticles. *Adv. Eng. Mater.* **5,** 560–562 (2003).
175. Sowade, E., Blaudeck, T. & Baumann, R. R. Preparation of spherical, ordered colloidal aggregates using inkjet printing. *MRS Proc.* **1453,** mrss12-1453-aaa03-04 (2012).
176. Sowade, E., Mitra, K. Y., Ramon, E., Martinez-Domingo, C., Villani, F., Loffredo, F., Gomes, H. L. & Baumann, R. R. Up-scaling of the manufacturing of all-inkjet-printed organic thin-film transistors: Device performance and manufacturing yield of transistor arrays. *Org. Electron.* **30,** 237–246 (2016).
177. Gamota, D., Brazis, P., Kalyanasundaram, K. & Zhang, J. Printed organic and molecular electronics. *Mater. Today* **7,** 53 (2004).
178. Ponce Ortiz, R., Facchetti, A. & Marks, T. J. High-k organic, inorganic, and hybrid dielectrics for low-voltage organic field-effect transistors. *Chem. Rev.* **110,** 205–39 (2010).
179. Zaumseil, J. & Sirringhaus, H. Electron and Ambipolar Transport in Organic Field-Effect Transistors. *Chem. Rev.* **107,** 1296–1323 (2007).
180. Torsi, L., Magliulo, M., Manoli, K. & Palazzo, G. Organic field-effect transistor sensors: a

tutorial review. *Chem. Soc. Rev.* **42,** 8612 (2013).

181. Bao, Z. Materials and Fabrication Needs for Low-Cost Organic Transistor Circuits. *Adv. Mater.* **12,** 227–230 (2000).
182. Sirringhaus, H. 25th Anniversary Article: Organic Field-Effect Transistors: The Path Beyond Amorphous Silicon. *Adv. Mater.* **26,** 1319–1335 (2014).
183. Subramanian, V., Chang, J. B., Vornbrock, A. D. L. F., Huang, D. C., Jagannathan, L., Liao, F., Mattis, B., Molesa, S., Redinger, D. R., Soltman, D., Volkman, S. K. & Zhang, Q. Printed electronics for low-cost electronic systems: Technology status and application development. in *ESSDERC 2008 - 38th Eur. Solid-State Device Res. Conf.* 17–24 (IEEE, 2008). doi:10.1109/ESSDERC.2008.4681691
184. Chang, J., Zhang, X., Ge, T. & Zhou, J. Fully printed electronics on flexible substrates: High gain amplifiers and DAC. *Org. Electron.* **15,** 701–710 (2014).
185. Grau, G., Kitsomboonloha, R., Kang, H. & Subramanian, V. High performance printed organic transistors using a novel scanned thermal annealing technology. *Org. Electron.* **20,** 150–157 (2015).
186. Kawase, T., Shimoda, T., Newsome, C., Sirringhaus, H. & Friend, R. H. Inkjet printing of polymer thin film transistors. *Thin Solid Films* **438–439,** 279–287 (2003).
187. Kawase, T., Sirringhaus, H., Friend, R. H. & Shimoda, T. Inkjet Printed Via-Hole Interconnections and Resistors for All-Polymer Transistor Circuits. *Adv. Mater.* **13,** 1601–1605 (2001).
188. Sirringhaus, H., Kawase, T., Friend, R. H., Shimoda, T., Inbasekaran, M., Wu, W. & Woo, E. P. High-Resolution Inkjet Printing of All-Polymer Transistor Circuits. *Science* **290,** 2123–2126 (2000).
189. Fukuda, K., Takeda, Y., Mizukami, M., Kumaki, D. & Tokito, S. Fully solution-processed flexible organic thin film transistor arrays with high mobility and exceptional uniformity. *Sci. Rep.* **4,** 3947 (2014).
190. Kim, Y. H., Yoo, B., Anthony, J. E. & Park, S. K. Controlled deposition of a high-performance small-molecule organic single-crystal transistor array by direct ink-jet printing. *Adv. Mater.* **24,** 497–502 (2012).
191. Kjellander, B. K. C., Smaal, W. T. T., Anthony, J. E. & Gelinck, G. H. Inkjet printing of TIPS-PEN on soluble polymer insulating films: A route to high-performance thin-film transistors. *Adv. Mater.* **22,** 4612–4616 (2010).
192. Kim, D., Jeong, Y., Koo, C. Y., Song, K. & Moon, J. Thin film transistors with ink-jet printed amorphous oxide semiconductors. *Jpn. J. Appl. Phys.* **49,** 05EB06 (2010).
193. Yan, H., Chen, Z., Zheng, Y., Newman, C., Quinn, J. R., Dötz, F., Kastler, M. & Facchetti,

A. A high-mobility electron-transporting polymer for printed transistors. *Nature* **457,** 679–686 (2009).

194. Minemawari, H., Yamada, T., Matsui, H., Tsutsumi, J., Haas, S., Chiba, R., Kumai, R. & Hasegawa, T. Inkjet printing of single-crystal films. *Nature* **475,** 364–367 (2011).
195. Sekitani, T., Noguchi, Y., Zschieschang, U., Klauk, H. & Someya, T. Organic transistors manufactured using inkjet technology with subfemtoliter accuracy. *Proc. Natl. Acad. Sci. U. S. A.* **105,** 4976–4980 (2008).
196. Chung, J. W., Ko, Y. H., Hong, Y. K., Song, W., Jung, C., Tang, H., Lee, J., Lee, M. H., Lee, B., Jin, Y., Lee, S., Yu, J. S., Park, J. & Kim, S. Flexible nano-hybrid inverter based on inkjet-printed organic and 2D multilayer MoS2 thin film transistor. *Org. Electron.* **15,** 6–11 (2014).
197. Wang, Y., Hu, D., Chen, M., Wang, X., Lu, H., Zhang, G., Wang, X., Wu, Z. & Qiu, L. Modulation of surface solubility and wettability for high-performance inkjet-printed organic transistors. *Org. Electron.* **15,** 3101–3110 (2014).
198. Wang, H., Cheng, C., Zhang, L., Liu, H., Zhao, Y., Guo, Y., Hu, W., Yu, G. & Liu, Y. Inkjet printing short-channel polymer transistors with high-performance and ultrahigh photoresponsivity. *Adv. Mater.* **26,** 4683–4689 (2014).
199. Basiricò, L., Cosseddu, P., Fraboni, B. & Bonfiglio, A. Inkjet printing of transparent, flexible, organic transistors. *Thin Solid Films* **520,** 1291–1294 (2011).
200. Zhao, Y., Di, C. A., Gao, X., Hu, Y., Guo, Y., Zhang, L., Liu, Y., Wang, J., Hu, W. & Zhu, D. All-solution-processed, high-performance n-channel organic transistors and circuits: Toward low-cost ambient electronics. *Adv. Mater.* **23,** 2448–2453 (2011).
201. Castro, H. F., Sowade, E., Rocha, J. G., Alpuim, P., Lanceros-Méndez, S. & Baumann, R. R. All-Inkjet-Printed Bottom-Gate Thin-Film Transistors Using UV Curable Dielectric for Well-Defined Source-Drain Electrodes. *J. Electron. Mater.* **43,** 2631–2636 (2014).
202. Castro, H. F., Sowade, E., Rocha, J. G., Alpuim, P., Machado, A. V., Baumann, R. R. & Lanceros-Méndez, S. Degradation of all-inkjet-printed organic thin-film transistors with TIPS-pentacene under processes applied in textile manufacturing. *Org. Electron.* **22,** 12–19 (2015).
203. Molesa, S. E., Volkman, S. K., Redinger, D. R., de la Fuente Vombrock, A. & Subramanian, V. A high-performance all-inkjetted organic transistor technology. in *IEDM Tech. Dig. IEEE Int. Electron Devices Meet. 2004.* 1072–1074 (IEEE, 2004). doi:10.1109/IEDM.2004.1419384
204. Kim, D., Lee, S. H., Jeong, S. & Moon, J. All-Ink-Jet Printed Flexible Organic Thin-Film Transistors on Plastic Substrates. *Electrochem. Solid-State Lett.* **12,** H195 (2009).

205. Tseng, H.-Y. & Subramanian, V. All inkjet-printed, fully self-aligned transistors for low-cost circuit applications. *Org. Electron.* **12,** 249–256 (2011).
206. Subramanian, V., Frechet, J. M. J., Chang, P. C., Huang, D. C., Lee, J. B., Molesa, S. E., Murphy, A. R., Redinger, D. R. & Volkman, S. K. Progress Toward Development of All-Printed RFID Tags: Materials, Processes, and Devices. *Proc. IEEE* **93,** 1330–1338 (2005).
207. Chung, S., Kim, S. O., Kwon, S. K., Lee, C. & Hong, Y. All-inkjet-printed organic thin-film transistor inverter on flexible plastic substrate. *IEEE Electron Device Lett.* **32,** 1134–1136 (2011).
208. Ko, S. H., Pan, H., Grigoropoulos, C. P., Luscombe, C. K., Fréchet, J. M. J. & Poulikakos, D. All-inkjet-printed flexible electronics fabrication on a polymer substrate by low-temperature high-resolution selective laser sintering of metal nanoparticles. *Nanotechnology* **18,** 345202 (2007).
209. Chung, S., Jang, J., Cho, J., Lee, C., Kwon, S.-K. & Hong, Y. All-Inkjet-Printed Organic Thin-Film Transistors with Silver Gate, Source/Drain Electrodes. *Jpn. J. Appl. Phys.* **50,** 03CB05 (2011).
210. Medina-Sánchez, M., Martínez-Domingo, C., Ramon, E. & Merkoçi, A. An Inkjet-Printed Field-Effect Transistor for Label-Free Biosensing. *Adv. Funct. Mater.* **24,** 6291–6302 (2014).
211. Lin, C. T., Hsu, C. H., Chen, I. R., Lee, C. H. & Wu, W. J. Enhancement of carrier mobility in all-inkjet-printed organic thin-film transistors using a blend of poly(3-hexylthiophene) and carbon nanoparticles. *Thin Solid Films* **519,** 8008–8012 (2011).
212. Mitra, K. Y., Sowade, E., Martínez-Domingo, C., Ramon, E., Carrabina, J., Gomes, H. L. & Baumann, R. R. Potential up-scaling of inkjet-printed devices for logical circuits in flexible electronics. in *Int. Conf. Exhib. Nanotechnologies Org. Electron. NANOTEXNOLOGY 2014* **106,** 106–114 (2015).
213. Gomes, H. L., Medeiros, M. C. R., Villani, F., Canudo, J., Loffredo, F., Miscioscia, R., Martinez-Domingo, C., Ramon, E., Sowade, E., Mitra, K. Y., Baumann, R. R., McCulloch, I. & Carrabina, J. All-inkjet printed organic transistors: Dielectric surface passivation techniques for improved operational stability and lifetime. *Microelectron. Reliab.* **55,** 1192–1195 (2015).
214. Ramon, E., Martínez-Domingo, C. & Carrabina, J. Geometric Design and Compensation Rules Generation and Characterization for All-Inkjet-Printed Organic Thin Film Transistors. *J. Imaging Sci. Technol.* **57,** 40402–1 (2013).
215. Hammerschmidt, J., Ueberfuhr, P., Eck, E., Zeiner, C., Thalheim, R. & Baumann, R. R. Characterization of fully inkjet-printed microsieves and of patterns for the mechanical

reinforcement of fragile membranes. in *Int. Conf. Non Impact Print. Digit. Fabr.* **2014,** 307–310 (2014).

216. Hammerschmidt, J., Sowade, E., Mitra, K. Y., Wohlleben, L. M. & Baumann, R. R. The Influence of Post-Treatment Strategies in Inkjet Printing on the Morphology of Layers and the Functional Performances of Electronic Devices. in *Int. Conf. Non Impact Print. Digit. Fabr.* **75,** 444–447 (2012).
217. Siregar, D. P., Kuerten, J. G. M. & van der Geld, C. W. M. Numerical simulation of the drying of inkjet-printed droplets. *J. Colloid Interface Sci.* **392,** 388–395 (2013).
218. Yoo, H. & Kim, C. Experimental studies on formation, spreading and drying of inkjet drop of colloidal suspensions. *Colloids Surfaces A Physicochem. Eng. Asp.* **468,** 234–245 (2015).
219. Choi, S., Pisano, A. P. & Zohdi, T. I. An analysis of evaporative self-assembly of micro particles in printed picoliter suspension droplets. *Thin Solid Films* **537,** 180–189 (2013).
220. Reinhold, I., Zapka, W., Voit, W., Steinhäußer, F., Stürmer, M., Madjarov, A. & Völker, M. Inkjet Printing of Phase-Change Materials With Xaar1001 Printheads. in *Int. Conf. Non Impact Print. Digit. Fabr.* 319–322 (2010).
221. Abbel, R., Teunissen, P., Rubingh, E., Lammeren, T. Van, Cauchois, R., Everaars, M., Valeton, J., Geijn, S. Van De & Groen, P. Industrial-scale inkjet printed electronics manufacturing—production up-scaling from concept tools to a roll-to-roll pilot line. *Transl. Mater. Res.* **1,** 15002 (2014).
222. Fujifilm Dimatix. *Materials Printer & Cartridges DMP-2831 & DMC-11601/11610 Datasheet*. (2008).
223. Fujifilm Dimatix. *Datasheet Fujifilm Dimatix SE3 printhead*. (2015).
224. Fujifilm Dimatix. *Datasheet Fujifilm Dimatix SX3 printhead*. (2015).
225. Fujifilm Dimatix. *Using the D-128 printhead*. (2012).
226. Fujifilm Dimatix. *Datasheet Materials Printer, Cartridges & Printheads DMP-3000, DMC-11601/11610, SX3, SE3, SE-DPN, D-128/1 DPN and D-128/10 DPN*. (2011).
227. Castro, H. F., Correia, V., Sowade, E., Mitra, K. Y., Rocha, J. G., Baumann, R. R. & Lanceros-Méndez, S. All-inkjet-printed low-pass filters with adjustable cutoff frequency consisting of resistors, inductors and transistors for sensor applications. *Org. Electron.* **38,** 205–212 (2016).
228. Fujifilm Dimatix. *SX3 Jetting Assembly Product Manual*. (2008).
229. Fujifilm Dimatix. *Materials Printer DMP 3000 Accessories Price List*. (2011).
230. Sowade, E., Mitra, K. Y., Gomes, H. L. & Reinhard, R. Inkjet-printed electronics: Transfer from lab to fab manufacturing. in *Smart Syst. Integr. Conf. 2013* 13–14 (2013).

231. Sowade, E., Göthel, F., Zichner, R. & Baumann, R. R. Inkjet printing of UHF antennas on corrugated cardboards for packaging applications. *Appl. Surf. Sci.* **332,** 500–506 (2015).
232. Hammerschmidt, D. Weise, R. R. B. Micro-Three-Dimensional Patterning by Inkjet Printing of UV Curable Inks. in *Int. Conf. Non Impact Print. Digit. Fabr.* 811–814 (2011).
233. IEEE Standard for Test Methods for the Characterization of Organic Transistors and Materials. *IEEE Std 1620-2008 (Revision IEEE Std 1620-2004)* 1–27 (2008). doi:10.1109/IEEEStd.2008.4696034
234. Puzzo, D. P., Bonifacio, L. D., Oreopoulos, J., Yip, C. M., Manners, I. & Ozin, G. a. Color from colorless nanomaterials: Bragg reflectors made of nanoparticles. *J. Mater. Chem.* **19,** 3500 (2009).
235. Zhang, J., Sun, Z. & Yang, B. Self-assembly of photonic crystals from polymer colloids. *Curr. Opin. Colloid Interface Sci.* **14,** 103–114 (2009).
236. Janz, S., Voisin, P., Suwito, D., Peters, M., Hermle, M. & Glunz, S. W. Photonic crystals as rear-side diffusers and reflectors for high efficiency silicon solar cells. in *24th Eur. PV Sol. Energy Conf. Exhib. 21-25 Sept. 2009, Hamburg, Ger.* 1529–1533 (2009).
237. Yan, X., Yao, J., Lu, G., Li, X., Zhang, J., Han, K. & Yang, B. Fabrication of non-close-packed arrays of colloidal spheres by soft lithography. *J. Am. Chem. Soc.* **127,** 7688–7689 (2005).
238. Jin, C., McLachlan, M. A., McComb, D. W., De La Rue, R. M. & Johnson, N. P. Template-Assisted Growth of Nominally Cubic (100)-Oriented Three-Dimensional Crack-Free Photonic Crystals. *Nano Lett.* **5,** 2646–2650 (2005).
239. García, P. D., Sapienza, R. & López, C. Photonic Glasses: A Step Beyond White Paint. *Adv. Mater.* **22,** 12–9 (2010).
240. Kim, S.-H., Lee, S. Y., Yang, S.-M. & Yi, G.-R. Self-assembled colloidal structures for photonics. *NPG Asia Mater.* **3,** 25–33 (2011).
241. Sowade, E., Hammerschmidt, J., Blaudeck, T. & Baumann, R. R. Verfahren und Vorrichtung zum Erzeugen einer dreidimensionalen Struktur auf einem Substrat. Patent DE102010063982 A1 (2012). at <http://register.dpma.de/DPMAregister/pat/PatSchrifteneinsicht?docId=DE102010063982A1>
242. Dong, H., Carr, W. W. & Morris, J. F. An experimental study of drop-on-demand drop formation. *Phys. Fluids* **18,** 72102 (2006).
243. Li, R., Ashgriz, N. & Chandra, S. Droplet generation from pulsed micro-jets. *Exp. Therm. Fluid Sci.* **32,** 1679–1686 (2008).
244. Basaran, O. a. Small-scale free surface flows with breakup: Drop formation and emerging

applications. *AIChE J.* **48,** 1842–1848 (2002).

245. Song, J. Defects and prevention in ceramic components fabricated by inkjet printing. *J. Mater. Process. Technol.* **155–156,** 1286–1292 (2004).
246. Kim, S. H., Lim, J. M., Jeong, W. C., Choi, D. G. & Yang, S. M. Patterned colloidal photonic domes and balls derived from viscous photocurable suspensions. *Adv. Mater.* **20,** 3211–3217 (2008).
247. Manoharan, V. N. Colloidal spheres confined by liquid droplets: Geometry, physics, and physical chemistry. *Solid State Commun.* **139,** 557–561 (2006).
248. Kim, S. H., Cho, Y. S., Jeon, S. J., Eun, T. H., Yi, G. R. & Yang, S. M. Microspheres with tunable refractive index by controlled assembly of nanoparticles. *Adv. Mater.* **20,** 3268–3273 (2008).
249. Kim, S. H., Lee, S. Y., Yi, G. R., Pine, D. J. & Yang, S. M. Microwave-assisted self-organization of colloidal particles in confining aqueous droplets. *J. Am. Chem. Soc.* **128,** 10897–10904 (2006).
250. Masuda, Y. Self-assembly Patterning of Nano/Micro-Particles. *KONA Powder Part. J.* **25,** 244–254 (2007).
251. Anselmann, R. Nanoparticles and nanolayers in commercial applications. *J. Nanoparticle Res.* **3,** 329–336 (2001).
252. Cho, Y. S., Yi, G. R., Kim, S. H., Pine, D. J. & Yang, S. M. Colloidal clusters of microspheres from water-in-oil emulsions. *Chem. Mater.* **17,** 5006–5013 (2005).
253. Zhao, X., Cao, Y., Ito, F., Chen, H.-H., Nagai, K., Zhao, Y.-H. & Gu, Z.-Z. Colloidal Crystal Beads as Supports for Biomolecular Screening. *Angew. Chemie* **118,** 6989–6992 (2006).
254. Yi, G. Generation of uniform photonic balls by template-assisted colloidal crystallization. *Synth. Met.* **139,** 803–806 (2003).
255. Mouaziz, H., Lacki, K., Larsson, a. & Sherrington, D. C. Synthesis of porous microspheres via self-assembly of monodisperse polymer nanospheres. *J. Mater. Chem.* **14,** 2421 (2004).
256. Shchukin, D. G. & Caruso, R. A. Template Synthesis and Photocatalytic Properties of Porous Metal Oxide Spheres Formed by Nanoparticle Infiltration. *Chem. Mater.* **16,** 2287–2292 (2004).
257. Kuncicky, D. M. & Velev, O. D. Surface-guided templating of particle assemblies inside drying sessile droplets. *Langmuir* **24,** 1371–1380 (2008).
258. Gokmen, M. T. & Du Prez, F. E. Porous polymer particles - A comprehensive guide to synthesis, characterization, functionalization and applications. *Prog. Polym. Sci.* **37,** 365–405 (2012).
259. Yi, G.-R., Manoharan, V. N., Klein, S., Brzezinska, K. R., Pine, D. J., Lange, F. F. & Yang,

S.-M. Monodisperse Micrometer-Scale Spherical Assemblies of Polymer Particles. *Adv. Mater.* **14,** 1137 (2002).

260. Ling, X. S. Dislocation dynamics: Scars on a colloidal crystal ball. *Nat. Mater.* **4,** 360–361 (2005).
261. Lipowsky, P., Bowick, M. J., Meinke, J. H., Nelson, D. R. & Bausch, A. R. Direct visualization of dislocation dynamics in grain-boundary scars. *Nat. Mater.* **4,** 407–411 (2005).
262. Zhao, Y., Xie, Z., Gu, H., Zhu, C. & Gu, Z. Bio-inspired variable structural color materials. *Chem. Soc. Rev.* **41,** 3297 (2012).
263. McGrath, J. G., Bock, R. D., Cathcart, J. M. & Lyon, L. A. Self-Assembly of 'Paint-On' Colloidal Crystals Using Poly(styrene- co - N -isopropylacrylamide) Spheres. *Chem. Mater.* **19,** 1584–1591 (2007).
264. Rossier-Miranda, F. J., Schroën, C. G. P. H. & Boom, R. M. Colloidosomes: Versatile microcapsules in perspective. *Colloids Surfaces A Physicochem. Eng. Asp.* **343,** 43–49 (2009).
265. Dinsmore, a D., Hsu, M. F., Nikolaides, M. G., Marquez, M., Bausch, a R. & Weitz, D. a. Colloidosomes: Selectively Permeable Capsules Composed of Colloidal Particles. *Science* **298,** 1006–1009 (2002).
266. Wang, Y., Wise, A. K., Tan, J., Maina, J. W., Shepherd, R. K. & Caruso, F. Mesoporous Silica Supraparticles for Sustained Inner-Ear Drug Delivery. *Small* 1–5 (2014). doi:10.1002/smll.201401767
267. Zhao, Y., Zhao, X., Hu, J., Xu, M., Zhao, W., Sun, L., Zhu, C., Xu, H. & Gu, Z. Encoded porous beads for label-free multiplex detection of tumor markers. *Adv. Mater.* **21,** 569–72 (2009).
268. Liu, S.-S., Wang, C.-F., Wang, X.-Q., Zhang, J., Tian, Y., Yin, S.-N. & Chen, S. Tunable Janus colloidal photonic crystal supraballs with dual photonic band gaps. *J. Mater. Chem. C* **2,** 9431–9438 (2014).
269. Shishkin, I. I., Rybin, M. V., Samusev, K. B., Golubev, V. G. & Limonov, M. F. Multiple Bragg diffraction in opal-based photonic crystals: Spectral and spatial dispersion. *Phys. Rev. B* **89,** 35124 (2014).
270. Lim, Y. Y., Goh, Y. M. & Liu, C. Surface Treatments for Inkjet Printing onto a PTFE-Based Substrate for High Frequency Applications. *Ind. Eng. Chem. Res.* **52,** 11564–11574 (2013).
271. Brodeala, A., Bonea, A., Ionescu, C., Vladescu, M. & Svasta, P. Physical properties of silver inkjet printed circuits. in *Proc. 35th Int Electron. Technol. Spring Semin.* 114–116 (2012).
272. Pierre, A., Sadeghi, M., Payne, M. M., Facchetti, A., Anthony, J. E. & Arias, A. C. All-Printed Flexible Organic Transistors Enabled by Surface Tension-Guided Blade Coating. *Adv.*

Mater. **26,** 5722–5727 (2014).

273. Sanchez-Romaguera, V., Ziai, M. A., Oyeka, D., Barbosa, S., Wheeler, J. S. R., Batchelor, J. C., Parker, E. A. & Yeates, S. G. Towards inkjet-printed low cost passive UHF RFID skin mounted tattoo paper tags based on silver nanoparticle inks. *J. Mater. Chem. C* **1,** 6395 (2013).
274. Tanner, L. H. The spreading of silicone oil drops on horizontal surfaces. *J. Phys. D. Appl. Phys.* **12,** 1473–1484 (1979).
275. Erbil, H. Y., McHale, G. & Newton, M. I. Drop evaporation on solid surfaces: Constant contact angle mode. *Langmuir* **18,** 2636–2641 (2002).
276. Erbil, H. Y. Evaporation of pure liquid sessile and spherical suspended drops: A review. *Adv. Colloid Interface Sci.* **170,** 67–86 (2012).
277. MacDonald, W. A., Looney, M. K., MacKerron, D., Eveson, R., Adam, R., Hashimoto, K. & Rakos, K. Latest advances in substrates for flexible electronics. *J. Soc. Inf. Disp.* **15,** 1075 (2007).
278. Choi, M.-C., Kim, Y. & Ha, C.-S. Polymers for flexible displays: From material selection to device applications. *Prog. Polym. Sci.* **33,** 581–630 (2008).
279. Zardetto, V., Brown, T. M., Reale, A. & Di Carlo, A. Substrates for flexible electronics: A practical investigation on the electrical, film flexibility, optical, temperature, and solvent resistance properties. *J. Polym. Sci. Part B Polym. Phys.* **49,** 638–648 (2011).
280. Wünscher, S., Abbel, R., Perelaer, J. & Schubert, U. S. Progress of alternative sintering approaches of inkjet-printed metal inks and their application for manufacturing of flexible electronic devices. *J. Mater. Chem. C* **2,** 10232–10261 (2014).
281. Bubnova, O., Khan, Z. U., Wang, H., Braun, S., Evans, D. R., Fabretto, M., Hojati-Talemi, P., Dagnelund, D., Arlin, J.-B., Geerts, Y. H., Desbief, S., Breiby, D. W., Andreasen, J. W., Lazzaroni, R., Chen, W. M., Zozoulenko, I., Fahlman, M., Murphy, P. J., Berggren, M. & Crispin, X. Semi-metallic polymers. *Nat. Mater.* **13,** 190–194 (2013).
282. Sheng Hsiung Chang, Chien-Hung Chiang, Feng-Sheng Kao, Chuen-Lin Tien & Chun-Guey Wu. Unraveling the Enhanced Electrical Conductivity of PEDOT:PSS Thin Films for ITO-Free Organic Photovoltaics. *IEEE Photonics J.* **6,** 1–7 (2014).
283. Ma, S., Ribeiro, F., Powell, K., Lutian, J., Møller, C., Large, T. & Holbery, J. Fabrication of Novel Transparent Touch Sensing Device via Drop-on-Demand Inkjet Printing Technique. *ACS Appl. Mater. Interfaces* **7,** 21628–21633 (2015).
284. Vosgueritchian, M., Lipomi, D. J. & Bao, Z. Highly Conductive and Transparent PEDOT:PSS Films with a Fluorosurfactant for Stretchable and Flexible Transparent Electrodes. *Adv. Funct. Mater.* **22,** 421–428 (2012).

285. Xiong, J., Jiang, F., Zhou, W., Liu, C. & Xu, J. Highly electrical and thermoelectric properties of a PEDOT:PSS thin-film via direct dilution–filtration. *RSC Adv.* **5,** 60708–60712 (2015).
286. Smith, T. A review of carbon black pigments. *Pigment Resin Technol.* **12,** 14–16 (1983).
287. Methode Electronics. *Nano-Silver and Nano-Carbon Inks. Digital Printable Nano-Ink Technology. Inks formulated for Critical Electronic Applications.* (2011). at <http://www.methode.com/Documents/TechnicalLibrary/MDC_Nano_Inks_Brochure.pdf>
288. Al-Hamry, A., Kang, H., Sowade, E., Dzhagan, V., Rodriguez, R. D., Müller, C., Zahn, D. R. T., Baumann, R. R. & Kanoun, O. Tuning the reduction and conductivity of solution-processed graphene oxide by intense pulsed light. *Carbon* **102,** 236–244 (2016).
289. Denneulin, A., Bras, J., Blayo, A., Khelifi, B., Roussel-Dherbey, F. & Neuman, C. The influence of carbon nanotubes in inkjet printing of conductive polymer suspensions. *Nanotechnology* **20,** 385701 (2009).
290. Sowade, E., Dinh, T. N., Arreba, A., Seifert, T., Blaudeck, T., Kanoun, O. & Baumann, R. R. Deposition and Self-Assembly of Multiwalled Carbon Nanotube Thin Films by Piezo Inkjet Printing. in *Proc. Smart Syst. Integr. 2011, March 22-23, 2011.* Paper 99 (VDE VERLAG GMBH, 2011).
291. Secor, E. B. & Hersam, M. C. Emerging Carbon and Post-Carbon Nanomaterial Inks for Printed Electronics. *J. Phys. Chem. Lett.* **6,** 620–626 (2015).
292. Kamyshny, A. & Magdassi, S. Conductive Nanomaterials for Printed Electronics. *Small* **10,** 3515–3535 (2014).
293. Niittynen, J., Sowade, E., Kang, H., Baumann, R. R. & Mäntysalo, M. Comparison of laser and intense pulsed light sintering (IPL) for inkjet-printed copper nanoparticle layers. *Sci. Rep.* **5,** 8832 (2015).
294. Wang, Y., Guo, H., Chen, J.-J., Sowade, E., Wang, Y., Liang, K., Marcus, K., Baumann, R. R. & Feng, Z.-S. Paper-Based Inkjet-Printed Flexible Electronic Circuits. *ACS Appl. Mater. Interfaces* **8,** 26112–26118 (2016).
295. Kang, H., Sowade, E. & Baumann, R. R. Direct Intense Pulsed Light Sintering of Inkjet-Printed Copper Oxide Layers within Six Milliseconds. *ACS Appl. Mater. Interfaces* **6,** 1682–1687 (2014).
296. Hammerschmidt, J., Wolf, F. M., Goedel, W. a. & Baumann, R. R. Inkjet printing of reinforcing patterns for the mechanical stabilization of fragile polymeric microsieves. *Langmuir* **28,** 3316–3321 (2012).
297. Moya, A., Sowade, E., del Campo, F. J., Mitra, K. Y., Ramon, E., Villa, R., Baumann, R. R. & Gabriel, G. All-inkjet-printed dissolved oxygen sensors on flexible plastic substrates. *Org. Electron.* **39,** 168–176 (2016).

298. Jang, J., Kim, S. H., Hwang, J., Nam, S., Yang, C., Chung, D. S. & Park, C. E. Photopatternable ultrathin gate dielectrics for low-voltage-operating organic circuits. *Appl. Phys. Lett.* **95,** 73302 (2009).
299. Veres, J., Ogier, S., Lloyd, G. & de Leeuw, D. Gate Insulators in Organic Field-Effect Transistors. *Chem. Mater.* **16,** 4543–4555 (2004).
300. Graddage, N., Chu, T.-Y., Ding, H., Py, C., Dadvand, A. & Tao, Y. Inkjet printed thin and uniform dielectrics for capacitors and organic thin film transistors enabled by the coffee ring effect. *Org. Electron.* **29,** 114–119 (2016).
301. Sowade, E., Ramon, E., Mitra, K. Y., Martínez-Domingo, C., Pedró, M., Pallarès, J., Loffredo, F., Villani, F., Gomes, H. L., Terés, L. & Baumann, R. R. All-inkjet-printed thin-film transistors: manufacturing process reliability by root cause analysis. *Sci. Rep.* **6,** 33490 (2016).
302. Sowade, E., Kang, H., Mitra, K. Y., Weiß, O. J., Weber, J. & Baumann, R. R. Roll-to-roll infrared (IR) drying and sintering of an inkjet-printed silver nanoparticle ink within 1 second. *J. Mater. Chem. C* **3,** 11815–11826 (2015).
303. Soltman, D., Smith, B., Morris, S. J. S. & Subramanian, V. Inkjet printing of precisely defined features using contact-angle hysteresis. *J. Colloid Interface Sci.* **400,** 135–139 (2013).
304. Dong, H., Carr, W. W. & Morris, J. F. Visualization of drop-on-demand inkjet: Drop formation and deposition. *Rev. Sci. Instrum.* **77,** 85101 (2006).
305. Nallan, H. C., Sadie, J. a, Kitsomboonloha, R., Volkman, S. K. & Subramanian, V. Systematic Design of Jettable Nanoparticle-Based Inkjet Inks: Rheology, Acoustics, and Jettability. *Langmuir* **30,** 13470–13477 (2014).
306. Famili, A., Palkar, S. a. & Baldy, W. J. First drop dissimilarity in drop-on-demand inkjet devices. *Phys. Fluids* **23,** 12109 (2011).
307. Verkouteren, R. M. & Verkouteren, J. R. Inkjet Metrology: High-Accuracy Mass Measurements of Microdroplets Produced by a Drop-on-Demand Dispenser. *Anal. Chem.* **81,** 8577–8584 (2009).

Documentation of authorship and contribution of third persons

This thesis has been submitted for the degree of “Doktor-Ingenieur” (Dr.-Ing.) to the Faculty of Mechanical Engineering at Technische Universität Chemnitz. I have composed and written this thesis. I have included joint authored work in my thesis mainly based on scientific publications. Parts of reference [154] in this thesis are reproduced with permission from Sowade, E., Blaudeck, T. & Baumann, R. R. Self-Assembly of Spherical Colloidal Photonic Crystals inside Inkjet-Printed Droplets. *Cryst. Growth Des.* **16,** 1017–1026 (2016). Copyright 2016 American Chemical Society.

Any help that I have received with the choice and assessment of materials and/or with the preparation of the thesis itself has been acknowledged and can be found in the publications, in the footnotes of this thesis and specifically in the following text section.

Several persons have contributed to the results of this thesis through funded or non-funded research projects, through student research projects, or through bachelor or master theses. The research works published in scientific journals have been conducted by multiple authors as stated in the references and list of publications. Relevant contributions of these authors were acknowledged in this dissertation. The manufacturing of thousands of thin-film transistors was costly in terms of time, since several manual and sophisticated process steps were involved. Thus, the manufacturing was mostly carried out together with my colleague Kalyan Yoti Mitra and the former student assistants Sunil Kapadia and Christoph Sternkiker.

The associated tasks of the student research projects and student theses were substantially conceptualized and designed by the author of this dissertation. The author of this dissertation coordinated, accompanied and supervised the tasks of the students, and contributed substantially to the acquisition, analysis, interpretation, revision, presentation, reappraisal and re-arrangement of the obtained data.

Following students contributed to the developments and to sections of this dissertation with their experimental support:
Tobias Seifert contributed to the investigation of the evaporation-driven self-assembly process of nanospheres in sessile single droplets as a function of ink composition (Figure 18C and D) in his bachelor thesis “Lösungsmittelvariationen für die drucktechnische Herstellung photonischer Schichten mittels Inkjet” (2009). *Sabine Riemenschneider* supported the statistical analysis of the

reliability of the in-flight self-assembly process (Figure 25) with her bachelor thesis “Herstellung und quantitative Erfassung suprapartikulärer Strukturen mittels Inkjet“ (2010).
Maxim Polomoshnov contributed with his student research project “Elektrische Leitfähigkeit inkjetgedruckter Silberschichten in Abhängigkeit von der Ausrichtung zur Druckrichtung” (2015) substantially to the investigation of the print layout design as a function of its orientation to the printing process presented in Chapter 6.1 (he also contributed data for the preparation of Figure 13, Figure 14 and Figure 29). *Tobias Seifert* has contributed to this before mentioned topic with his master thesis “Deposition of functional materials using Aerosol Jet Technology and drop on demand Inkjet Printing – a comparison” (2012). *Tobias Seifert* generated the raw data of the lines for Figure 37A and captured the images for Figure 37B. *Frank Göthel* initiated unintentionally with his master thesis “Inkjet printing of conductive, patterned thin films on corrugated cardboards for packaging issues” the reflections about the influence of the print pattern orientation angle. He contributed to the development of the print pattern layout of Figure 13.
The study about the different silver inks (Figure 42, Figure 43, Figure 45) was experimentally supported by following students: *Zhongchen Feng* (bachelor thesis “Benchmark zum elektrischen Widerstand von inkjetgedruckten Silbernanopartikeltinten“, 2016), *Zhenxing Xu* (bachelor thesis “Inbetriebnahme eines Rolle-zu-Rolle Inkjetdrucksystems zur Herstellung von Silberelektroden auf Polymerfolien“, 2016), *Maxim Polomoshnov*, *Christoph Sternkiker*, *Parvin Rastegar* and *Sunil Kapadia*. *Anastasia Vlasova* contributed to the investigation of the shrinkage of deposited dielectrics (Figure 46). *Christoph Sternkiker* contributed partially to statistical relevant data of Figure A13.

Dr. Eloi Ramon, Carme Martinez-Domingo, Dr. Ana Alcalde, Marta Pedró, Jofre Pallarès, Dr. Fausta Loffredo, Dr. Fulvia Villani, Prof. Dr. Henrique Leonel Gomes, Prof. Dr. Lluís Terés and *Prof. Dr. Jordi Carrabina* contributed within the EU FP7 project TDK4PE and in the frame of the preparation of conference presentations and journal publications to the design of the TFTs, the selection of materials, their electrical characterization and the statistical analysis.
Dr. Thomas Blaudeck contributed to the design of experiments and the analysis of the presented research about printed nanospheres.

List of publications

Articles in peer-reviewed journals:

1. Moya, A., Sowade, E., del Campo, F. J., Mitra, K. Y., Ramon, E., Villa, R., Baumann, R. R. & Gabriel, G. All-inkjet-printed dissolved oxygen sensors on flexible plastic substrates. Org. Electron. 39, 168–176 (2016).
2. Wang, Y., Guo, H., Chen, J.-J., Sowade, E., Wang, Y., Liang, K., Marcus, K., Baumann, R. R. & Feng, Z.-S. Paper-Based Inkjet-Printed Flexible Electronic Circuits. ACS Appl. Mater. Interfaces 8, 26112–26118 (2016).
3. Castro, H.F., Correia, V., Sowade, E., Mitra, K.Y., Rocha, G., Baumann, R.R., Lanceros-Mendez, S. All-inkjet-printed low-pass filters with adjustable cutoff frequency consisting of resistors, inductors and transistors for sensor applications. *Org. Electron.* **38,** 205–212 (2016).
4. Sowade, E., Polomoshnov, M. & Baumann, R. R. The design challenge in printing devices and circuits: Influence of the orientation of print patterns in inkjet-printed electronics. *Org. Electron.* **37,** 428–438 (2016).
5. Al-Hamry, A., Kang, H., Sowade, E., Dzhagan, V., Rodriguez, R. D., Müller, C., Zahn, D. R. T., Baumann, R. R. & Kanoun, O. Tuning the reduction and conductivity of solution-processed graphene oxide by intense pulsed light. *Carbon* **102,** 236–244 (2016).
6. Sowade, E., Blaudeck, T. & Baumann, R. R. Self-Assembly of Spherical Colloidal Photonic Crystals inside Inkjet-Printed Droplets. *Cryst. Growth Des.* **16,** 1017–1026 (2016).
7. Sowade, E., Mitra, K. Y., Ramon, E., Martinez-Domingo, C., Villani, F., Loffredo, F., Gomes, H. L. & Baumann, R. R. Up-scaling of the manufacturing of all-inkjet-printed organic thin-film transistors: Device performance and manufacturing yield of transistor arrays. *Org. Electron.* **30,** 237–246 (2016).
8. Dinh, N. T., Sowade, E., Blaudeck, T., Hermann, S., Rodriguez, R. D., Zahn, D. R. T., Schulz, S. E., Baumann, R. R. & Kanoun, O. High-resolution inkjet printing of conductive carbon nanotube twin lines utilizing evaporation-driven self-assembly. *Carbon* **96,** 382–393 (2016).
9. Sternkiker, C., Sowade, E., Mitra, K. Y., Zichner, R. & Baumann, R. R. Upscaling of the Inkjet Printing Process for the Manufacturing of Passive Electronic Devices. *IEEE Trans. Electron Devices* **63,** 426–431 (2016).
10. Sowade, E., Kang, H., Mitra, K. Y., Weiß, O. J., Weber, J. & Baumann, R. R. Roll-to-roll infrared (IR) drying and sintering of an inkjet-printed silver nanoparticle ink within 1 second.

J. Mater. Chem. C **3,** 11815–11826 (2015).

11. Sowade, E., Blaudeck, T. & Baumann, R. R. Inkjet Printing of Colloidal Nanospheres: Engineering the Evaporation-Driven Self-Assembly Process to Form Defined Layer Morphologies. *Nanoscale Res. Lett.* **10,** 362 (2015).
12. Gomes, H. L., Medeiros, M. C. R., Villani, F., Canudo, J., Loffredo, F., Miscioscia, R., Martinez-Domingo, C., Ramon, E., Sowade, E., Mitra, K. Y., Baumann, R. R., McCulloch, I. & Carrabina, J. All-inkjet printed organic transistors: Dielectric surface passivation techniques for improved operational stability and lifetime. *Microelectron. Reliab.* **55,** 1192–1195 (2015).
13. Castro, H. F., Sowade, E., Rocha, J. G., Alpuim, P., Machado, A. V., Baumann, R. R. & Lanceros-Méndez, S. Degradation of all-inkjet-printed organic thin-film transistors with TIPS-pentacene under processes applied in textile manufacturing. *Org. Electron.* **22,** 12–19 (2015).
14. Niittynen, J., Sowade, E., Kang, H., Baumann, R. R. & Mäntysalo, M. Comparison of laser and intense pulsed light sintering (IPL) for inkjet-printed copper nanoparticle layers. *Sci. Rep.* **5,** 8832 (2015).
15. Sowade, E., Göthel, F., Zichner, R. & Baumann, R. R. Inkjet printing of UHF antennas on corrugated cardboards for packaging applications. *Appl. Surf. Sci.* **332,** 500–506 (2015).
16. Seifert, T., Sowade, E., Roscher, F., Wiemer, M., Gessner, T. & Baumann, R. R. Additive Manufacturing Technologies Compared: Morphology of Deposits of Silver Ink Using Inkjet and Aerosol Jet Printing. *Ind. Eng. Chem. Res.* **54,** 769–779 (2015).
17. Lorwongtragool, P., Sowade, E., Watthanawisuth, N., Baumann, R. & Kerdcharoen, T. A Novel Wearable Electronic Nose for Healthcare Based on Flexible Printed Chemical Sensor Array. *Sensors* **14,** 19700–19712 (2014).
18. Castro, H. F., Sowade, E., Rocha, J. G., Alpuim, P., Lanceros-Méndez, S. & Baumann, R. R. All-Inkjet-Printed Bottom-Gate Thin-Film Transistors Using UV Curable Dielectric for Well-Defined Source-Drain Electrodes. *J. Electron. Mater.* **43,** 2631–2636 (2014).
19. Kang, H., Sowade, E. & Baumann, R. R. Direct Intense Pulsed Light Sintering of Inkjet-Printed Copper Oxide Layers within Six Milliseconds. *ACS Appl. Mater. Interfaces* **6,** 1682–1687 (2014).
20. Zichner, R., Sowade, E. & Baumann, R. R. Inkjet printed WLAN antenna for an application in smartphones. *Jpn. J. Appl. Phys.* **53,** 05HB06 (2014).
21. Belgardt, C., Sowade, E., Blaudeck, T., Baumgärtel, T., Graaf, H., von Borczyskowski, C. & Baumann, R. R. Inkjet printing as a tool for the patterned deposition of octadecylsiloxane monolayers on silicon oxide surfaces. *Phys. Chem. Chem. Phys.* **15,** 7494–504 (2013).

22. Sowade, E., Hammerschmidt, J., Blaudeck, T. & Baumann, R. R. In-Flight Inkjet Self-Assembly of Spherical Nanoparticle Aggregates. *Adv. Eng. Mater.* **14,** 98–100 (2012).

Back covers in peer-reviewed journals:

1. Sowade, E., Kang, H., Mitra, K. Y., Weiß, O. J., Weber, J. & Baumann, R. R. Roll-to-roll infrared (IR) drying and sintering of an inkjet-printed silver nanoparticle ink within 1 second. *J. Mater. Chem. C* **3,** 11975–11976 (2015).
2. Belgardt, C., Sowade, E., Blaudeck, T., Baumgärtel, T., Graaf, H., von Borczyskowski, C. & Baumann, R. R. Inkjet printing as a tool for the patterned deposition of octadecylsiloxane monolayers on silicon oxide surfaces. *Phys. Chem. Chem. Phys.* **15,** 7897–7898 (2013).
3. Sowade, E., Hammerschmidt, J., Blaudeck, T. & Baumann, R. R. In-Flight Inkjet Self-Assembly of Spherical Nanoparticle Aggregates. *Adv. Eng. Mater.* **14** (2012).

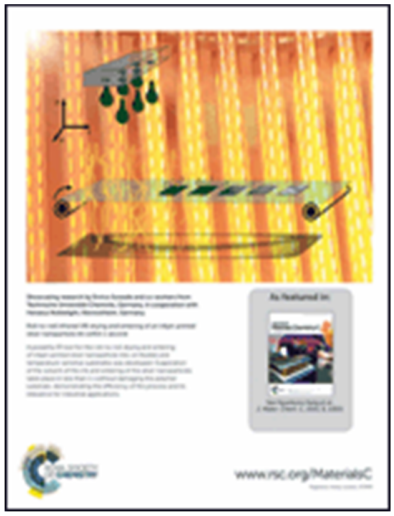

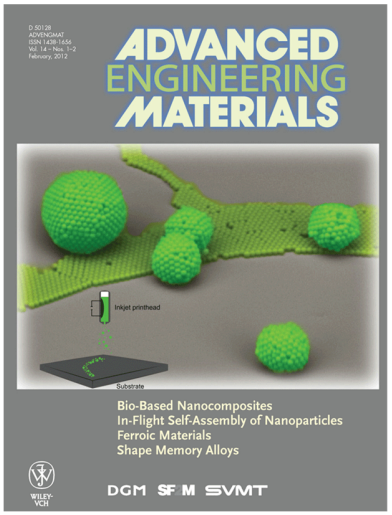

Patents:

1. Sowade, E., Hammerschmidt, J., Blaudeck, T. & Baumann, R. R. Verfahren und Vorrichtung zum Erzeugen einer dreidimensionalen Struktur auf einem Substrat. Patent DE102010063982 A1 (2012). at http://register.dpma.de/DPMAregister/pat/PatSchrifteneinsicht?docId=DE102010063982A1
2. Mitra, D., Sowade, E. & Baumann, R. R. Verfahren zur Strukturierung einer Schicht und Vorrichtung mit einer strukturierten Schicht. Submitted patent application (September 09, 2016)

Invited presentations:

1. Sowade, E. & Baumann, R. R. Printing of functional materials for smart applications. *BCMaterials Anu. Work. 5th New Mater. a Better Life Work. Bilboa, Spain, Novemb. 18,* (2016).
2. Sowade, E. & Baumann, R. R. Printing as a powerful tool for the deposition of functional material patterns. *TechConnect World Innov. Conf. Expo, Washingt. D.C., USA, May 22-25* (2016).
3. Hammerschmidt, J., Sowade, E. & Baumann, R. R. Membranes with pore sizes from some ten nanometers to some microns for biological applications in point of care diagnostics. *EMN (Energy Mater. Nanotechnology) Meet. Dubai, United Arab Emirates, April 5-8* (2016).
4. Sowade, E. & Baumann, R. R. Printing beyond color - manufacturing of smart objects. *Nanomercosur, Buenos Aires, Argentina, Oct. 06-10* (2015).
5. Sowade, E. & Baumann, R. R. Research and development environment for printed electronics in Chemnitz (Germany) and its connection over the world. *Nanomercosur, Buenos Aires, Argentina, Oct. 06-10* (2015).
6. Sowade, E. & Baumann, R. R. Process development for functional layers and devices based on printing technologies. *Natl. Inst. Ind. Technol. - INTI, Buenos Aires, Argentina, Oct. 09* (2015).
7. Sowade, E., Mitra, K. Y., Ramon, E., Villani, F., Gomes, H. L., Carrabina, J. & Baumann, R. R. Inkjet printing of thin-film transistors on flexible substrates. *581. Wilhelm und Else Heraeus-Seminar Flexible, Stretchable Printable High Perform. Electron. Bad Honnef, Ger., January 12-14* (2015).
8. Sowade, E., Belgardt, C., Blaudeck, T. & Baumann, R. R. Self-Assembly of molecules and nanoparticles in inkjet-printed droplets. *EMN (Energy Mater. Nanotechnology) Open Access Week Meet. Chengdu, China, Oct. 21-24* (2013).

Conference contributions:

1. Sowade, E., Mitra, K. Y., Ramon, E., Martinez-Domingo, C., Villani, F., Gomes, H. L. & Baumann, R. R. Manufacturing of all-inkjet-printed transistor arrays on flexible polymer substrates. *SPIE Org. Photonics + Electron. San Diego, USA, August 29 - Sepember 1* (2016).
2. Mitra, K. Y., Sowade, E., Ramon, E., Villani, F., Loffredo, F., Gomes, H. L. & Baumann, R.

R. Performance and reliability mapping for all Inkjet-printed TFT arrays using industrial inkjet accessories. *Int. Exhib. Conf. Print. Electron. Ind. - LOPEC, Munich, Ger. April 5-7* (2016).

3. Mitra, K. Y., Polomoshnov, M., Weise, D., Sowade, E., Martinez-Domingo, C. & Baumann, R. R. All Inkjet-printed OTFT manufactured on paper substrate for cheap printed electronic applications. *Spring Meet. Eur. Mater. Res. Soc. (E-MRS), Lille, Fr. May 11-15* (2015).
4. Sternkiker, C., Sowade, E., Mitra, K. Y., Zichner, R. & Baumann, R. R. Inkjet printing of passive electronic components using industrial printheads. *581. Wilhelm und Else Heraeus-Seminar Flexible, Stretchable Printable High Perform. Electron. Bad Honnef, Ger. , January 12-14* (2015).
5. Mitra, K. Y., Sowade, E., Martínez-Domingo, C., Ramon, E., Carrabina, J., Gomes, H. L. & Baumann, R. R. Potential up-scaling of inkjet-printed devices for logical circuits in flexible electronics. in *AIP Conf. Proc. 1646* **106,** 106–114 (2015).
6. Mitra, K. Y., Sowade, E., Sternkiker, C., Martínez-Domingo, C., Ramon, E., Carrabina, J. & Baumann, R. R. Investigation on Electrical Stress over Metal-Insulator-Metal (MIM) Structures Based on Compound Dielectrics for the Inkjet-Printed OTFT Stability. *Appl. Mech. Mater.* **748,** 129–133 (2015).
7. Willert, A., Sowade, E., Helmert, M., Zichner, R. & Baumann, R. R. Functional Material Deposition and Functionality Forming – Applications and Machinery. *Mater. Res. Soc. Fall Meet. Exhib. Boston, USA, Novemb. 30 - December 5* (2014).
8. Weise, D., Mitra, K. Y., Sowade, E. & Baumann, R. R. Intense Pulsed Light Sintering of Inkjet Printed Silver Nanoparticle Ink: Influence of Flashing Parameters and Substrate. in *Mater. Res. Soc. Fall Meet. Exhib. Boston, USA, Novemb. 30 - December 5* (2014).
9. Sowade, E., Mitra, K. Y., Ramon, E., Villani, F., Gomes, H. L., Carrabina, J. & Baumann, R. R. Reliability of Industrial Inkjet Printing for the Manufacturing of Thin-Film Transistors. in *Mater. Res. Soc. Fall Meet. Exhib. Boston, USA, Novemb. 30 - December 5* (2014).
10. Mitra, K. Y., Sowade, E., Sternkiker, C., Martinez-Domingo, C., Ramon, E., Carrabina, J. & Baumann, R. R. Investigation on electrical stress over metal-insulator-metal (MIM) structures based on compound dielectrics for the inkjet-printed OTFT stability. in *5th Int. Conf. Flex. Print. Electron. (ICFPE), Beijing, China, Oct. 21-23* (2014).
11. Zichner, R., Hammerschmidt, J., Weise, D., Sowade, E. & Baumann, R. R. Inkjet printing and sintering techniques of functional layers for electronic applications. in *Inkjet Conf. Düsseldorf, Ger. Sept. 30 - Oct. 1* (2014).
12. Mitra, K. Y., Sowade, E., Martinez-Domingo, C., Ramon, E. & Baumann, R. R. Potential up-scaling of Inkjet-printed devices for logical circuits in flexible electronics. in *7th Int. Symp.*

Flex. Org. Electron. (ISFOE14), Thessaloniki, Greece, July 9-12 (2014).

13. Mitra, K. Y., Sowade, E., Martinez-Domingo, C., Ramon, E. & Baumann, R. R. Inkjet Printing of functional devices e.g. organic TFT´s and towards circuits. in *8th Int. Summer Sch. Nanosci. Nanotechnologies, Org. Electron. Nanomedicine (ISSON14), Thessaloniki, Greece, July 6-12* (2014).
14. Mitra, K. Y., Martinez-Domingo, C., Sowade, E., Ramon, E., Gomes, H. L. & Baumann, R. R. Inkjet-printed diodes based on metal-insulator-semiconductor (MIS) structure for rectifying application in flexible electronics. in *Int. Exhib. Conf. Print. Electron. Ind. - LOPEC, Munich, Ger. May 26-28* (2014).
15. Sowade, E., Mitra, K. Y., Villani, F., Gomes, H. L., Carrabina, J. & Baumann, R. R. Manufacturing of thin-film transistors using industrial inkjet printheads. in *Int. Exhib. Conf. Print. Electron. Ind. - LOPEC, Munich, Ger. May 26-28* (2014).
16. Ramon, E., Sowade, E., Mitra, K. Y. & Baumann, R. R. An inkjet adaptive backend strategy for low-yield OTFT digital circuit. *Int. Exhib. Conf. Print. Electron. Ind. - LOPEC, Munich, Ger. May 26-28* (2014).
17. Sowade, E., Belgardt, C., Blaudeck, T. & Baumann, R. R. Self-Assembly of Molecules and Colloidal Particles in Evaporating Inkjet Droplets. in *Mater. Res. Soc. Fall Meet. Exhib. Boston, USA, December 1-6* (2013).
18. Mitra, K. Y., Martinez-Domingo, C., Sowade, E., Ramon, E., Gomes, H. L. & Baumann, R. R. Inkjet-Printed Rectifying Metal-Insulator-Semiconductor (MIS) Diodes for Flexible Electronic Applications. in *Mater. Res. Soc. Fall Meet. Exhib. Boston, USA, December 1-6* (2013).
19. Weise, D., Grimm, A., Weiss, U., Mitra, K. Y., Sowade, E. & Baumann, R. R. Conductivity and Microstructure of Inkjet-Printed Silver Tracks Depending on the Digital Pattern, Sintering Process, Substrate and Ink. in *Mater. Res. Soc. Fall Meet. Exhib. Boston, USA, December 1-6* (2013).
20. Weise, D., Mitra, K. Y., Sowade, E. & Baumann, R. R. Intense pulsed light sintering of inkjet printed silver patterns on a flexible polymeric substrate and the influence of flashing parameters. in *Swiss ePrint – Swiss Conf. Print. Electron. Funct. Mater. Basel, Switzerland, Novemb. 21-22* (2013).
21. Mitra, K. Y., Sowade, E., Ramon, E., Villani, F., Gomes, H. L., Carrabina, J. & Baumann, R. R. Manufacturing of electronic devices using industrial piezo inkjet printheads. in *Swiss ePrint – Swiss Conf. Print. Electron. Funct. Mater. Basel, Switzerland, Novemb. 21-22* (2013).
22. Kang, H., Sowade, E. & Baumann, R. R. Photonic Sintering of Inkjet Printed Copper Oxide

Layer. in *29th Int. Conf. Digit. Print. Technol. / Digit. Fabr. (NIP29), Seattle, USA, Sept. 29 -October 3* (2013).

23. Sowade, E., Hammerschmidt, J., Mitra, K. Y., Kang, H., Weise, D. & Baumann, R. R. Der Inkjetdruck als Beschichtungstechnologie für funktionale Schichtsysteme. in *16. Werkstofftechnisches Kolloquium und 10. Ind. Oberflächen- und Wärmebehandlungstechnik, Chemnitz, Ger. Sept. 5-6* (2013).
24. Birgi, Ö., Mitra, K. Y., Sowade, E., Baumann, R. R., Ramon, E. & Martinez-Domingo, C. Suitability of inkjet printed OTFTs for Logical circuits. in *5th Int. Sci. Conf. Print Media Technol. Jr. Sci. PhD Students (Printing Futur. Days), Chemnitz, Ger. Sept. 10-12* (2013).
25. Kang, H., Sowade, E. & Baumann, R. R. Influence of photonic sintering parameters on electrical properties in the inkjet-printed copper oxide layers. in *Int. Exhib. Conf. Print. Electron. Ind. - LOPEC, Munich, Ger. June 11-13* (2013).
26. Sowade, E., Mitra, K. Y., Ramon, E., Villani, F., Gomes, H. L., Carrabina, J. & Baumann, R. R. Manufacturing of electronic devices using laboratory inkjet printing and basic approaches towards up-scaling. in *Int. Exhib. Conf. Print. Electron. Ind. - LOPEC, Munich, Ger. June 11-13* (2013).
27. Weber, J., Sowade, E., Siegel, F., Mitra, K. Y., Zissing, H. & Baumann, R. R. Tools for Curing, Drying and Sintering in Printed Electronics. in *Int. Exhib. Conf. Print. Electron. Ind. - LOPEC, Munich, Ger. June 11-13* (2013).
28. Sowade, E., Mitra, K. Y., Gomes, H. L. & Baumann, R. R. Inkjet-printed electronics: Transfer from lab to fab manufacturing. in *Smart Syst. Integr. - Int. Conf. Exhib. Integr. Issues Miniaturized Syst. Amsterdam, Netherlands, March 13-14* (2013).
29. Willert, A., Espig, M., Sowade, E. & Baumann, R. R. Adapted printed battery development for driving a smart miniaturised cholesterol sensing system. in *Smart Syst. Integr. - Int. Conf. Exhib. Integr. Issues Miniaturized Syst. Amsterdam, Netherlands, March 13-14* (2013).
30. Medeiros, M. C. R., Martinez-Domingo, C., Ramon, E., Negrier, A. T., Sowade, E., Mitra, K. Y., Baumann, R. R., McCulloch, I., Carrabina, J. & Gomes, H. L. Inkjet-Printed Organic Electronics: Operational Stability and Reliability Issues. in *ECS Trans.* **53,** 1–10 (2013).
31. Sowade, E., Blaudeck, T. & Baumann, R. R. Preparation of spherical, ordered colloidal aggregates using inkjet printing. in *MRS Proc.* **1453,** mrss12–1453–aaa03–04 (2013).
32. Sowade, E., Belgardt, C., Blaudeck, T. & Baumann, R. R. Bottom-Up Nanoengineering by Combining Directed Self-assembly and Inkjet Printing. in *Mater. Res. Soc. Fall Meet. Exhib. Boston, USA, Novemb. 25-30* (2012).
33. Lorwongtragool, P., Sowade, E., Hammerschmidt, J., Kerdcharoen, T. & Baumann, R. R.

Inkjet Printing of Chemiresistive Sensors for the Detection of Volatile Organic Compounds. in *28th Int. Conf. Digit. Print. Technol. / Digit. Fabr. (NIP28), Quebec, Canada, Sept. 9-13* (2012).

34. Hammerschmidt, J., Sowade, E., Mitra, K. Y., Wohlleben, L. M. & Baumann, R. R. The Influence of Post-Treatment Strategies in Inkjet Printing on the Morphology of Layers and the Functional Performances of Electronic Devices. in *28th Int. Conf. Digit. Print. Technol. / Digit. Fabr. (NIP28), Quebec, Canada, Sept. 9-13* (2012).
35. Lorwongtragool, P., Sowade, E., Kerdcharoen, T. & Baumann, R. R. All Inkjet-Printed Chemical Gas Sensors Based on CNT/Polymer Nanocomposites: Comparison between Double Printed Layers and Blended Single Layer. in *ECTI-CON2012 - 9th Int. Conf. Electr. Eng. Comput. Telecommun. Inf. Technol. Assoc. Hua Hin, Thailand, May 16-18* (2012).
36. Lorwongtragool, P., Sowade, E., Baumann, R. R. & Kerdcharoen, T. Towards Polymer/CNT Gas Sensor using Inkjet printing. in *7th Annu. Conf. Thai Phys. Soc. (SPC), Phra Nakhon Si Ayutthaya, Thailand, May 9-12* (2012).
37. Sowade, E., Blaudeck, T. & Baumann, R. R. Preparation of Spherical, Ordered Colloidal Aggregates Using Inkjet Printing. in *Mater. Res. Soc. Spring Meet. Exhib. San Fr. USA, April 9-12* (2012).
38. Benchirouf, A., Sowade, E., Al-Hamry, A., Blaudeck, T., Kanoun, O. & Baumann, R. R. Investigation of RFID passive strain sensors based on carbon nanotubes using inkjet printing technology. in *9th Int. Multi-Conference Syst. Signals Devices (SSD), Chemnitz, Ger. March 20-23* (2012).
39. Lorwongtragool, P., Sowade, E., Dinh, N. T., Kanoun, O., Kerdcharoen, T. & Baumann, R. R. Inkjet printing of chemiresistive sensors based on polymer and carbon nanotube networks. in *9th Int. Multi-Conference Syst. Signals Devices (SSD), Chemnitz, Ger. March 20 - 23* (2012).
40. Sowade, E. & Baumann, R. R. Smart Objects - Einführung in gedruckte Funktionalitäten. in *Erfinderworkshop Begreifbare Interaktion, Fak. Inform. TU Dresden, Dresden, Ger. March 2* (2012).
41. Sowade, E. & Baumann, R. R. Printing Technologies. in *Train. Week EU FP7 Proj. TDK4PE, Barcelona, Spain, Febr. 6-8* (2012).
42. Lorwongtragool, P., Sowade, E., Dinh, N. T., Kanoun, O., Kerdcharoen, T. & Baumann, R. R. All Inkjet-printed Chemical Sensor Based on CNT/Polymer layers. in *4th Int. Sci. Conf. Print Media Technol. Jr. Sci. PhD Students (Printing Futur. Days), Chemnitz, Ger. Novemb. 7-10* (2011).
43. Müller, M., Roscher, F., Sowade, E., Seifert, T., Wiemer, M., Gessner, T. & Baumann, R.

R. Aerosol Jet as a Deposition Method for Conductive Layers in Micro-Systems-Technology using Nanoparticle Inks. in *4th Int. Sci. Conf. Print Media Technol. Jr. Sci. PhD Students (Printing Futur. Days), Chemnitz, Ger. Novemb. 7-10* (2011).

44. Benchirouf, A., Sowade, E., Blaudeck, T., Kanoun, O. & Baumann, R. R. Design and Characterization of Inkjet-printed Passive Wireless Strain Sensor Based on Carbon Nanotubes. in *4th Int. Sci. Conf. Print Media Technol. Jr. Sci. PhD Students (Printing Futur. Days), Chemnitz, Ger. Novemb. 07-10* (2011).
45. Seifert, T., Sowade, E., Hammerschmidt, J. & Blaudeck, T. Ink variation for the deposition of three-dimensional nanoparticle patterns using inkjet printing. in *4th Int. Sci. Conf. Print Media Technol. Jr. Sci. PhD Students (Printing Futur. Days), Chemnitz, Ger. Novemb. 7-10* (2011).
46. Dinh, N. T., Sowade, E., Blaudeck, T., Kanoun, O. & Baumann, R. R. Sheet resistances and strain dependent characteristics of inkjet-printed carbon nanotube thin film. in *4th Int. Sci. Conf. Print Media Technol. Jr. Sci. PhD Students (Printing Futur. Days), Chemnitz, Ger. Novemb. 07-10* (2011).
47. Sowade, E. Applikationen inkjetgedruckter Dünnschichtsysteme auf Basis von Kohlenstoffnanoröhren (CNTs)Title. in *OES-Weiterbildungsseminar "Drucktechnologien für den Funktionsdruck", Chemnitz, Ger. Sept. 28* (2011).
48. Sowade, E., Dinh, N. T., Arreba, A., Seifert, T., Blaudeck, T., Kanoun, O. & Baumann, R. R. Deposition and Self-Assembly of Multiwalled Carbon Nanotube Thin Films by Piezo Inkjet Printing. in *Smart Syst. Integr. - Int. Conf. Exhib. Integr. Issues Miniaturized Syst. Dresden, Ger. March 22-23* (2011).
49. Dinh, N. T., Kanoun, O., Arreba, A., Blaudeck, T., Sowade, E., Belau, R. & Baumann, R. R. Performance of Liquid-Deposited Multiwalled Carbon Nanotube Films under Strain. in *Smart Syst. Integr. - Int. Conf. Exhib. Integr. Issues Miniaturized Syst. Dresden, Ger. March 22-23* (2011).
50. Willert, A., Lucas, J., Sowade, E., Rahnfeld, C., Heilmann, A. & Baumann, R. R. Precise Absorbent Ink Deposition and Optical Inspection System. in *Mater. Res. Soc. Fall Meet. Exhib. Boston, USA, Novemb. 29 - December 3* (2010).
51. Hammerschmidt, J., Eck, E.-M., Sowade, E., Goedel, W. & Baumann, R. R. Inkjet-Printed Microsieves. in *7th ROND Conf. Örnsköldsvik, Sweden, March 1* (2011).
52. Hammerschmidt, J., Eck, E.-M., Sowade, E., Jahn, S. F., Ebert, S., Morschhauser, A., Goedel, W. & Baumann, R. R. Complete Digital Fabrication of Polymeric Microsieves. in *26th Int. Conf. Digit. Print. Technol. / Digit. Fabr. (NIP26), Austin TX, USA, Sept. 19-23* (2010).

53. Sowade, E., Belgardt, C., Hammerschmidt, J., Baumgärtel, T., Blaudeck, T., Graaf, H., Baumann, R. R. & Borczyskowski, C. von. Evaporation-assisted self-assembly of functional layers upon inkjet printing. in *Int. Exhib. Conf. Print. Electron. Ind. - LOPEC, Frankfurt a. M., Ger. May 31 - June 2* (2010).

54. Arreba, A., Sowade, E., Dinh, N. T., Blaudeck, T., Kanoun, O. & Baumann, R. R. Morphology and conductivity characterizations of inkjet-printed multi-walled carbon nanotubes. in *6th Zsigmondy Colloq. Ger. Colloid Soc. Chemnitz, Ger. March 22-24* (2010).

55. Sowade, E., Seifert, T., Hammerschmidt, J., Blaudeck, T., Baumann, R. R., Perelaer, J., Schubert, U. S. & Baumann, R. R. Structured layers of sub-micron spherical colloids by inkjet printing. in *6th Zsigmondy Colloq. Ger. Colloid Soc. Chemnitz, Ger. March 22-24* (2010).

56. Sowade, E., Seifert, T., Hammerschmidt, J., Blaudeck, T. & Baumann, R. R. Inkjet-Printing of Polymer Microspheres. in *3th Int. Sci. Conf. Print Media Technol. Jr. Sci. PhD Students (Printing Futur. Days), Chemnitz, Ger. Novemb. 2-5* (2009).

57. Sowade, E., Hammerschmidt, J., Polster, D., Wagner, R., Baumgärtel, T., Blaudeck, T., Graaf, H., Cichos, F., Borczyskowski, C. von & Baumann, R. R. Inkjet Printing of Polymer Microspheres. in *25th Int. Conf. Digit. Print. Technol. / Digit. Fabr. (NIP25), Louisville, USA, Sept. 19-25* (2009).

58. Sowade, E., Hammerschmidt, J., Polster, D., Wagner, R., Baumgärtel, T., Blaudeck, T., Graaf, H., Cichos, F. & Borczyskowski, C. von. Inkjet-Printing of Polymer Microspheres. in *DPG Spring Meet. Dresden, Ger. March 22-27* (2009).

APPENDIX A

Formation of colloidal hemispheres on hydrophobic PTFE substrates

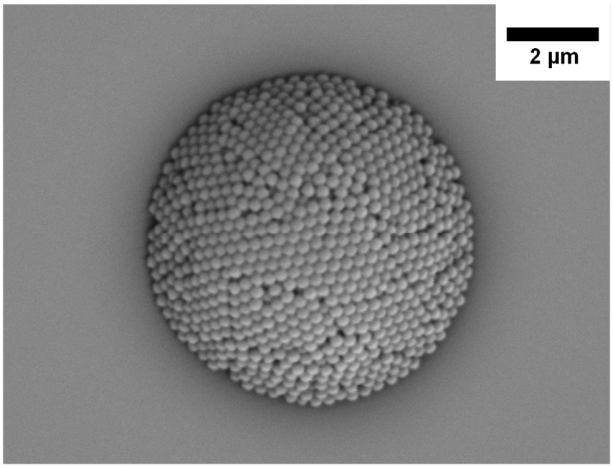

Figure A1: Inkjet-printed colloidal hemisphere using BS305 (adapted from [154])

APPENDIX B

Inkjet-printed higher-order cluster with N < 100 using BL280

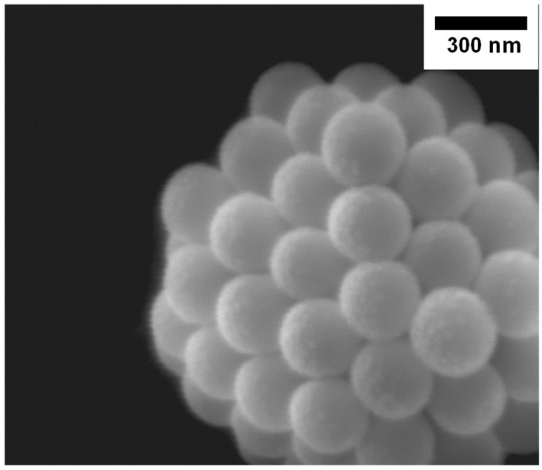

Figure A2: Inkjet-printed higher-order cluster

APPENDIX C

Inkjet-printed SCAs based on BS305 with similar sizes and inkjet-printed SCA based on PSC221

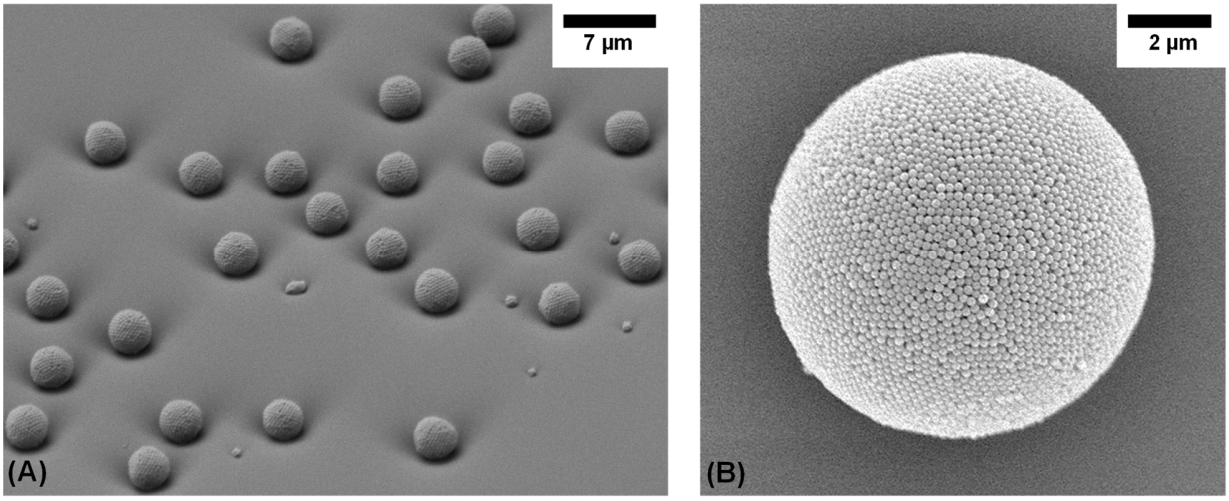

Figure A3: (A) inkjet-printed SCAs based on BS305 with similar sizes, and (B) SCA based on PSC221 (adapted from [154])

APPENDIX D

Microreflectance spectra of SCAs and the processing of the spectra using the Savitzky-Golay filter with a second-order polynomial and a moving window of 100 data points

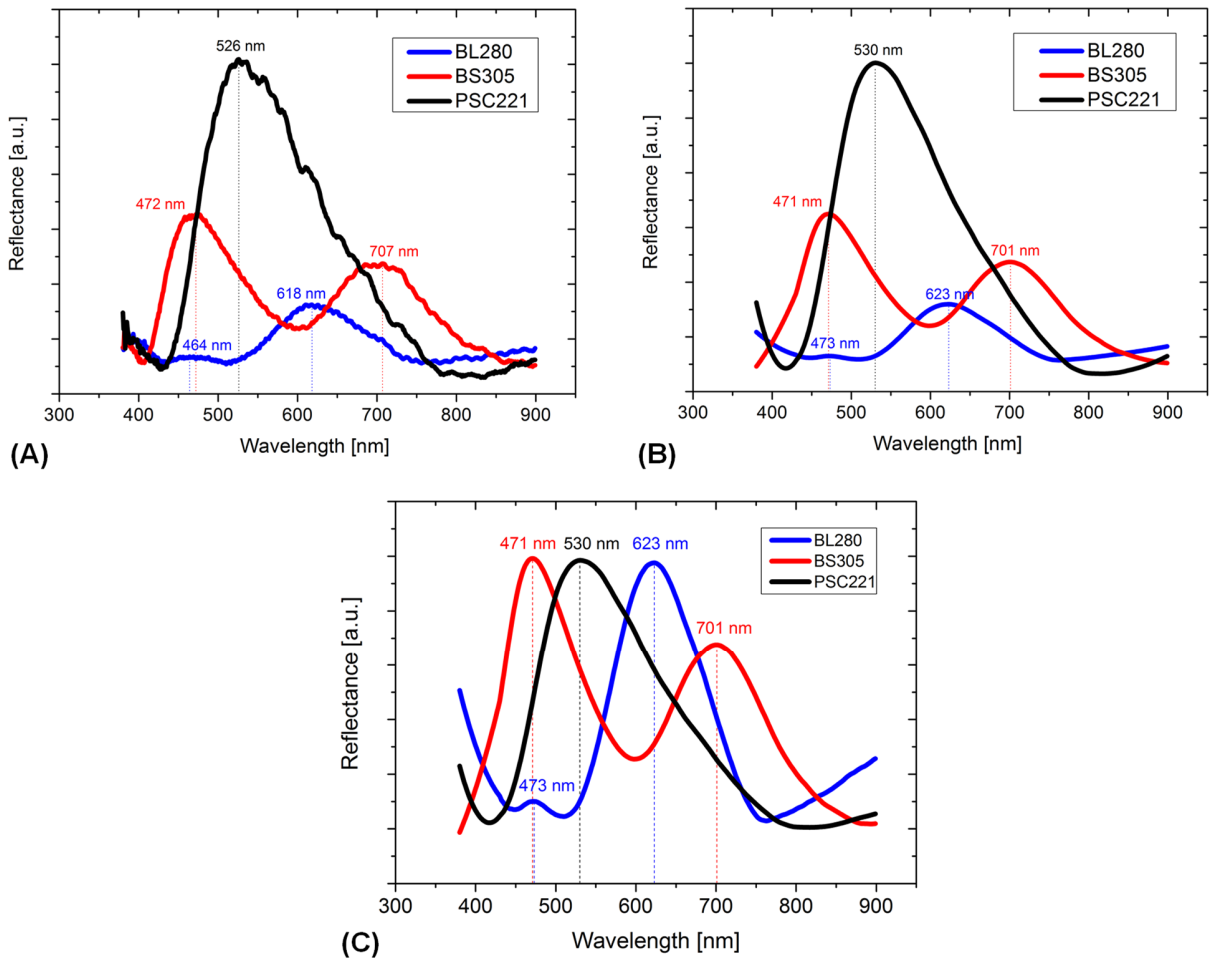

Figure A4: Influence of data processing on microreflectance spectra of inkjet-printed SCAs based on BL280, BS305 and PSC221; (A) plot of the raw data as obtained from the spectrometer software; (B) plot after data smoothing using the Savitzky-Golay filter with a second-order polynomial considering a moving window of 100 data points and (C) after normalizing the reflection

APPENDIX E

Waveform, drop ejection and photographs of the printed patterns of Sun Chemical EMD5603 and UTDots UTDAgIJ1

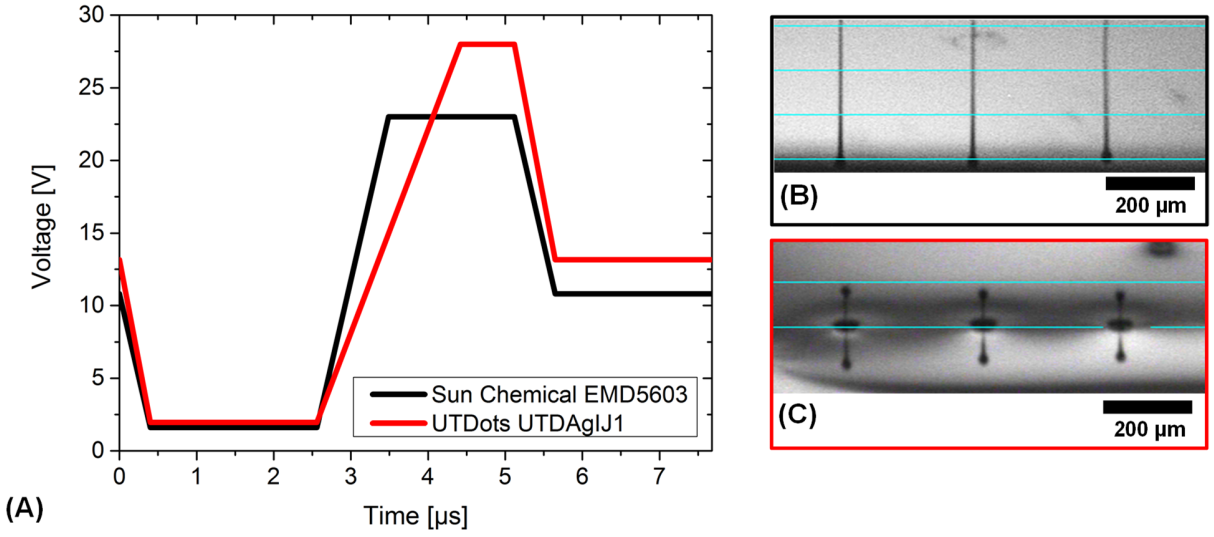

Figure A5: (A) waveforms applied to the inkjet printhead of the inks from Sun Chemical and UTDots, (B) shows the drop ejection of the Sun Chemical ink and (C) shows the drop ejection of the UTDots ink (the droplets moving upwards are a mirror image of the silicon nozzle plate of the printhead), both captured with a drop-watcher camera of the DMP 2831 by applying the corresponding waveform depicted in (A) (adapted from [95])

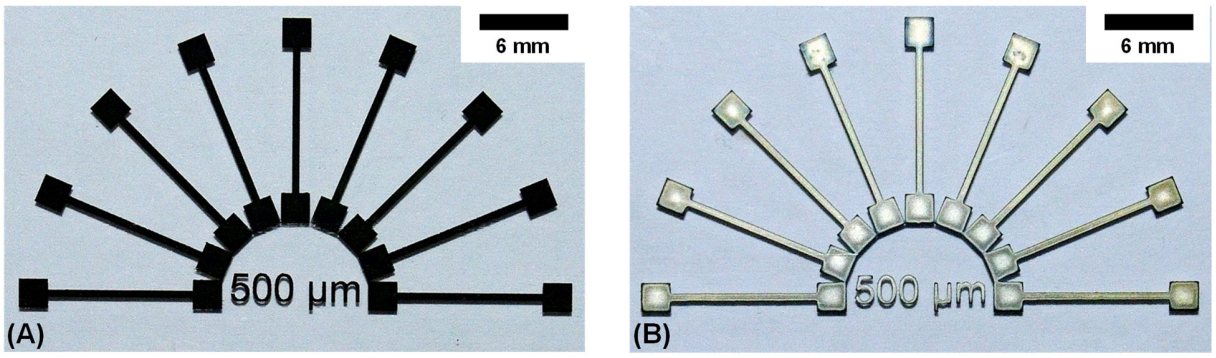

Figure A6: Photographs of the inkjet-printed pattern layouts with (A) EMD5603 and (B) UTDotAgIJ1 ink at a print resolution of 847 dpi; the EMD5603 ink appears black in the photograph due to its smooth highly reflective silver surface[95]

APPENDIX F

Smoothening of profiles obtained by profilometry of EMD5603 and UTDAgIJ1 and dependency of print resolution of layer height

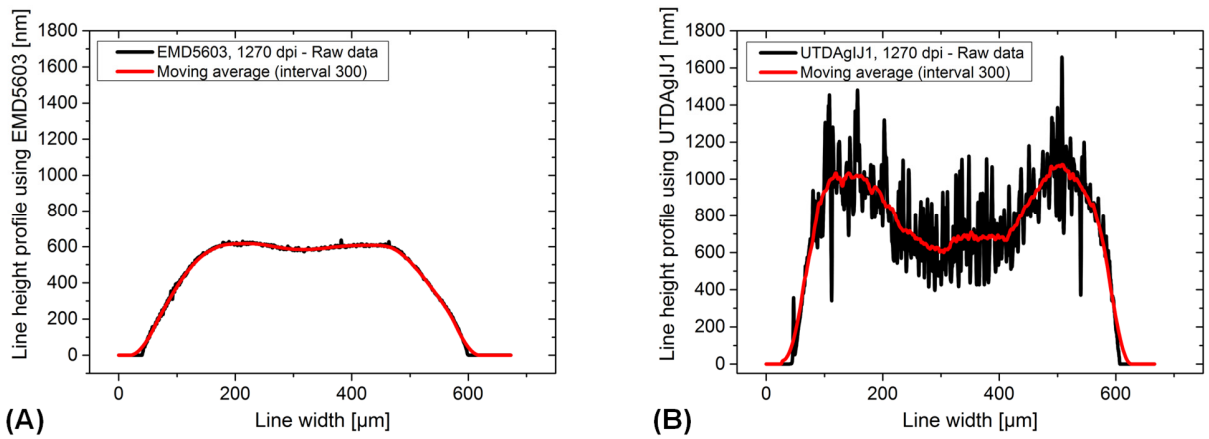

Figure A7: Comparison of raw data line height profiles of the printed inks (A) EMD5603 and (B) UTDAgIJ1 at exemplarily 1270 dpi and the smoothened profiles based on the moving average (adapted from [95])

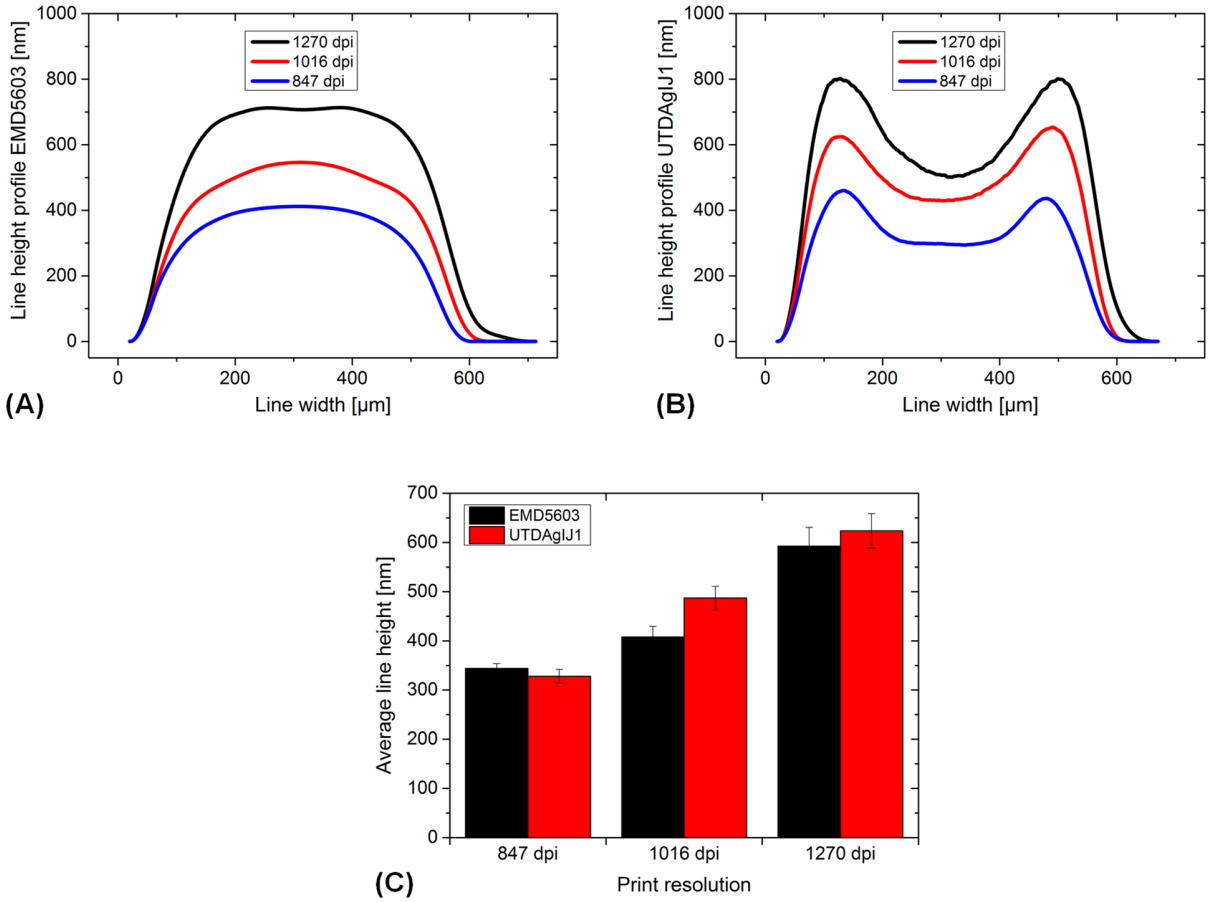

Figure A8: Averaged surface profilometry scans of the inkjet-printed lines using (A) EMD5603 and (B) UTDAgIJ1 as a function of print resolution; (C) shows the averaged line heights (adapted from [95])

APPENDIX G

Percentage of area increase based on a 4 mm x 4 mm digital print pattern using the ink Harima NPS-JL and influence of print resolution and post-treatment temperature on sheets resistance

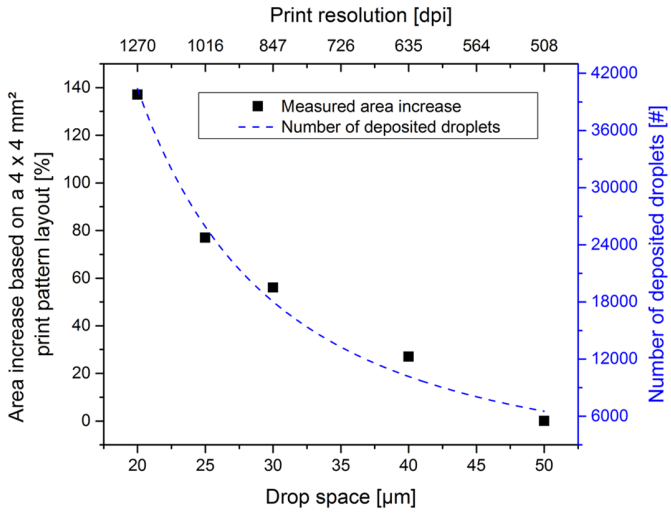

Figure A9: Area increase and number of deposited droplets of an inkjet-printed square pattern with the digital size of 4 mm x 4 mm as a function of print resolution

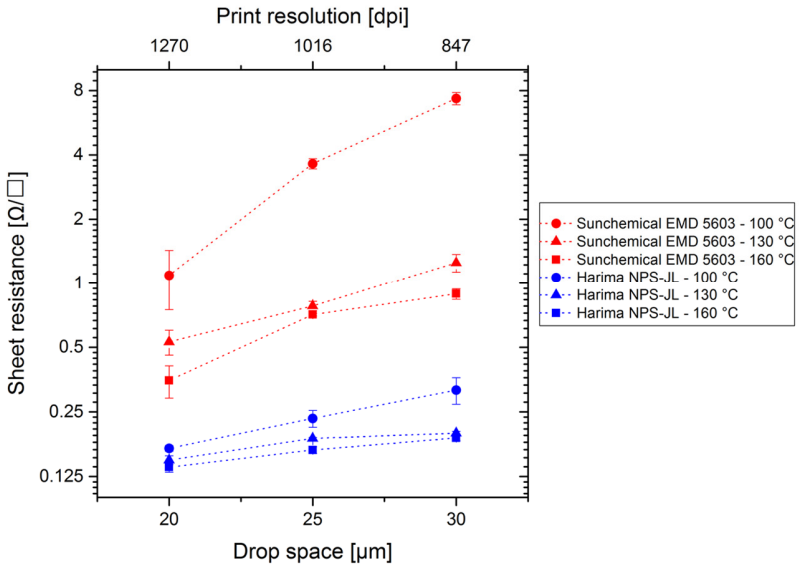

Figure A10: Sheet resistance as a function of print resolution and drying and sintering temperature using the inks Sun Chemical EMD5603 and Harima NPS-JL

APPENDIX H

Cross-sectional view of a TFT stack printed with the dielectric Sun Chemical EMD6415 that shows high layer thickness due to ink contraction after the deposition as presented in Figure 46

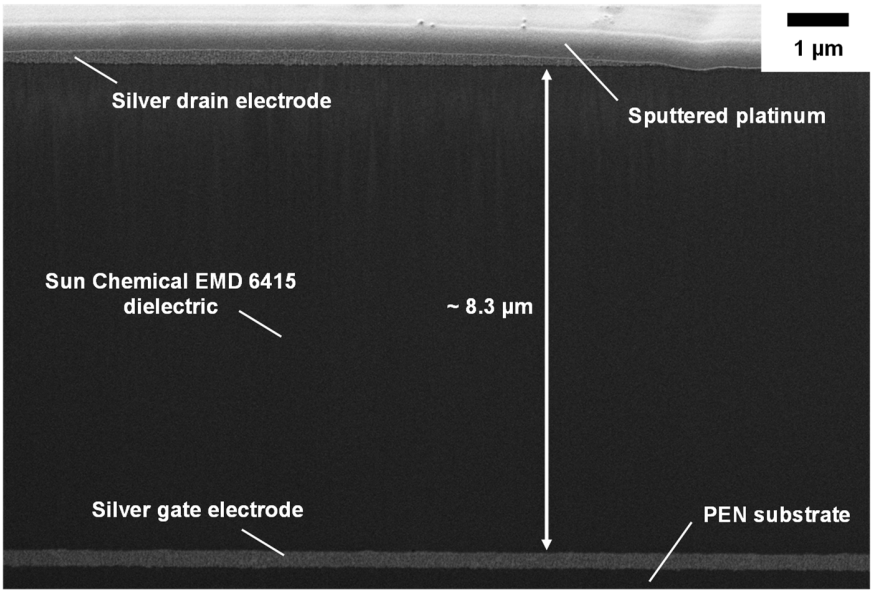

Figure A11: Cross-sectional view of a TFT printed with the DMP 2831 using Sun Chemical EMD6415 as dielectric material

APPENDIX I

Influence of printing parameters on the dielectric layer applied in the TFT

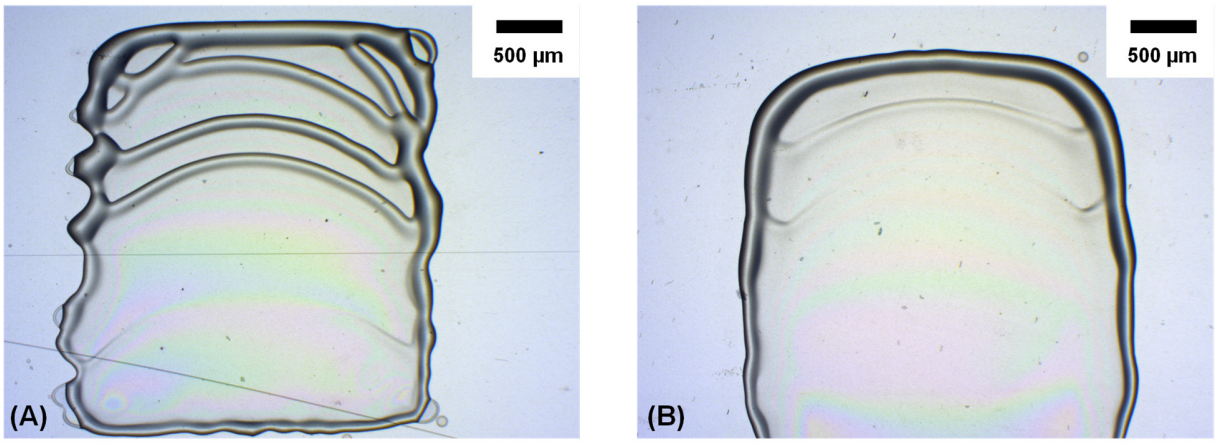

Figure A12: The evaporation process determines the final morphology of the cPVP dielectric layer and needs to be adjusted precisely; (A) shows a cPVP film with multi coffee-rings in the center area due to inhomogeneous drying resulting from a slow printing process (16 nozzles, 10 pL nominal droplet volume and the substrate was heated to 40 °C - too less material deposited per area and time leading to premature drying so that evaporation is inhomogeneous) (adapted from [176]); (B) is a optimization of (A) with reduced multiple coffee-ring effect due to faster material deposition (27 nozzles, 10 pL nominal droplet volume and the substrate heated to 35 °C)

APPENDIX J

Reduction of channel length by decreasing the S-D electrode channel length in the print pattern layout

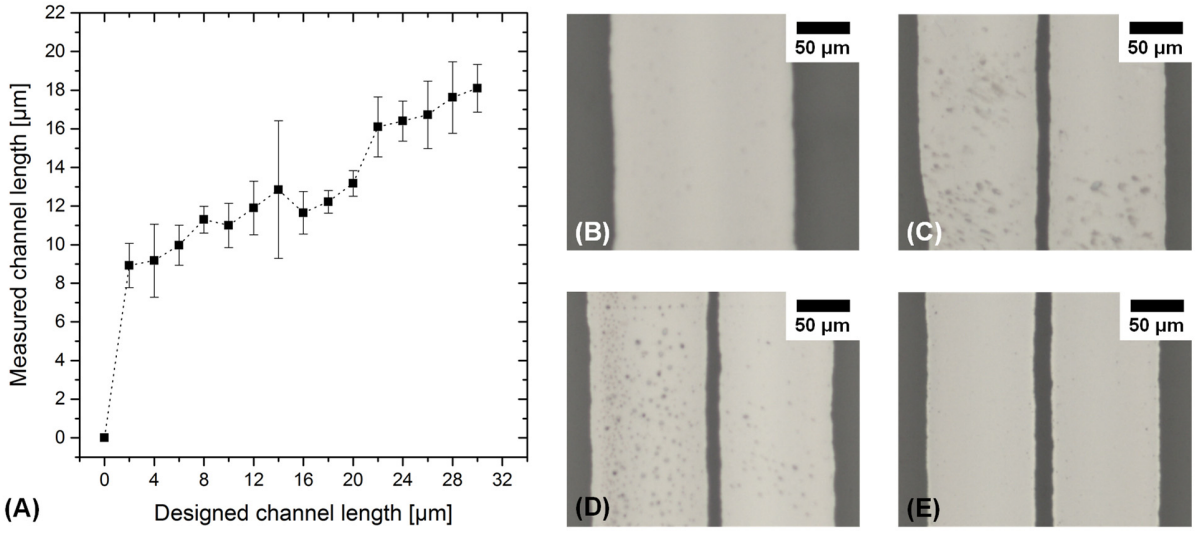

Figure A13: (A) channel length obtained by measurement using light microscopy images as a function of designed channel length in the print pattern layout file; (B)-(E) are microscopic images of the S-D electrode channel at a designed channel length of (B) 0 µm, (C) 2 µm, (D) 12 µm and (E) 30 µm; the printing was performed with the DMP 3000 equipped with SE3 printheads, Sun Chemical EMD5603 and a print resolution of 635 dpi